



DISSERTATION

Mechanical and metallographic characterization of the ternary  
Sn/Bi/In solder system for self-healing applications

Ausgeführt am Institut für  
Werkstoffwissenschaften und Werkstofftechnologie  
der Technischen Universität Wien  
Getreidemarkt 9  
1060 Wien  
unter der Anleitung von

Univ.-Prof. Dipl.-Ing. Dr.techn. Ernst Kozeschnik

durch

Dipl. Ing. DAVID MELINC, BSc

Matrikelnummer 1125165



---

Datum

David Melinc



Die approbierte gedruckte Originalversion dieser Dissertation ist an der TU Wien Bibliothek verfügbar.  
The approved original version of this doctoral thesis is available in print at TU Wien Bibliothek.

This work was supported by FFG within the framework of the project SOLARIS, project number: 864808.

I confirm that going to press of this thesis needs the confirmation of the examination committee.

### *Affidavit*

I declare in lieu of oath, that I wrote this thesis and performed the associated research myself, using only literature cited in this volume. If text passages from sources are used literally, they are marked as such.

I confirm that this work is original and has not been submitted elsewhere for any examination, nor is it currently under consideration for a thesis elsewhere.

---

City and Date

---

Signature

# Kurzfassung

In dieser Arbeit werden mechanische und metallographische Untersuchungen am ternären Sn/Bi/In-Lotsystem für selbstheilende Anwendungen vorgestellt. Die Studie beginnt mit einer detaillierten Analyse des ternären Systems unter Anwendung der CALPHAD-Methode, um den Zusammensetzungsbereich der Lote auf gewünschte mikrostrukturelle Eigenschaften in Bezug auf die besondere Umgebung in mikroelektronischen Geräten zu untersuchen. Die Lötlegierung Sn<sub>37</sub>Bi<sub>4</sub>In wurde aufgrund ihrer mechanischen und mikrostrukturellen Eigenschaften, ergänzt durch wärmeausgelöste Heilungseffekte bei niedrigen Temperaturen, ausgewählt. Eine erweiterte Untersuchung des Einflusses von Temperatur und Legierungselementen, einschließlich Langzeitstabilitätstests oberhalb der Solidustemperatur, bewertet die Entwicklung der Mikrostruktur und der mechanischen Leistung. Um festzustellen, ob das Sn<sub>37</sub>Bi<sub>4</sub>In-Lot, das stellvertretend für das ternäre System steht, bei anwendungstypischen Temperaturen ausheilen kann, werden hundeknochenförmige Proben geformt, bearbeitet und durch Zug-Druck-Zyklen plastisch geschädigt (Belastungsprotokoll). Im anschließenden Heilungsschritt wird der Effekt der flüssigkeitsunterstützten Heilung mit unterschiedlichen Flüssigphasenanteilen genutzt. Bei der Auswertung wird die mechanische Leistung der zuvor ermüdeten Proben und der geheilten Proben anhand von Spannungs-Dehnungs-Kurven aus Zugversuchen beurteilt und in signifikante Materialparameter für die weitere Auswertung umgerechnet.

# Abstract

This work presents mechanical and metallographic investigations in the Sn/Bi/In ternary solder system for self-healing applications. The study starts with a detailed analysis of the ternary system under the application of the CALPHAD method to scan the composition range of solders for desired microstructural properties related to the distinct environment in microelectronic devices. The solder alloy Sn<sub>37</sub>Bi<sub>4</sub>In is chosen due to its pursuant mechanical and microstructural properties complemented with heat-triggered healing effects at low temperatures. An extended investigation on the influence of temperature and alloying elements, including long-term stability tests above the solidus temperature, evaluates the evolution of microstructure and mechanical performance. To determine whether the Sn<sub>37</sub>Bi<sub>4</sub>In solder, as a representative for the ternary system, can be healed at application-typical temperatures, dog bone-shaped specimens are mold, machined, and plastically damaged during tension-compression cycling (loading protocol). In the subsequent healing step, the effect of liquid-assisted healing with different liquid phase fractions is utilized. In the evaluation process, the mechanical performance of beforehand fatigued samples and the healed samples is assessed by stress-strain curves of tensile tests and converted into significant materials parameters for further evaluation.

It Always  
Seems  
Impossible  
Until it's done

-Nelson Mandela

# Publications

Damage and Healing method to study liquid assisted healing properties of cyclic failed bulk solder; D. Melinc, J. Magnien, G. Siroky, D. Kieslinger, E. Kozeschnik; 2020 21st International Conference on Thermal, Mechanical and Multi-Physics Simulation and Experiments in Microelectronics and Microsystems (EuroSimE); Cracow, Poland; July 2020; <https://doi.org/10.1109/EuroSimE48426.2020.9152735>

Lap shear test for solder materials: Local stress states and their effect on deformation and damage; G. Siroky, J. Magnien, D. Melinc, E. Kozeschnik, D. Kieslinger, E. Kraker, W. Ecker; Microelectronics Reliability; Volume 109; June 2020; <https://doi.org/10.1016/j.microrel.2020.113655>

Healing solders: A numerical investigation of damage-healing experiments; G. Siroky, D. Melinc, J. Magnien, E. Kozeschnik, D. Kieslinger, E. Kraker, W. Ecker; 2020 21st International Conference on Thermal, Mechanical and Multi-Physics Simulation and Experiments in Microelectronics and Microsystems (EuroSimE); Cracow, Poland; July 2020; <https://doi.org/10.1109/EuroSimE48426.2020.9152751>

Effect of solder joint size and composition on liquid-assisted healing; G. Siroky, E. Kraker, J. Magnien, D. Melinc, D. Kieslinger, E. Kozeschnik, W. Ecker; Microelectronics Reliability; Volume 119; February 2021; <https://doi.org/10.1016/j.microrel.2021.114066>

# Acknowledgement

I would like to express my appreciation and sincere thanks to my research supervisor, Prof. Dr. Ernst Kozeschnik, who has provided me the guidance and encouragement throughout the pursuit of this degree. Further I would like to thank Dr. Julien Magnien, Dr. Elke Kraker, Dr. Werner Ecker, Dr. Thomas Koch and Dr. Kurt Caloun. Their advice, technical and organizational support has been invaluable and kept my motivation and determination at the highest level. I would like to thank Mr. Dietmar Kieslinger, Mr. Holger Rottmann for providing the framework of this exciting research project and their excellent teamwork. I also wish to thank my colleague Dr. Georg Siroky for his valuable discussions and critical reflections and Mr. Laszlo Solyom, Mr. Christian Zaruba and Edith Asiemo for their active support that fundamentally helped to realize this research.

Finally, I would like to express my profound gratitude to my life-partner, Kim Grömminger for her encouragement and support throughout life.



# Nomenclature

## Abbreviations used in text

Bi	Bismuth
BSE	Back scattered electrons
CTE	Coefficient of Thermal Expansion
DSC	Differential Scanning Calorimetry
HCF	High cycle fatigue
Hf	Heat flow
IMC	Intermetallic Compound
In	Indium
LC	load cycles
LCF	Low cycle fatigue
OPS	Oxide polishing suspension
PCB	Printed Circuit Board
RoHS	Restriction of Hazardous
SAC	SnAgCu
SE	Secondary electrons
SEM	Scanning electron microscopy
SMA	Shape memory alloy
SMD	Surface Mounted Device
Sn	Tin
TM	Thermo-mechanically
TMF	Thermo-mechanically fatigue
$T_{sol}$	Solidus temperature
$T_x$	“x” % Liquid phase fraction
$T_{liq}$	Liquidus temperature
UTS	Ultimate Tensile Strength

## Symbols used in formulas

$\alpha$	Coefficient of thermal expansion
$A$	Cross-section of the sample in the gage
$b$	Fatigue strength exponent
$c$	Fatigue ductility exponent
$C$	Material-dependent constant
$\delta$	Phase shift Between the cyclic thermal and mechanical loading
$\frac{da}{dN}$	Crack growth per cycle
$\epsilon_{mech}$	Cyclic mechanical strain
$\epsilon_{therm}$	Cyclic thermal strain
$\epsilon_t$	Total strain
$\epsilon_{pl}$	Plastic strain
$\epsilon_{el}$	Elastic strain
$\epsilon_f'$	Fatigue ductility coefficient
$E$	Activation energy for diffusion
$E$	Young’s modulus
$E_t$	Young’s modulus of the tensile regime
$E_c$	Young’s modulus of the compression regime
$D$	Diffusion coefficient
$D_0$	Maximum diffusion coefficient
$F$	Force
$G_m^\Phi$	Molar Gibb energy
$G_i^{\Phi,0}$	Gibbs energy of pure component i
$L_0$	Initial length
$\Delta L$	Length difference
$L_v$	Interaction coefficient

$\Delta K$	Stress intensity factor
$\Delta K_{th}$	Threshold of fatigue crack growth
$K_c$	Stress intensity factor at autonomous crack growth
$m$	Slope
$N_f$	Number of cycles until failure
$n^\Phi$	Number of moles
$P_D$	Power dissipation
$sR_{ja}$	Junction to ambient thermal resistance
$R$	Universal gas constant
$R$	Stress ratio
$\Delta\sigma$	Amplitude
$\sigma_f$	Fatigue limit
$\sigma_f'$	Fatigue strength coefficient
$\sigma_m$	Mean stress
$\sigma_{max}$	Maximum stress in a cycle
$\sigma_{min}$	Minimum stress in a cycle
$\sigma_U$	Ultimate tensile stress
$\sigma_y$	Yield strength
$\Delta T$	Temperature difference
$T_{amb}$	Ambient temperature
$T$	Temperature
$T_j$	Junction temperature
$v$	Power of polynomial series
$x_i$	Mole fraction of component i

## Table of content

1.	INTRODUCTION .....	1
2.	OBJECTIVES .....	3
3.	STATE OF THE ART .....	4
3.1.	SOLDER, SOLDER JOINT, AND APPLICATION .....	4
3.2.	WHY SOLDER JOINTS ARE FAILING .....	7
3.3.	PHYSICS OF FAILURE: WÖHLER DIAGRAM FOR LOW AND HIGH CYCLE FATIGUE. 10	
3.4.	DEFINITION OF HEALING MECHANISMS .....	21
3.4.1.	INTRINSIC HEALING MECHANISM OF NANO-VOIDS.....	23
3.4.2.	HEALING METHODS OF MACROCRACKS .....	24
3.5.	APPLICATION-TYPICAL ENVIRONMENTAL TESTS.....	25
3.6.	CALPHAD METHOD .....	27
3.7.	CANDIDATES FOR LEAD-FREE SOLDER ALLOYS .....	28
3.8.	DIFFERENTIAL SCANNING CALORIMETRY .....	30
3.9.	TENSILE TEST FOR MECHANICAL VALIDATION.....	32
4.	EXPERIMENTAL.....	36
4.1.	SAMPLE PRODUCTION FOR MECHANICAL TESTS AND MICROSTRUCTURE ANALYSIS .....	36
4.1.1.	PRODUCTION OF SOLDER ALLOYS.....	36
4.1.2.	PRODUCTION OF DOG BONE-SHAPED SAMPLES .....	37
4.2.	DSC .....	38
4.3.	MICROSCOPY.....	39
4.3.1.	OPTICAL MICROSCOPY AND PREPARATION.....	40
4.3.2.	DIGITAL MICROSCOPY .....	41
4.3.3.	SCANNING ELECTRON MICROSCOPY (SEM).....	42
4.4.	LOADING PROTOCOL .....	44
4.5.	HEALING PROTOCOL.....	44
4.6.	LONG-TERM STABILITY TEST .....	45
4.7.	TENSILE TEST.....	46
5.	RESULTS AND DISCUSSIONS .....	48
5.1.	ALLOY DEVELOPMENT (CALPHAD).....	48
5.1.1.	CALPHAD INVESTIGATIONS OF THE SN/BI/IN-SYSTEM.....	48
5.1.2.	CALPHAD INVESTIGATIONS OF THE SN37BI4IN ALLOY .....	53
5.1.3.	COMPARISON OF CALPHAD CALCULATIONS AND DSC EXPERIMENT .....	57
5.1.4.	CONCLUSIONS OF THE CHAPTER.....	59
5.2.	INFLUENCE OF THE TEMPERATURE ON THE MICROSTRUCTURE OF THE SN37BI4IN SOLDER.....	60
5.2.1.	MICROSTRUCTURE OF THE REFERENCE SAMPLES (AS CAST) .....	61
5.2.2.	HEAT-TREATED AT 120 °C.....	63
5.2.3.	HEAT-TREATED AT 130 °C.....	65

5.2.4.	HEAT-TREATED AT 140 °C.....	70
5.2.5.	MECHANICAL PROPERTY CHANGES INDUCED BY HEAT TREATMENT.....	74
5.2.6.	CONCLUSION OF THE CHAPTER.....	77
5.3.	INFLUENCE OF ALLOYING ELEMENTS.....	80
5.3.1.	INFLUENCE OF BI CONTENT ON THE MICROSTRUCTURE.....	81
5.3.2.	INFLUENCE OF IN CONTENT ON THE MICROSTRUCTURE .....	84
5.3.3.	MECHANICAL PROPERTY CHANGES INDUCED BY VARIATION OF COMPOSITION..	87
5.3.4.	CONCLUSIONS OF THE CHAPTER.....	89
5.4.	LONG-TERM STABILITY (NON-EUTECTIC SYSTEM ABOVE $T_{SOL}$ ).....	92
5.4.1.	INFLUENCE OF THE AGING DURATION ON THE MICROSTRUCTURE.....	92
5.4.2.	MECHANICAL PROPERTIES INDUCED BY AGING @120 °C .....	94
5.4.3.	CONCLUSIONS OF THE CHAPTER.....	97
5.5.	MECHANICAL TESTING OF SN37BI4IN SOLDER .....	98
5.5.1.	CYCLIC LOADING PROTOCOL.....	98
5.5.2.	THE „FORCE OVER TIME“-DIAGRAM.....	99
5.5.3.	HYSTERESIS .....	100
5.5.4.	ASSESSMENT OF FATIGUE DAMAGE PRODUCTION .....	102
5.5.5.	TENSILE TESTS OF LOADED AND HEALED SAMPLES .....	103
5.5.6.	CONCLUSIONS OF THE CHAPTER.....	106
6.	CONCLUSIONS OF THE THESIS.....	109
7.	SUMMARY.....	111
	REFERENCES.....	112
	LIST OF FIGURES .....	116
	LIST OF TABLES .....	120
	APPENDIX.....	121
A.	SETTINGS FOR THE TENSILE TEST .....	121
B.	AGEING EFFECT ON THE SURFACE MICROSTRUCTURE AT 120 °C.....	125

# 1. Introduction

As the sole electrical, mechanical, and thermal link between component and substrate (see figure 1), solders play a fundamental role in microelectronic applications. Nevertheless, the E.U. directive 2002/95/E.C. (unofficial abbreviation RoHS, Restriction of Hazardous Substances) established in 2003 (and replaced by directive 2011/65/E.U.) restrict the use of certain hazardous substances in electrical and electronic equipment, leading to a decisive turning point. The directives regulate the use and placing on the market of hazardous substances in electrical equipment and electronic components.

Due to the RoHS directive, the use of lead-free solders is mandatory in industrial applications. The directives aim to ban problematic components from electronic waste. Among other things, this includes replacing leaded soldering of electronic components with unleaded soldering, banning environmentally harmful flame retardants in cable insulation, and promoting the introduction of appropriate substitute products that are as equivalent as possible. Furthermore, the electrical components and parts used must themselves be free of problematic substances.

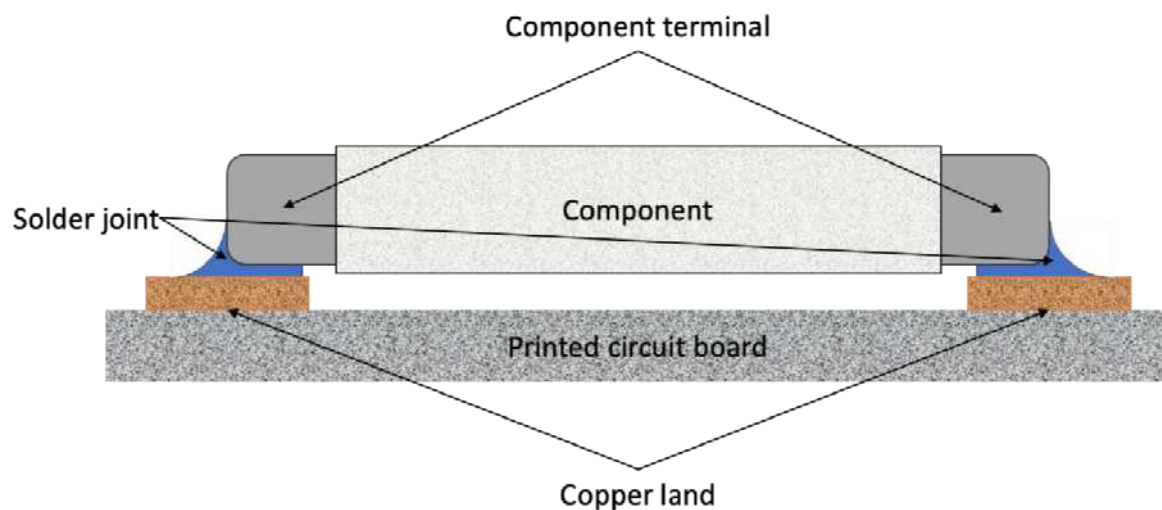


Figure 1: Typical SMD component mounted on a PCB with a rigid lap joint

The implementation of the RoHS directives requires a change in many widely used production processes. The use of lead-free solder is often seen as problematic. Tin-silver, tin-copper, and tin-bismuth, among others, are used as substitutes for the lead-containing alloys, which generally represent a deterioration in the joint quality or an increase in costs.

Originating from the significant change in microelectronics to lead-free solders and the development of microelectronic devices to increasingly integrated designs, with a constantly increasing number of components attached to a decreasing substrate surface area, the necessity of solder joint reliability grows. The failure of a solder joint is often caused by fatigue and typically triggered by localized straining effects initiated by thermo-mechanical stress, which leads to crack initiation, crack propagation, and, finally, to failure. The omnipresent fatigue damage based on contraction and expansion of the joined components combined with the temperature variations represents an intensely demanding environment in which a sudden failure of a single joint of hundreds may lead to the failure of the product. These events can occur in bulk, intermetallic layer between solder and component or substrate, or

between the solder and intermetallic layer [1]. The resulting demands for solder joints reliability with a focus on thermal and mechanical loads have typically been addressed by improving the material properties by alloying the solder or improving the interfacial strength between the solder and substrate [2, 3, 4, 5]. The strategy to use the distinct environment in microelectronic devices with varying temperatures to heal the solder material and extend the reliability and lifetime of solder joints under service conditions is a new idea that builds the foundation of this work. Different healing mechanisms for metals depending on damage size can be distinguished: intrinsic healing mechanism of nanovoids and cracks (precipitation and nanoSMA-dispersoids) [6, 7, 8, 9, 10, 11] and assisted healing methods of macro cracks (SMA-clamp&melt, solder tubes/capsules, coating agent, electro-healing concepts) [12, 13, 14]. Alloys from the Sn/Bi solder system are reported to show liquid-assisted healing effects under compressive forces and at elevated temperatures through local melting, utilizing the clamp&melt approach [15, 16]. For this healing mechanism, an alloy must have a two-phase region where the solid and the liquid phase can coexist. The ability to heal damage depends on the availability and morphology of the liquid phase [17]. The possible extension of the service life of a self-healing solder joint can lead to increased reliability, the prevention of sudden failure, and reduced electrical waste.

Although for the development of solders with self-healing properties, investigations of mechanical and microstructural characteristics are essential, no such analyses for the Sn/Bi/In system are reported. For the development of the novel idea, to use the demanding environment of a solder joint in microelectronic applications, the Sn/Bi/In solder system on the bulk level is used due to reported beneficial healing properties of the Sn/Bi system [1, 18, 19, 20]. The addition of In affects the mechanical characteristics to more ductile behavior and leads to a reduced melting temperature [21, 22, 23].

## 2. Objectives

The objective of this study is to investigate self-healing properties for a lead-free solder at typical application temperatures. The distinct environment in microelectronic devices with varying temperatures should provide the trigger and driving force for liquid-assisted healing. A prolonged lifetime of solder joints in real structures is aspired by benefiting from the mechanical and thermal straining environment. The mechanical and microstructural characteristics of self-healing in solders are therefore studied.

In the development of a self-healing solder, the application of the CALPHAD method and the required melting characteristics of microelectronic applications form the starting point. The candidate solder alloy's mechanical and metallographic characterization should reflect the influence of temperature, long-term stability above solidus temperature, and alloying elements and confirm the mechanical and metallographic characteristics. A plastic deformation-based damaging protocol utilizing mechanical cyclic loading in the range of low cycle fatigue and a healing protocol reflecting the environment during application is defined to investigate the next generation of lead-free solders capabilities. An analysis of fatigued and healed solder samples complements the Sn/Bi/In system study regarding the solder system's mechanical and microstructure suitability as a candidate for low-temperature, self-healing solder. The results shall contribute to a better understanding of the material degradation due to cyclic mechanical and thermal loading.

### 3. State of the art

In this section, fundamental terms and concepts used in the course of this thesis are reviewed. The chapter defines the expression “solder”, why solder joints are failing, and the physics and metallurgy behind the effects. A description of healing mechanisms in metals and the CALPHAD method completes this section’s theoretical part, and a subsequent explanation of essential testing techniques concludes this chapter.

#### 3.1. Solder, solder joint, and application

Soldering is a thermal process used for the cohesive joining of materials, whereby a liquid phase is created by melting the solder (fusion soldering) or by diffusion at the interfaces (diffusion soldering) [24]. The molten solder interacts with the joining materials and forms an alloy at the corresponding surfaces. Hereby the workpiece is not melted in-depth: the liquidus temperature of the base materials is not reached (the melting temperature difference between solder and base material should not be less than 50 °C). After solidification of the soldering alloy, a material-to-material bond is produced, as in welding.

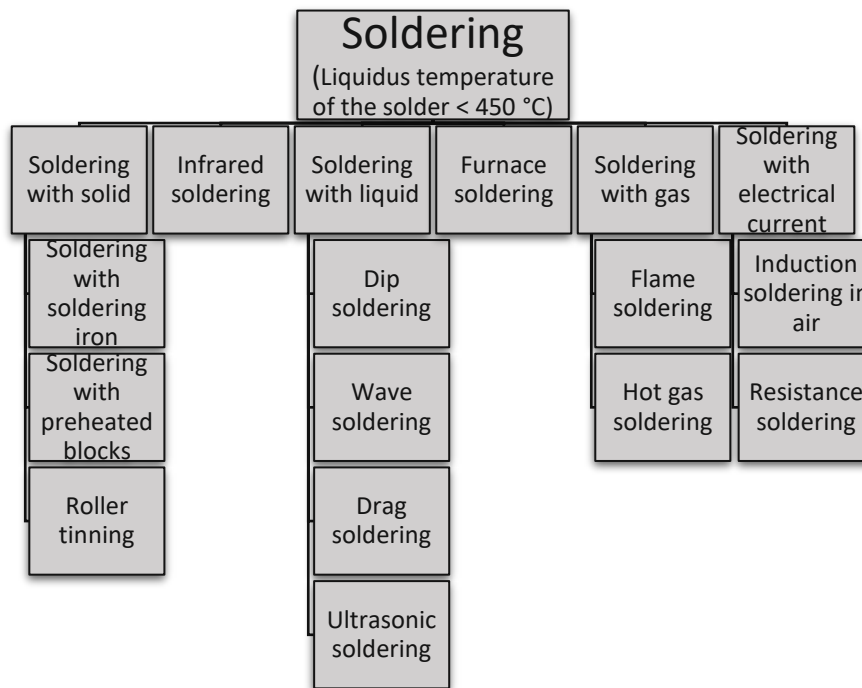


Figure 2: Graphical classification of soldering processes [DIN ISO 857-2:2005-A.1]

The classification of soldering processes is according to DIN ISO 857-2:2005-A.1, based on different principles (see figures 2 and 3).

- According to the type of solder joint:
  - coat soldering (coating by soldering)
  - joint soldering (joining by soldering)
    - gap soldering
    - open-joint soldering
- According to the liquidus temperature of the solder:
  - soldering (Liquidus temperature of the solder < 450 °C)
  - brazing (Liquidus temperature of the solder > 450 °C)



- high-temperature soldering (Liquidus temperature of the solder > 900 °C)

- According to the type of energy source.
- According to the type of solder supply.

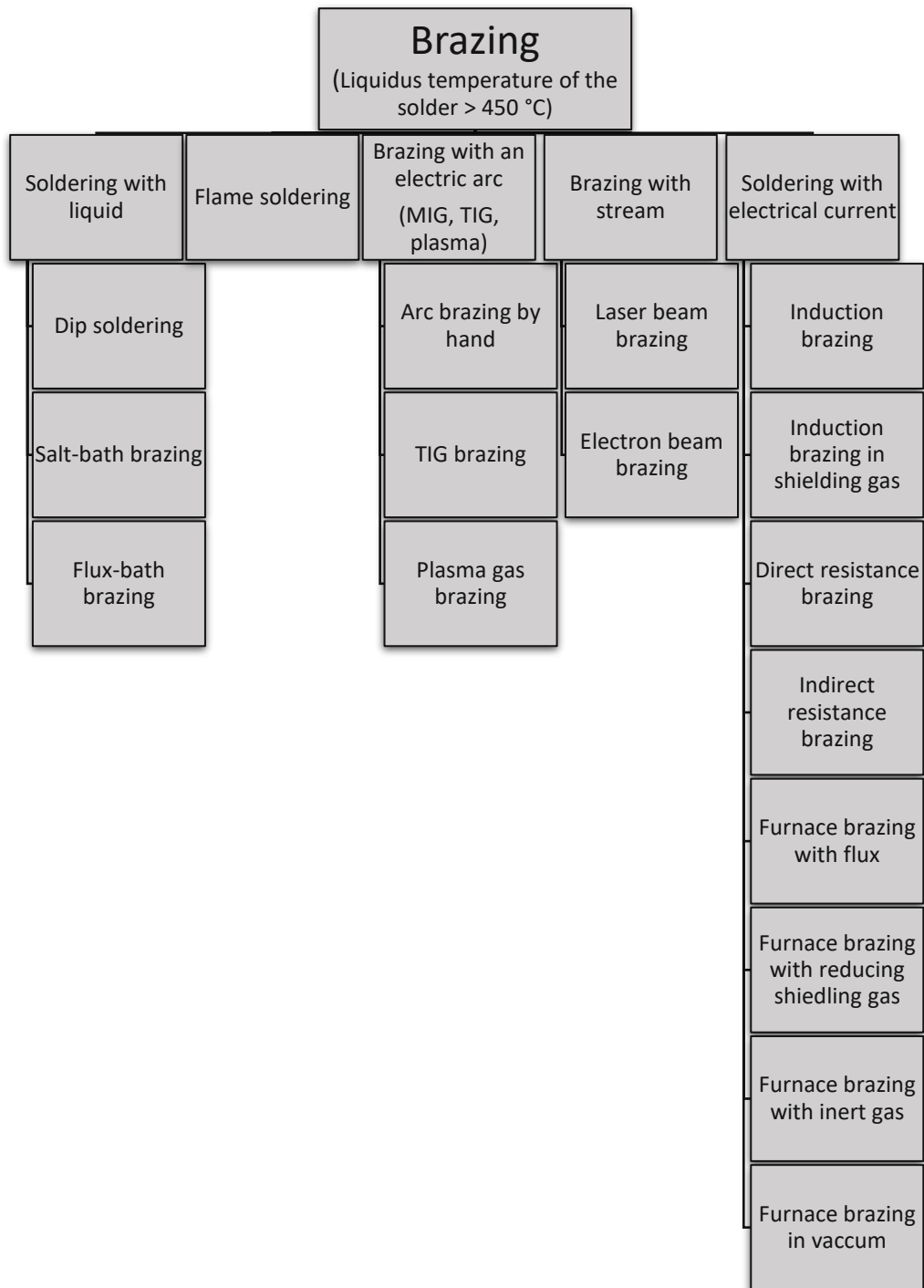


Figure 3: Graphical classification of brazing (and high temperature soldering) processes [DIN ISO 857-2:2005-A.1]

Soldering is widely used in electrical engineering and electronics and is hereby carried out almost exclusively with solder due to the temperature sensitivity of the joined components and substrates. There are two main categories of joints for electronic assemblies:

- Through-hole joints

Through-hole joints rely on a wire lead passed through a hole in the circuit board, then soldered to connect to a metal track. Four different types of through-hole connections have been specified:

- non-plated through-hole, straight lead
- non-plated through-hole, clinched lead
- plated through-hole, straight lead
- plated through-hole, clinched lead (see figure 4)

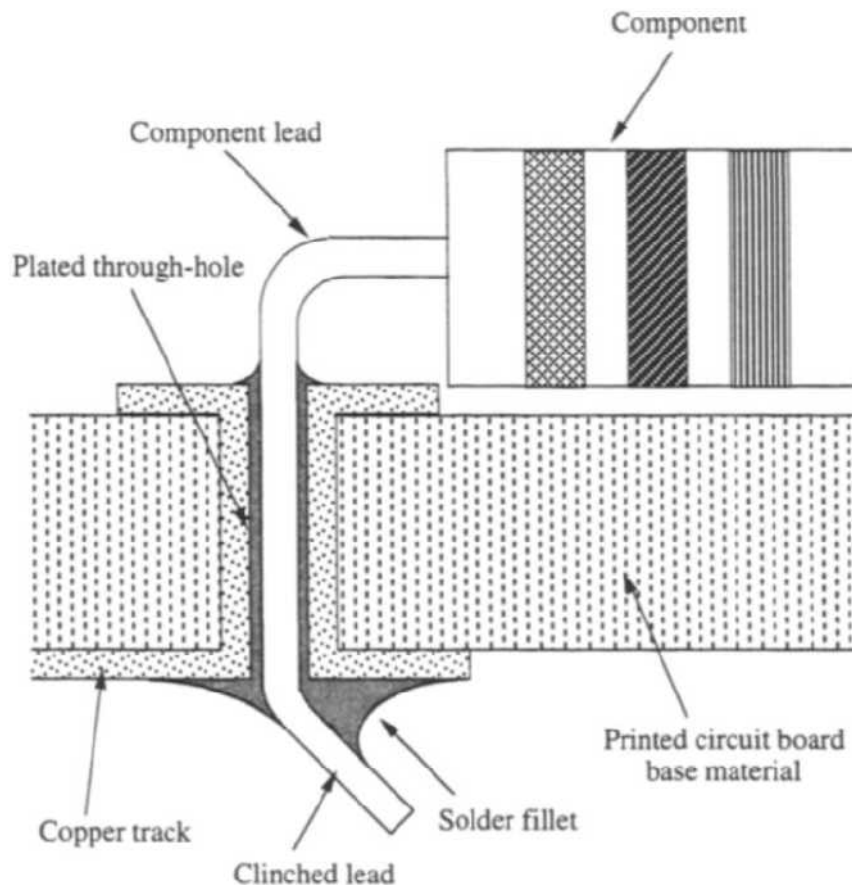


Figure 4: Plated through-hole, clinched lead; Taken from [25], page 29

- Surface mount joints

In today's electronics, a lot of surface-mount device (SMD) components are used. As the name suggests, they are soldered directly to solder patches on the surface of a printed circuit board (PCB). This technique makes very dense assemblies and, above all, double-sided assembly of the PCB possible. With SMD technology, the electrical properties of the circuits are positively influenced, especially at higher frequencies. The space required by the components is reduced due to the possible small sizes of the latter. As a result, the devices can be manufactured smaller and, at the same time, much more cost-effectively. Typical representatives are:

- Chips
- Metal electrode face bonded (MELF)

- Small outline diodes (SOD)
- Small outline integrated circuits (SOIC)
- Small outline transistors (SOT)

The two associated types of surface mounted component soldered joints are:

- Surface-mounted butt joint (see figure 5)
- Surface-mounted overlap joints

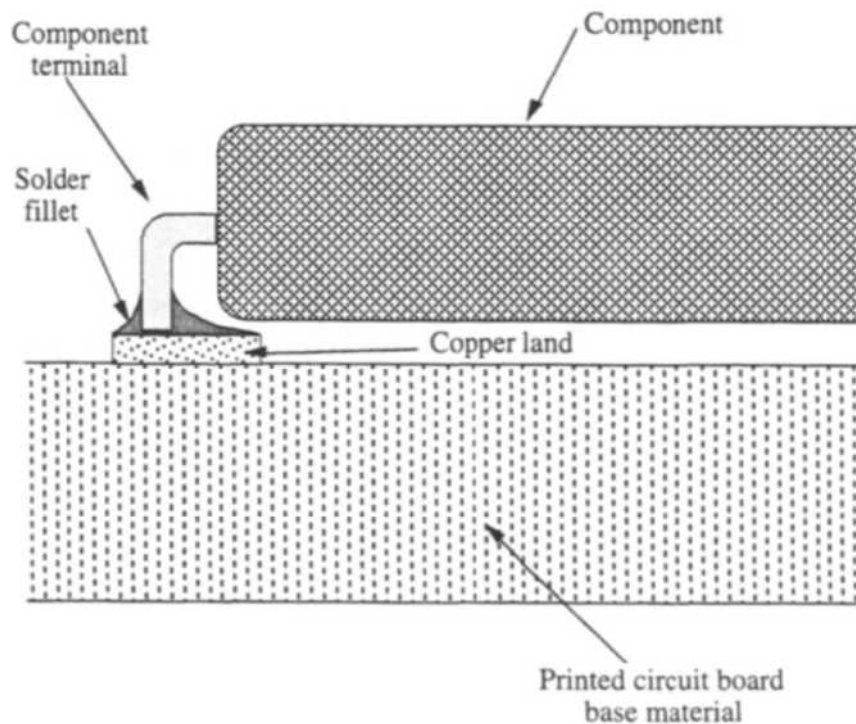


Figure 5: Compliant surface mount butt joint; Taken from [25], page 39

Unlike through-hole joints, in surface mount joints, the strength regarding tensile and shear load of the solder joint is not directly proportional to the component's ability to bear corresponding stress but the actual solder and adhesion of the solder patch on the PCB. This can lead to a sudden failure of the PCB due to breaking of the solder joint or stripping of the solder patch [24, 25, 26].

### 3.2. Why solder joints are failing

In all industries where electronics are manufactured, solder fatigue is a significant cause of electronic assembly failure over time and, therefore, a serious problem [24, 25, 26]. When solder fatigue occurs, it can result in a deformed or non-functional product. Thermo-mechanically (TM) induced low cycle fatigue (LCF) in the solder joint is thereby one of the most common reasons for failing solder joints [27].

One of the leading causes of solder joints failing in TM demanding applications is a mismatch in the coefficient of thermal expansion (CTE), which can lead to cracks and open solder joints over time (see figures 6 and 7). CTE is a material property that quantifies how much a material expands or contracts with temperature changes.

Consequently, temperature cycles can introduce mechanical fatigue damage in the solder based on differences in CTEs between component and substrate, inducing mechanical stresses in the solder joint due to a displacement (see equation (1))

$$\Delta L = \alpha \cdot \Delta T \cdot L, \quad (1)$$

whereby  $\alpha$  is the material-dependent coefficient of thermal expansion,  $\Delta T$  is the temperature difference, and  $L$  is the initial material length.

An initial evaluation of potentially used materials regarding CTE can consequently be essential when designing a product, determining the layout of parts in a product, and determining if a component is at risk of solder joint fatigue during its life cycle due to shear stress.

For example, figure 6 illustrates the heating process of a low CTE component soldered to a high CTE PCB. As the assembly heats up, the component shape barely changes, while the substrate expands and pulls on the solder balls, leading to shear loads on the solder joint. The opposite effect occurs as the assembly cools down. Over time, as the temperature changes from hot, during application, to cold (e.g., in winter), the solder fatigues and eventually breaks (see figure 7).



Figure 6: Illustration of CTE mismatch during application

In addition to the classic CTE mismatch, solder fatigue can also occur in overloaded PCBs with significantly different CTE than their packaging. This can result in excessive bending of the board during temperature variations, leading to a superposition of shear and tensile stress in the solder. This is typically caused by boards that are screwed into rigid metal packages and enter harsh environments such as aerospace or automotive applications.

Figure 8 illustrates such an example of a circuit board screwed into an aluminum housing. The rigid aluminum housing expands and contracts at a different rate than the relatively flexible PCB. As it expands and contracts, the housing can bend and stress the solder joints, finally leading to a “peel-off effect”.

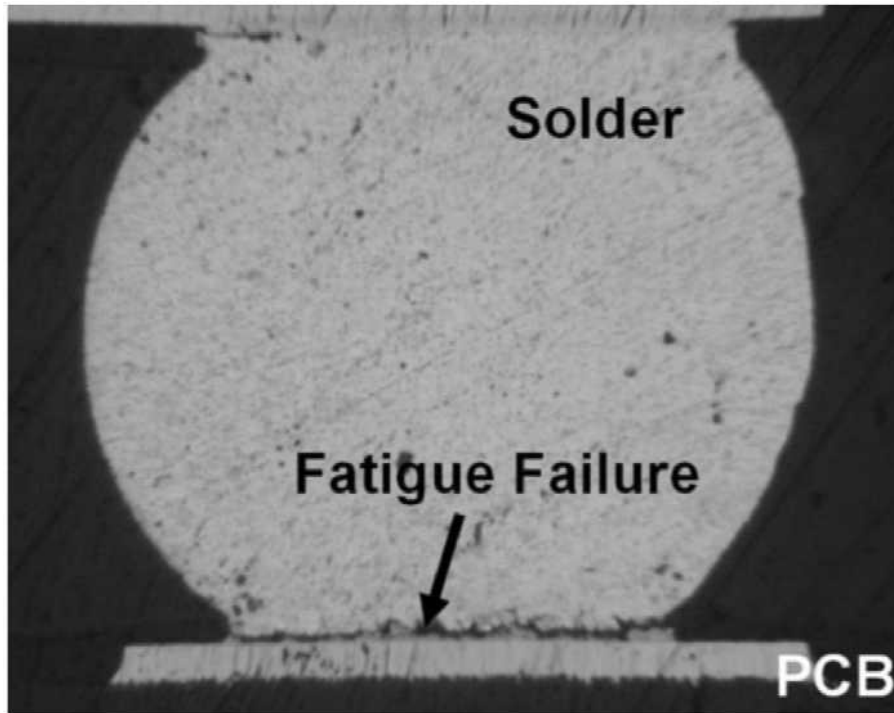


Figure 7: Permanent damage, due to CTE fatigue; Taken from [28], page 6

As described in [29], when metallic materials are subjected to alternating cyclic stresses, microcracking starts in grain areas near the surface. The surface area is especially prone to microcracking since the tensile and compression forces induced by cyclic stress increase with distance to the neutral axis, typically positioned in the middle (compare figure 8). Microcrack formation is followed continuously by microcrack propagation. Grains close to the surface are passed through with a relatively small propagation velocity of some  $10^{-8}$  mm/load cycle (L.C.). When the number of load cycles increases, one of the  $45^\circ$  microcracks usually swings into a plane at  $90^\circ$  to the applied nominal stress and now propagates as a macrocrack with constantly increasing speed (from  $10^{-6}$  mm/L.C. to  $10^{-2}$  mm/L.C.) until the product fails.

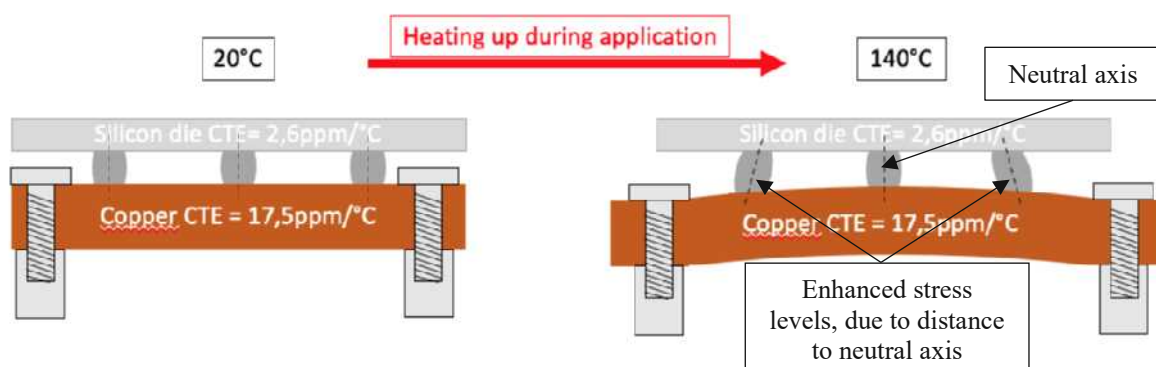


Figure 8: Illustration of fatigue damage due to clamped expanding PCB board

Although solder joints are usually loaded with shear stress in a microelectronic application, the stress state can locally vary widely due to the shape variations of the joint. The actual stress state in a solder joint can range from multiaxial compression to multiaxial tension [30]. Although the lap-shear test is not standardized for the use of solder joints, it is most commonly used to represent the joint's elasto-plastic properties (monotonic [31] or cyclic deformation [32]) in a stress/strain diagram. A variation of specimen geometries used for lap-shear tests leads to

difficulties when comparing between studies. Thus, an actual comparison of material properties is only possible and meaningful within a study using the same specimen geometry [33] (see figure 9). The lap-shear samples complicate the following analysis further due to the difficult differentiation between material and compound properties. A possible effect in the course of fluid-assisted healing at the beginning of fatigue damage can be difficult to measure due to the mixing of the properties. The use of accurate technique and knowledge of uncertainty factors is paramount at the beginning of implementing a new concept such as self-healing solder. Tensile and compression stresses are the basis of any shear state but form fewer uncertainty factors.

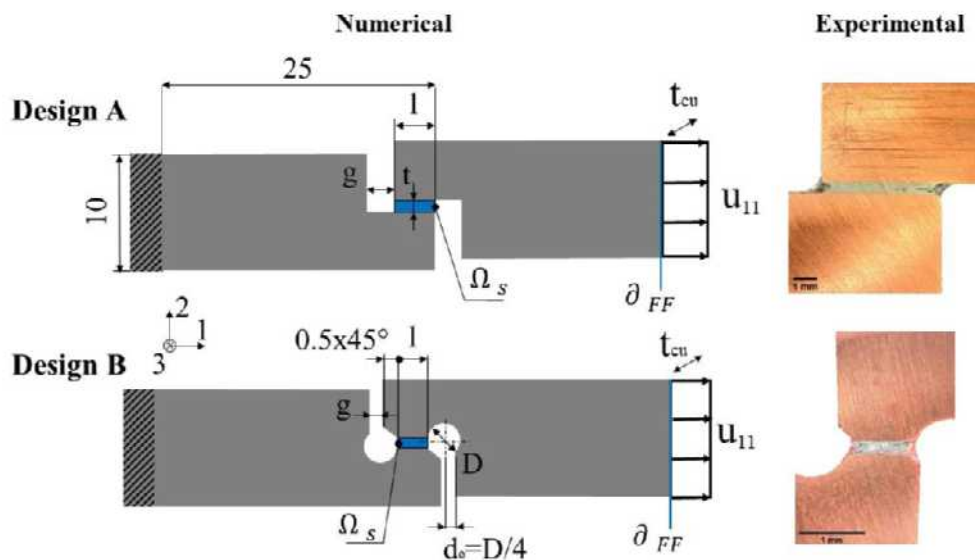


Figure 9: Different lap shear geometries; Taken from [33]

### 3.3. Physics of Failure: Wöhler diagram for low and high cycle fatigue

Material fatigue describes a slowly progressing damage process in material under environmental influences such as changing mechanical load, changing temperature, UV radiation, ionizing radiation, possibly under the additional influence of a corrosive medium [34].

A distinction is made between:

- isothermal mechanical fatigue
- thermal fatigue
- thermo-mechanical fatigue
- creep-fatigue
- tribological fatigue

Typically, solder joints in application are exposed to thermo-mechanical loads that will not let them fail after one cycle. This means, that the load of a single cycle is below the ultimate tensile strength of a joint but fatigues the joint after several loading cycles, leading to a collapse of the joint after an uncertain number of loading cycles.

Thermo-mechanical fatigue (TMF) is the superposition and mutual causation of a mechanical fatigue load and cyclic thermal fatigue load. A product or a material sample under thermo-mechanical load is at the same time subject to cyclic mechanical strain  $\epsilon_{\text{mech}}$  and a cyclic thermal strain  $\epsilon_{\text{therm}}$ . Thus, the material is subject to total elongation  $\epsilon_{\text{total}}$ :

$$\epsilon_{\text{total}} = \epsilon_{\text{mech}} + \epsilon_{\text{therm}} \quad (2)$$

Between the cyclic thermal and mechanical loading, a phase shift of  $\delta$  may exist, which noticeably affects the fatigue life and the plastic deformation properties of the product. Based on the phase shift, one distinguishes several cases of a thermo-mechanical test (see figure 10):

- In-Phase-Test (I.P.):  $\delta = 0^\circ$
- Out Of-Phase-Test (O.P.):  $\delta = 180^\circ$
- Clockwise-Diamond-Test (CD):  $\delta = +90^\circ$
- Counter-Clockwise-Diamond-Test (CCD):  $\delta = -90^\circ$

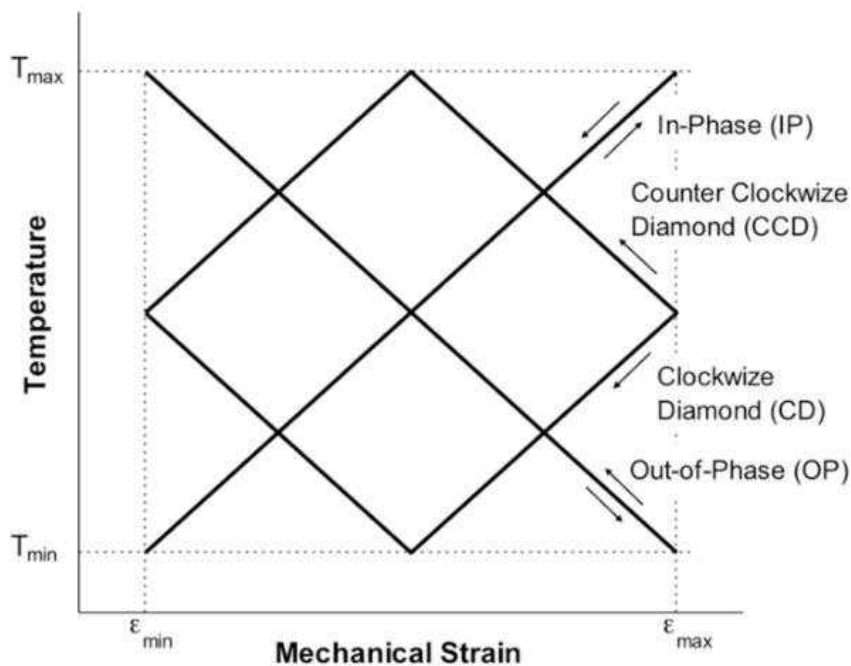


Figure 10: Temperature-strain cycles for different TMF tests; Taken from [35]

As a result of several TMF tests, stress-cycle (S-N) diagrams can be obtained, an essential tool for calculating, estimating, and verifying fatigue strength or operational strength. August Wöhler developed it in response to the Timelkam railroad accident.

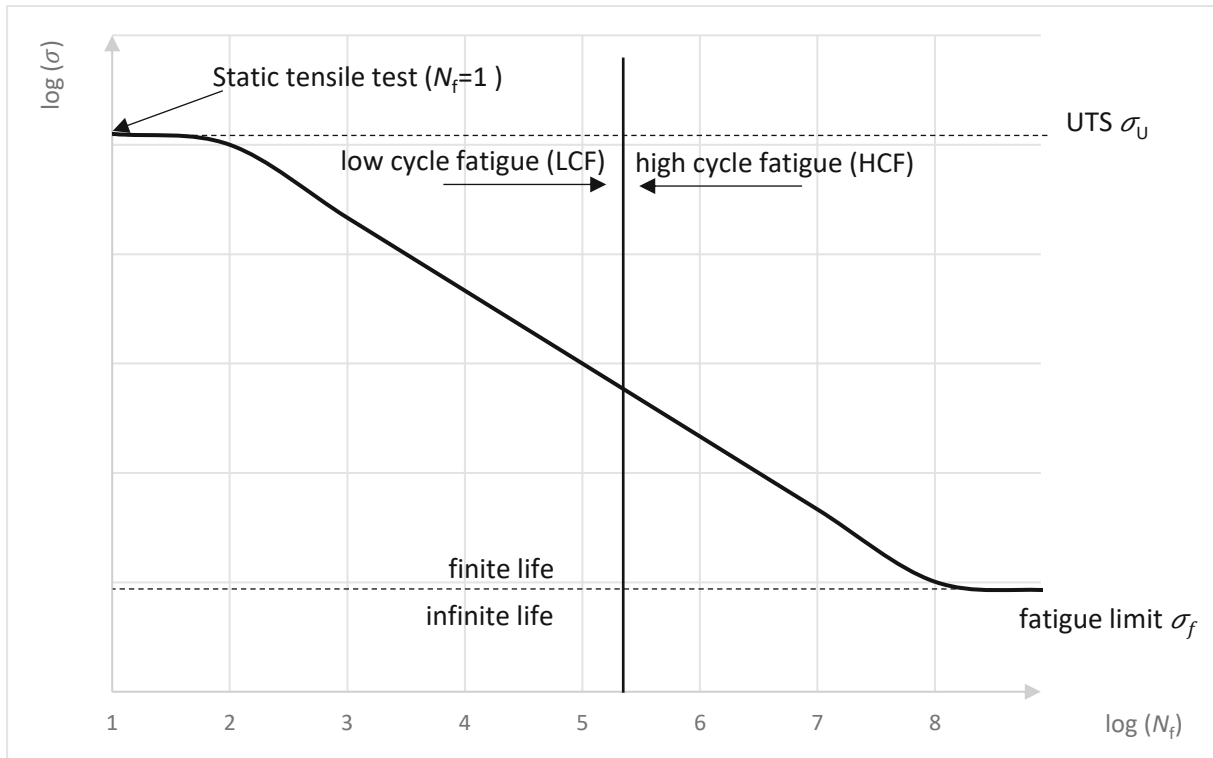


Figure 11: S-N diagram with marked LCF/HCF; reproduced from [34]

Figure 16 and table 1 show influencing factors of external mechanical cyclic loads.

Table 1: Influencing factors of cyclic fatigue

Factor	Explanation/Example
Amplitude	$\Delta\sigma = \frac{\sigma_{\max} - \sigma_{\min}}{2}$ ; constant, varies in time
Mean stress	$\sigma_m = \frac{\sigma_{\max} + \sigma_{\min}}{2}$
Load type	Axial tensile/compression, shear
Number of cycles	LCF, HCF
Chronicle loading sequence	Time under load, frequency

The stress ratio  $R$  is another essential relation between the minimum and maximum value in a cycle (see equation (3)) and is commonly used to define the type of stress in each cycle (see figures 12 to 15).

$$R = \frac{\sigma_{\min}}{\sigma_{\max}} \quad (3)$$

The S-N curve in figure 11 relates stress amplitude  $\sigma_m$  in uniaxial loading direction over lifetime (number of cycles until failure  $N_f$ ) at a given temperature with the number of cycles after which the sample fails  $N_f$ . The lower horizontal asymptote in figure 11 visualizes the fatigue limit  $\sigma_f$  and the upper horizontal asymptote in the S-N diagram defines the UTS  $\sigma_U$  equivalent to a tensile test of the tested sample (see figure 17). If stress never exceeds a certain fatigue limit  $\sigma_f$ , the lifetime theoretically increases to infinite life because no fatigue damage accumulates,



and failure is therefore unforeseen. If  $\sigma_f < \sigma_{\max} < \sigma_U$  the sample probably can endure several cycles. If  $\sigma_{\max}$  equals  $\sigma_U$  the sample collapses after one cycle as in a monotonic tensile test.

$$R = \frac{\sigma_{\min}}{\sigma_{\max}} = -1$$

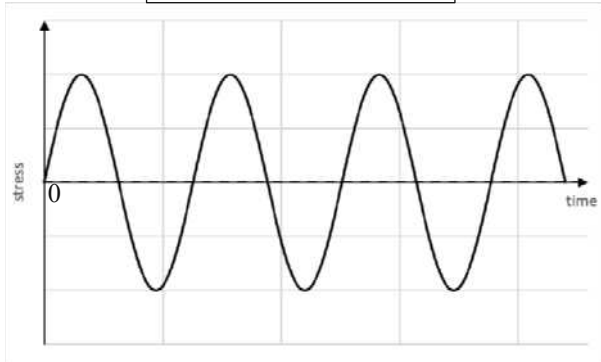


Figure 12: Completely reversed stress cycle; Inspired by [36], page 320

$$R: -1 < \frac{\sigma_{\min}}{\sigma_{\max}} < 0$$

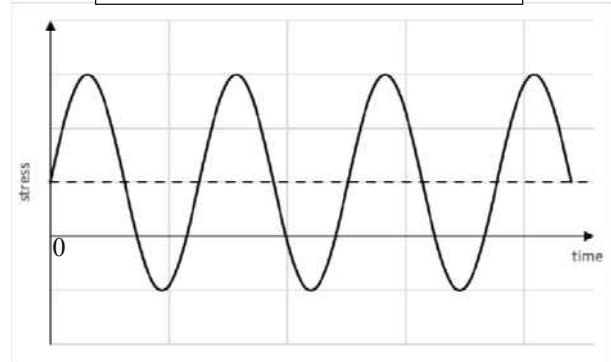


Figure 13: Stress alternating between tension and compression; Inspired by [36], page 320

$$R = \frac{\sigma_{\min}}{\sigma_{\max}} = \frac{0}{\sigma_{\max}} = 0$$

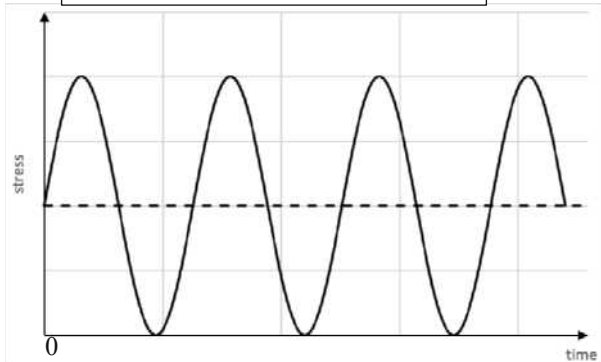


Figure 14: Stress alternating between tension and no stress; Inspired by [36], page 320

$$R: 0 < \frac{\sigma_{\min}}{\sigma_{\max}} < 1$$

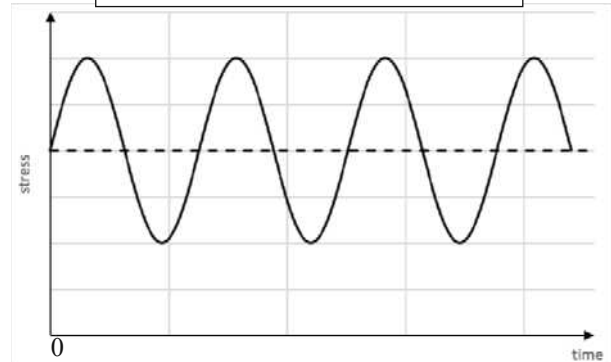


Figure 15: Stress alternating between higher and lower tension; Inspired by [36], page 320

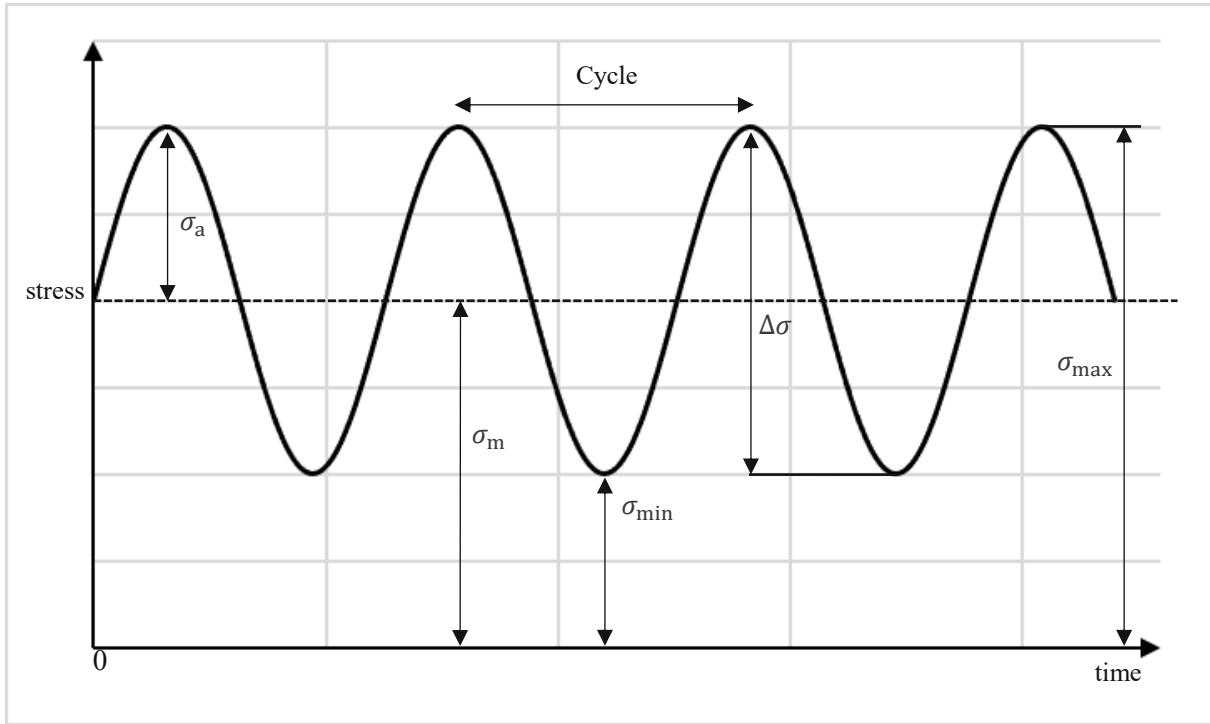


Figure 16: Influencing factors of cyclic fatigue

The resistance against fatigue failure of a material or a strained product represents the capacity of the material to accommodate deformation energy. The area inside one hysteresis loop is equivalent to the absorbed energy of the sample during the respective loading cycle (see figure 17). Depending on  $\sigma_{\max}$  and the materials fatigue resistance properties, the sample can endure a significant number of cycles or fail instantly. In the first half cycle from origin 0 to X (at  $\epsilon_{\max}$ ), a large plastic deformation occurs, because  $\sigma_{\max}$  significantly exceeds the yield strength  $\sigma_y$  and the sample is therefore plastically elongated. The deloading section to Y (at  $\epsilon_{\min}$ ) and the following loading section to X ( $\epsilon_{\max}$ ) again cause a relatively small plastic deformation, and the enclosed area is smaller.

The procedure of failure due to fatigue can be divided into three steps (see figure 18). Two asymptotical limits outline the middle section of the curve. With  $\Delta K$  being the stress intensity factor indicating the stress distribution at the tip of the crack, the limit on the left represents the threshold  $\Delta K_{\text{th}}$  of fatigue crack growth, also called the threshold value. If the cyclic stress intensity factor is above the threshold, the crack can propagate and constantly grow (regime I). In the middle range (regime II), the curve generally has (in log scale) a linear course. This course is described by the so-called Paris-Erdogan law (equation (4)).

$$\frac{da}{dN} = C(\Delta K)^m \quad (4)$$

Here  $\frac{da}{dN}$  defines the crack growth in  $\mu\text{m}$  per cycle,  $m$  is the slope, and  $C$  is a material-dependent constant. The right-hand side asymptote describes the stress above which crack propagation becomes unstable, ultimately leading to forced fracture (regime III). The right asymptote,  $K_{\max} = K_c$ , describes the autonomous crack growth resulting in the failure of the sample.

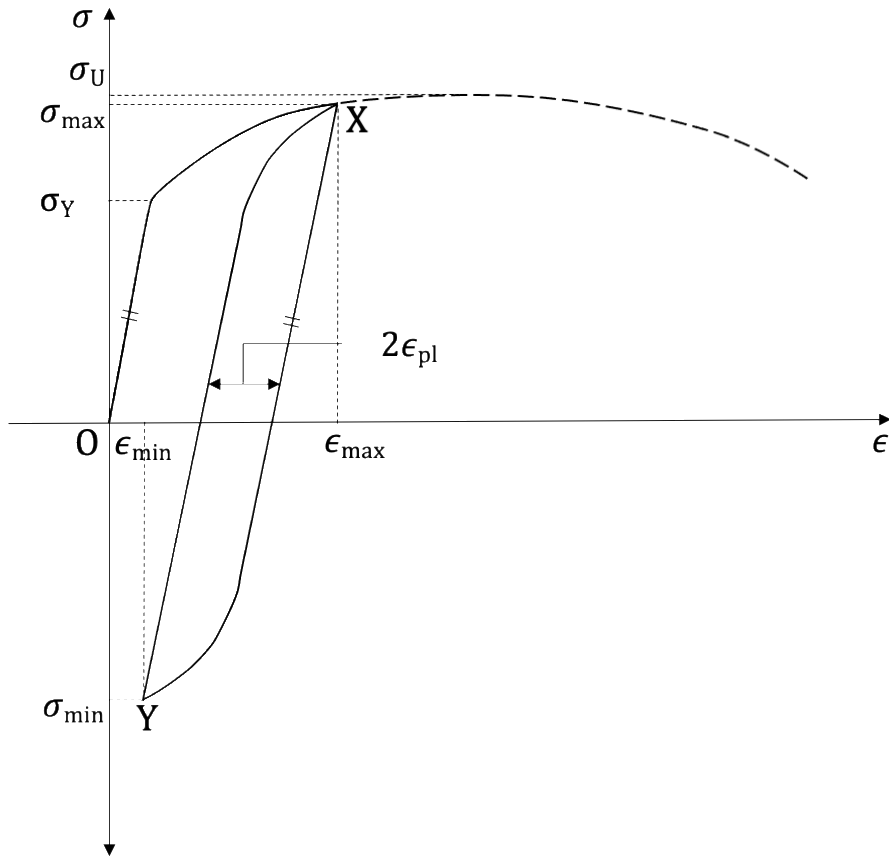


Figure 17: Schematic stress-strain loop of a high-stress amplitude cycle after the first application of  $\sigma_{max}$ ; Reproduced from [34], page 146

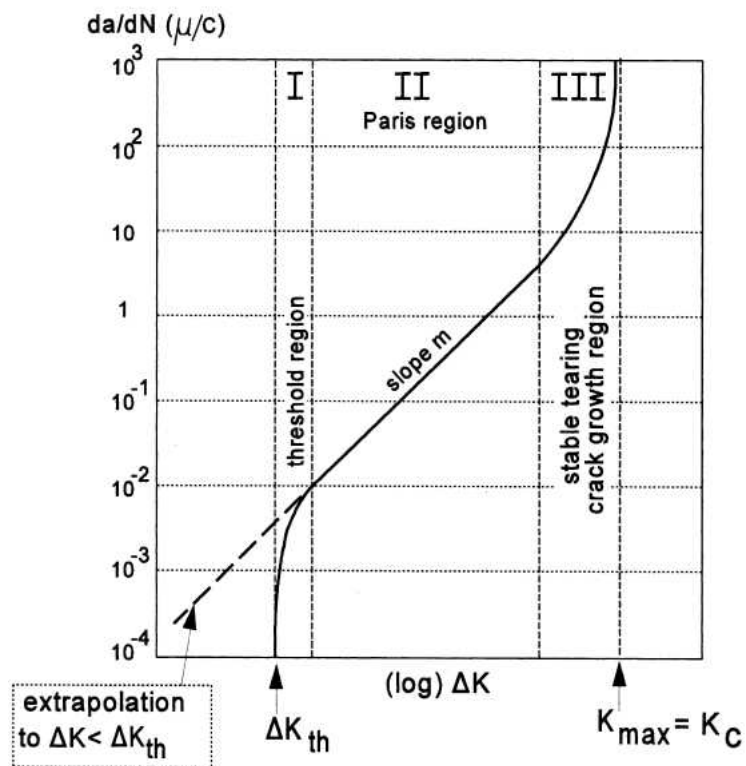


Figure 18: Evolution of the crack growth, due to mechanical fatigue; Taken from [34], page 218

Figure 11 shows that a slight reduction of the stress amplitude represents a significant increase in lifetime. A distinction regarding cycle number and therefore required loads has been established, namely low cycle fatigue (LCF) and high cycle fatigue (HCF) (see figure 11).

LCF labels fatigue tests with a maximum quantity of  $10^4$  cycles, and HCF tests employ up to  $10^7$  cycles. The maximum strain and, therefore, maximum load in LCF and HCF tests vary. In LCF, the load exceeds the yield strength, which entails that in every cycle, plastic deformation occurs, whereby the load of an HCF test dwells in the elastic regime of the tensile test. The Basquin equation can express the relation of material fatigue with its stress amplitude in the elastic section:

$$\frac{\Delta\sigma}{2} = \sigma_f'(2N_f)^b \quad (5)$$

With  $\frac{\Delta\sigma}{2}$  being the stress amplitude,  $\sigma_f'$  is the fatigue strength coefficient, a parameter that scales with ultimate tensile strength (UTS), and  $b$  is the fatigue strength exponent. In contrast to HCF, in LCF, the load creates plastic deformation each cycle. It is common to link strain to lifetime instead of stress to lifetime in HCF for this condition. Coffin Manson developed the corresponding relation for plastic deformation:

$$\frac{\Delta\epsilon_{pl}}{2} = \epsilon_f'(2N_f)^c \quad (6)$$

Whereby  $\frac{\Delta\epsilon_{pl}}{2}$  is the plastic strain amplitude,  $\epsilon_f'$  is the fatigue ductility coefficient and  $c$  being the fatigue ductility exponent. Since the Coffin Manson relation does not take elastic deformation into account and the total strain in LCF is composed of the superposition of plastic  $\epsilon_{pl}$  and the elastic  $\epsilon_{el}$  strain. To improve the Coffin Manson equation, it has to be expanded by the Basquin equation converted with the Young's modulus  $E$  (see figure 19). The total strain is therefore defined as:

$$\frac{\Delta\epsilon_t}{2} = \frac{\Delta\epsilon_{pl}}{2} + \frac{\Delta\epsilon_{el}}{2} = \epsilon_f'(2N_f)^c + \frac{\sigma_f'}{E}(2N_f)^b \quad (7)$$

Apart from this commonly used relation, there are other models based on different kinds of damage mechanisms. Lee et al. [37] have summarized fourteen different models regarding five different fatigue life models: stress-based, plastic strain-based, based on creep strain, based on energy, and damage accumulation-based models. Table **Error! Reference source not found.** gives an overview of fourteen solder joint fatigue models.

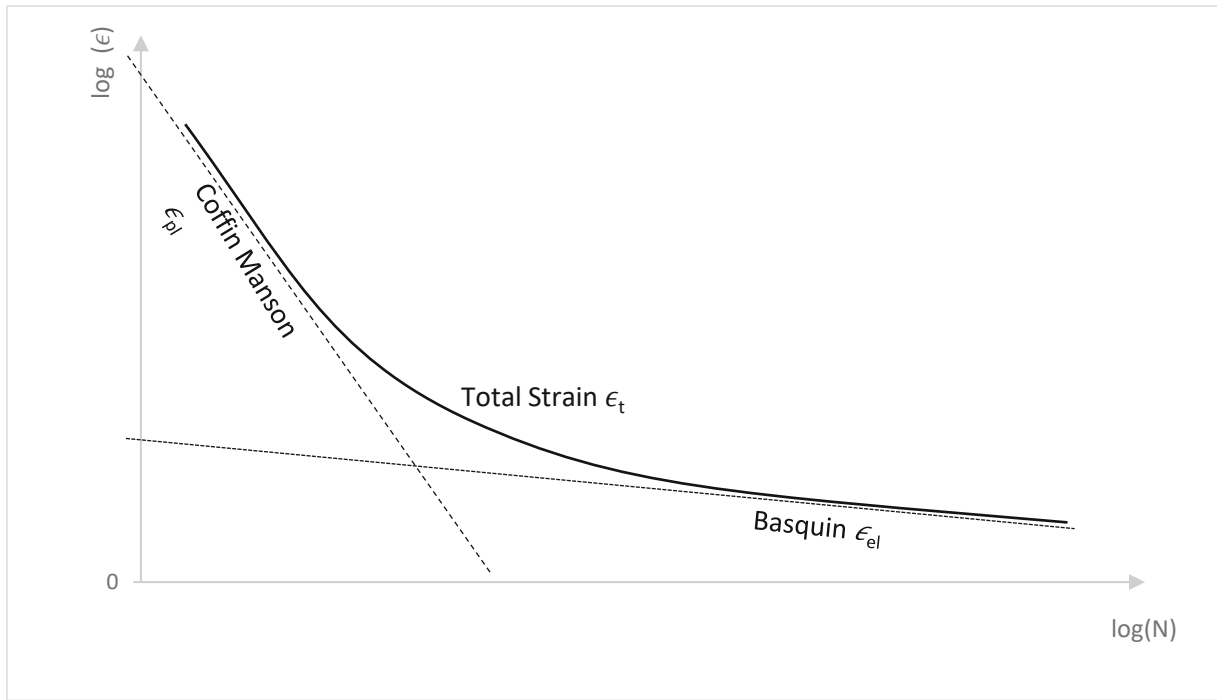


Figure 19: Total strain vs. number of cycle equation is a combination of the Coffin Manson and Basquin equation; Inspired by [37], page 235

Table 2: Overview of solder joint fatigue models; Reproduced from Lee et al. [37]

	Fatigue model	Equation	Required parameters	Model class	Coverage	Constants
1	Coffin Manson	$\frac{\Delta\epsilon_{pl}}{2} = \epsilon_f'(2N_f)^c$	Plastic strain	Plastic strain	LCF	$c$ ... constant $\epsilon_f'$ ... fatigue ductility coefficient
2	Total strain (Coffin Manson Basquin)	$\frac{\Delta\epsilon}{2} = \epsilon_f'(2N_f)^c + \frac{\sigma_f'}{E}(2N_f)^b$	Strain range	Plastic strain and elastic strain	HCF and LCF	$b$ ... fatigue strength exponent $c$ ... fatigue ductility exponent $\epsilon_f'$ ... fatigue ductility coefficient $\sigma_f'$ ... fatigue strength exponent
3	Solomon	$\Delta\gamma_p N_p^\alpha = \theta$	Plastic shear strain	Plastic shear strain	LCF	$\alpha$ ... constant $\theta$ ... inverse fatigue ductility coefficient
4	Engelmaier	$N_f = \frac{1}{2} \left[ \frac{\Delta\gamma_t}{2\epsilon_f'} \right]^{\frac{1}{c}}$	Total shear strain	Total shear strain	LCF	$c = -0.442 - 6e - 4T_s + 1,74e - 2\ln(1 + f)$ $T_s$ ... mean cyclic solder joint temp [°C] $f$ ... cyclic frequency (cycles/day) $2\epsilon_f' = 0.65$
5	Miner	$\frac{1}{N_f} = \frac{1}{N_p} + \frac{1}{N_c}$ $\frac{1}{N_f} = \frac{F_{pp}}{N_{pp}} + \frac{F_{cc}}{N_{cc}} + \frac{F_{cp}}{N_{cp}} + \frac{F_{pc}}{N_{pc}}$	Plastic shear and matrix creep failure	Superposition (plastic and creep)	Plastic shear and matrix creep	$N_p$ ... plastic failure $N_c$ ... creep failure
6	Kecht and Fox	$N_f = \frac{C}{\Delta\gamma_{mc}}$	Matrix creep, shear strain	Matrix creep	Matrix creep	$c = 890 \%$
7	Syed	$N_f = ([0.022D_{gbs}] + [0.063D_{mc}])^{-1}$	Gbs energy and mc energy	Accumulation of creep strain energy	Implies full coverage	$D_{gbs}$ ... accumulated equivalent creep strain/cycle $D_{mc}$ ... accumulated equivalent matrix creep/cycle

8	Dasgupta	$N_f = \left( \frac{\Delta \bar{W}_{total}}{W_0} \right)^{\frac{1}{k}}$	Energy	Total strain energy	Joint geometry accounted for	$\Delta \bar{W}_{total}$ ... total strain energy density $W_0 = 0.1573$ $k = -0.6342$
9	Liang	$\bar{N}_f = C(W_{ss})^{-m}$	Energy	Stress/strain energy; density-based	Constants from isothermal LCF tests	$C, m$ ... temperature-dependent material constants $W_{ss}$ ... stress-strain hysteresis energy
10	Heinrich	$N_o = 18083 \Delta W^{-1.46}$ $N_o = 7860 \Delta W^{-1.00}$	Energy	Energy density-based	Hysteresis curve	$\Delta W$ ... viscoplastic strain energy/cycle
11	Darveaux	$N_{aW} = N_{os} + \frac{a - (N_{os} - N_{op}) \frac{da_p}{dN}}{\frac{da_s}{dN} - \frac{da_p}{dN}}$	Damage and energy	Energy density-based	Hysteresis curve	$a$ ... total possible crack length $\frac{da}{dN}$ ... crack growth $N_o$ ... crack initiation
12	Pan	$C = N_f^* C(a\dot{E}_p + b\dot{E}_c)$	Strain energy density and plastic energy density	Strain energy density	Hysteresis curve	$C$ ... strain energy density $E_p$ ... plastic strain creep energy density/cycle $E_c$ ... creep strain energy density/cycle
13	Solkarts	$N_f = \frac{1 - (1 - d_f)^{k-1}}{(k + 1)L}$	Damage	Damage accumulation	Hysteresis curve and damage evolution	$d$ ... 0.5 for solder (damage parameter) $k$ ... material constant
14	Noris and Landzberg	$AF = \left( \frac{\Delta \gamma_t}{\Delta \gamma_0} \right)^2 \left( \frac{f_0}{f_t} \right)^{\frac{1}{3}} e^{1414 \left( \frac{1}{T_0} - \frac{1}{T_t} \right)}$	Temperature and frequency	Temperature and frequency	Test condition vs. use condition	$T$ = temperature $e^{1414 \left( \frac{1}{T_0} - \frac{1}{T_t} \right)}$ = isothermal fatigue life ratio

Due to internal microscopic effects, samples can either cyclically harden or soften as a response to the applied loads. In figure 20,  $\sigma_a$  increases due to cyclic strain hardening of the specimen, which is more common in initially soft materials. In figure 21, the sample gets cyclically softer, which is often seen in materials that are hardened to a significant level, either by thermal treatment or a prior deformation process. In general, both cyclic strain hardening and softening stabilize after a, usually relatively low number of cycles compared to the number of cycles to failure. This stabilizing process is less predictable in the case of soft materials compared to hardened materials.

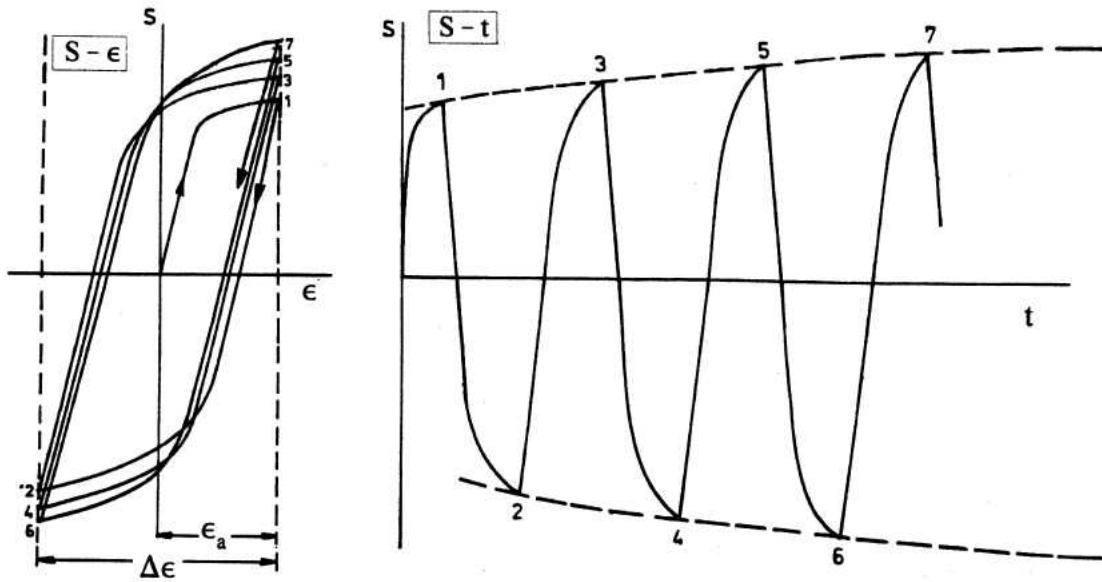


Figure 20: Cyclic hardening; Taken from [34], page 163

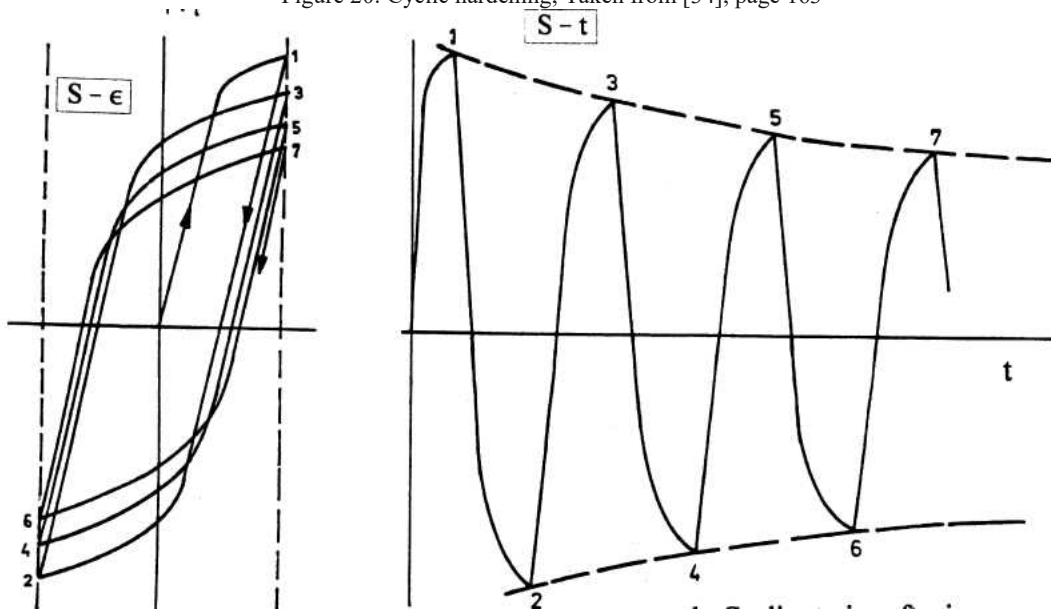


Figure 21: Cyclic softening; Taken from [34], page 163

Two phenomena tightly related to macroscopic cyclic plasticity are plastic shake-down or stress relaxation and cyclic creep [34]. Cyclic plastic deformation with positive  $\sigma_m$  can lead to plastic shake down (see figure 22). A process that can lead to a cyclic reduction of  $\sigma_m$ , possibly to zero. This stress relaxation process can occur because dislocation rearrangements are enabled by active cyclic slip. Residual stress on the surface can vanish if cyclic plastic deformation occurs in this layer and the cyclic stress level is high enough.



Cyclic creep is occurring under high cyclic stress and positive mean stress  $\sigma_m$  (see figure 23). The cyclic plastic deformation due to cyclic tensile stress is partly consumed by permanent tensile deformation, which is related to plastic shake-down because both are dislocation mechanisms, but due to the nature of the control parameters (stress-controlled), cyclic reduction of  $\sigma_m$  cannot take place, the sample becomes longer.

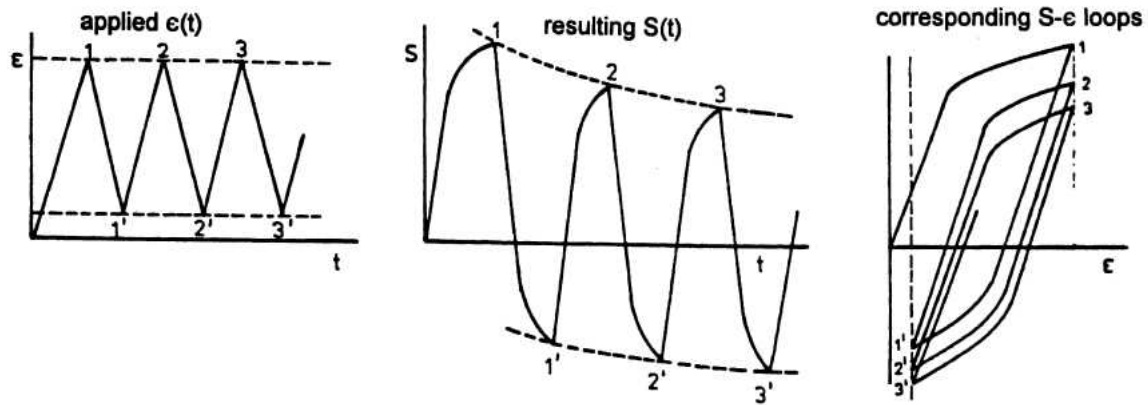


Figure 22: Plastic shake-down, or stress relaxation; Taken from [34], page 166

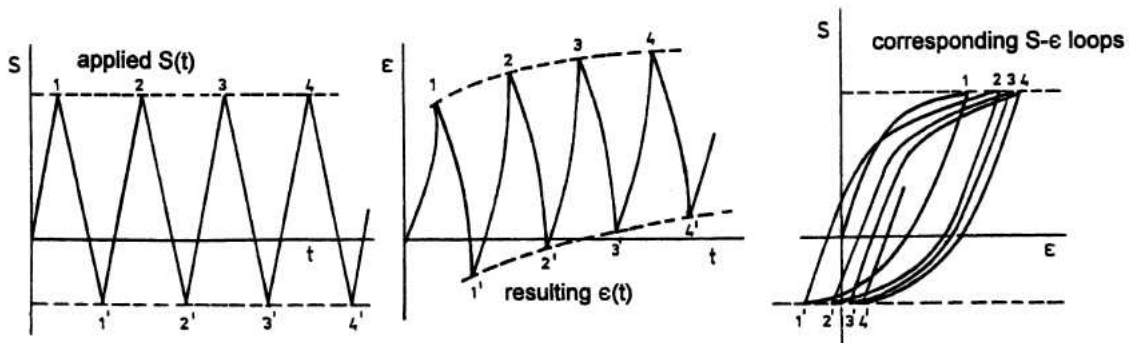


Figure 23: Cyclic creep; Taken from [34], page 166

### 3.4. Definition of healing mechanisms

Self-healing materials embody a change of paradigm from the traditional damage prevention paradigm [38] and allow an intrinsic repair of the functionality (e.g., strength) after macroscopic damage or total mechanical failure in contrast to the exchange of damaged parts. So far, the composition and microstructure are designed and optimized such that mechanical damage initialization and propagation (in the form of internal and surface cracks, voids, and internal damage) are postponed as long and as much as possible. At the moment, it applies to all metals or metallic systems that, once a crack or defect generated by creep, fatigue, mechanical overload, or plastic deformation occurred, that damage will never vanish and can act as the initiator of total failure.

Polymer-based systems dominate the field of self-healing materials, which has been reviewed several times [39, 40, 41, 42, 43, 44]. The reason for this is that self-healing concepts are highly compatible with the energetical properties of polymers. Chemical processes in polymer release, even at room temperature, a significant amount of energy, which converts into a fast diffusional process.

In contrast to other materials like polymers [45, 46, 47] and composites [48], in the case of metals and metallic systems, self-healing is hard to attain due to the small size of the atoms instead of the large polymer molecules of a potential healing agent and “low directional temporary mobility” of the latter at operating temperature. These properties are essential for a chance of self-healing but in direct conflict with the excellent mechanical properties of metals.

For self-healing, a non-collective atomic motion of the “healing agent”-atoms, to the damaged area is necessary. When these atoms are on-site, they must get immobile again suddenly. Due to the high melting temperature of most metallic systems, the intrinsic low atomic mobility at room temperature of metallic atoms in the crystal lattice features a severe limiting factor. The small size of the metal atoms and the fact that the motion of a metallic atom is equivalent to the motion of a vacancy in the opposite direction makes the healing process of a superatomic dimensional damaged area even more challenging.

Nevertheless, different metallic self-healing tactics have been developed. Divided according to the length of a crack, different approaches are employed, based on intrinsic healing mechanism of nanovoids and nano-cracks (precipitation and nanoSMA-dispersoids) [6, 7, 8, 9, 10, 11] and assisted healing methods of macrocracks (SMA-clamp&melt, solder tubes/capsules, coating agent, electro-healing concepts) [13, 14].

In general, it has to be mentioned that a specific self-healing strategy must always be applicable for the base material and that the healing approaches operate primarily in the mentioned scale (see figure 24). Within the first group, damage in the nanoscale is repairable, macrocracks are not healable, and when these have developed, they lead to total failure. Since creep and fatigue failure starts with nano-scaled voids and cracks, which in the course of the lifetime coalesce to macro damage, it is safe to say that these concepts can slow the failure process down. The group of macro-scale healing concepts works primarily when the stage of macroscopic damage is reached.

In all these diffusion-based concepts, the critical factor for self-healing of metal concepts is the atomic mobility of the solute “healing agent”-atoms and the matrix atoms (because the diffusive displacement of the solute atoms through the crystal lattice also depends on the diffusive displacement of the matrix atoms in the opposite direction). Since atomic motion in a solid is a diffusion process, it is strongly dependent on the temperature, as in

$$D = D_0 e^{-\frac{E}{RT}} \left[ \frac{\text{m}^2}{\text{s}} \right], \quad (8)$$

whereby  $D$  is the diffusion coefficient,  $D_0$  is the frequency factor,  $E$  is the activation energy for diffusion,  $R$  is the universal gas constant, and  $T$  is the temperature (K).

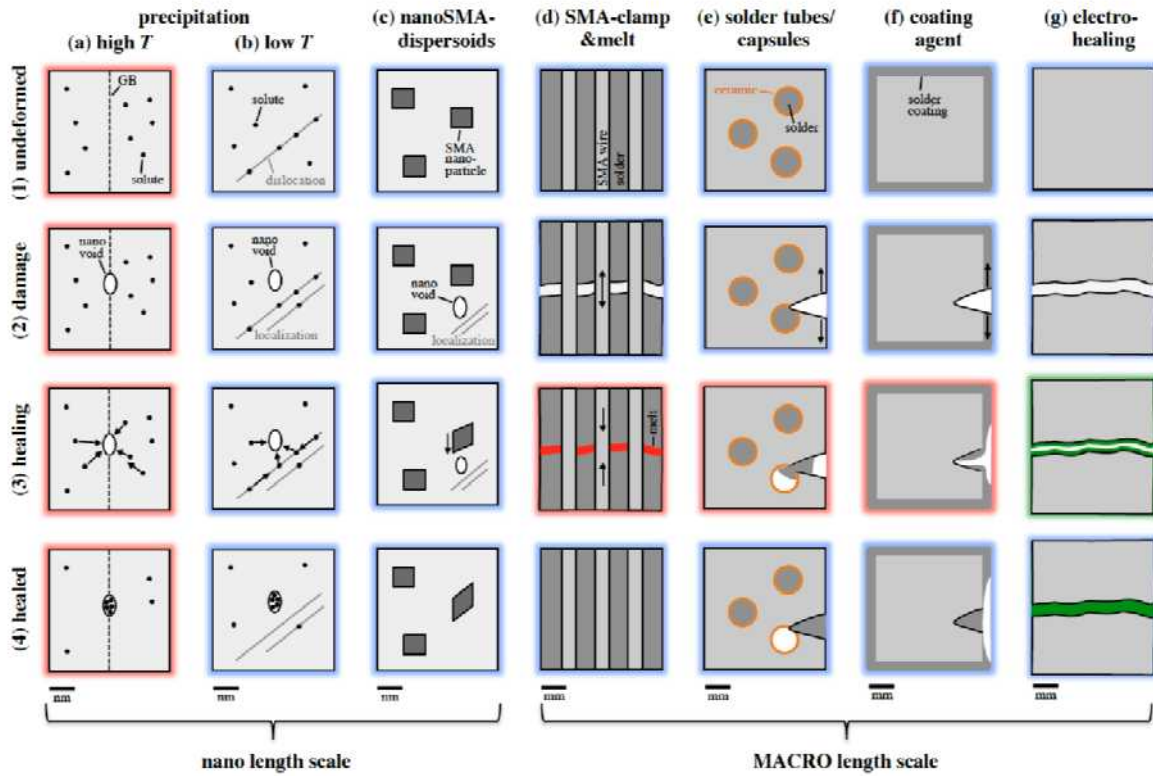


Figure 24: Self-healing mechanisms ordered by length scale; Taken from [49], page 390

### 3.4.1. Intrinsic healing mechanism of nano-voids

#### High T/low T precipitation

For the “high T”, “low T”-precipitation healing methods to work, the temporary reduction or total removal of mechanical forces, responsible for the development of inflicted damage of the material, is essential to allow reformation of chemical and physical bonds across the damage site. Examples of metals employing this type of self-healing mechanism distinguish barely from other commercially available alloys, and the “healing agent” is not a separately identifiable phase in the microstructure but is an alloying element in a supersaturated state (figure 24 (a1,b1)). Furthermore, the healing step occurs at conditions nearly identical to operating conditions (at least regarding temperature).

#### High T precipitations

For the “high T”-precipitation concept to work correctly, it is crucial that the precipitation mobilization should not happen spontaneously in the whole microstructure but strictly localized in the regions of nano-voids [50, 51]. Figure 24 (a2) shows the principle of the intrinsic healing mechanism of a nano-defect alongside grain boundaries, which attract solute atoms throughout the healing process due to favorable stress states in the defects (figure 24 (a3)) and end as a nucleation site of precipitations (figure 24 (a4)). It is essential to mention that the temperature must not be too high since this would lead to nucleation of precipitation at sites other than nano-voids.

## Low T precipitation

The “low T”-precipitation is closely related to the “high T”-precipitation concept, with the big difference of the lower temperature throughout all stages (see figure 24 (b1-b4)) [52, 53]. In contrast to the “high T”-precipitation healing, the solute healing agent tend to segregate in dislocation cores (b2). Because of pipe diffusion, the atoms in the dislocation cores are highly mobile, even at low temperatures when the localized dislocations in pile-ups lead to stress concentration and formation of nano-voids (figure 24 (b3)), the atoms of the “healing agent” diffuse by pipe diffusion to the nanovoids and end up repairing the damaged area (figure 24 (b4)).

## nanoSMA-dispersoids

The initial microstructure of this concept involves a host matrix with embedded SMA nanoparticles. See figure 24 (c1) [10, 11]. The nanoparticles are stabilized in their austenite phase (high-temperature phase) by the host matrix. When damage occurs in the form of localized dislocation and, therefore, the development of nano-voids, the nanoparticles get activated, as depicted in figure 24 (c2). The particles transform from the austenite phase to the martensite phase, accompanied by substantial particle shape changes (figure 24 (c2)). These execute local strain fields on the host matrix and lead to a compressive force of the nanovoids on the host matrix (figure 24 (c4)).

## 3.4.2. Healing methods of macrocracks

### SMA-clamp&melt

The design of self-healing metals to heal macro damage, based on liquid-assisted healing, concentrated the last years on the basis of metal-matrix composites, which are base materials (e.g., solder) reinforced with shape-memory wires. In the desired damage-healing event, the base material matrix is partially liquefied at elevated temperature, and the SMA wires pull the fractured surfaces together [15, 16, 54].

Figure 24 (d1) shows the specially designed microstructure reinforced with SMA wires, in which the structural stability during the healing process is maintained by allowing the available liquid phase solely at the crack surface to participate in the damage recovery. When the stress on the SMA-solder composite exceeds the UTS of the solder, a crack through the solder is produced, presented in figure 24 (d2). The SMA wires have a higher UTS, so the stress leads to a transformation to martensite. From externally applied heating above the austenite temperature of the SMA wires, the composite transforms the SMA to austenite, which leads to compressive stress on the separated parts of the composite (figure 24 (d3)). Further increase of the temperature above the solidus temperature of the solder lets the solder melt, and the parts can rejoin. Since this kind of healing mechanism never depletes of “healing agent”, damaged areas can always and arbitrarily often be healed, which is implied by figure 24 (d4) and figure 24 (d1) being the same.

### Solder tubes/capsules

The solder tubes/capsules idea as a self-healing mechanism for metal is exceptional because the concept emulates the original self-healing concept employed in polymers [55, 56]. The central idea of the solder tubes-/capsules concept is that solder material is capsuled in ceramic tubes or ceramic capsules and embedded in a host matrix of

high melting material, shown in figure 24 (e1). In the case of damage (figure 24 (e2)), the solder containers break, and the liquid “healing agent” escapes (figure 24 (e3)) and seals damaged areas in the base material (figure 24 (e4)).

Despite the close conceptual analogy to the self-healing mechanism of the polymers, this concept bears complications: 1) the filling of the ceramic capsules/tubes; 2) how the enclosures crack when healing is necessary (figure 24 (e3)); 3) wetting and connection of the crack surfaces; 4) the healing process of the crack leads to new voids in the bulk (see figure 24 (e4)). In practice, the described conditions appear too difficult to be fulfilled in metallic systems.

#### Coating agent

The central idea of the coating agent healing concept is that the base material stays the same, and a layer of “healing agent” (e.g., solder) is applied (figure 24 (f1)) as a coating. Therefore, the concept can be applied to a variety of materials [14, 57]. The temperature has to be increased to trigger the healing process in damaged areas on the surface (figure 24 (f3)), whereby the solder liquefies and fills up the crack, as in figure 24 (f4).

#### Electro-healing

The electro-healing concept is relevant for damages of the macro scale. This concept does not need any solder or composite matrix as a remedy [58]. The damaged sample must be immersed in an electrolytic solution, and a voltage has to be applied (figure 24 (g3)). The electrochemical reaction leads to the deposition of external material between the crack surfaces, eventually closing it (figure 24 (f4)). The disadvantage of this technique is that the damaged area must be externally accessible (cracks on the surface, crack through whole thickness).

### 3.5. Application-typical environmental tests

Nowadays, electrical circuits are used in many different devices and application areas. Each of these areas is characterized by individual environmental influences. An important factor for the functionality of an electrical component or circuit is the temperature. The temperature at which an electrical device or component operates is called the operating temperature.

Most devices are manufactured according to one of the various defined temperature ranges. Typical ranges are listed in table 3. However, each manufacturer defines its temperature grades, so designers must pay close attention to the actual data sheet specifications.

The utilization of such ratings ensures that a product is suitable for its application and can withstand the environmental conditions within which it is used. Normal operating temperature ranges are influenced by several factors, like the power dissipation of the device [59]. These factors are used to define the “threshold temperatures” of a product, above which the device will cease to function. The device operates normally between the maximum normal operating temperature and the maximum operating temperature [60]. For example, a resistor may have a threshold temperature of 70 °C and a maximum temperature of 155 °C, between which it exhibits thermal derating [59].

Table 3: Typical temperature ranges, corresponding *designations* and applications

Temperature range	Designation (Temperature range for :)	typical application
0-70 °C	Commercial temperature app.	Consumer electronics, e.g., Radio, TV
-20-85 °C	Industrial temperature app.	Industrial electronics
-40-85 °C	Extended Industrial temperature app.	Industrial electronics
-40 to 125 °C	Automotive app.	Engine-related electronics in the automotive sector, e.g., ECU, A.C. control units
-55 to 125 °C	Military temperature app.	Military applications, aerospace industry

For printed circuit boards (PCBs), the operating temperature may be equal to the junction temperature  $T_J$  of the semiconductor of the device. Nevertheless, the ambient temperature  $T_{amb}$  for integrated circuit boards strongly influences the junction temperature, leading to the equation for the junction temperature:

$$T_J = T_{amb} + P_D \cdot R_{ja}, \quad (9)$$

whereby  $P_D$  is the power dissipation and  $R_{ja}$  is the junction to ambient thermal resistance.

Electrical and mechanical devices and components used in military and aerospace applications may need to withstand increased environmental variability, including temperature range. At the U.S. Department of Defense, the U.S. Military Standard has been defined for all products used by the U.S. Armed Forces. The environmental design of a product and the test limits to the conditions it will undergo during its service life are specified in MIL-STD-810.

Since some devices generate heat during operation, they may require thermal management to ensure that they are within their specified operating temperature range, specifically, that they are operating at or below the maximum operating temperature of the device.

However, operating temperature ranges only define the maximum and minimum temperature, whereas most tests prescribed by manufacturers assume a relative residence time at a certain temperature (see figure 25).

The current standard for connecting components and PCBs in the automotive industry is soft soldering with tin-silver-copper (SAC) solders. In the field of power semiconductors, both power density and typical operating temperature and the required service life are increasing. Whereas the LV124 standard, which is currently mainly used by the German automotive industry, still requires 300 thermal shock cycles in the temperature range from -40 °C to +100 °C, the new GMW3172 standard already requires 1000 cycles in the temperature range from -40 °C to +140 °C. A similar trend can be seen with the solder joint temperature: SAC solders can only be used up to a maximum operating temperature of 100 °C or just above, but current high-power LEDs or power transistors could tolerate up to 140 °C at the contact points.

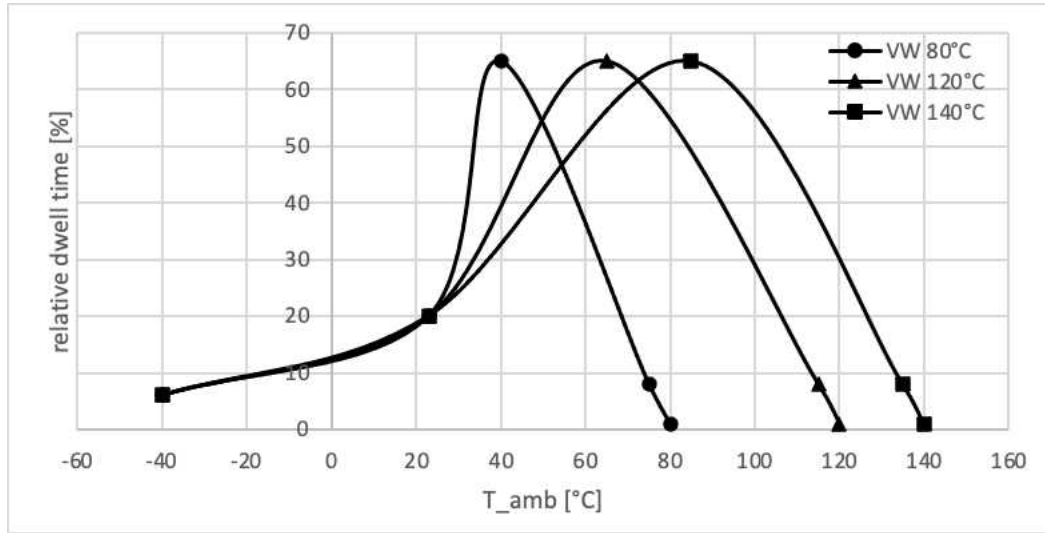


Figure 25: Different acuity levels of test temperatures defined by automotive producers

### 3.6. CALPHAD method

Thermodynamic calculations in MatCalc [61] are based on the CALPHAD method [62]. CALPHAD stands for CALculation of PHase Diagrams and is introduced in the early 1970s. The CALPHAD method aims to obtain a consistent description of a phase diagram and thermodynamic properties of certain elements to predict a set of stable phases including their thermodynamic properties in domains without experimental information and for metastable states during the simulation of phase transformations.

Experimental information on phase equilibrium in a system and all thermodynamic information and properties from thermochemical and thermophysical studies on occurring phases are collected and described with a suitable mathematical model, including a set of adjustable parameters. Based on the experimental data, phase diagrams and thermodynamic properties of all phases can be calculated by adjusting the parameters.

For this purpose, the free energy is preferred since most experimental data are obtained at known temperature and pressure and the other thermodynamic quantities can be derived from them. Minimizing the Gibbs energy of a given system at constant pressure yields the thermodynamic equilibrium. In a multiphase equilibrium, the thermodynamic equilibrium is obtained by minimizing the sum of all Gibbs energies of the stable phases.

$$G_m = \sum_{\Phi} n^{\Phi} G_m^{\Phi} = \text{minimum}, \quad (10)$$

with  $n^{\Phi}$  being the number of moles and  $G_m^{\Phi}$  is the molar Gibbs energy of phase  $\Phi$ .

The CALPHAD method is characterized by realistic and practical mathematical models for the Gibbs energy of each phase. The Gibbs energy  $G_m$  in a binary system can be expressed by:

$$G_m^{\Phi} = \sum_{i=A,B} x_i G_i^{\Phi,0} + RT \sum_{i=A,B} x_i \ln x_i + x_A x_B \sum_{\nu} L_{\nu} (x_A - x_B)^{\nu} \quad (11)$$

This equation starts from the left with the reference state, whereby  $x_i$  is the mole fraction of component  $i$ , and  $G_i^{\Phi,0}$  the Gibbs energy of pure component  $i$  with  $\Phi$  structure. This is followed by the ideal mixing term. The right one

is the excess Gibbs energy of mixing, with  $L_v$  being the interaction coefficient, and  $v$  the power of polynomial series. For different solution models, different values for  $v$  are used.  $v = 0$  is used for a regular solution model, if  $v$  is between 0 and 1, it is a sub-regular solution model, and so on.

One of the strengths of the CALPHAD method is that the individual descriptions of the subsystems can be combined to describe a more complex system. Once thermodynamic descriptions are established for all constituent binaries, preliminary descriptions for the ternaries can be obtained by extrapolating the binary model parameters.

In this work, an iteration of the Cost 531 solder database [63] is used, which is a product of the international project Research Action 531. This database uses a semi-empirical approach for modeling the database, meaning that the approach is built up on the experimental data and, therefore, strongly depends on the latter's quality and amount. The included elements are quoted in table 4, with both typical solder elements and typical elements used in substrates are represented. 55 binaries, and an assortment of 20 ternary systems, are available. The used iteration of this database (MatCalc solder database) is mainly refined in the solder typical elements, adding Ga to it and removing substrate elements.

Table 4: Elements included in the COST 531 database

Ag	Au
Bi	Cu
In	Ni
Pb	Pd
Sb	Sn
Zn	

### 3.7. Candidates for lead-free solder alloys

Depending on the application, alloying elements in solders can vary strongly. Starting with all non-toxic and non-precious metals, semimetals, and transition metals, accentuated in figure 26 and the melting temperatures in mind, the list is reduced to the red highlighted elements in figure 27, creating an overview of remotely possible constituents for a lead-free, low-temperature solder. The remaining elements can be added for specific mechanical or chemical reasons, but as main components, they drop out for the application as low melting solder because of their inappropriate melting point.

The farther the melting point of an element is apart from the aspired two-phase area (110 °C-160 °C), the less this specific element can be used in a suitable solder alloy. This simple assessment leads to the following ternary and quaternary systems applicable for low-temperature solder:

- Sn/Bi/In [21, 22, 23, 64]
- Sn/Bi/Ga [65]
- Sn/Bi/In/Zn [66]
- Sn/Bi/Ga/Zn [67]
- Sn/Bi/Ga/In [68]



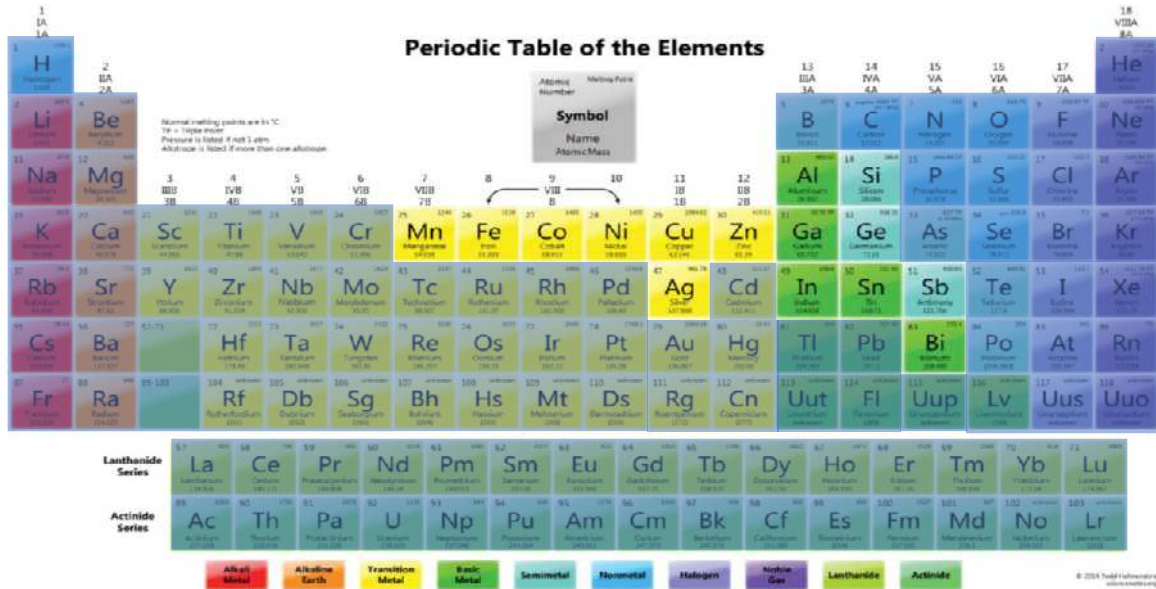


Figure 26: Periodic table of elements with highlighted potential alloying elements

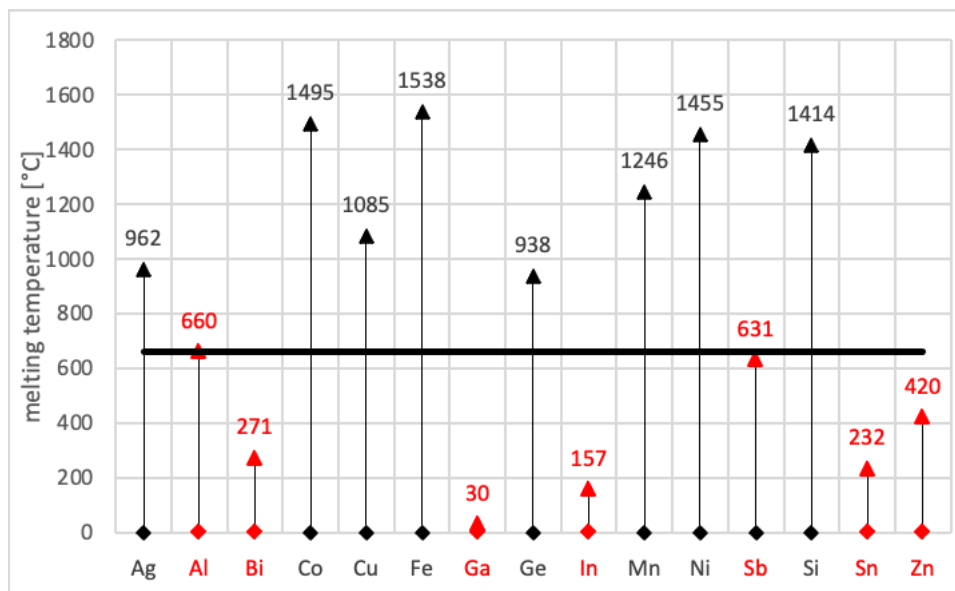


Figure 27: Potential alloying elements for lead-free solder and their melting temperature with indicated maximal temperature area for low-temperature applications; The black line marks the maximum temperature for major constituents

While defining appropriate alloying elements, other physical properties may play a role as well. For example, the volume change at the solidus temperature can be an important attribute of self-healing alloys. Typically, the volume of the solid phase is smaller than the volume of the liquid phase. However, Bi and thus Bi/Si systems show an impressive anomaly. During solidification, a full metric expansion of the eutectic phase occurs [69]. This anomaly is studied in the course of this project by Siroky et al. [70] in connection with enhanced void healing during solidification (see figure 28).

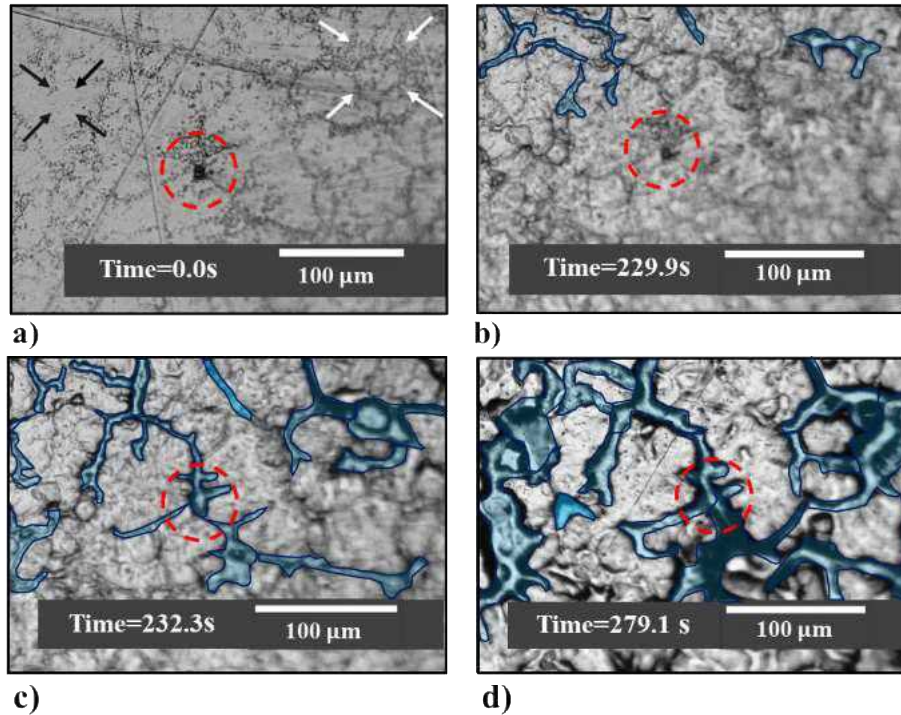


Figure 28: In-situ heating experiment of Sn-30 wt%-Bi. a) Initial microstructure, indicating a 10  $\mu\text{m}$  void (dashed circle) close to a eutectic domain (white arrow) and primary phase (black arrow). b) Onset of eutectic phase melting. c) Void filling with liquid eutectic phase. d) Semi-solid microstructure before re-solidification; Taken from [70]

### 3.8. Differential Scanning Calorimetry

Differential Scanning Calorimetry (DSC) is a thermal analysis technique [71], which measures the differences in heat exchange between a sample to be analyzed and a reference (e.g., empty alumina crucible) (see figure 29). It is used to determine phase transitions, the melting and crystallization temperatures.

Typically, the analysis is carried out under the sweeping of inert gas (e.g., nitrogen or argon) to avoid any material reaction to be studied with the atmosphere.

DSC measurements are based on the fact that during a physical transformation, such as a phase transition, a certain amount of heat is exchanged between the sample and the environment. The direction of this heat exchange between the sample and the equipment depends on the endothermic or exothermic nature of the transition process. Melting, for example, is an endothermic phase transition because it absorbs heat, which shows in a DSC measurement. Similarly, the sample can undergo exothermic processes, such as solidification, when it transmits heat to the environment. Depending on the specific apparatus, an endothermic reaction is shown as a peak or a valley, and an exothermic reaction is vice versa.

Depending on the parameter kept constant, two DSC methods are known:

- Power-compensated DSC, which keeps the power supply constant [72].

With this method, the sample and reference are placed in two different furnaces but the same heat chamber (figure 30). Reference and samples are simultaneously heated, and the temperature is always kept equal in both ovens and varies linearly. The differences in the energies absorbed or released by the sample and the reference are measured. When a transition occurs, depending on whether it is endothermic or exothermic, the sample will absorb or release

energy. A power generator provides more or less energy than the reference, which is recorded as a function of time or temperature.

- Heat-flux DSC, which keeps the heat flow constant [73].

The sample and the reference are placed in the same furnace (figure 31). A platinum probe is used to control and record the temperature evolution of the apparatus. The temperature signal is then converted into a heat output signal. This technique measures the differences in heat flow between the sample and the reference during a temperature cycle. The heating temperature, provided by electrical resistance, varies linearly.

As stated by Höhne in [74], lower measured heat flow (compared to the theoretical heat flow dashed line in figure 32) at the start of an event may be influenced by the thermal conductivity  $L$  of the sample with the crucible. With increasing temperature and the heat flow approaching the magnitude of the phase transition peak, the measured course and the heat flow's theoretical course converge noticeably. At a certain point, the sample temperature and the measured temperature finally coincide ( $T_{\text{limit}}$  in figure 32). The limiting factor for the duration until theoretical and measured values correspond is the thermal conductivity  $L$  between the point of temperature measurement and sample.

In the case of an alloy, the theoretical melting curve can be calculated. By comparing the areas of the theoretical and the measured curves, it is possible to estimate the actual temperatures of an event. Furthermore, for DSC measurements, the rule applies that in the case of two temperature-wise overlapping events, the measured signal for two different events in a sample must be the sum (superposition) of the two individual functions from each event (figure 33).

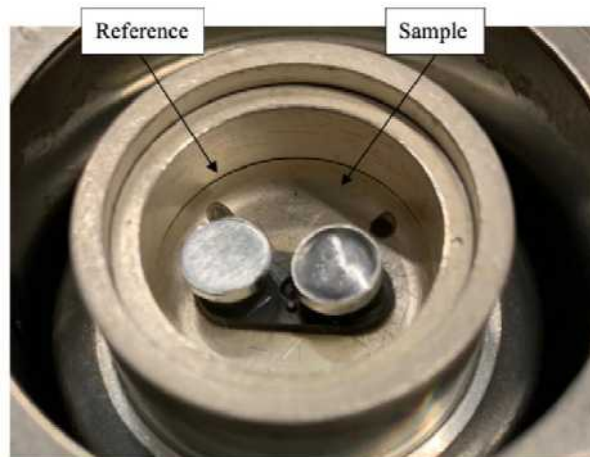
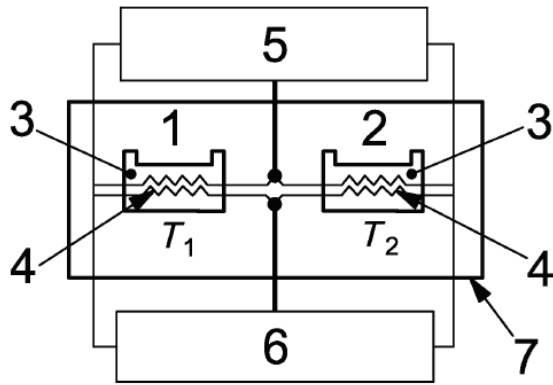
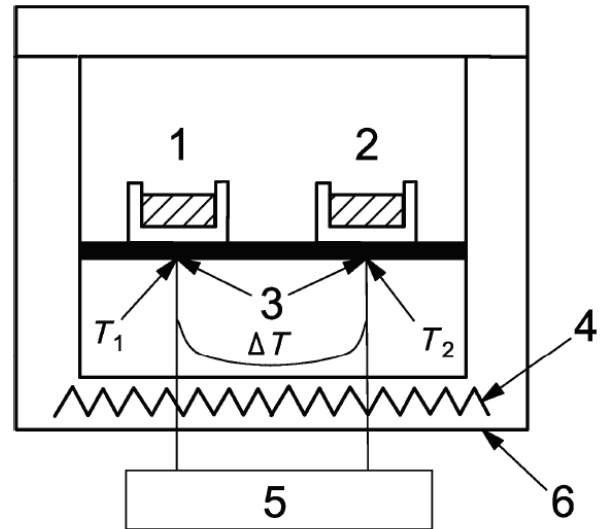


Figure 29: Heat-flux-DSC furnace with reference on the left and sample on the right



1 Sample position	6 Circuit for comp. of the heat flow
2 Reference position	7 surrounding (block) at const. temperature
3 Thermocouple	
4 Heating wire	
5 Circuit for measuring $T_1$ and $T_2$	

Figure 30: Power-compensated DSC; Taken from [75], page 15



1 Sample position	5 Circuit for measuring $T_1$ , $T_2$ and $\Delta T$
2 Reference position	6 Surrounding furnace
3 Thermocouple	
4 Heating wire	

Figure 31: Heat-flux DSC; Taken from [75], page 14

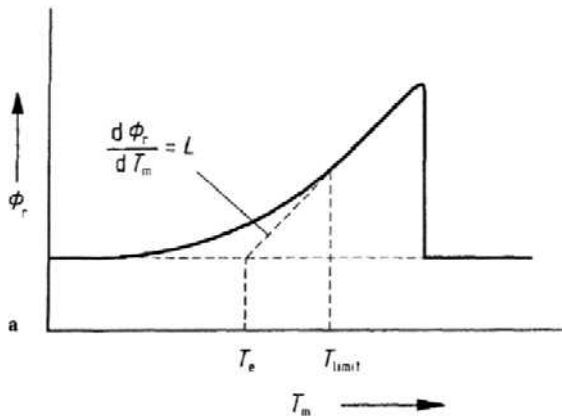


Figure 32: Determination of the starting temperature of an event when smearing occurs, with  $\phi_r$  being the true heat flow into the sample, the measured temperature  $T_m$ , the thermal conductivity between the crucible and the sample  $L$ , the extrapolated peak onset temperature  $T_e$  and the temperature, at the sample temperature and the measured temperature coincide,  $T_{limit}$ ; Taken from [74], page 136

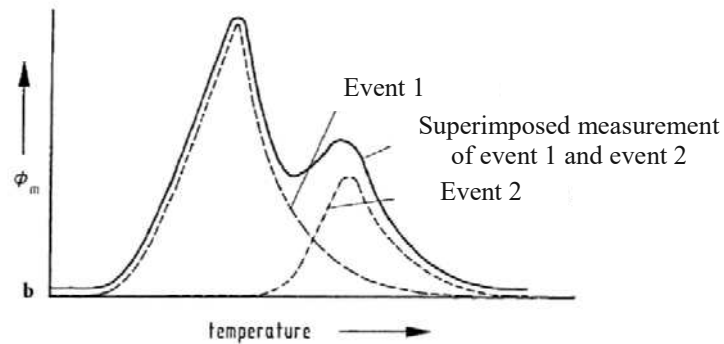


Figure 33: - - -: Hypothetic (measured) curves of the individual events at  $T_1$ ,  $T_2$ ; - : Recorded (superposed) curve measured for two successive events; Taken from [74], page 131

### 3.9. Tensile test for mechanical validation

To develop a superior solder material, the investigation of the mechanical properties and the evolving microstructure is necessary [76, 77]. The tensile test enables an assessment of the mechanical properties of solders in application. The course of action is detailed in the DIN EN ISO 6892-1.

In the tensile test, a sample is loaded with uniaxial tensile stress until failure to determine one or multiple mechanical parameters. Some of the most important values are:

- Elastic modulus
- Ultimate tensile strength (UTS)
- Yield strength
- Uniform elongation
- Toughness

During testing, the elongation increases with pre-adjusted velocities, which can vary in different sections of the measurements. Throughout the experiment, the resisting force  $F$  of the sample against the progressing elongation is measured with a loading cell and is continuously recorded alongside the elongation. The stress  $\sigma$  is calculated from the force  $F$  and the cross-section of the sample  $A$  in the gage section defined by the length  $L_0$  (see figure 35):

$$\sigma = \frac{F}{A} \left[ \frac{\text{N}}{\text{m}^2} \right] \quad (12)$$

This conversion of the force entails, that the recorded data is unbiased regarding the analyzed form of the sample and dimensions.

The elongation  $\Delta L$  in relation to the original gauge length  $L_0$  defines the strain  $\varepsilon$ :

$$\varepsilon = \frac{L - L_0}{L_0} = \frac{\Delta L}{L_0} \quad (13)$$

The tensile test results are usually illustrated in a stress-strain diagram (see figure 35). At the beginning of the experiment, most materials act linear elastic, meaning that the deformation inflicted in this section disappears completely when the sample is unloaded. The corresponding material parameter, which characterizes the linear elastic deformation property, is the Young's modulus  $E$  and corresponds to the slope of the so-called Hooke's line.

$$E = \frac{\Delta \sigma}{\Delta \varepsilon} \left[ \frac{\text{N}}{\text{m}^2} \right] \quad (14)$$

From the point on where the yield strength  $\sigma_Y$  is exceeded, plastic deformation starts alongside the elastic deformation. After the yield point, the course is strongly dependent on the material-specific mechanical properties, like strain hardening, brittleness, or ductility. Often, this transition is not identified by a kink of the trajectory as with mild steel (see figure 36), in which cases the yield strength is stated at a defined plastic deformation (typically yield strength at 0.2 % plastic deformation; e.g., stress/strain curve of steel and Polycarbonate in figure 36). Beyond the yield point, the cross-section of ductile sample is uniformly plastically elongated over the gauge section until the ultimate tensile strength (UTS)  $\sigma_U$  is reached.

From the UTS onwards, ductile samples start necking in the plane where the sample cross-section is weakest. After necking, the damage process for ductile samples starts with the nucleation of microvoids, which can grow into

microcracks as the load progresses and finally lead to failure by cracking or fracture. The material separation is thus the result of the progressive coalescence of the voids into cavities and subsequent shearing off of the remaining webs as soon as a critical volume fraction is reached (see figure 34)

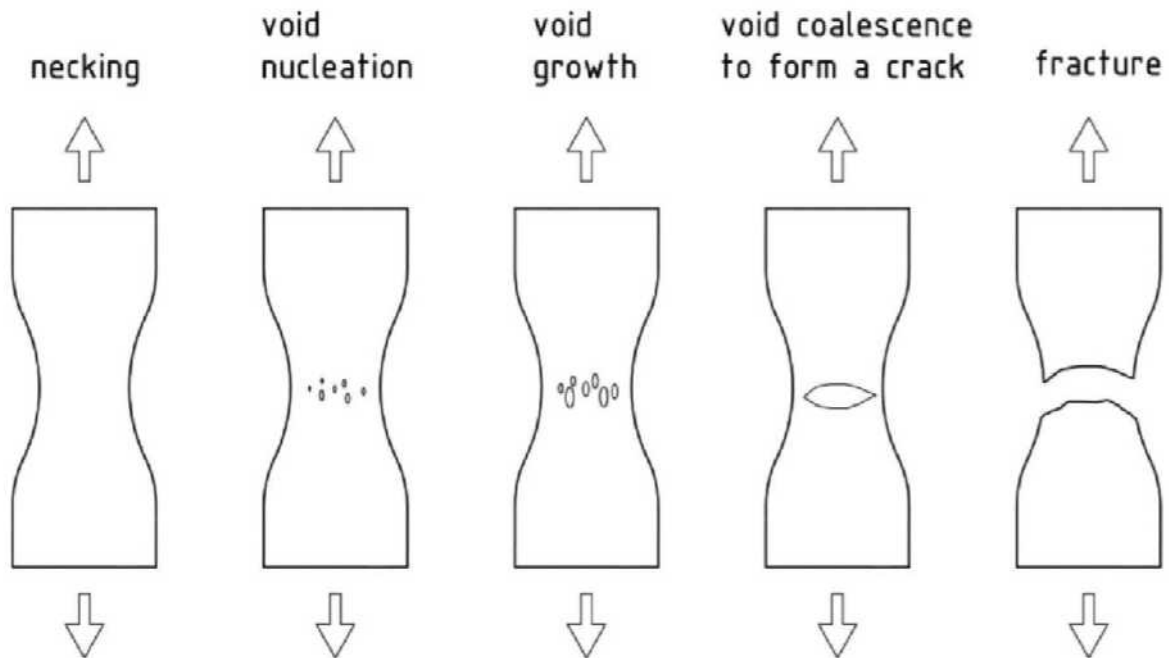


Figure 34: Evolution of a failing ductile sample under uniaxial tensile stress. Taken from [78], page 294

The opposite are brittle materials, which do not show significant plastic deformation before failing. Nevertheless, all materials have in common that the plastic deformation formed between yield point and failure remains after unloading, in contrast to the elastic deformation.

Another important test value is the toughness because it depicts the overall performance of a sample. Toughness is related to the area under the stress-strain curve, which determines the ability to absorb energy during deformation. Tough materials usually have a balance of strength and ductility. Most metals are tough because they have high strength while absorbing a lot of deformation energy without breaking (see figure 37).

If the surrounding conditions, like temperature, vary, the examiner must keep the thermal expansion of the machine frame or the loading cell in mind. Therefore, it is necessary to record the surrounding conditions like pressure or temperature outside the regular testing ranges defined in DIN EN ISO 6892-1.

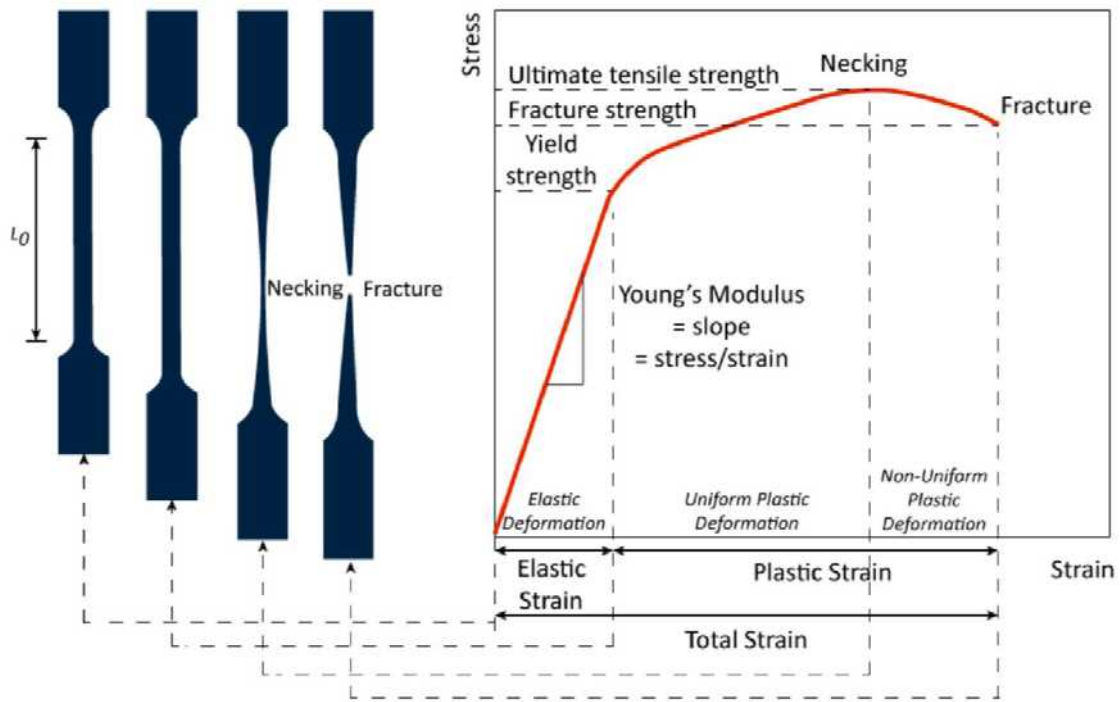


Figure 35: Stress/strain diagram of a ductile material; Taken from [79], page 3

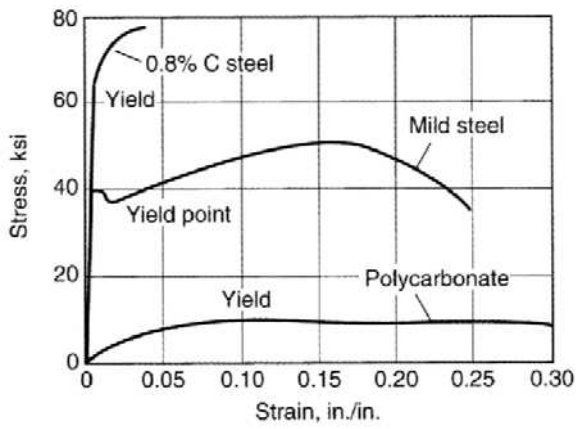


Figure 36: Stress/strain curve of different materials; Taken from [76], page 18

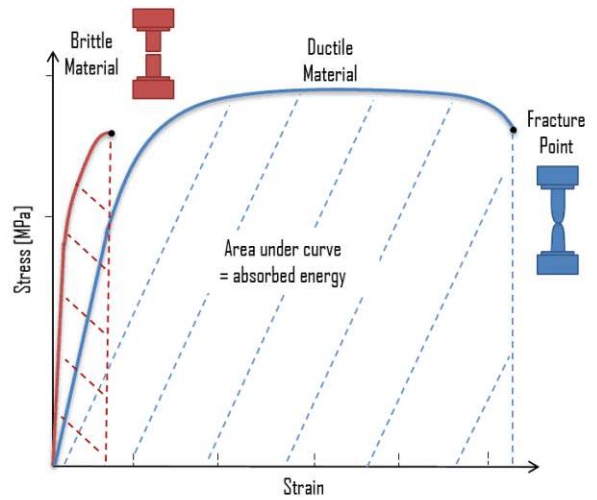


Figure 37: Stress/strain curve of a brittle and ductile material, respectively; Taken from [80]

## 4. Experimental

This chapter describes the necessary steps for manufacturing, testing and evaluation processes used in this thesis. The detailed description of the processes includes the procedure and the used machines so that a descendant can use and reproduce the acquired knowledge of the thesis.

### 4.1. Sample production for mechanical tests and microstructure analysis

In the course of this work, all tests are performed on a bulk level, avoiding the uncertainty factors based on solder gap thickness, solder length and other production effects of lap-shear tests. The solder alloys have been made from pure alloying components in different embodiments, like granular or blocks. The solid materials have been chopped into small pieces, mixed, melted in an enamel pot, and solidified in a copper mold. This protocol is conducted three times to guarantee homogeneous solder alloys.

#### 4.1.1. Production of solder alloys

In this study, all solder alloys have been melted in an enamel crucible under an argon atmosphere on an inductive heating plate. Typically, a total of 200g solder alloy (the combination of all the components) are weighed in with the Sartorius 225D scale in a one-time-use paper cup. Therefore, Sn and Bi are used in a granular form. In is cut from a 100g block in small chunks to minimize the concentration gradient in the first place. Subsequently, all components are placed in the crucible, and a lid machined from high-temperature transparent Perspex with a screwed-in gas-inlet for the argon gas is placed on (see figure 38). The argon gas flow is adjusted to approximately 2l/min to minimize oxidation during the melting. The crucible is placed on the inductive heating plate and heated up to 150 °C above the specific, calculated liquidus temperature of the respective alloy and held at that temperature for 5 minutes, during which the alloy is thoroughly mixed by evenly swiveling.

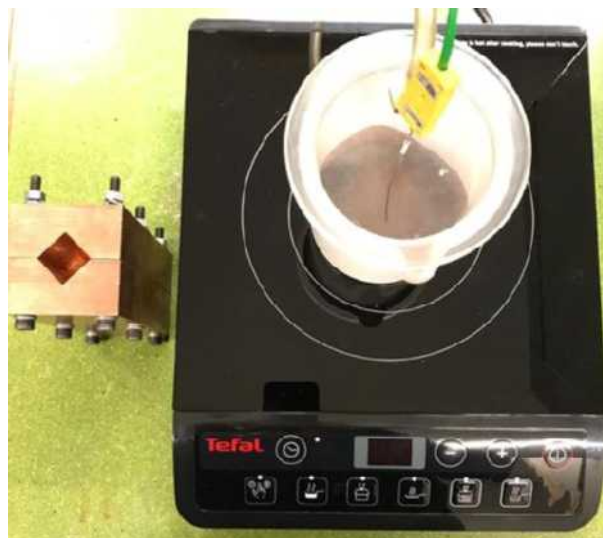


Figure 38: Enamel crucible on the inductive heating plate with high-temperature Perspex lid on, gas inlet and thermo-gauge in Copper block to solidify remaining solder material.



## 4.1.2. Production of dog bone-shaped samples

The molten solder is poured into a high-temperature silicone mold (see figure 39), held together with a vise and two aluminum plates to distribute the pressure on the silicone form evenly. In one casting process, six cylindrical dog-bone-shaped tensile test samples are produced, whereby each specimen is 50 mm in total length with a gauge section of 5 mm and a gauge diameter of 3 mm (see figure 40). This approach is chosen to make small charge sizes possible and to produce a sufficiently high number of samples under identical circumstances.

The silicone mold is coated with talcum powder before each casting process to extend the lifetime of the silicone mold. The samples are cooled down in the mold for 10 minutes, and then the sprue is trimmed off and put back in the enamel crucible for further molding processes. With 200g of alloy, approximately 12 samples can be produced. The excess solder material is then filled in a copper mold (see figure 38) for solidification and stored for later use or other tests (e.g., DSC investigation).



Figure 39: 6 solid solder samples after molding process in a high-temperature silicone mold

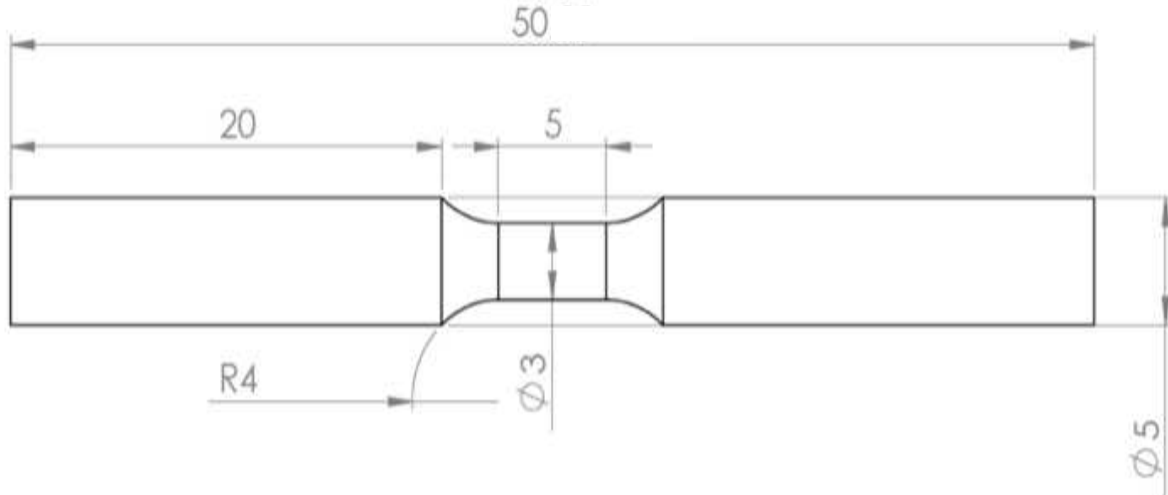


Figure 40: Dimensions of a solder sample; Measurements in mm



Figure 41: A solder sample before (upper) and after (lower) machining in its final form.

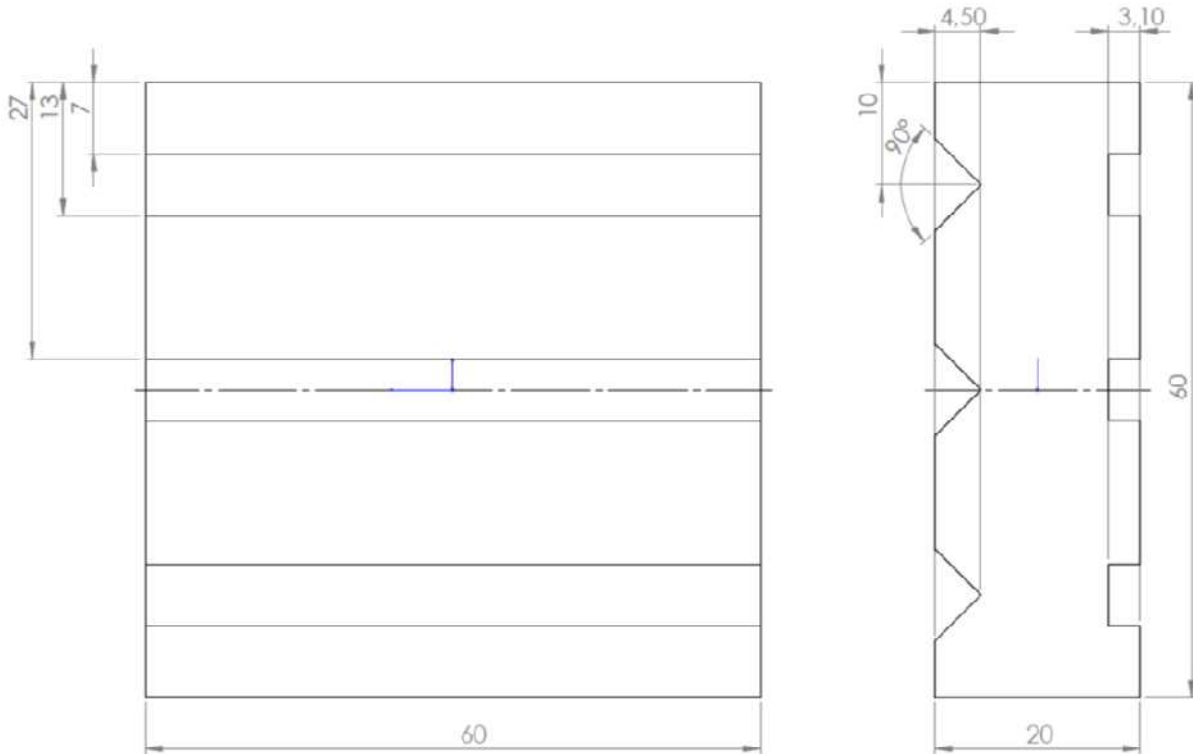


Figure 42: Milled block for grinding the samples in dog bone shape; Measurements in mm

For mechanical testing, the dog-bone-shaped specimens are further machined. With a 320K grinding disc, the clamping areas of each sample are flattened on both sides to 3 mm thickness ( see figures 41 and 49).

Three samples at a time are therefore affixed with double-sided adhesive tape on the “V”-shaped grooves of a milled holder (figure 42) to grind the first side and afterward mounted on the other side of the holder (box-shaped grooves) to grind the second side parallel to the first. After each sample, the adhesive tape is replaced with a new one. The danger of tearing out the sample and damaging it entirely or at least alter it incomparably is otherwise not negligible.

## 4.2. DSC

For CALPHAD validation and alloy quality control, the TA Q2000 DSC is used with an empty standard aluminum crucible as a reference. Approximately 9-11 mg of the solder are weighed in with the Sartorius 225D scale, placed in an aluminum standard crucible pan and pressed with an aluminum standard crucible lid (see figure 43). From

each alloy sample, three specimens are tested for three runs, respectively. Each run starts at room temperature (25 °C), heats up with 10 °C/min to about 40 °C above  $T_{liq}$  of the tested alloy. After 2 minutes of holding at that temperature, the sample is cooled down with 10 °C/min to 25 °C and held there for 2 minutes (figure 44).

The sole purpose of the first run is to improve the sample's contact area and conductivity in the aluminum crucible and, therefore, must not be interpreted as a property of specimens. Runs two and three are the actual measurements (see figure 45).

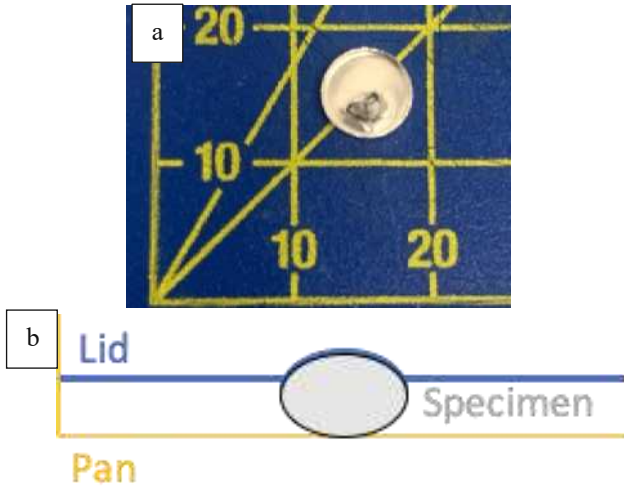


Figure 43: a) Complete DSC sample; b) simplified structure of a DSC sample

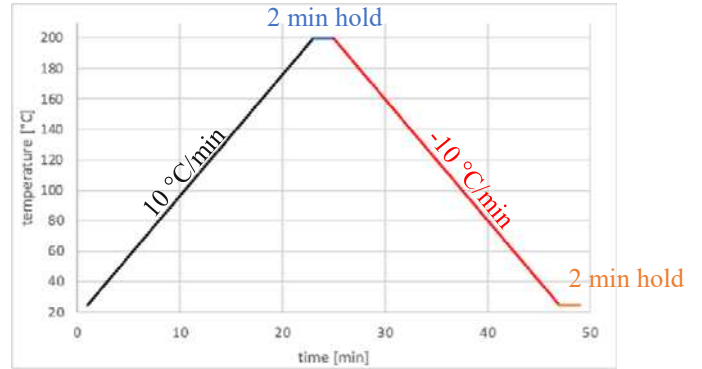


Figure 44: Heating, cooling rates, and isothermal steps in a DSC run

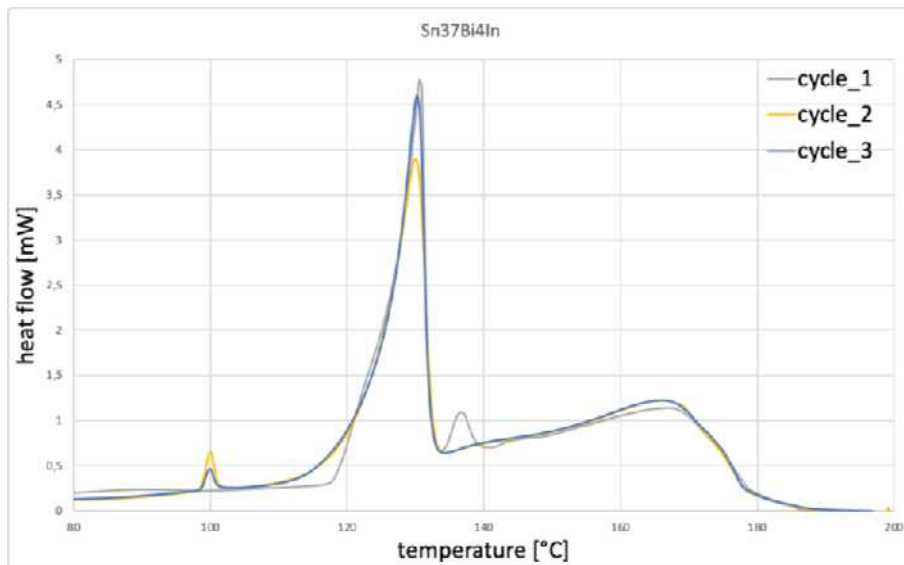


Figure 45: Typical DSC measurements, including the settling cycle (cycle\_1) and the two measurement cycles (cycle\_2 and cycle\_3).

### 4.3. Microscopy

Different microscopes are necessary at different development stages of solder alloys, damage identification, and evaluation. The optical microscope is essential for crack evaluation and is used for microstructural investigations before SEM microscopy and EDAX assessments. The digital microscope gives a three-dimensional insight if the cracks are broad enough.

### 4.3.1. Optical microscopy and preparation

Samples examined with the optical microscope are embedded in a slow curing resin (ARALDIT AY 103-1 and ARADUR HY 956 EN). After 24 hours, the solid resin blocks are ground and polished to uncover cracks in the interior of the samples (see figure 46).



Figure 46: Damaged solder sample embedded in slow curing resin after grinding and polishing

This resin is characterized by a low-temperature curing process, which is necessary since an excessively elevated temperature would alter the microstructure and probably influence cracks or other damage features.

The grinding process starts with 320K grit wet paper by hand on a grinding disc with water. This grit is used until approximately two-fifths of the samples are ground down. From this point on, the following grinding steps are necessary to polish the scratch marks from the previous step. The successive steps are 500K, 1000K, 2000K, 9  $\mu\text{m}$ , 3  $\mu\text{m}$  and oxide polishing suspension (OPS). From the 1000K step onwards, the grinding process is semi-automatically performed with a Struers TegraForce 5 grinding machine. The 1000K step takes roughly 30 seconds, the 2000K step approximately one minute, and the 9  $\mu\text{m}$ , 3  $\mu\text{m}$ , and OPS step five minutes, respectively (see table 5 for an overview). Three samples are for this purpose mounted on a sample holder (see figure 47).

Table 5: Grinding Process of embedded samples for optical and SEM microscopy

Grit	Machine/ Assembly	Time [min]
320K	Per hand on grinding disc	ca. 2
500K	Per hand on grinding disc	ca. $\frac{1}{2}$
1000K	Struers TegraForce 5	ca. $\frac{1}{2}$
2000K	Struers TegraForce 5	ca. 1
9 $\mu\text{m}$	Struers TegraForce 5	5
3 $\mu\text{m}$	Struers TegraForce 5	5
OPS	Struers TegraForce 5	5



Figure 47: sample holder with three chucked samples

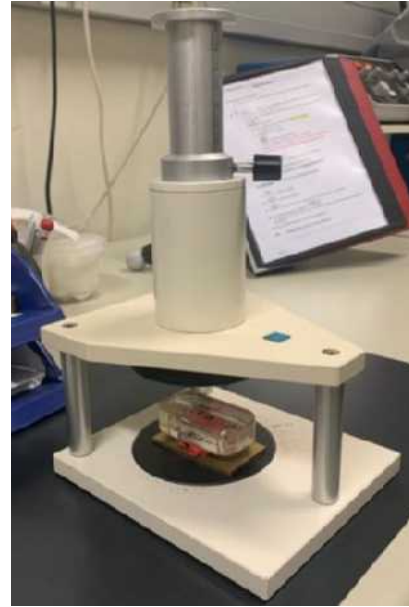


Figure 48: optical microscopy sample on modeling clay in alignment press.

After polishing, the samples are individually affixed with modeling clay on a plate and pressed in a small alignment press (see figure 48) to level the samples evenly and simplify the handling under the microscope. The sample is then examined under an optical microscope. For an initial control of the sample, 25 times magnification is used, and an overview picture is taken. All damage symptoms are then photographed with 100 times magnification.

### 4.3.2. Digital microscopy

After the tensile test, the samples are inspected with the Keyence VHX 6000 digital microscope (figure 50). The specimen is held with a small clamp (see figure 49), and all sides are photographed with 30 times magnification. A panorama picture is taken with 100 times magnification from each sample, and the height and width of each crack are evaluated.



Figure 49: Dog bone shaped solder sample



Figure 50: Keyence VHX 6000 digital microscope

### 4.3.3. Scanning electron microscopy (SEM)

After examination under the optical and digital microscope, the samples are examined under a Philips XL30 scanning electron microscope (SEM) with an EDAX module. Therefore, samples are placed in the SEM chamber to analyze the surface and the sample cross-section (see figure 51). Both, secondary electron ( in the following SE; see figure 52) and back-scattered electron (in the following BSE; see figure 53), are used to analyze topology (SE) and the optical distribution of phases and elements of the plane of interest (BSE). The EDAX module is used to scan specific areas or the whole frame. An accelerating voltage of 20keV is chosen for all measurements. The polaroid 4x4.5" format is used as a reference size for all magnifications.

Since the Philips XL30 SEM has a minimal energy resolution of 130eV, the Sn and In excitation energies are nearly identical due to the close InLa and SnLa values (157eV difference).



Figure 51: Attachment of 6 samples on a conductive plate in the SEM microscope

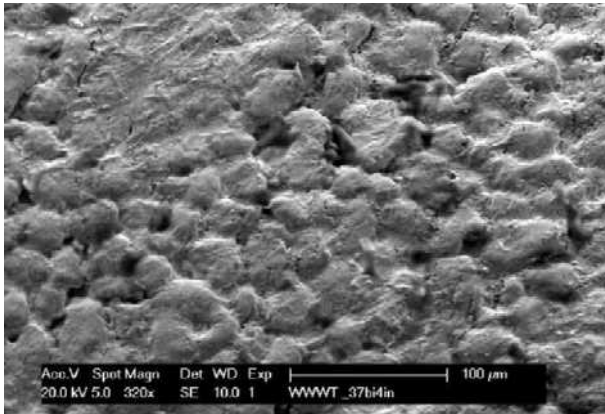


Figure 52: Typical S.E. image of a Sn37Bi4In-sample after heat treatment

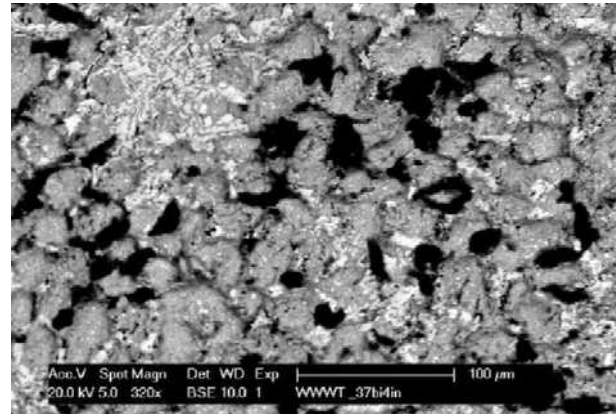


Figure 53: Typical BSE image of a Sn37Bi4In-sample after heat treatment with 320 times magnification

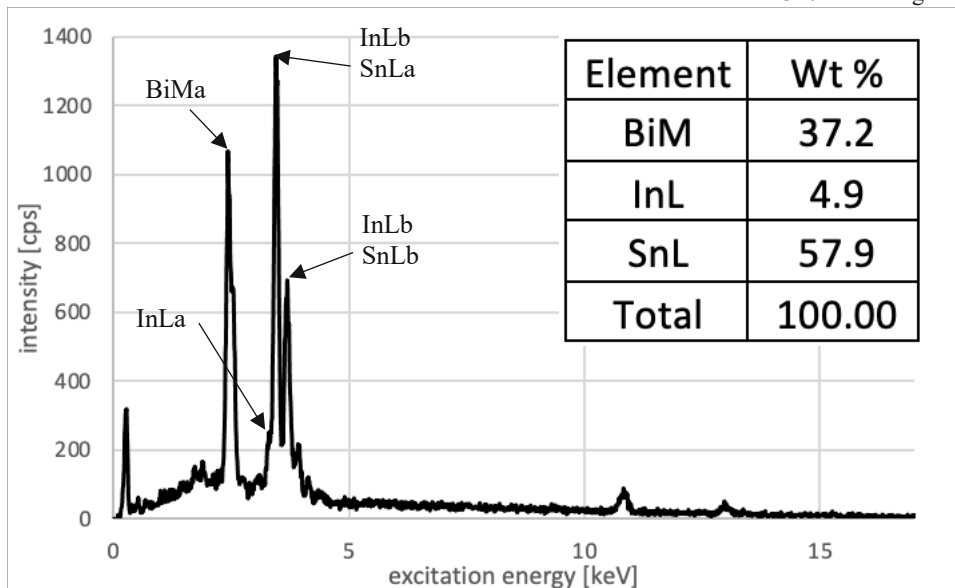


Figure 54: Representative EDX analysis of a Sn37Bi4In-sample after heat treatment with analysis table

## 4.4. Loading protocol

The loading protocol is carried out on the Zwick/Roell Z250 tensile test machine fitted with a 10 kN loading cell. A sample is placed in the lower clamp with a big clamping plate and a 3 mm sheet metal at the bottom to prevent uneven clamping and tightened loosely. The vertical orientation of the sample is verified with a bubble level to ensure uniaxial loading. Subsequently, the upper clamp is moved down, so the distance from the lower and upper pair of clamps is 2 mm. At this position, the right side of the upper clamping plates is brought into contact with the sample, followed by firmly tightening the upper left clamping plate and, at last, firmly tightening of the lower-left clamping plate (see figure 57). After 10 minutes of alignment and relaxation, the upper and lower clamps are firmly tightened again, and the loading protocol is started. The used parameters for the loading protocol are collected in table 6.

Table 6: Parameters for the loading protocol conducted with the Zwick/Roell Z250 tensile test machine

Parameter	Adjustment
Displacement (in regard to the initial state) [ $\mu\text{m}$ ]	250
Loading velocity [ $\frac{\text{mm}}{\text{s}}$ ]	0.5
Holding duration [s]	10
Unloading displacement (in regard to the initial state) [ $\mu\text{m}$ ]	0
Unloading velocity [ $\frac{\text{mm}}{\text{s}}$ ]	-0.5

Special attention during the test should be paid to the compression regime. A typical problem during testing is the loosening of the clamps on the sample due to the relaxation of the solder in the clamps. In a correct execution, only decreasing maximum forces in the tensile regime are observed. Increasing minimum forces during compression/relaxation regime implies slippage of the solder sample in the clamps (notice almost identical minimum forces in the first (= -655 N) and last (= -662 N) cycle in figure 177 later).

## 4.5. Healing protocol

The healing protocol is executed for each sample individually on a Heidolph MR Hei-End heating plate (see figure 55). The sample is placed on a piece of aluminum foil lying on a milled aluminum block, whereby conductive paste between the foil and aluminum block and thermocouple and aluminum block improves thermal conductivity. The foil is used to ensure a clean surface for each sample and must be changed accordingly. The sample temperature is monitored by a K-type thermocouple held on the milled aluminum block with a screw.

A massive aluminum block is placed on the heating plate, which acts as a heat buffer, so the heating plate does not cool down when the sample, including the milled aluminum block, is placed on it, which would lead to severe overshooting of the temperature due to over-regulation of the plate.

The healing protocol is performed at three temperatures, translating to three liquid phase fractions (see figures 78 later and 7). As soon as the thermometer gauges the desired temperature, a ten-minute timer is started. When the timer is up, the milled block is dragged on the second massive aluminum block held at room temperature, which acts as a heat sink to accelerate the cooling process and to keep the cooling process comparable throughout the different samples.



Table 7: Three different healing protocols, including temperatures of the set heating temperature, the logged temperature near the sample, and healing duration

Heating temperature [°C]	Liquid phase fraction (CALPHAD) [wt%]	Milled block temperature [°C]	Healing duration [min]
122	17	120	10
132	57	130	10
142	67	140	10

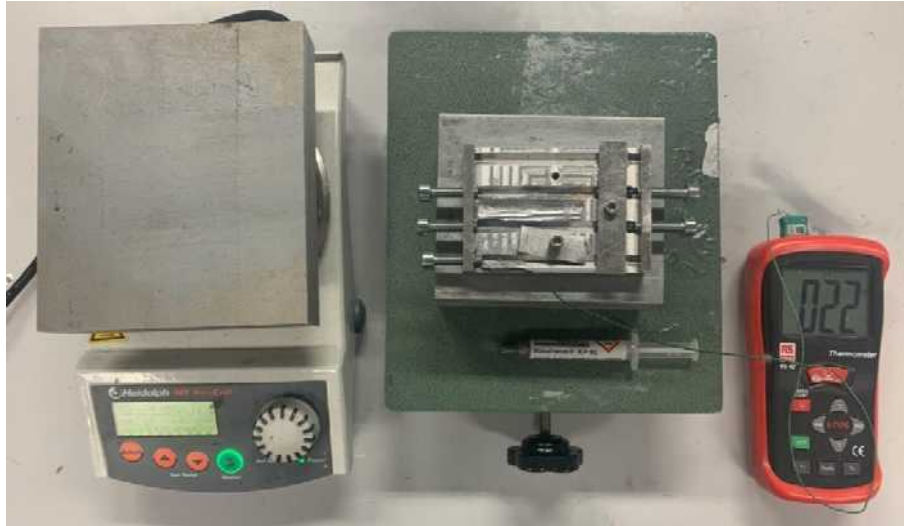


Figure 55: Components for the healing protocol

## 4.6. Long-term stability test

For the long-term stability test, three samples per group are put into a Memmert UNB 200 oven (see figure 56 ) and heated up to 120 °C (above solidus temperature). The six groups were:

- 10 minutes
- 1 day (24 hours)
- 5 days (120 hours)
- 10 days (240 hours)
- 20 days (480 hours)
- 40 days (960 hours)

The samples are placed on a ceramic tile in the oven to avoid unwanted reactions with a material (see insert in figure 56). In this test, no inert gas has been used to see if any oxidizing processes on air alter the material characteristics.



Figure 56: Oven used for long-term stability test on air; Insert shows tile with samples.

## 4.7. Tensile test

The tensile test is executed with the Zwick Z250 and a 10 kN load cell. The clamping procedure is equivalent to the one introduced for the loading protocol (chapter 4.4. Loading protocol). The traverse speed in the elastic regime in chapter 5.5.5 Tensile tests of loaded and healed samples is 0.00025 mm/s and is then accelerated to 0.05 1/min till the end of the test. At 1 mm traverse travel, the test is ended.

For the other tensile tests, the elastic regime velocities are 0.05 mm/s and then decelerated to 0.0012 mm/s.

Further necessary machine adjustments are summarized in the Appendix A.



Figure 57: Clamped sample in Zwick/Roeller Z250 tensile/compression machine



## 5. Results and Discussions

This chapter starts with CALPHAD calculations of the ternary Sn/Bi/In solder system, the presentation of the chosen solder Sn37Bi4In and compares the calculated and measured melting characteristics. The influence of the temperature and composition on the microstructure and the mechanical characteristics of this alloy lead to the demonstration of the healing features of the Sn37Bi4In as a representative of the ternary system after being damaged with a tensile fatigue protocol.

### 5.1. Alloy development (CALPHAD)

In this section, the CALPHAD results concerning the performed analysis of the Sn/Bi/In ternary and, in particular, the Sn37Bi4In alloy are presented and discussed. This includes investigating the liquid phase evolution ( $T_{sol}$ ,  $T_{liq_3}$ ,  $T_{liq_{10}}$ ,  $T_{liq_{25}}$ ,  $T_{liq_{50}}$ ,  $T_{liq}$ ), the occurring phases, and the chemical composition of the phases in the temperature interval 25 °C to 200 °C.

#### 5.1.1. CALPHAD investigations of the Sn/Bi/In-system

Starting with the melting and compositional properties of the Bi/In, In/Sn, Bi/In binary systems (figures 59, 60, and 61), the phase fraction diagram of the Bi24In alloy, as illustrated in figure 59, shows a eutectic composition at 67 wt% Bi and 109 °C melting temperature. With increasing Bi, the liquidus temperature  $T_{liq}$  increases steeply while keeping the solidus temperature  $T_{sol}$  at 109 °C. Due to the rapid increase of  $T_{liq}$  (and with the lever rule in mind), the immense liquid phase fraction above 109 °C can be assumed (see figure 58). Although  $T_{sol}$  (109 °C) and  $T_{liq}$  (162 °C) at 24 wt%-In are exactly as desired, the high proportion of the liquid phase (77 %) at 110 °C makes this alloy inappropriate for the intended purpose.

With Bi being the strong but brittle main component and the brittle BiIn phase [81] one of the two solid phases of the Bi24In alloy, the addition of Sn, known in its pure form as a ductile element, complements the binary system as a fitting alloying element for a potential self-healing solder application.

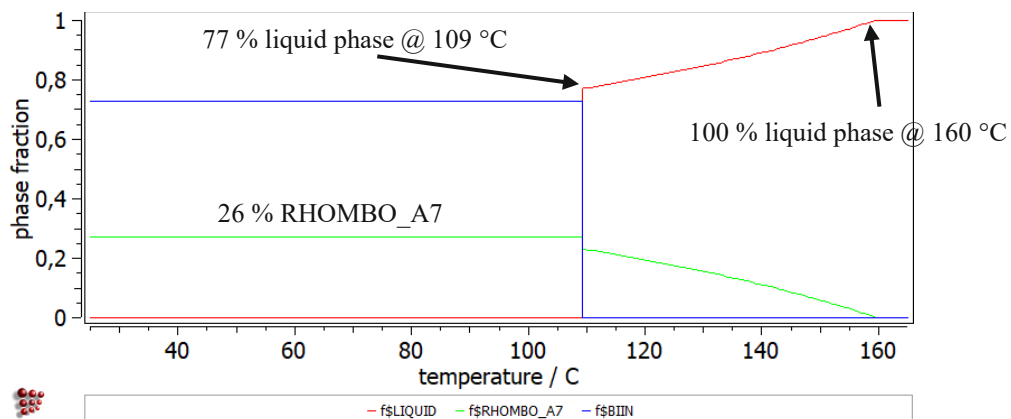


Figure 58: Phase fraction diagram of the Bi24In alloy calculated with MatCalc v6.03 using the Cost 531 database

Sn shows melting temperature reduction effects and eutectic temperatures in the target range (figure 60 and 61). Compared with the Bi/In diagram, the Sn diagrams show miscibility gaps on each end of the phase diagrams and fewer phase transitions.

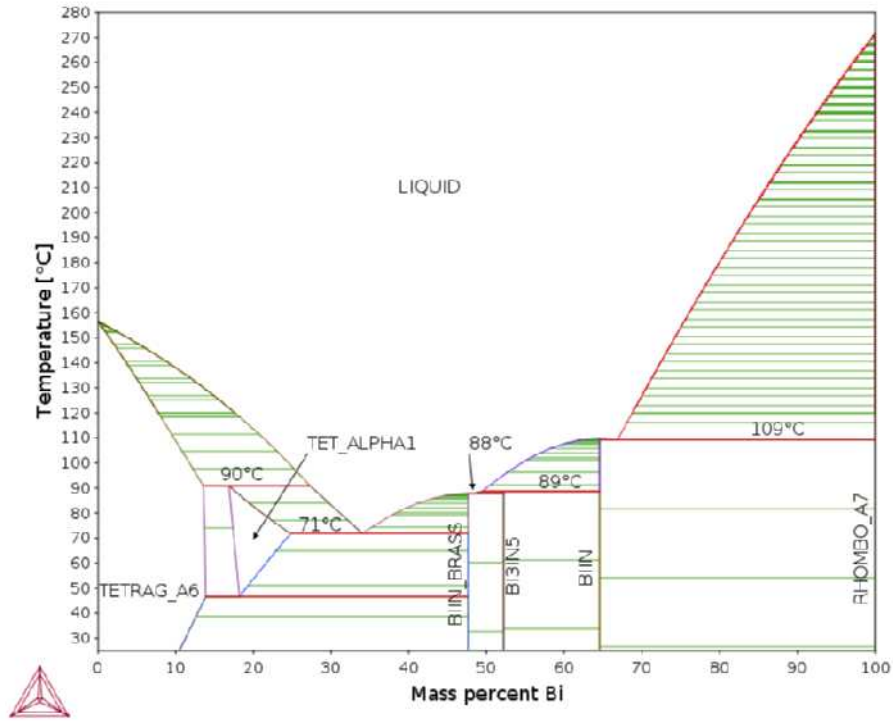


Figure 59: Bi/In binary phase diagram calculated with ThermoCalc (<https://thermocalc.com>) using the Cost 531 database

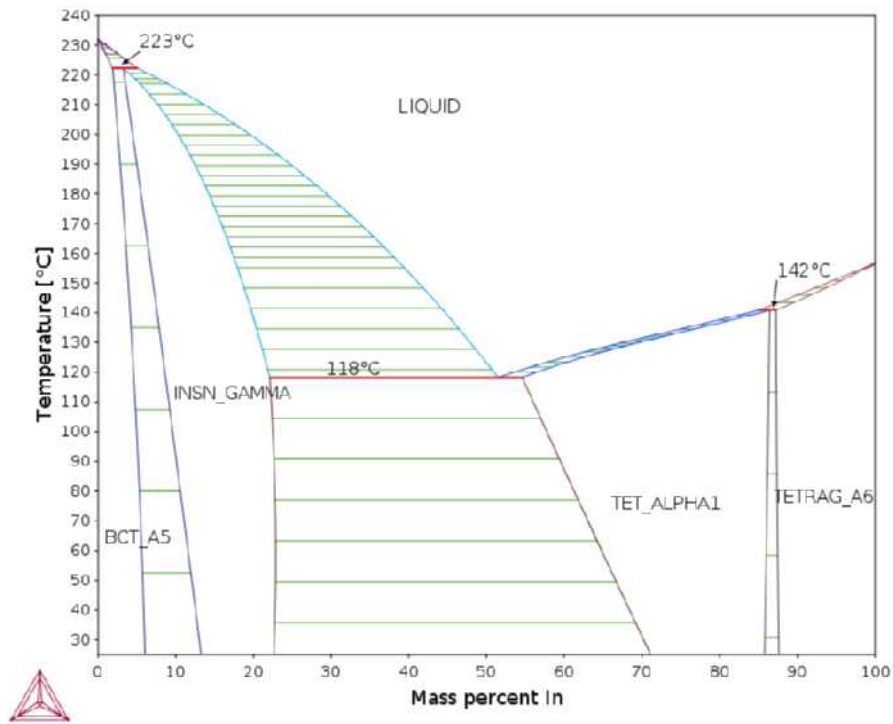


Figure 60: In-Sn binary phase diagram calculated with ThermoCalc (<https://thermocalc.com>) using the Cost 531 database

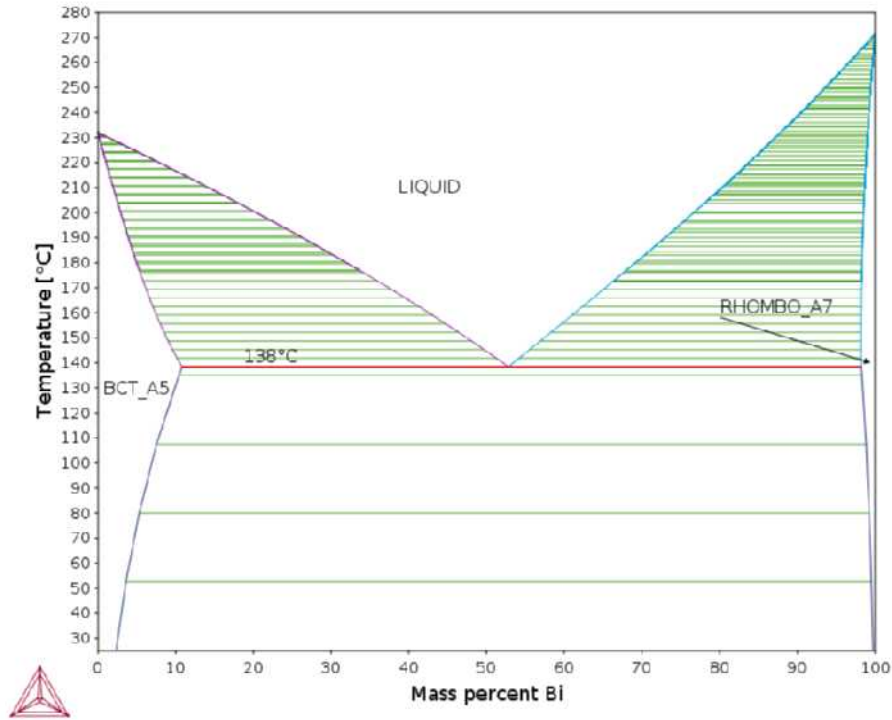


Figure 61: Bi-Sn binary phase diagram calculated with ThermoCalc (<https://thermocalc.com>) using the Cost 531 database

The containing elements of the ternary Sn/Bi/In system, which give the alloy an appropriate set of microstructural and mechanical properties for the desired self-healing application (see table 8), combined with fitting melting temperature range variances add up to an excellent candidate for low-temperature, self-healing solder alloy. The liquid surface projection shown in figure 62 highlights interesting parts of the system regarding melting temperature (red rectangles).

Table 8: Relevant properties for solder applications

Bismuth (Bi)	Indium (In)	Tin (Sn)
Melting temperature 271 °C	Melting temperature 156 °C	Melting temperature 231 °C
Beneficial for micro hardening and shear strength	Decreases melting temperature	Essential for the intermetallic layer with the substrate (IMC)
Expands during solidification	Increases wettability	Increases ductility
Bad electrical conductor	Increases ductility	Intensively investigated in solder applications
Alloy gets brittle	It does not react with water but oxidizes in combination with more potent oxidation agents	Can form brittle intermetallics, if the content is too high
Prone to oxidation	Limited global availability	$\alpha$ -tin/ $\beta$ -tin transition (tin pest)

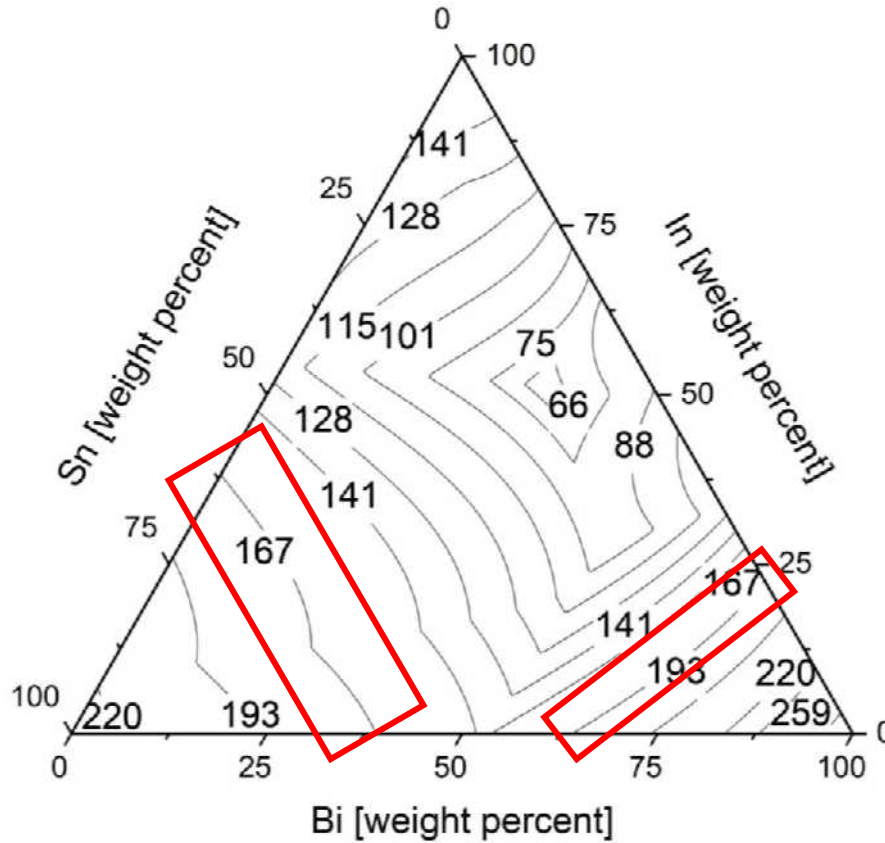


Figure 62: Liquid surface projection of the Sn/Bi/In ternary, calculated with MatCalc v6.03 using the MatCalc solder database

In the course of finding a candidate in the ternary system, the entire Sn/Bi/In system is scanned to find a solder alloy with the desired melting properties. To investigate the liquid phase development of specific alloy composition, six temperatures, namely  $T_{sol}$ ,  $T_{liq\_3}$ ,  $T_{liq\_10}$ ,  $T_{liq\_25}$ ,  $T_{liq\_50}$ ,  $T_{liq}$  of each calculation, has been extracted (see figure 63) and used for the evaluation process.  $T_{sol}$  defines the temperature at which the liquid phase first appears (solidus temperature).  $T_{liq}$  denotes the temperature at which only the liquid phase exists (liquidus temperature). Because these two temperatures leave out much information such as, for instance, the shape of the liquid phase in a phase fraction diagram, four more temperatures have been chosen.  $T_{liq\_x}$  describes, respectively, at which temperature the liquid phase reaches “x” %. With this source of melting temperature information, the ternary system can be scanned for specific alloys. Figures 63 to 65 show different views of the Sn/Bi/In-ternary system, with all six temperatures plotted as separate planes. Figures 66 and 67 illustrate the liquidus temperature and solidus temperature projections, respectively.

For this thesis, the  $T_{sol}$  temperature is chosen at 110 °C, and a two-phase pasty area of 50 °C is considered necessary to be applicable with a wide range of temperature variations and to evaluate different liquid phase fractions and the influence of latter on self-healing effects. With these constraints in mind, Bi concentrations from 0.5 to 99.5 wt% and In concentrations between 0.5 and 40.4 wt% individually are possible.

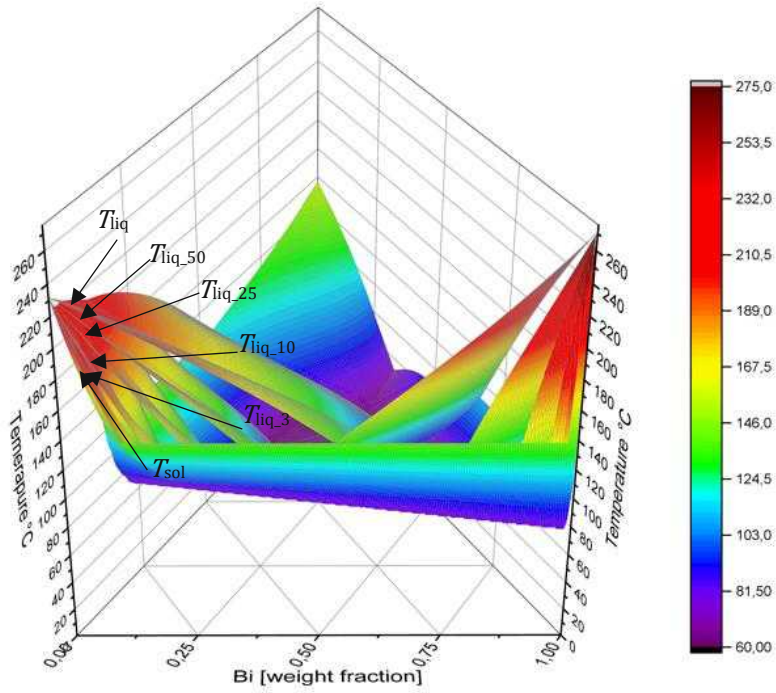


Figure 63: The ternary system Sn/Bi/In calculated with MatCalc v6.03 using the MatCalc solder database; View on the In = 0 plane.

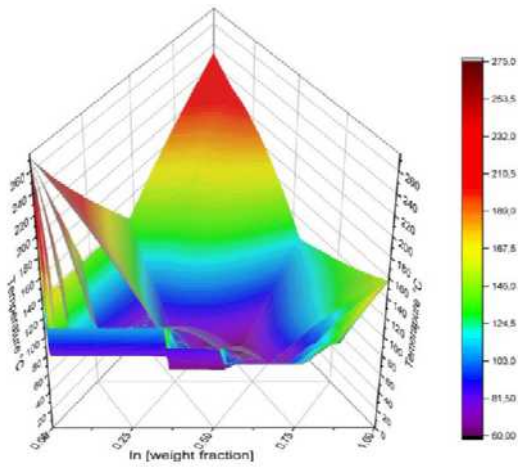


Figure 64: The ternary system Sn/Bi/In calculated with MatCalc v6.03 using the MatCalc solder database; View on the Sn = 0 plane.

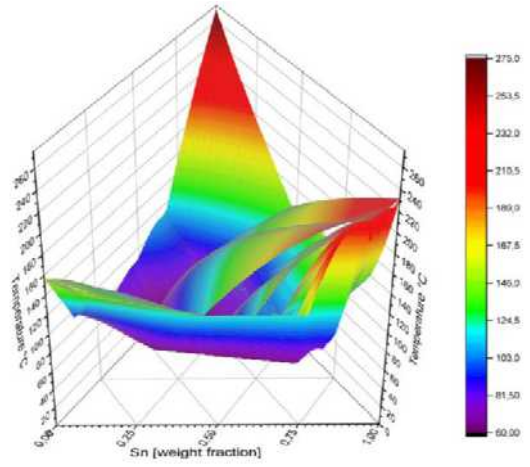


Figure 65: The ternary system Sn/Bi/In calculated with MatCalc v6.03 using the MatCalc solder database; View on the Bi = 0 plane.



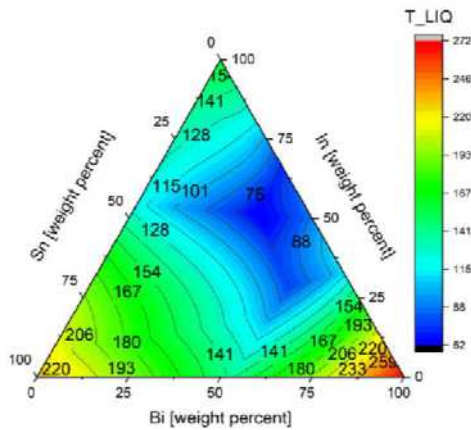


Figure 66: The ternary system Sn/Bi/In calculated with MatCalc v6.03 using the MatCalc solder database. View on the  $T_{liq}$  plane

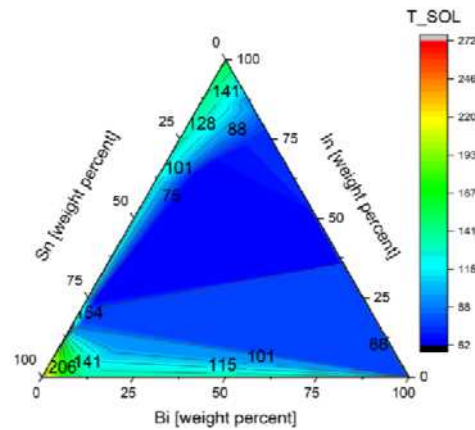


Figure 67: The ternary system Sn/Bi/In calculated with MatCalc v6.03 using the MatCalc solder database. View on the  $T_{sol}$  plane.

### 5.1.2. CALPHAD investigations of the Sn37Bi4In alloy

Originating from a preferable evenly increasing liquid phase with increasing temperatures to see the effect of varying liquid phase fraction on self-healing, a Sn-based solder alloy with 37 wt% Bi and 4 wt% In (in the following “Sn37Bi4In”) is chosen (see figure 68).

An increase of the In content lowers the  $T_{sol}$  and  $T_{liq}$  temperatures substantially. Higher Bi content lowers the solidus and liquidus temperature minimally. It makes the alloy harder but also more brittle since the RHOMBO\_A7 phase becomes more prominent, which is also visible in analyzed samples with different compositions (see chapter 5.3.1. Influence of Bi content on the microstructure), furthermore higher Bi or higher In content leads to arising of a brittle BiIn phase. The Bi content is chosen in regard to form enough RHOMBO\_A7 phase fraction so that a potential solder alloy shows mechanical resistance but is low enough that, when heated up, liquidizes first. Therefore, a crack, which develops mainly in the Bi-rich phase, can be healed. Keeping the melting (see figure 69) and microstructural properties (see figure 74) in mind, the Bi content is set to 37 wt%, and the In content has been set to 4 wt%.

Figures 69 to 73 show the phase fraction diagram and the chemical composition of the foreseen phases liquid, BCT\_A5, RHOMBO\_A7, and INSN\_GAMMA calculated with MatCalc v6.03 and the MatCalc solder database. Nevertheless, in the range where a phase is not stable (e.g., liquid phase below 110 °C), the phase composition adjusts so that the negative driving force reaches a minimum and the chemical potential difference of all phase components is equal. In terms of the chemical composition of phases, the relevant range is given by the region in which the phase is active.

The phase fraction diagram in figure 69 illustrates that the solid solder at 25 °C in equilibrium consists of the three phases BCT\_A5 (Sn-rich phase; figure 71), RHOMBO\_A7 (Bi-rich phase; figure 72), and INSN\_GAMMA (In-rich phase; figure 73). At 63 °C, the INSN\_GAMMA phase disappears completely. The shapes of the INSN\_GAMMA and the BCT\_A5 phase in figure 69 make it evident that the INSN\_GAMMA phase vanishes in favor of the BCT\_A5 phase formation in a solid-solid transition. As the temperature inclines, the amount of the RHOMBO\_A7 phase declines slightly, and the BCT\_A5 phase amount inclines correspondingly until the liquid

phase appears at 110 °C. From here on, both the BCT\_A5 and the RHOMBO\_A7 phase amount decreases fast until the RHOMBO\_A7 phase disappears completely at 127 °C. The BCT\_A5 phase keeps declining with a reduced slope until it vanishes at 164 °C.

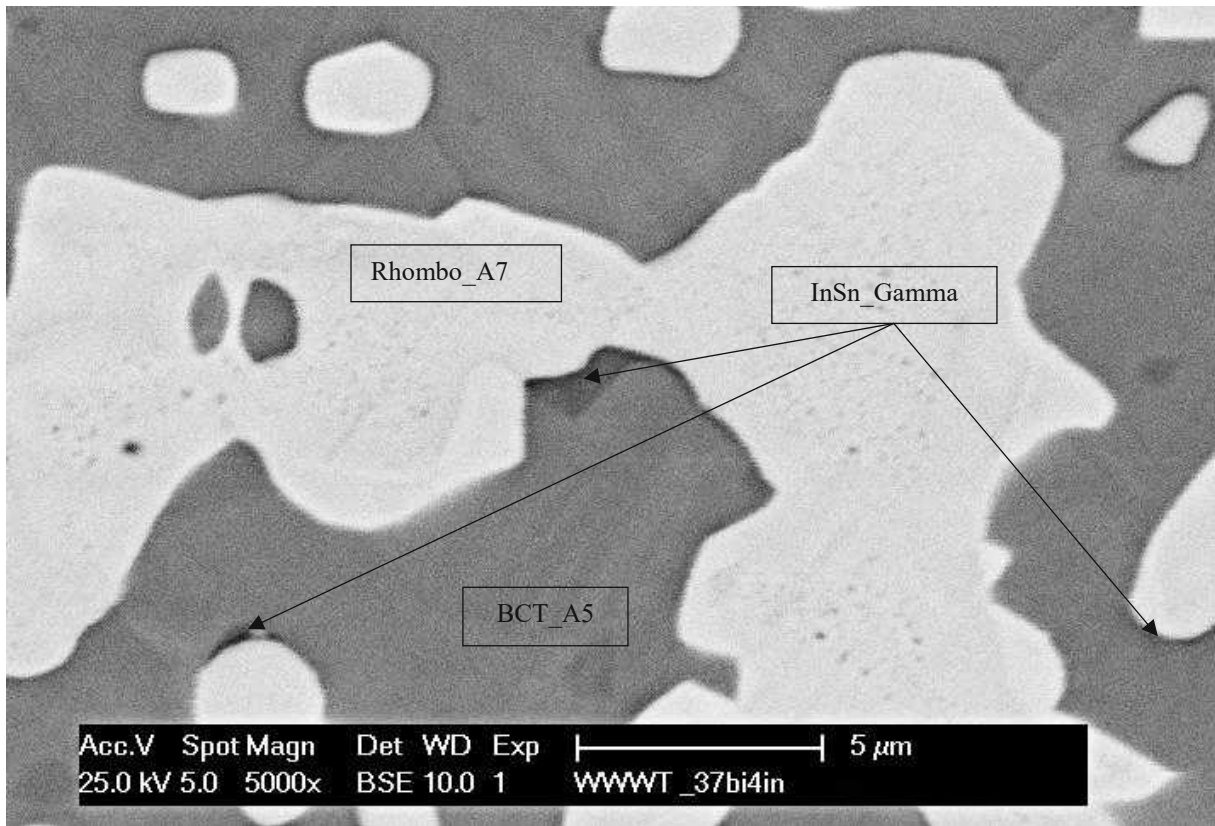


Figure 68: Picture of the microstructure of Sn37Bi4In taken with SEM Philips XL30

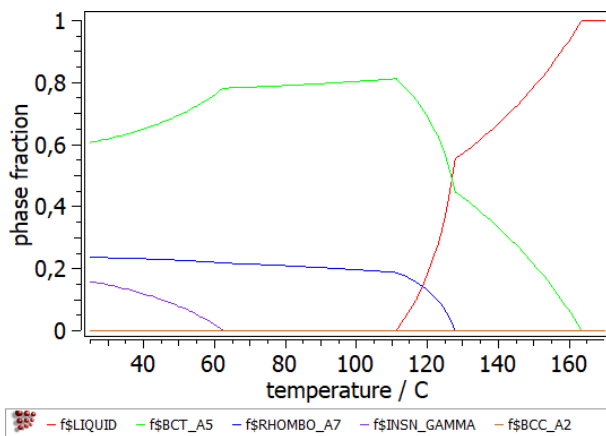


Figure 69: Phase fraction diagram of the SN37Bi4In alloy between 25 °C and 170 °C.

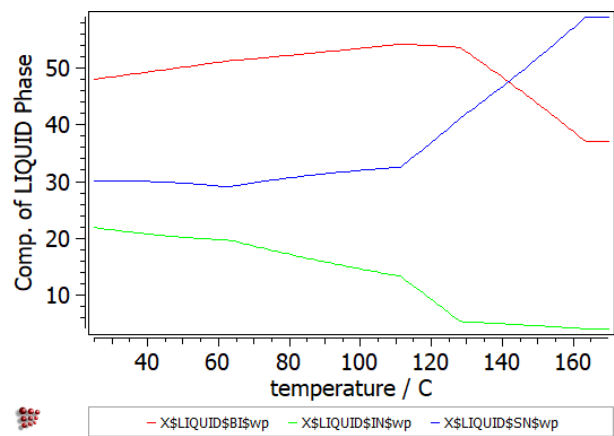


Figure 70: Chemical composition of the liquid phase of the SN37Bi4In alloy between 25 °C and 170 °C

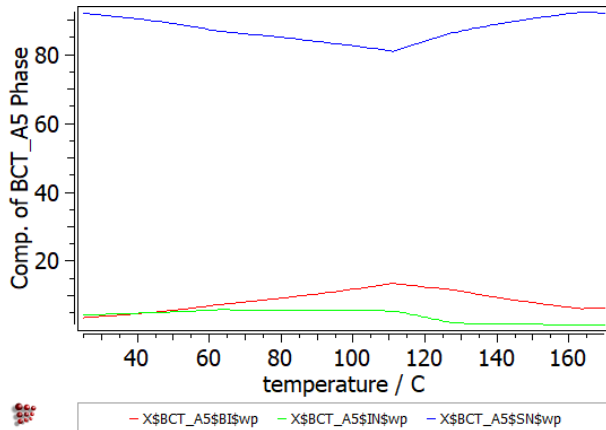


Figure 71: Chemical composition of the BCT\_A5 phase of the SN37Bi4In alloy between 25 °C and 170 °C

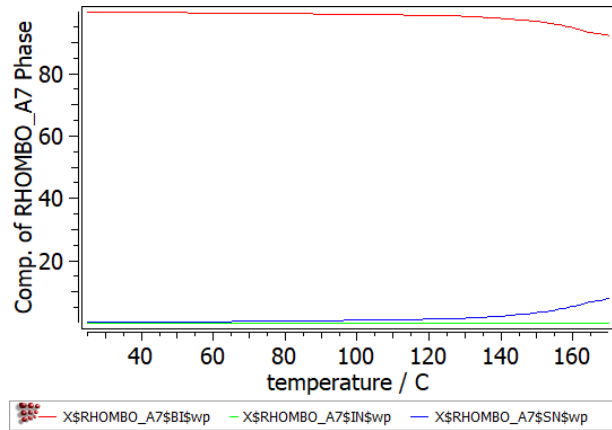


Figure 72: Chemical composition of the RHOMBO\_A7 phase of the SN37Bi4In alloy between 25 °C and 170 °C

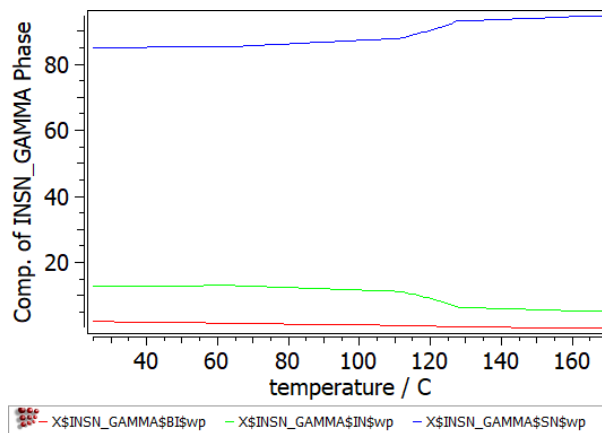


Figure 73: Chemical composition of the INSN\_GAMMA phase of the SN37Bi4In alloy between 25 °C and 170 °C

The INSN\_GAMMA phase composition diagram in figure 73 stands out with a high In content of 12 wt%, which points to the conclusion that, at room temperature, most In in equilibrium is concentrated in this phase. Above 63 °C, the phase vanishes entirely in the BCT\_A5 phase.

As shown in figure 72, the RHOMBO\_A7 phase consists throughout the viewed temperature range to over 97 wt% of Bi until the phase finally vanishes at 127 °C.

Figure 71 displays the chemical composition of the BCT\_A5. At 25 °C, the BCT\_A5 phase consists of 92 wt% Sn, 4 wt% Bi, and 4 wt% In. This composition linearly changes to 80 wt% Sn, 15 wt% Bi, and 4 wt% In at 110 °C. The sharp drop of the BCT\_A5 phase between 110 °C and 130 °C in the phase fraction diagram (figure 69) accounts for the fast decline in In content superimposed with the decline of Bi content of the BCT\_A5 phase in figure 71. Above 127 °C, the Bi content in the BCT\_A5 phase decreases from 10 wt% to 5 wt% until the phase completely disappears at 164 °C.

The chemical composition of the liquid phase is depicted in figure 70. At 110 °C, the liquid phase consists of 31 wt% Sn, 54 wt% Bi, and 15 wt% In. Between 110 °C and 127 °C, the percental amount of Bi remains unchanged, whereas the Sn content increases to 38 wt%, and the In content accordingly decreases to 8 wt%. The rise of the Sn content and the respective decrease of Bi and In continues until it reaches the final composition: 59 wt% Sn 37 wt% Bi and 4 wt% In at 164 °C.

The typical solidification microstructure of the Sn37Bi4In alloy is shown in figures 68 and 74 to 76. As shown in figure 74, the solder consists of two phases, a dark grey matrix phase and an evenly branched light grey phase.

With higher magnification (figures 68, 76), a third phase in the form of slightly darker dots is visible. The light grey areas with dark dots in figure 68 are the Bi-rich RHOMBO\_A7. The grey and dark grey phases are the BCT\_A5 matrix and the INSN\_GAMMA phase. The INSN\_GAMMA phase is predominantly found at the interfaces of BCT\_A5 and RHOMBO\_A7 areas, whereby it can be expected that the RHOMBO\_A7 phase serves as a nucleation site for the INSN\_GAMMA phase. Although the calculations predicted higher INSN\_GAMMA content, minimal dark grey areas are found, which may have two reasons. First, it is a solid-solid transition, which may be retarded drastically since the solder samples are cooled very fast (see figure 79), and a frozen state from higher temperatures of the solid alloy is, therefore, to be expected. Second, the CALPHAD calculations used a stepped equilibrium approach with an infinitely slow cooling rate and may overestimate the achievable quantity of the INSN\_GAMMA phase beforehand.

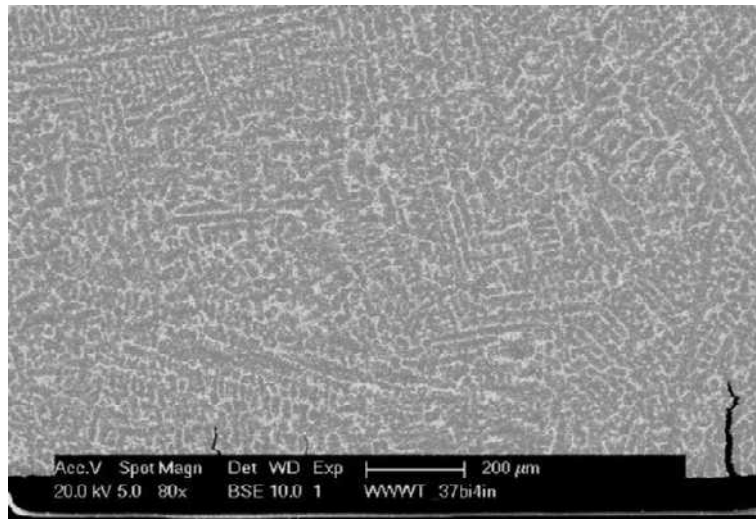


Figure 74: Picture of the microstructure of Sn37Bi4In with 80 times microscope magnification

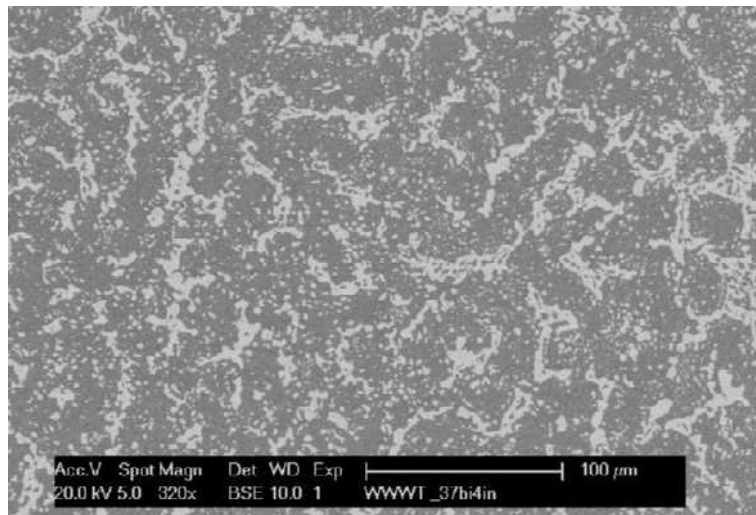


Figure 75: Picture of the microstructure of Sn37Bi4In with 320 times microscope magnification

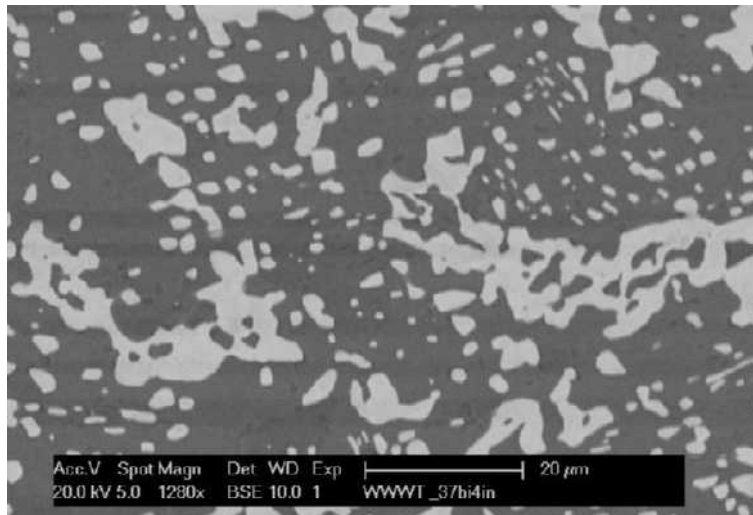


Figure 76: Picture of the microstructure of Sn37Bi4In with 1280 times microscope magnification

### 5.1.3. Comparison of CALPHAD calculations and DSC experiment

DSC samples are analyzed with a heating and cooling rate of 10K/min to validate the predicted melting behavior of the Sn37Bi4In solder alloy (see figure 77). The grey line is the heat flow (in the following “hf”) at a given temperature and displays the temperature difference between the sample and an empty reference aluminum crucible as a function of temperature. The green line in figure 77 is the hf signal slope. It is used to clarify the beginning and end of a phase transition event. The start of an event is noticeable as soon as the slope starts to increase. The temperature at which the slope starts declining is the temperature at which the event is finished.

The hf measurement shows three events at 100 °C, 130 °C and a reaction between 135 °C and 165 °C. The small peak at 100 °C complies with the reaction  $TET\_ALPHA(In\text{-rich}) + INSN\_GAMMA(Sn\text{-rich}) \Rightarrow liquid$ . The reaction corresponding to the highest peak at 127 °C is  $BCT\_A5 + RHOMBO\_A7 \Rightarrow BCT\_A5 + liquid$ . Between 130 °C and 165 °C, the Sn-rich phase vanishes in the endothermic reaction  $BCT\_A5 + liquid \Rightarrow liquid$ . The CALPHAD calculations do not predict the first reaction at 100 °C since it only shows phases in equilibrium. Although the material has been molten, mixed, and molded several times, small areas with higher In concentration might still be possible. The small overall discrepancy between calculation and DSC measurements comes from the finite heating rate, which shifts the events to slightly higher temperatures because the temperature keeps rising while an event is still not finished, therefore the alteration of the slope is used to illustrate the beginning and the end of an event.

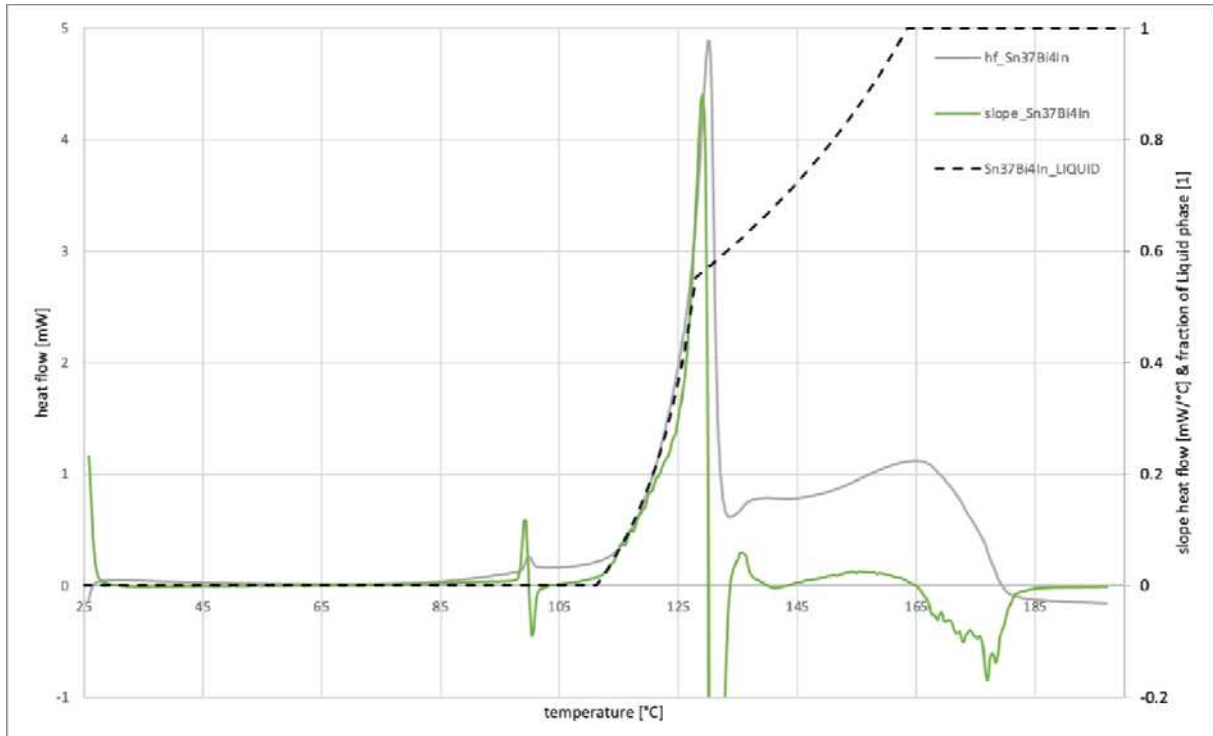


Figure 77: DSC test of the Sn37Bi4In solder alloy with a heating rate of 10K/min; The heat flow (hf) (grey curve) is superimposed with the slope of the hf measurement (green curve) and the comparison of the calculated (dashed black curve) and estimated liquid phase evolution (blue curve)

## 5.1.4. Conclusions of the chapter

Originating from the investigation of the binary and ternary phase diagrams of the alloying elements Bi, In and Sn (figures 59 to 61) and the consequent definition of the desired liquid phase development, the Bi/In and the In/Sn phase diagrams include several alloys with adequate solidus (solidus temperature plateaus at 71 °C, 88 °C, 89 °C, 90 °C, 109 °C, and 118 °C) and liquidus temperatures ranging from 71 °C to over 270 °C. However, deficiencies at closer examination regarding the shape of the liquid phase fraction curve in the binary systems make the addition of the third alloying element necessary. The mechanically hard but brittle nature of Bi, the melting temperature reducing characteristic of In, and the necessity of Sn to build joining intermetallics with substrate material like copper and nickel complemented with the ductile behavior of Sn and In defines the ternary Sn/Bi/In system regarding mechanical and microstructural features.

The complete ternary Sn/Bi/In system is studied using MatCalc 6.03 and the MatCalc solder database. Therefore, the system is divided into 0.5 wt% sections from 0 wt% to 99.999 wt% of all alloying elements, respectively, leading to over 19,700 calculated compositions. From each composition, specific liquid phase fractions are calculated ( $T_{sol}$ ,  $T_{liq\_3}$ ,  $T_{liq\_10}$ ,  $T_{liq\_25}$ ,  $T_{liq\_50}$ ,  $T_{liq}$ ), outlining the course of the liquid phase alongside the temperature. With these parameters, the ternary system is investigated regarding the influence of the alloying elements on the shape of the liquid phase, leading to an alloy composition with desired solidus and liquidus temperature and development of the liquid phase in between these temperatures.

The Sn<sub>37</sub>Bi<sub>4</sub>In solder is in this thesis chosen as a representative of the ternary system to show healing properties after undergoing a mechanical loading and thermal healing protocol. This alloy features a solidus temperature of 110 °C and a liquidus temperature of 165 °C (see figure 69). At room temperature, the microstructure consists of three phases. A Sn-rich matrix (BCT\_A5), a Bi-rich phase (RHOMBO\_A7) forming round particles evenly distributed throughout the matrix, and a Sn-rich phase (INSN\_GAMMA) developing from the BCT\_A5 phase below 63 °C in a solid-solid transition. Although predicted by calculations, the INSN\_GAMMA phase does not develop as anticipated due to the fast cooling process during the molding process, suppressing the solid-solid transition. Between 110 °C and 127 °C, both remaining phases decrease fast in favor of the arising liquid phase. At 127 °C, the RHOMBO\_A7 phase vanishes completely, and leaving the liquid phase and the solid BCT\_A5 matrix as the only remaining phases until the BCT\_A5 phase fades out at 165 °C.

Typically, the gap between solidus and liquidus temperature is chosen to be below 30 °C, since the more an alloy deviates from a eutectic alloy, the more likely a decomposition process will occur [82]. In a liquid-assisted self-healing approach, a wider gap is needed to adjust the healing effect to the occurring thermo-mechanical loads and, therefore, damage during service by increasing the liquid phase fraction accordingly. Therefore, for the investigated alloys, a wide two-phase section between 110 °C and 165 °C is chosen.

## 5.2. Influence of the temperature on the microstructure of the Sn37Bi4In solder

As discussed previously in chapter 5.1.2. CALPHAD investigations of the Sn37Bi4In alloy, the Sn37Bi4In solder has a melting range from 110 °C to 165 °C. Solder samples have been heated to 120 °C, 130 °C or 140 °C and held at this temperature for 10 minutes to understand the influence of enhanced diffusion processes on the microstructure. Both microstructural and topographical feature changes on the surface are considered in the analysis process. The fundamental characteristics are visualized with the BSE detector, and the topography is mapped with the SE module in the SEM microscope. A concluding EDX analysis evaluates the chemical concentrations on the surfaces.

Table 7 and figure 78 show the correlation of applied temperature and expected liquid phase fraction of the Sn37Bi4In alloy. As illustrated, the liquid phase rises quickly between 117 °C and 127 °C from 15 % to 55 %. Thus, much liquid phase is available at 130 °C and 140 °C compared to 120°C.

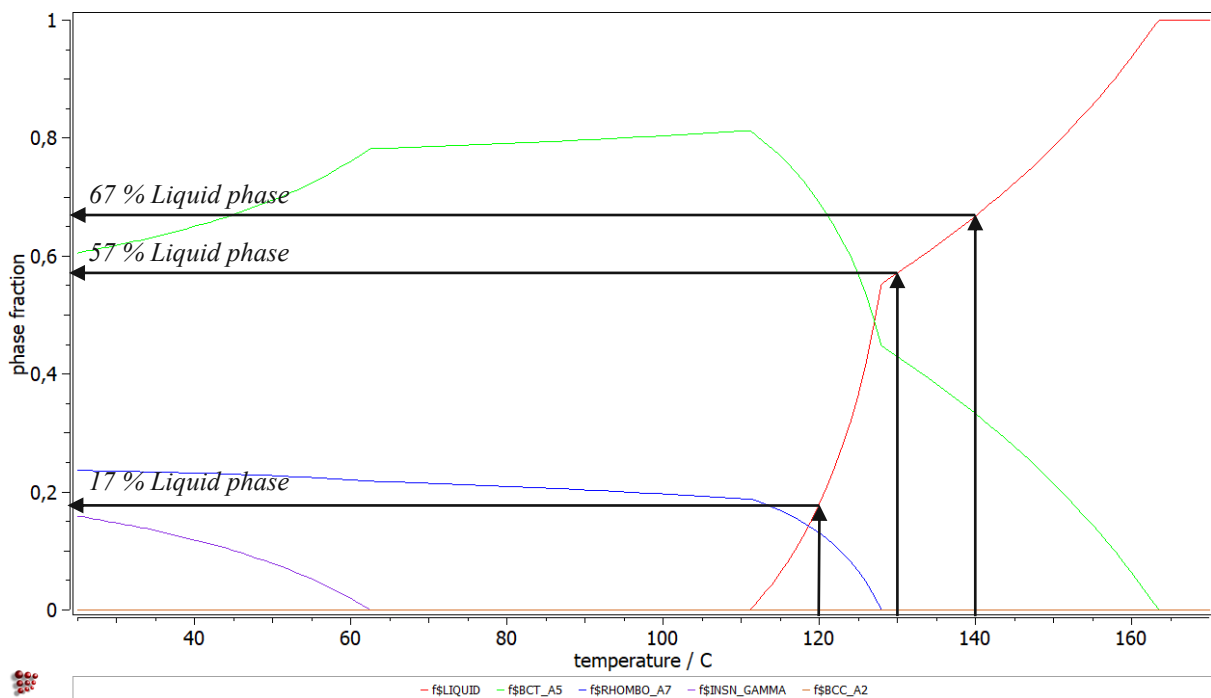


Figure 78: Liquid phase fraction at 120 °C, 130 °C, and 140 °C

In figure 79, the cooling curves of the different heating temperatures are illustrated, and essential values of the cooling processes are summarized in table 9. Since the 120 °C is closest to the solidus temperature (110 °C), the duration in the partial liquid section is the shortest. The ability of the solder to heal cracks is retarded because of the small amount of liquid phase (17 %) and the short duration until the sample solidified (9 s).

At 130 °C, the solder forms significantly more liquid phase (57 %) and has, although a higher cooling rate (1.45 °C/s), 30 % more time during cooling to solidify evenly.

The cooling rate of the 140 °C group is equal to the 130 °C group (1.45 °C/s). The samples of this group produce 67 % of liquid phase and have, during the cooling process, 70 % longer liquid content.



Table 9: Significant values during the cooling process

	Average cooling rate until 110 °C [K/s]	Duration until 110 °C [s]
120 °C	1.25	9
130 °C	1.45	12
140 °C	1.45	21

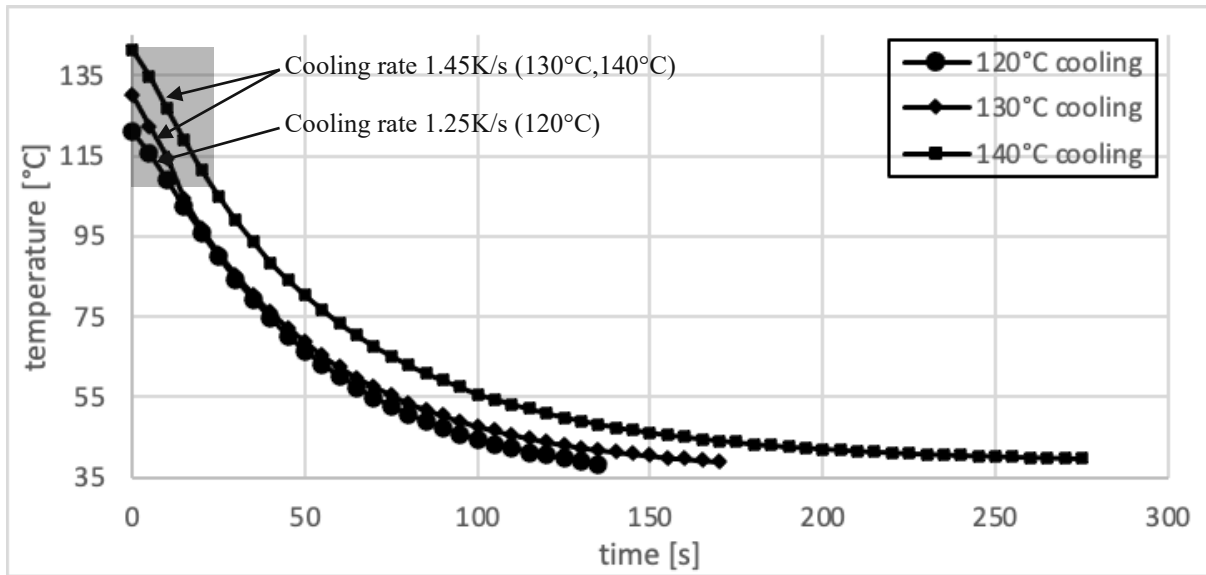


Figure 79: Cooling curve of the different temperatures 120 °C, 130 °C, and 140 °C

### 5.2.1. Microstructure of the reference samples (As cast)

The “as cast” samples have not been exposed to any heat treatment, apart from the initial casting process in the silicone mold. The cooling curve of the casting process in figure 80 illustrates that the cooling rate until the material solidifies (110 °C) is 4 °C/s. Undercooling effects cause the deceleration of the cooling curve at 98 °C during solidification. These samples show the same chemical distribution on the surface of the samples as the ground samples of the Sn37Bi4In solder show on the inside (compare figures 182 and 86). The topology illustrated in figures 81, 83, 85 show a rippled surface with single hills and no preferred direction. A direct comparison of figures 85 and 86 imply that the high flat points are primarily Sn-rich hills, and the valleys are Bi-dominated.

The BSE analysis in figures 82, 84, and 86 confirms that the light-colored Bi-rich RHOMBO\_A7 phase is evenly distributed in the dark grey Sn-matrix. In the left upper corner of figure 81, minor flaws imbedded by  $\mu\text{m}$ -sized holes are visible. These defects may have developed due to the use of talcum powder as protection for the silicone mold during the casting process.

The EDX analysis in figure 87 confirms that the “as cast”-Sn37Bi4In alloy sample only differs in the Sn and In amounts slightly from the weights in the alloy composition.

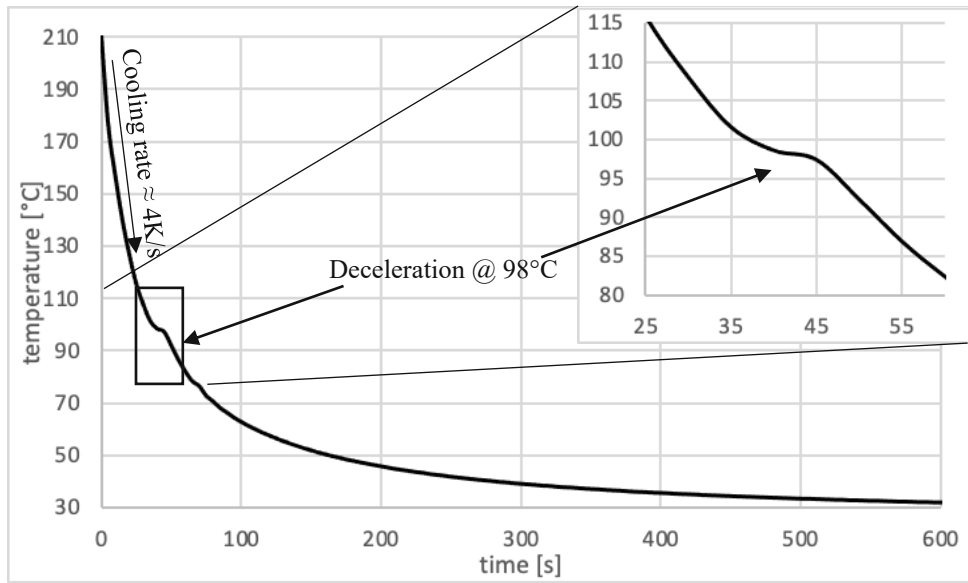


Figure 80: Cooling curve in the silicon mold during casting process with zoomed-in inlay of the point of stagnation

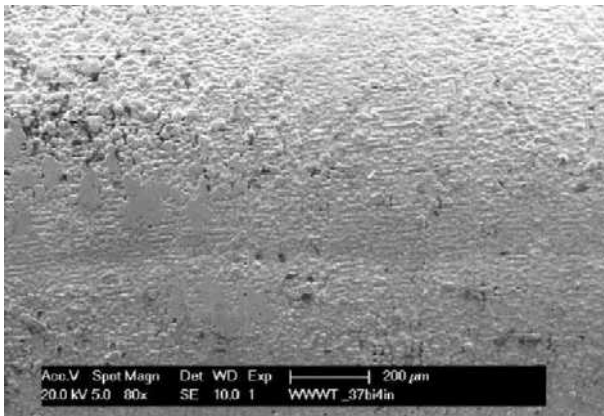


Figure 81: SE image of an "as cast"-sample with 80 times magnification

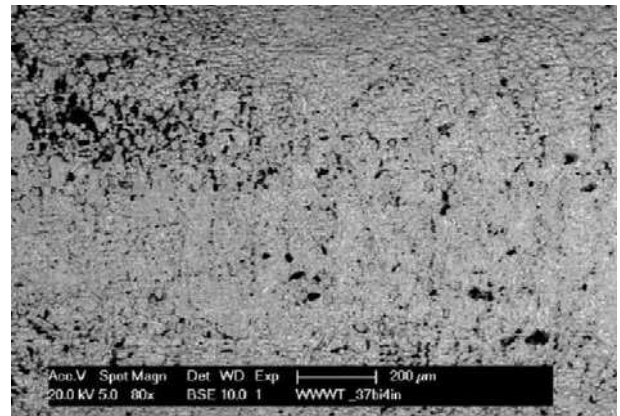


Figure 82: BSE image of an "as cast"-sample with 80 times magnification

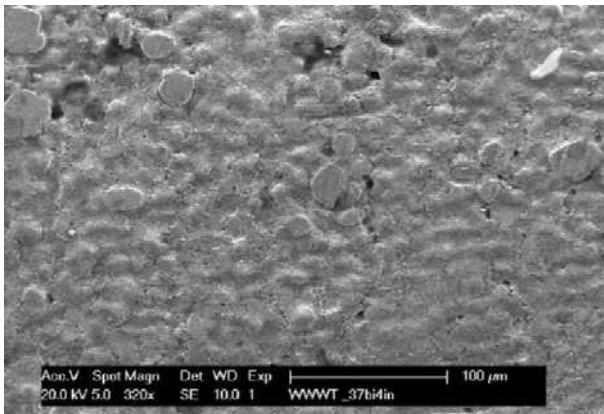


Figure 83: SE image of an "as cast"-sample with 320 times magnification

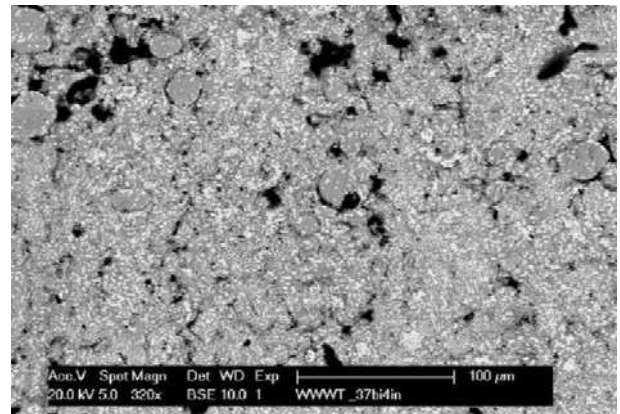


Figure 84: BSE image of an "as cast"-sample with 320 times magnification

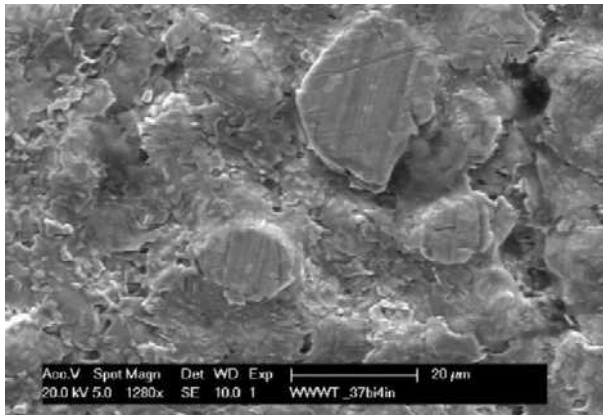


Figure 85: SE image of an "as cast"-sample with 1280 times magnification

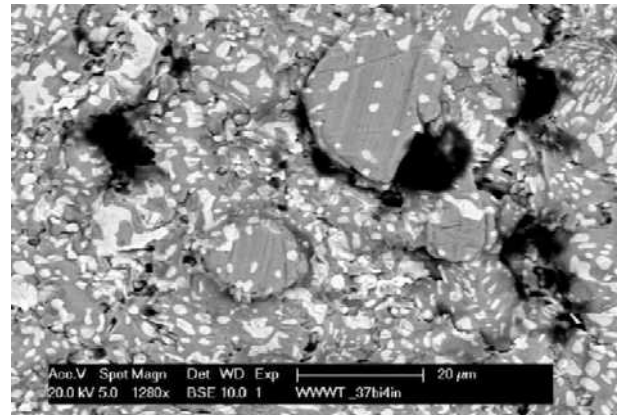


Figure 86: BSE image of an "as cast"-sample with 1280 times magnification

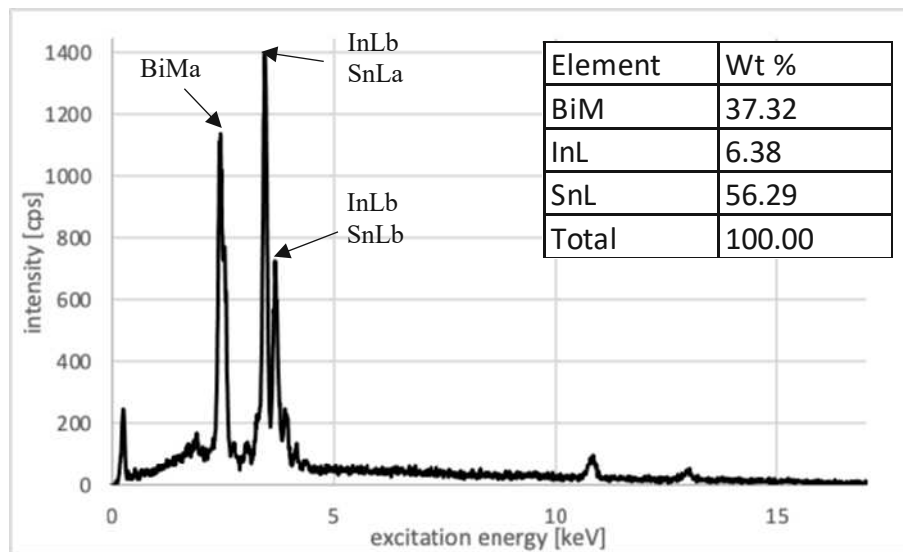


Figure 87: EDX analysis of an "as-cast" sample

### 5.2.2. Heat-treated at 120 °C

The topology in figures 88, 90, and 92 shows the eutectic network built by the Sn-rich phase. A comparison between figure 83 and 90 illustrate the effect of the 17 % liquid phase at 120 °C and slower cooling rates on the topology. Instead of the evenly distributed single hills in the "as-cast" samples, a more evenly distributed network of hills has been established in the "120 °C"- samples. It can be assumed that the single hills of the "as-cast" samples have molten during the heating procedure, leaving a topographically more homogeneous surface. A retracting process of the Bi may cause the exposure of cracks on the surface in figure 88 during heat treatment. The presumption is that the RHOMBO\_A7 phase seeped through the solid Sn-matrix into the inner areas of the sample when transitioning from solid to liquid [83].

The BSE evaluations of the same areas ( figures 89,91, and 93) illustrate that the light-colored Bi-rich phase is less present than in the previous sample group.

The EDX analysis in figure 94 supports this presumption with less Bi on the surface area, whereby the Sn and In values stay the same compared to the "as-cast" sample.

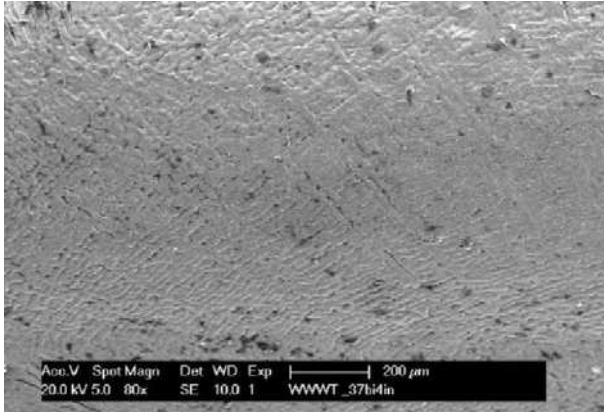


Figure 88: SE image of a „120 °C“-sample with 80 times magnification

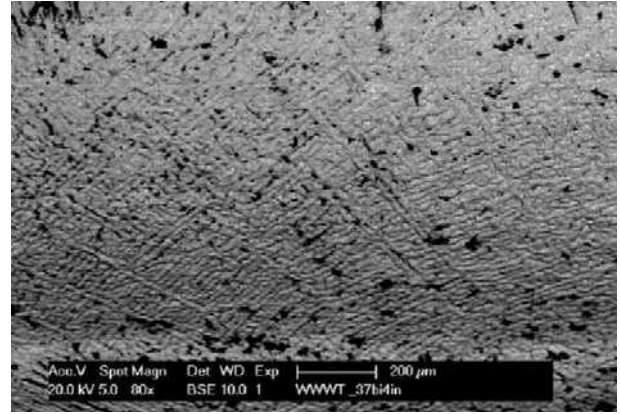


Figure 89: BSE image of a „120 °C“-sample with 80 times magnification

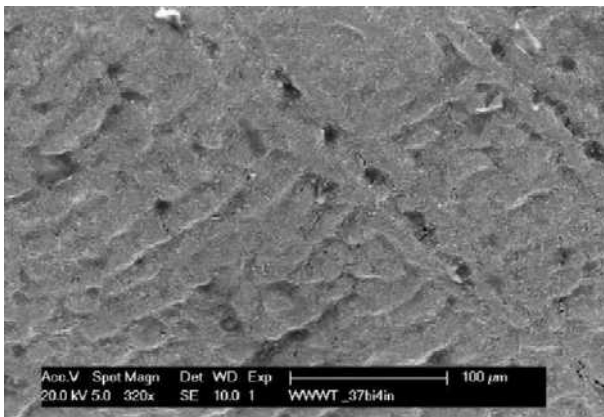


Figure 90: SE image of a „120 °C“-sample with 320 times magnification

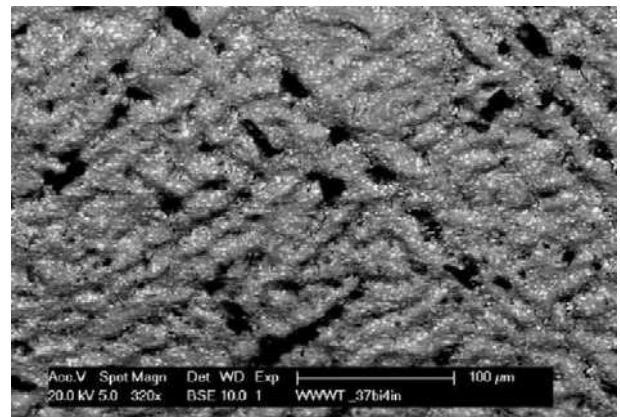


Figure 91: BSE image of a „120 °C“-sample with 320 times magnification

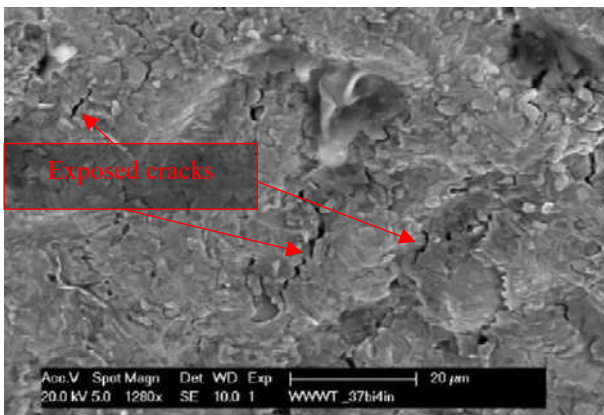


Figure 92: SE image of a „120 °C“-sample with 1280 times magnification

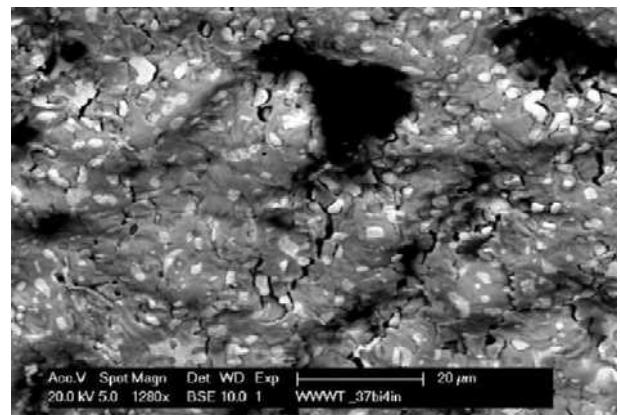


Figure 93: BSE image of a „120 °C“-sample with 1280 times magnification

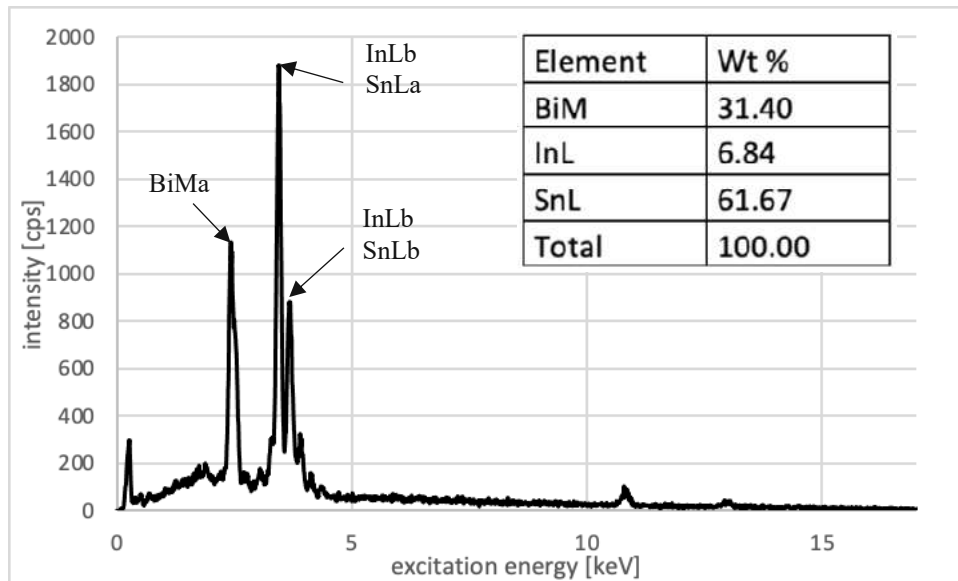


Figure 94: EDX analysis of a "120 °C"-sample

In contrast to the changes on the surface, the microstructure of the inner area of the "120 °C"-samples (see figure 95) is the same as in the "as cast"- sample group (figure 75), with small evenly distributed Bi particles.

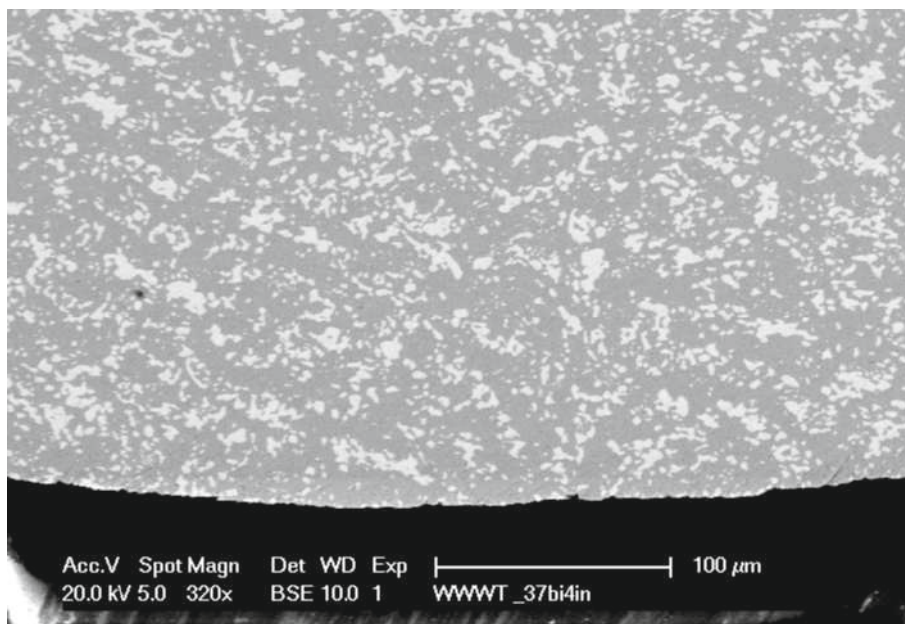


Figure 95: BSE image of the cross-section of a „120 °C“-sample with 320 times magnification

### 5.2.3. Heat-treated at 130 °C

The high percentage of the liquid phase and the duration of the heat treatment of the 130 °C sample group caused the sample to sag and the bottom side to touch the heated surface. Since the bottom side (figures 98 and 99) was in direct contact with the hot aluminum block, the conductivity is increased, and therefore, the microstructure and the topology are different on the top and bottom side of the sample. The comparison of the top (figure 97) and bottom (figure 99) cross-section shows both topological and microstructural differences. The edge region of the top surface exhibit more high and low points and fewer light grey areas at the edge compared to the bottom region.

A comparison of the inner areas of the top and bottom BSE images shows a small difference in Bi concentration. No difference from the inner to the edge area regarding Bi concentration is notable in the top cross-section (figure 97). On the other hand, the inner area in the bottom image (figure 95) features bigger particles at the expense of fewer small particles, and the outer edge area is predominantly Bi-rich. A conclusion is that the sample cools heterogeneously from top to bottom, leading to prolonged high temperature in the lower area and an enhanced Bi area growth.

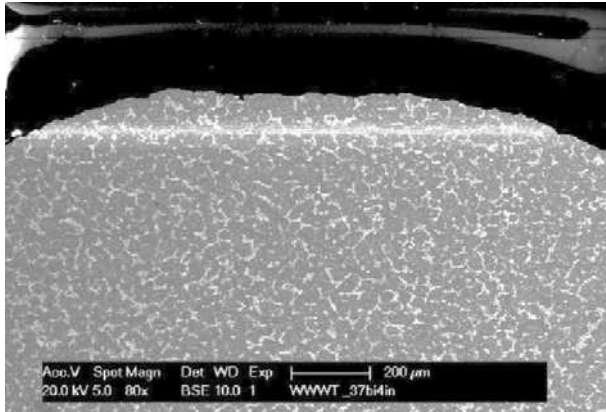


Figure 96: BSE image of the top side cross-section of a „130 °C“-sample with 80 times magnification

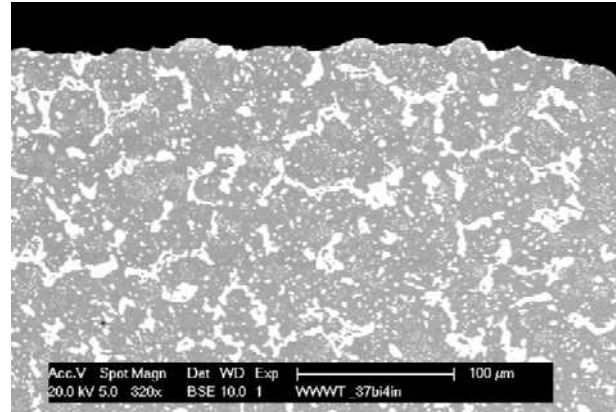


Figure 97: BSE image of the top side cross-section of a „130 °C“-sample with 320 times magnification

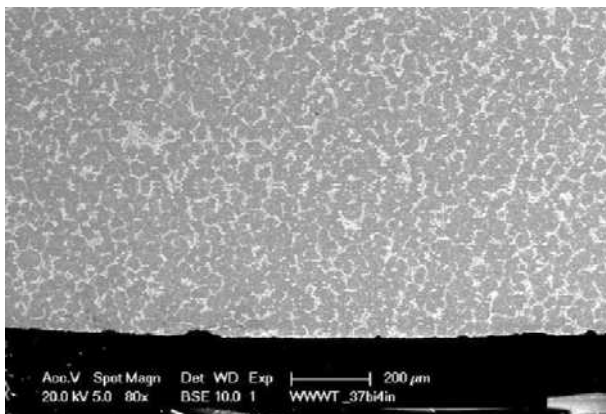


Figure 98: BSE image of the bottom side cross-section of a „130 °C“-sample with 80 times magnification

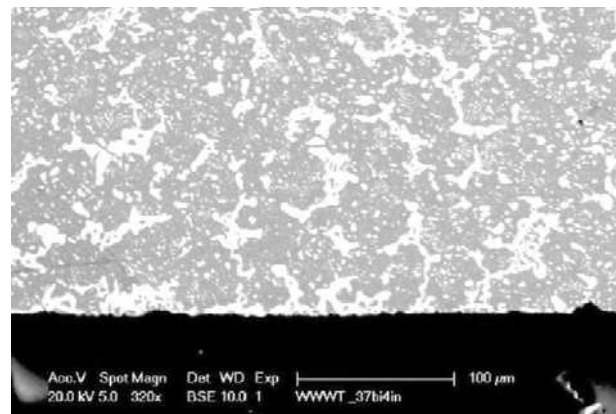


Figure 99: BSE image of the bottom side cross-section of a „130 °C“-sample with 320 times magnification

### 130 °C top side

Compared to the “as cast” sample, figures 100, 102, and 104 depict further flattening of the surface with only small elevations in an otherwise flat surface. The topology is characterized by unrelated single round structures.

Figures 101, 103, and 105 show that the Bi-rich phase seems to retract from the top side of the sample surface when the solder is partly liquid. In contrast to both previous sample groups, figure 103 shows inhomogeneously distributed light-colored areas build up in between the BCT\_A5 network. The magnification of this area (figure 105) illustrates the rectangular shape of the light-colored areas, which is typical for Bi crystals.

The average composition on the top side of the 130 °C sample is, according to the EDX measurement, roughly the same as the “as-cast” composition with slightly lower Bi content, though the distribution is unevenly distributed.

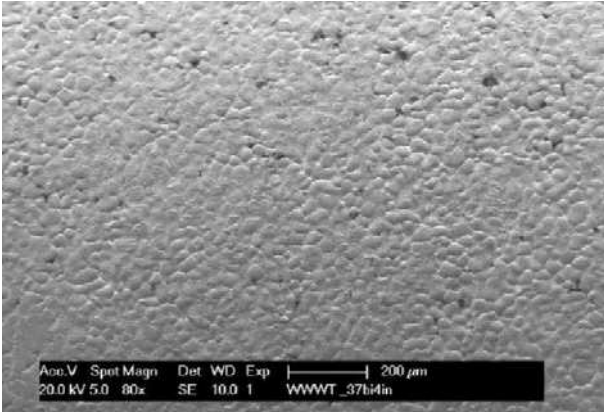


Figure 100: SE image of the top side of a „130 °C“-sample with 80 times magnification

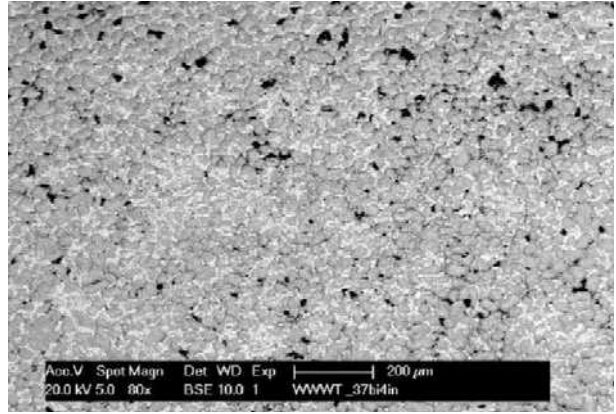


Figure 101: BSE image of the top side of a „130 °C“-sample with 80 times magnification

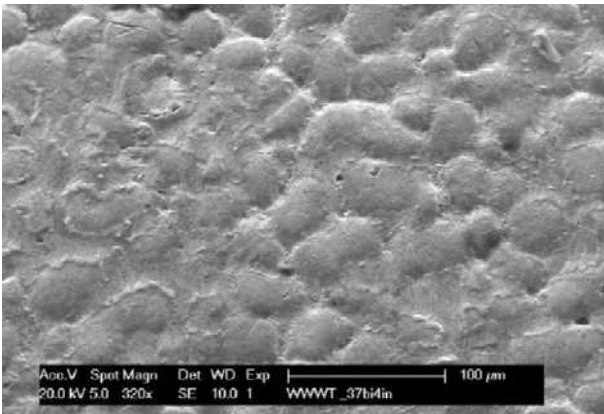


Figure 102: SE image of the top side of a „130 °C“-sample with 320 times magnification

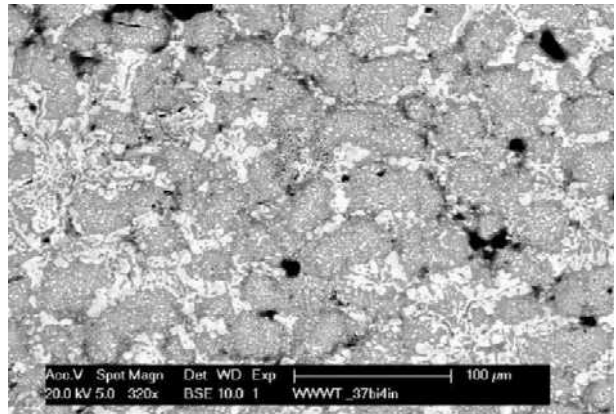


Figure 103: BSE image of the top side of a „130 °C“-sample with 320 times magnification showing bulking Bi areas



Figure 104: SE image of the top side of a „130 °C“-sample with 1280 times magnification with typical rectangular Bi crystals in between the homogenous matrix

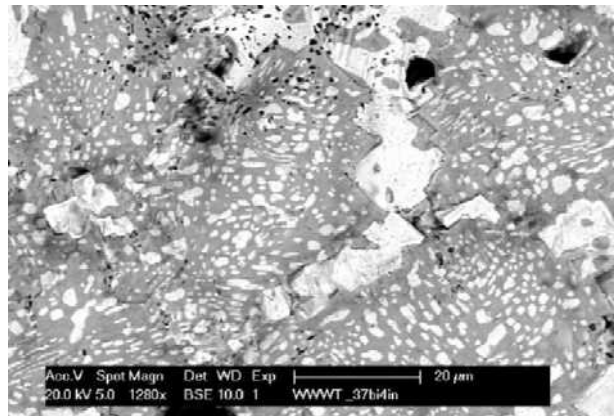


Figure 105: BSE image of the top side of a „130 °C“-sample with 1280 times magnification with typical rectangular Bi crystals in between the homogenous matrix

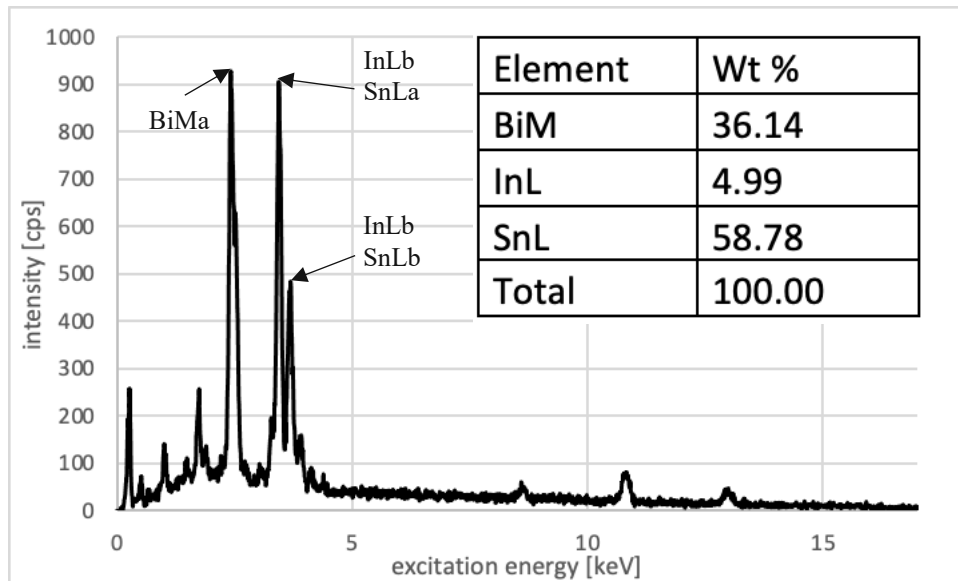


Figure 106: EDX analysis of the top side of a "130 °C"-sample

### 130 °C bottom side

As mentioned before, the bottom side of the "130 °C"-sample is in direct contact with the heated aluminum block and, therefore, heated more efficiently and the cooling process may be retarded compared to the top surface. Consequently, the microstructure and the topology alter vastly compared to the top side of the same sample. The topology is characterized by a superimposition of flat areas, hills, and round features, as depicted in figure 107. The flat areas indicate that direct contact between the sample and the aluminum foil is most probable (see the flat areas in the upper section of figure 107). The black spots in figures 108 and 110 can be explained by the hills on the surface and thereto shade-off effects of the close surrounding for the EBS detector. In figure 111, the surface is similar to the surface found in the "as-cast" and 120 °C samples (compare figure 111 to figures 85 and 92). The microstructure on the bottom side of this sample is characterized by its extensive Bi-rich areas throughout the sample (figure 110). A large amount of the RHOMBO\_A7 phase seems to have seeped through the solder matrix to the lowest point and formed a linked layer of Bi, homogeneously distributed on the surface (see figure 112). However, an even distribution of the available phases (BCT\_A5 and RHOMBO\_A7) is still recognizable. As expected by the BSE analysis (figures 108, 110, and 112), the Bi content on the surface is increased with 41.3 wt% Bi, 51.8 wt%-Sn and 6.9 wt%-In.



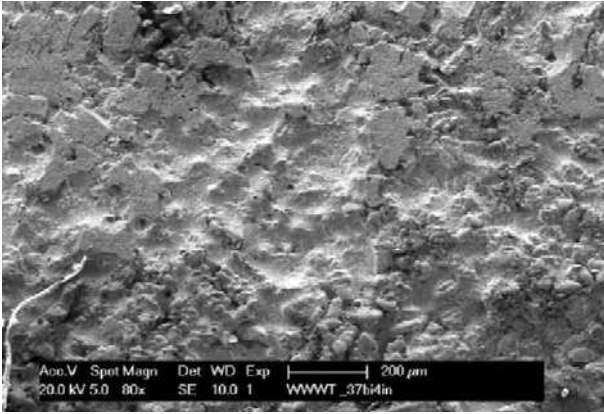


Figure 107: SE image of the bottom side of a “130 °C“-sample with 80 times magnification

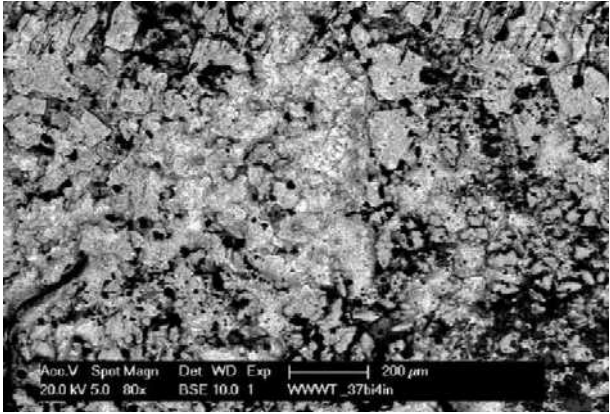


Figure 108: BSE image of the bottom side of a “130 °C“-sample with 80 times magnification

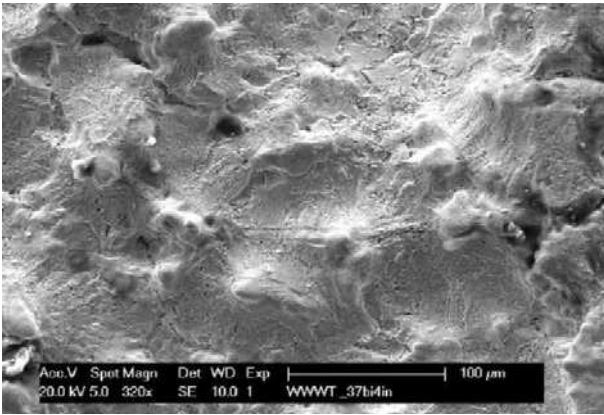


Figure 109: SE image of the bottom side of a “130 °C“-sample with 320 times magnification

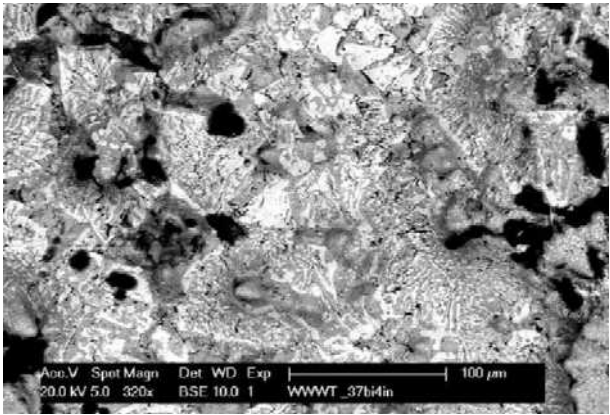


Figure 110: BSE image of the bottom side of a “130 °C“-sample with 320 times magnification

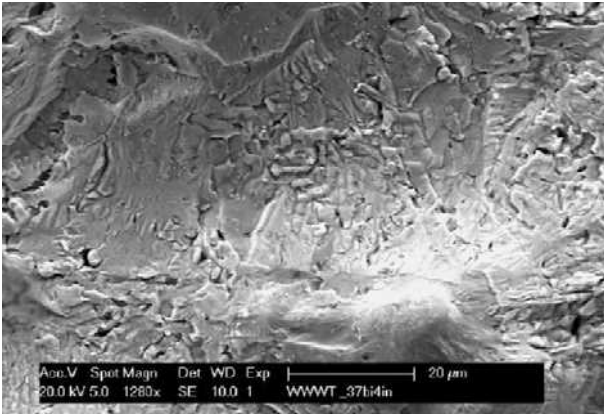


Figure 111: SE image of the bottom side of a “130 °C“-sample with 1280 times magnification

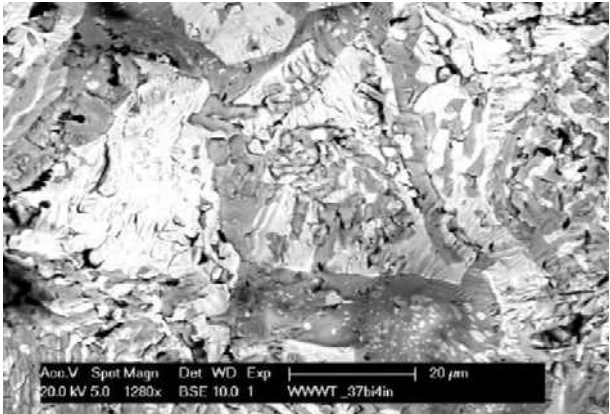


Figure 112: BSE image of the bottom side of a “130 °C“-sample with 1280 times magnification

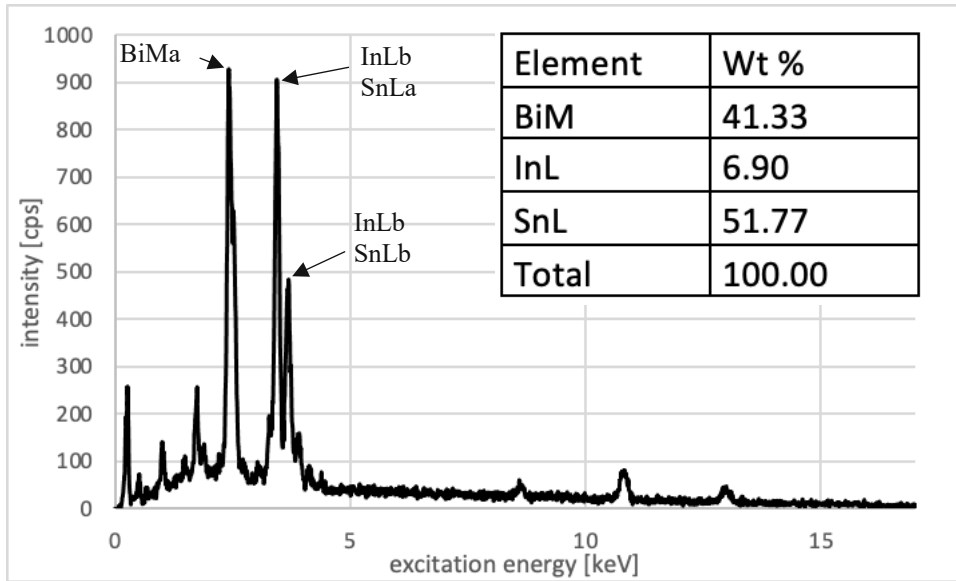


Figure 113: EDX analysis of the bottom side of a "130 °C"-sample

### 5.2.4. Heat-treated at 140 °C

As already mentioned, for the 130 °C samples, the bottom side of the 140 °C samples touched the heated aluminum block directly as well, leading to different metallographic and topographic features on the top and bottom sides. The top cross-section depicted in figures 114 and 115 shows similar topography and distribution of the phases as the 130 °C top cross-section (see figure 97) with no significant changes from the inner to the outer chemical distribution.

In the bottom cross-section (figures 116 and 117), a clear difference in microstructure is apparent. The Bi phase has an increased tendency to form large-scale structures, and a connected network of RHOMBO\_A7 phase has developed.

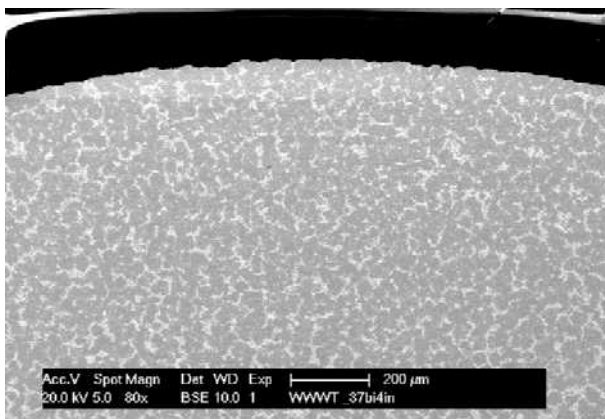


Figure 114: BSE image of the top side cross-section of a "140 °C"-sample with 80 times magnification

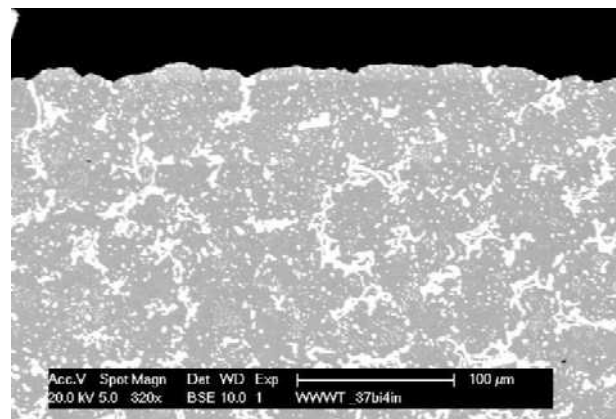


Figure 115: BSE image of the top side cross-section of a "140 °C"-sample with 320 times magnification

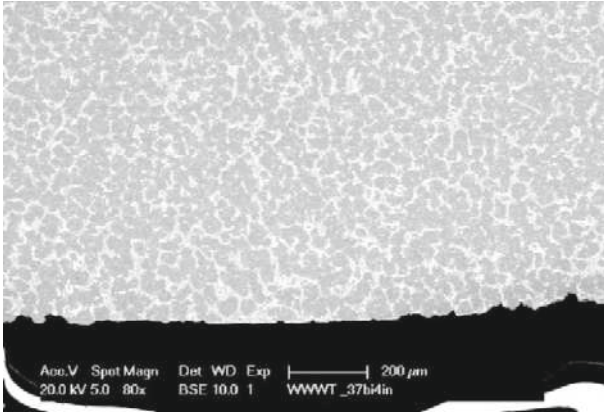


Figure 116: BSE image of the bottom side cross-section of a “140 °C”-sample with 80 times magnification

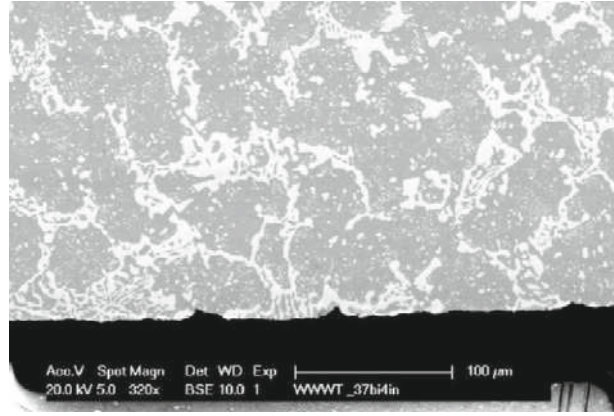


Figure 117: BSE image of the bottom side cross-section of a “140 °C”-sample with 320 times magnification

### 140 °C top side

As on the top side of the 130 °C samples, the topography of the top side of the 140 °C (figures 118,120 and 122) sample is defined by a round-shaped BCT\_A5 matrix, compared to the 130 °C samples (figure 102), the height differences between high and low points of the 140 °C sample (figure 120) is more prominent in the 140 °C samples (notice the dark spots in figure 121).

The chemical distribution, illustrated in the BSE analysis (figures 119,121, and 123), has developed further to strictly localized, concentrated Bi-rich areas, whereby the large part of the areas between the Sn-rich round-shaped structures is characterized by collapsed valleys, which can be explained by the contraction of the liquid Bi phase to the inner of the sample and emerging during cooling through discrete areas (figure 121).

The EDX measurement shows that the average composition on the surface of the “140 °C” top side is approximately the same as the composition of the “as cast” samples.

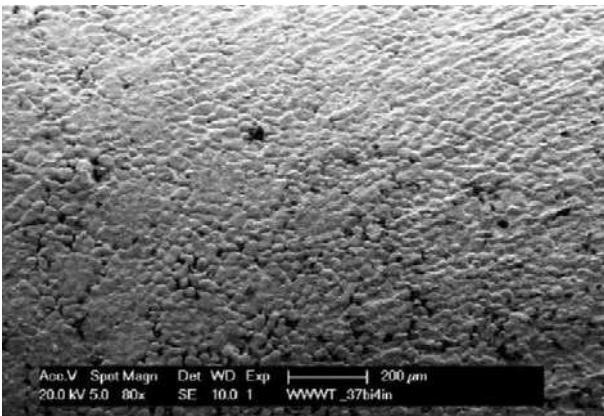


Figure 118: SE image of the top side of a „140 °C”-sample with 80 times magnification

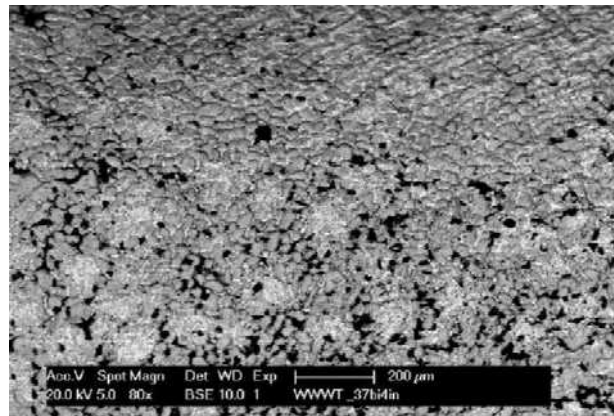


Figure 119: BSE image of the top side of a „140 °C”-sample with 80 times magnification

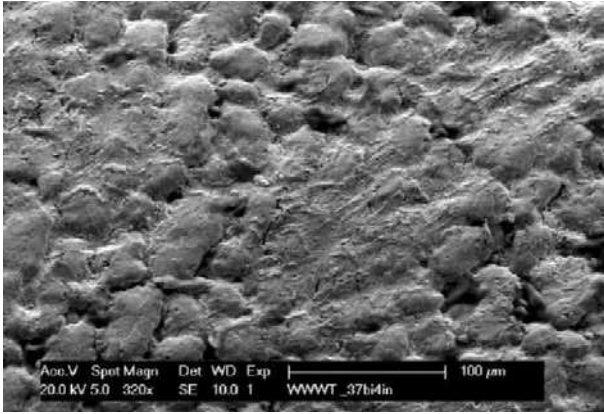


Figure 120: SE image of the top side of a „140 °C“-sample with 320 times magnification

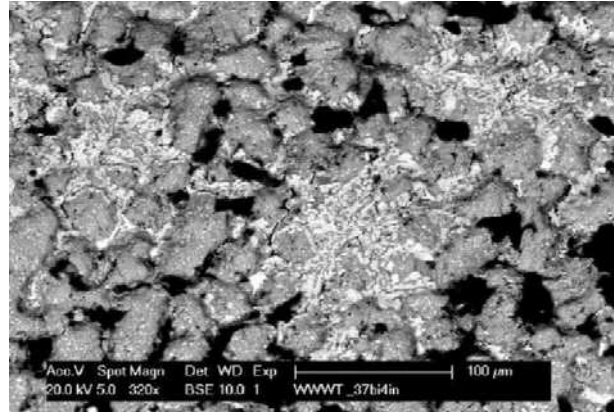


Figure 121: BSE image of the top side of a „140 °C“-sample with 320 times magnification

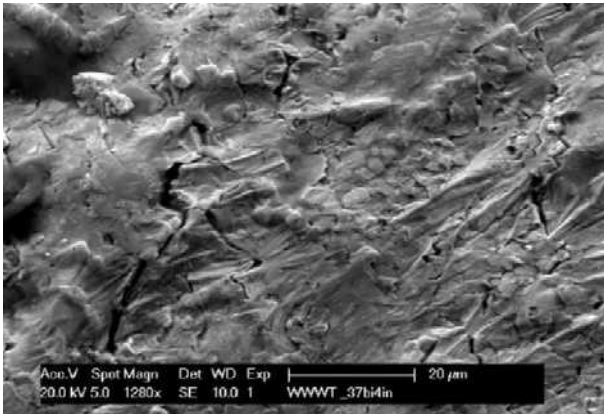


Figure 122: SE image of the top side of a „140 °C“-sample with 1280 times magnification

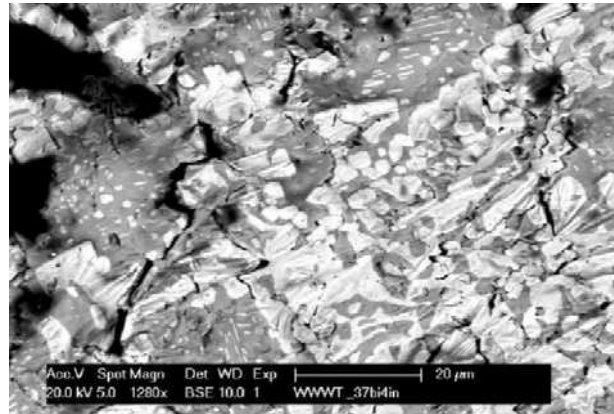


Figure 123: BSE image of the top side of a „140 °C“-sample with 1280 times magnification

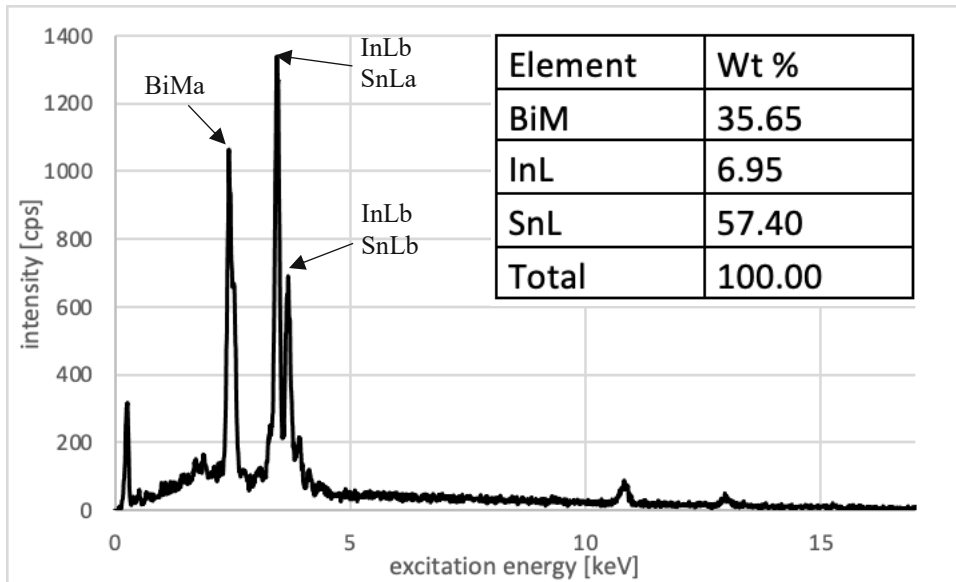


Figure 124: EDX analysis of the top side of a "140 °C"-sample

### 140 °C bottom side

The topology on the bottom side of the 140 °C samples is almost flat. Only a few defects are visible in figures 125, 127, and 129. It can be assumed that the extended heat input through the bottom leads to Bi seeping through the

solid solder matrix, to the interface between the solder sample and the aluminum foil. As soon as the sample temperature drops below the solidification temperature of the Bi-rich phase, the RHOMBO\_A7 phase expands and closes all holes compared to the top side.

The microstructure supports this assumption, as illustrated in figures 126, 128, and 130. Extensive light-colored areas and a continuous network of Bi-rich phase with extensive extended RHOMBO\_A7 areas indicate that the Bi may have penetrated through a still solid network of Sn-rich phase.

The composition on the bottom side of the 140 °C samples has changed after 10 minutes at 140 °C radically to a primarily Bi-rich distribution with over 54 wt% Bi, only 41 wt% Sn, and 4.4 wt% In (see figure 131).

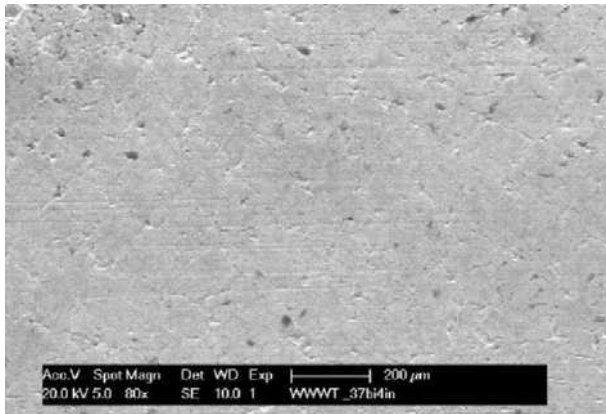


Figure 125: SE image of the bottom side of a „140 °C“-sample with 80 times magnification

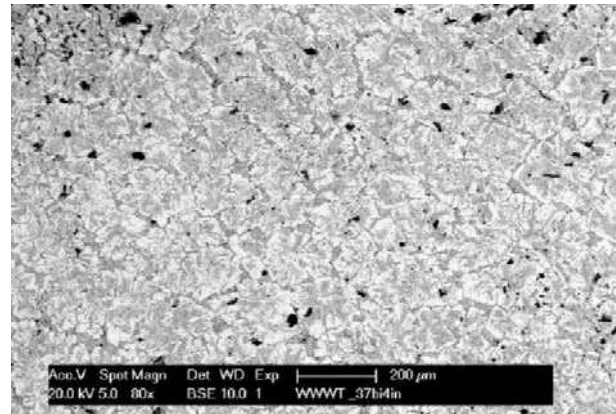


Figure 126: BSE image of the bottom side of a „140 °C“-sample with 80 times magnification

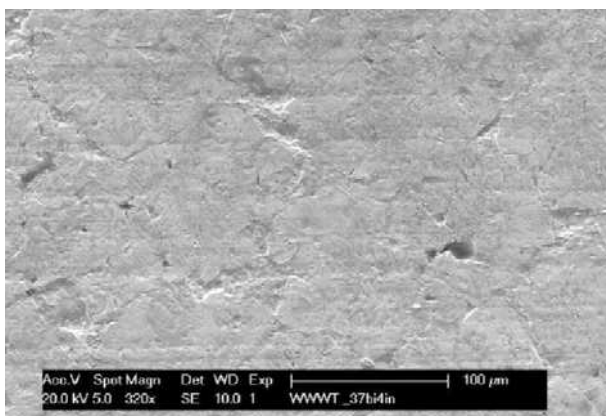


Figure 127: SE image of the bottom side of a „140 °C“-sample with 320 times magnification

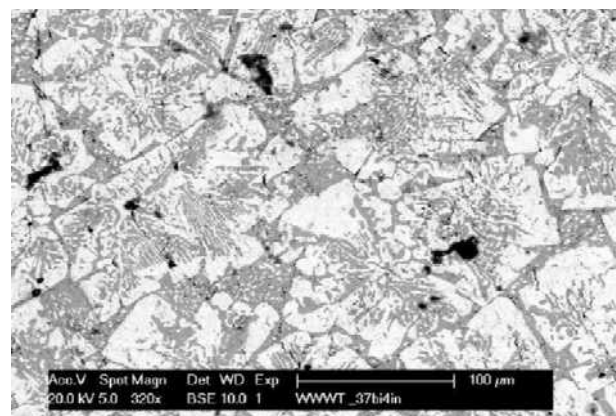


Figure 128: BSE image of the bottom side of a „140 °C“-sample with 320 times magnification

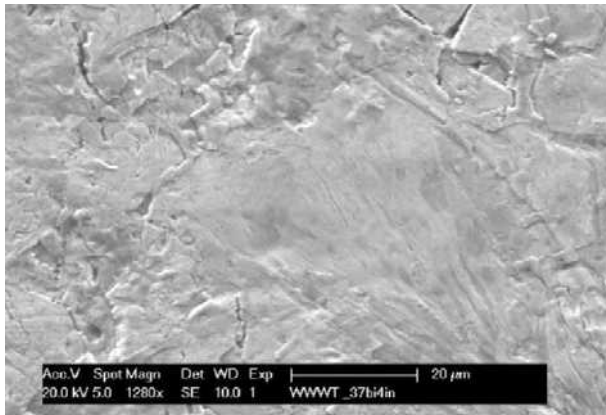


Figure 129: SE image of the bottom side of a „140 °C“-sample with 1280 times magnification

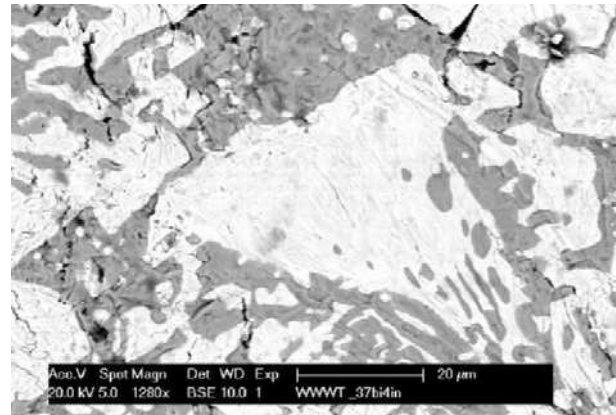


Figure 130: BSE image of the bottom side of a „140 °C“-sample with 1280 times magnification

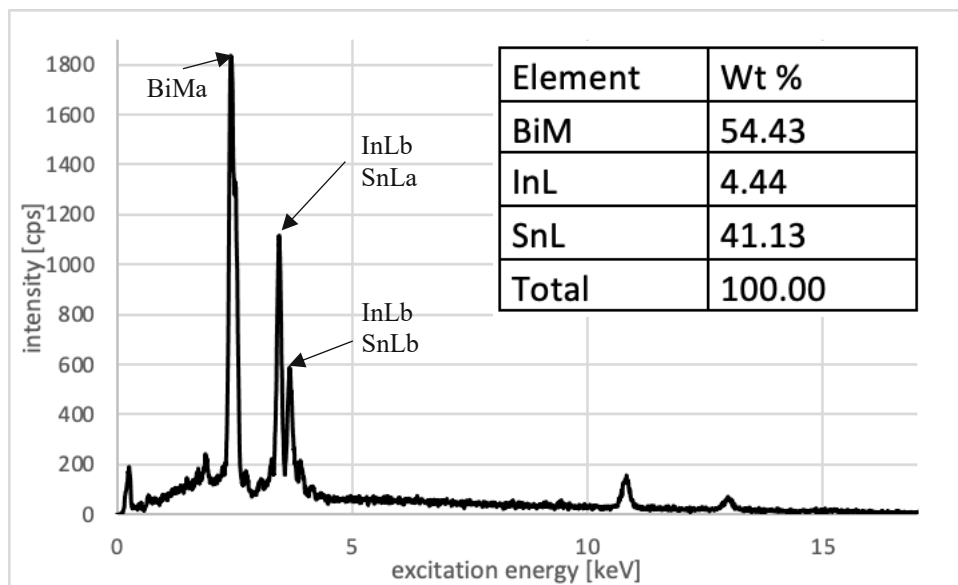


Figure 131: EDX analysis of the bottom side of a "140 °C"-sample

### 5.2.5. Mechanical property changes induced by heat treatment

Initiated by the heat treatment, the mechanical characteristics of the Sn37Bi4In solder alloy have mainly changed in necking ability (see figures 132 to 136 and table 10). Although the sample groups differ in applied heat treatment, the test results are similar. The toughness comparison in figure 135 illustrates the rapid failure of the samples of the “130 °C”- and “140 °C”-heat treatments beyond crossing the point of uniform elongation. While the mean toughness values of the aged samples, in table 10, are substantially lower than the reference sample, the 120 °C samples show a slight tendency to higher values compared to the “as-cast” Sn37Bi4In solder, as shown in figure 135.

A minor increase in Young’s modulus and UTS measurements is possible, which may be related to the alteration of the composition or the change in form caused by the heat treatment. The group of samples aged at 120 °C shows a potential increase in Young’s modulus, UTS, and uniform elongation. Apart from the reduced necking ability, the samples in group 130 °C show similar values as the untreated reference samples. In the samples treated at 140

°C, an increase in UTS is connected with reducing the uniform elongation, which may be related to the higher Bi concentration on the surface.

Table 10: Important tensile test values of the Sn37Bi4In compared to samples heat-treated at different temperatures. (only suitable for comparative purposes)

	Sn37Bi4In (reference)	Heat treatment @120 °C	Heat treatment @130 °C	Heat treatment @140 °C
Young's modulus [ $\frac{N}{mm^2}$ ]	31.6	35.4	32.0	35.0
UTS [ $\frac{N}{mm^2}$ ]	97.1	99.7	98.4	102.0
Uniform elongation [%]	9.4	9.8	9.7	8.0
Toughness [ $\frac{N}{mm^2}$ ]	4513	1660	943	1391

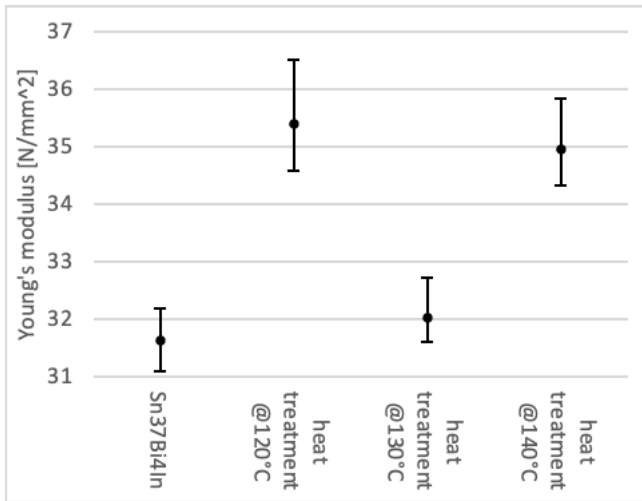


Figure 132: Comparison of heat-treated and untreated reference samples (Sn37Bi4In) regarding Young's modulus

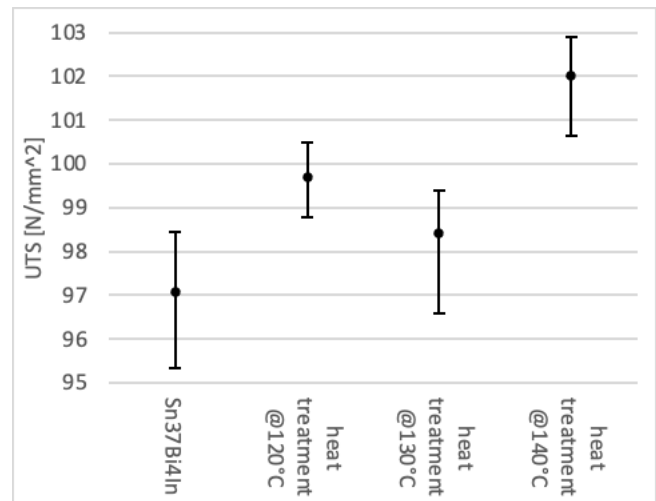


Figure 133: Comparison of heat-treated and untreated reference samples (Sn37Bi4In) regarding UTS

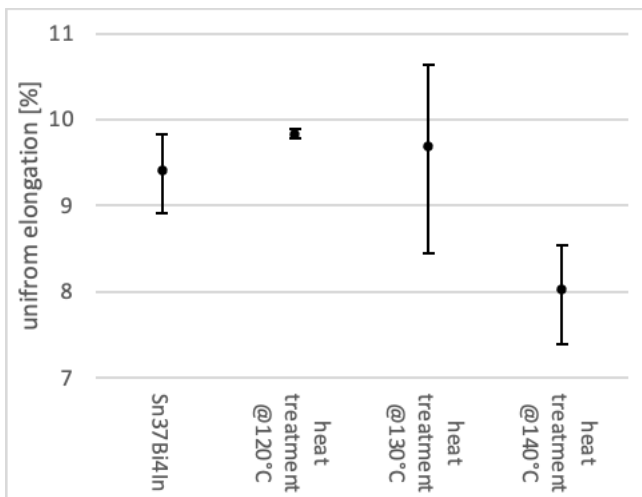


Figure 134: Comparison of heat-treated and untreated reference samples (Sn37Bi4In) regarding uniform elongation

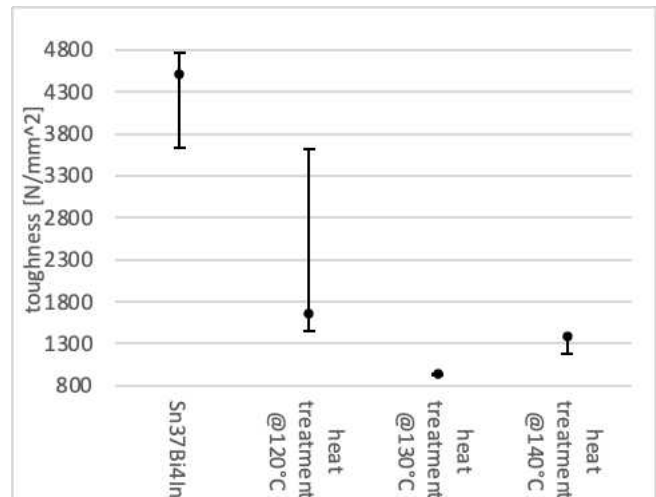


Figure 135: Comparison of heat-treated and untreated reference samples (Sn37Bi4In) regarding toughness

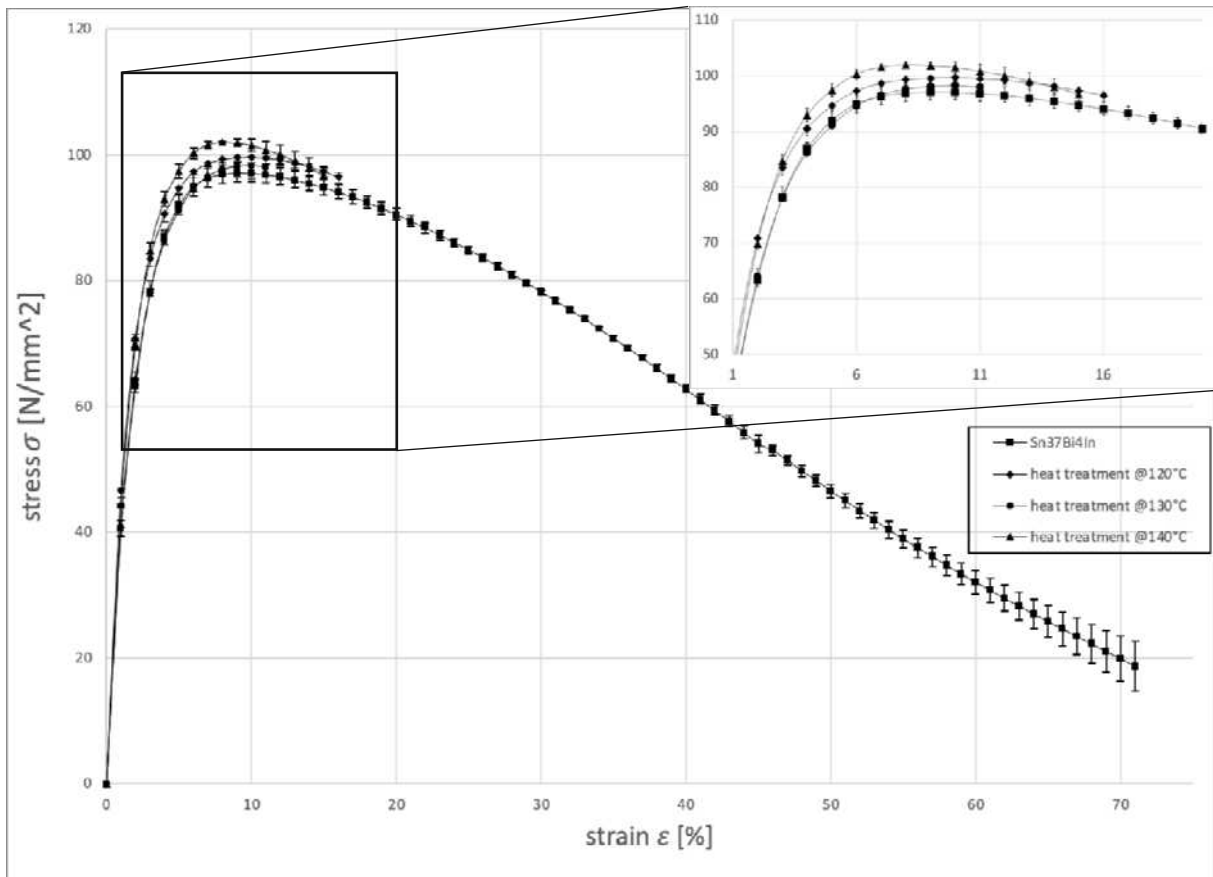
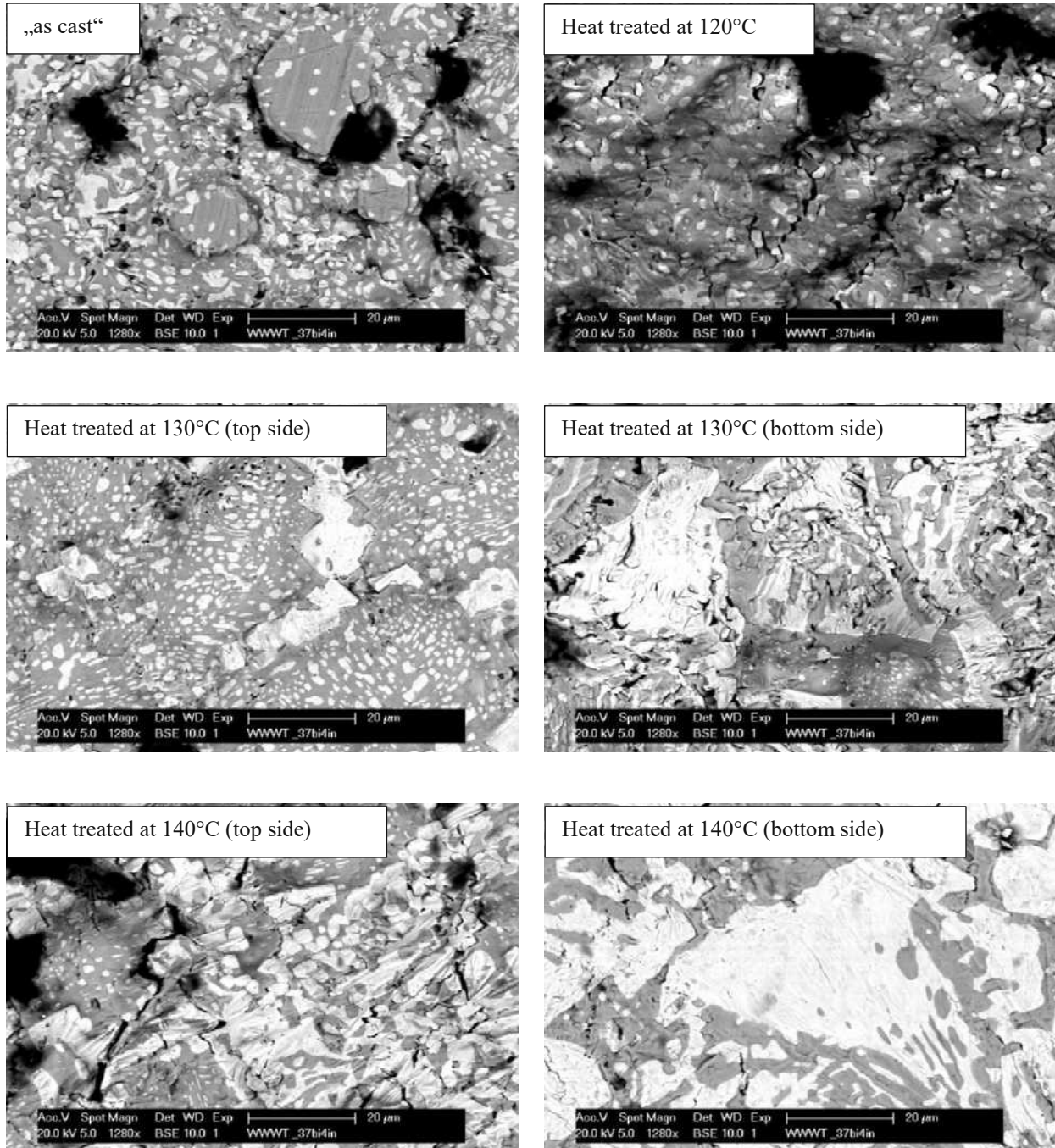


Figure 136: Tensile test of the Sn37Bi4In and heat-treated samples ( @120 °C, @130 °C, @140 °C)



## 5.2.6. Conclusion of the chapter

To further investigate the influence of the temperature apart from triggering healing effects, the chemical composition and topography of the surfaces and the cross-section of four sample groups have been studied (see figure 137).



Figures 137: Comparison of the surfaces after heat treating at different temperatures with 1280 times magnification

The “as-cast” samples show a uniform distribution of the Bi-rich phase in the Sn-rich matrix. This group's surface is characterized by Sn hills formed during the casting process in the silicon mold. As already seen in the cross-section, the Bi is present on the surface in a network of predominantly small round-shaped particles ( $<5 \mu\text{m}^2$ ) with few larger particles, evenly distributed, probably formed by the coalescence of many small particles.

The sample group exposed to 120 °C shows a reduced amount of RHOMBO\_A7 phase on the surface. The size, form, and uniform distribution of the Bi particles are equal to the previous group. Large particles are absent on the surface. The surface shows exposed cracks, unlike the other groups. During the sample exposure to the heat source, a portion of the Bi on the surface has transformed to the liquid state and therefore contracted due to an anomaly of the element. This contraction may have led to an exposure of cracks and may have deprived the surface of Bi.

The amount of liquid phase (57 %) in the samples, exposed to 130 °C, lead to plastic deformation during heat treatment, causing a distinguishable top and bottom surface. The bottom surface is in direct contact with the aluminum foil on the heated milled aluminum block, increasing the heat transfer and reducing cooling rates when the sample is cooled. This difference in temperature exposure of the top side compared to the bottom side shows relevant contrasts in the development of the microstructure. Although the chemical composition on the top surface corresponds with the “as-cast” samples, deviations in distribution and form of the Bi particles are remarkable. The up to 100 µm long Bi-rich areas between the flattened Sn hills show Bi-typical angular shapes. The Sn hills themselves are speckled with small Bi particles with sizes typical for the Sn37Bi4In alloy. Apart from isolated valleys, the entire top surface appears flatter than in the “as-cast” samples. On the other side, the bottom surface shows substantial alterations of the microstructure regarding topology and distribution of phases. The topology of the surface is overall heterogeneous, with flat surfaces resulting from the sample touching the hot aluminum foil (cross-sections of up to 100 µm<sup>2</sup>). The EBS images show connected Bi-rich areas with cross-sections of up to 50 µm<sup>2</sup>. These large RHOMBO\_A7 areas can be explained by the high proportion of Bi in the liquid phase and the high proportion of liquid phase formation at 130 °C. Based on the anomaly of the element, the Bi expands and coalesces during the solidification process, leading to a network of large Bi-rich phase.

The last sample group (140 °C) also deformed, leading to unequal top and bottom surfaces. On the top surface, the topology and microstructure are comparable to the 130 °C top surface, with enhanced features. A flat surface with more, deeper appearing holes and even stronger located Bi-rich areas with minimal occurrences of small Bi particle on the Sn hills. Due to extensive direct contact of the whole contemplated area with the heating plate, the topology of the bottom side is flat. The surface's chemical composition consists of over 50 % of Bi, showing the uniform distribution of large RHOMBO\_A7 regions (> 50 µm<sup>2</sup>) connected in a continuous network. In the cross-section EBS images, the top section does not differ from the untreated samples, whereas large Bi-rich areas are visible in the bottom section compared to the "as-cast" samples.

After passing through the aging process, the stress-strain diagrams show that the heat treatment hardly affected the mechanical properties of the alloy. The most prominent change is the decrease of necking ability. In summary, it can be said that aging processes at different temperatures do not show a clear tendency for the Young's modulus, UTS and uniform elongation. Toughness tends to decrease after aging samples at a higher temperature.



### 5.3. Influence of alloying elements

The influence of alloying elements on the microstructure, the mechanical properties (figures 138 and 139 and table 11) and the occurring phases is significant. A change of microstructure and, in addition to that, mechanical characteristics due to variations of the chemical composition can lead to a sudden failure if a brittle phase becomes prominent. An assessment of the microstructural, mechanical and melting properties of similar compositions is important for the evaluation process of a self-healing solder alloy.  $\pm 2$  wt% of Bi and In, respectively, are therefore investigated to find microstructural and mechanical differences.

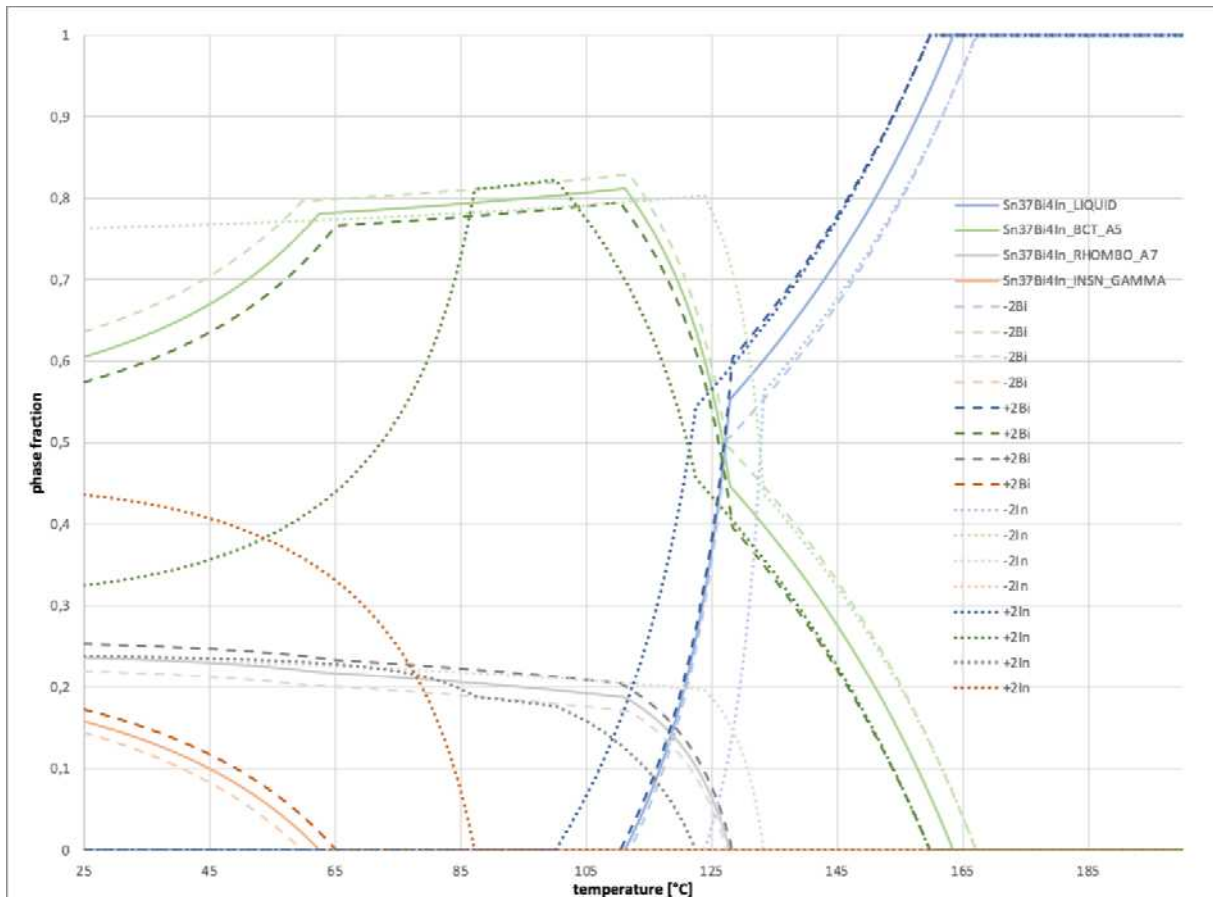


Figure 138: Phase fraction diagram of the Sn37Bi4In, Sn39Bi4In(+2Bi), Sn35Bi4In(-2Bi), Sn37Bi6In(+2In) and (+2In) alloys between 25 °C and 200 °C; conducted with MatCalc 6.03 and the MatCalc solder database.

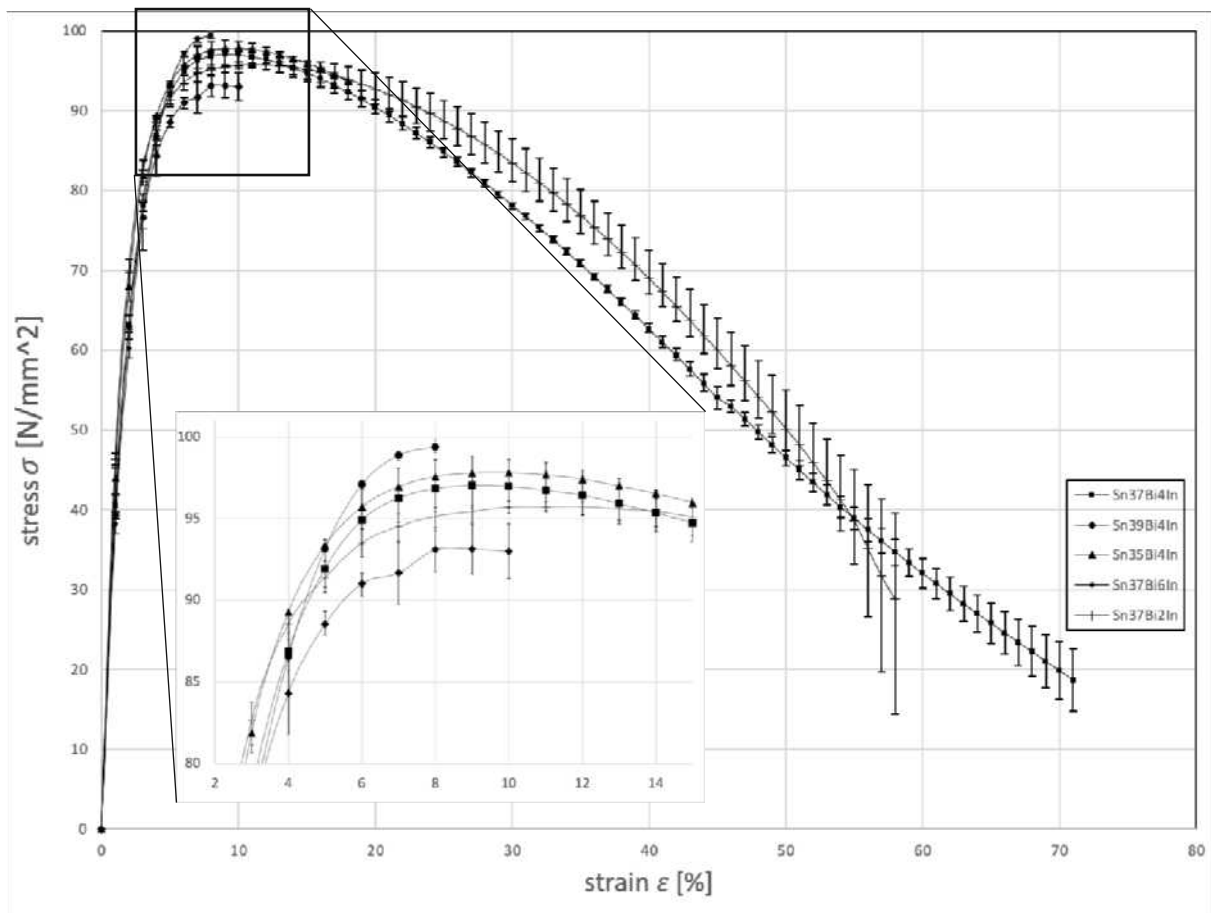


Figure 139: Tensile test of the Sn37Bi4In, Sn39Bi4In, Sn35Bi4In, Sn37Bi6In, and Sn37Bi2In alloys

### 5.3.1. Influence of Bi content on the microstructure

The CALPHAD calculations indicate that a variation of the Bi content leads to small changes of the present phases compared to the Sn37Bi4In. Figure 140 shows the variations of the involved phases liquid, BCT\_A5, RHOMBO\_A7 and INSN\_GAMMA.

The BCT\_A5 phase is indirectly proportional to the Bi content. This can be explained by Sn being the main component of the BCT\_A5 phase, whose content rises/falls equally to the increase/decrease of Bi and In. Higher Sn content leads to a shift in the Sn/In phase diagram (see figure 60), a more prominent BCT\_A5 proportion, and a decreased propensity to form the competing INSN\_GAMMA phase. By increasing the BCT\_A5 phase, which is the last solid phase when heating the alloy, the liquidus temperature is minimally increased.

An increase of the Bi content points in the opposite direction with more RHOMBO\_A7 phase, lowering the Sn content, leading to a lower BCT\_A5 formation and an enhanced solid/solid transformation to the INSN\_GAMMA phase.

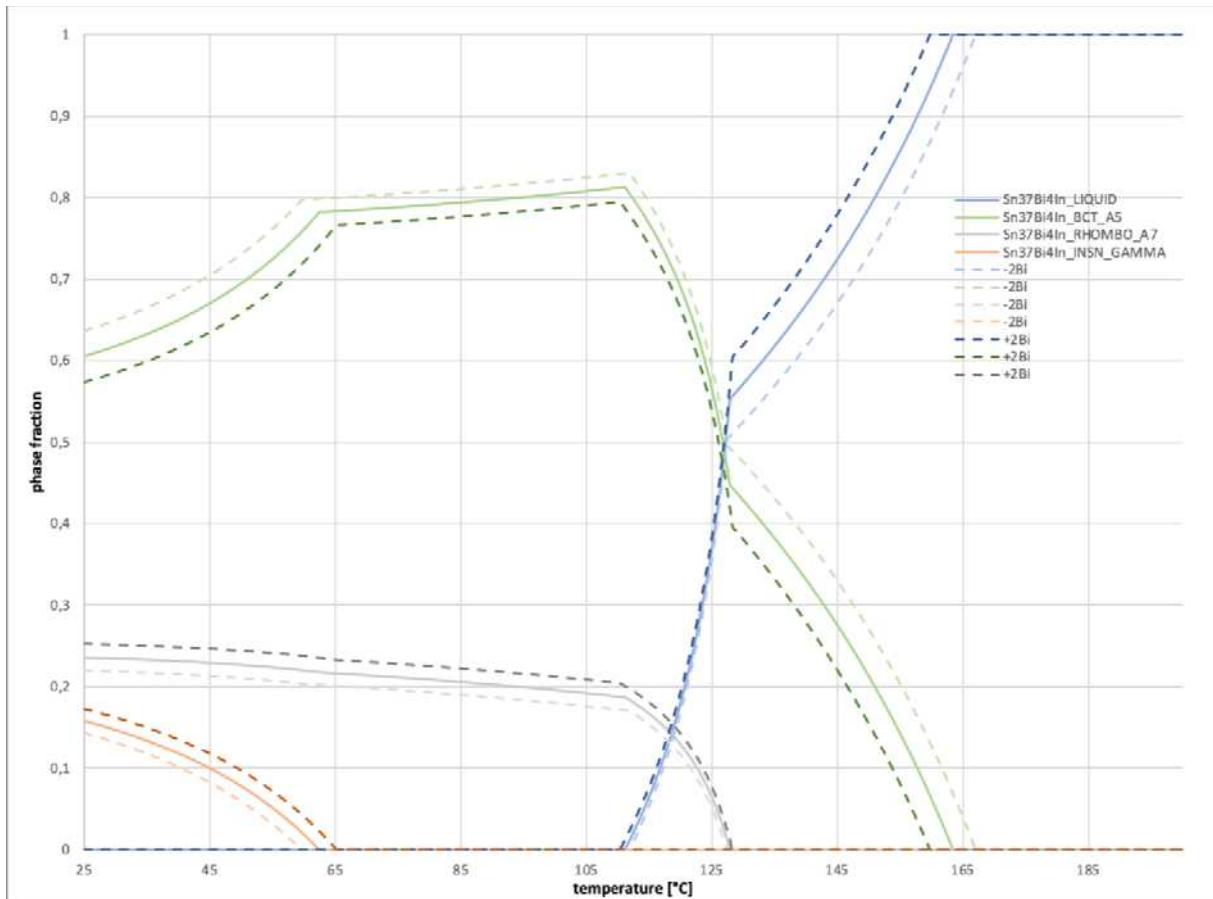


Figure 140: Phase fraction diagram of the Sn37Bi4In, Sn39Bi4In(+2Bi), and Sn35Bi4In(-2Bi) alloys between 25 °C and 200 °C; conducted with MatCalc 6.03 and MatCalc solder database.

### The microstructure of the +2 wt% Bi alloy (Sn39Bi4In)

The microstructure of the Sn39Bi4In solder alloy shows a tendency to form Bi clusters of different sizes, up to 150 μm diameters (see figures 141, 142, and 143). Nevertheless, even in prominent constellations, the Bi forms net-like constructs in the Sn-rich matrix (see figure 143) in contrast to the large Bi-rich areas of the microstructure in the chapters 130 °C bottom side and 140 °C bottom side (see figures 112 and 130 respectively). The Sn39Bi4In alloy shows a tendency to form BiIn in between, see figure 143.

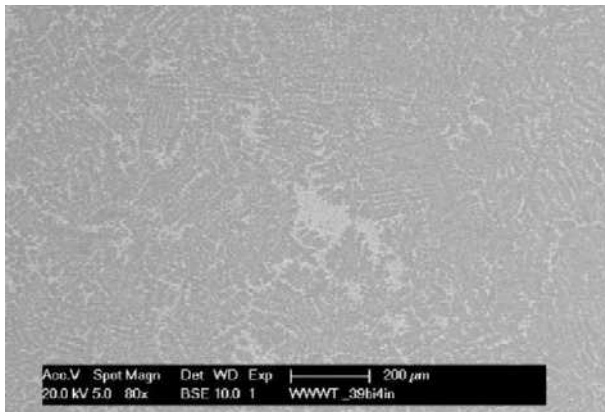


Figure 141: Picture of the microstructure of Sn39Bi4In with 80 times magnification

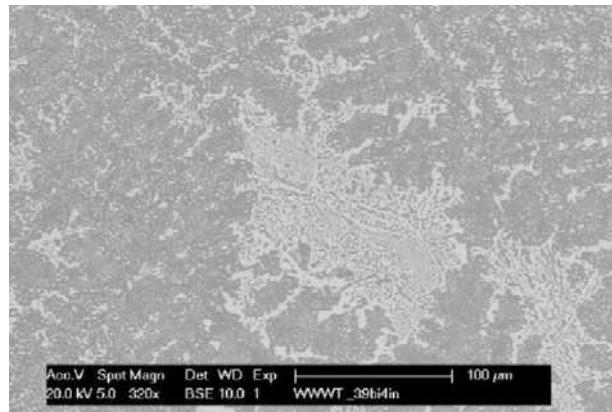


Figure 142: Picture of the microstructure of Sn39Bi4In with 320 times magnification

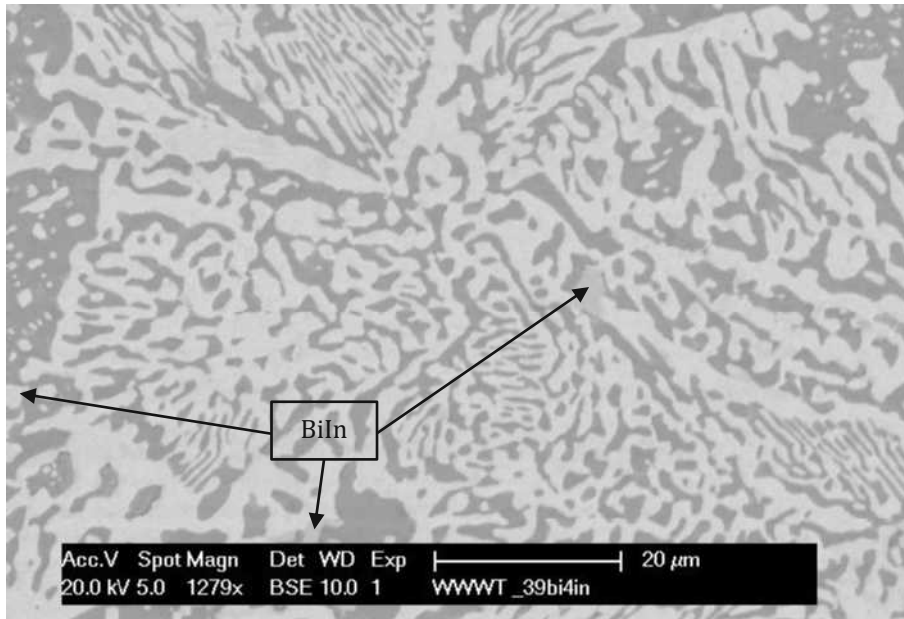


Figure 143: Picture of the microstructure of Sn39Bi4In with 1280 times magnification

### The microstructure of the -2 wt% Bi alloy (Sn35Bi4In)

The reduction of the Bi content leads to a refined, linearly organized distribution of the RHOMBO\_A7 phase in the BCT\_A5 matrix (figures 144 and 145). Small needles of RHOMBO\_A7 particles between the main branches cover the whole area with sizes smaller than  $3 \mu\text{m}^2$  (see figure 146).

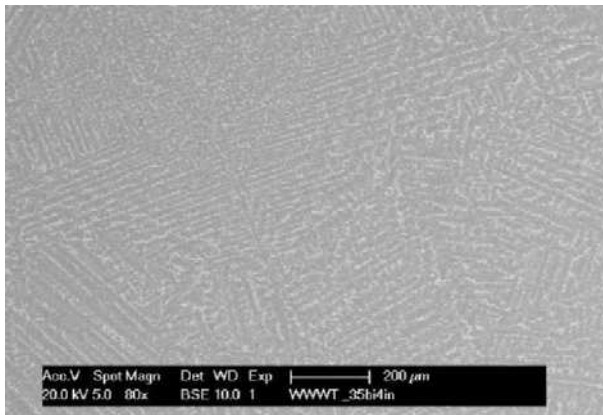


Figure 144: Picture of the microstructure of Sn35Bi4In with 80 times magnification

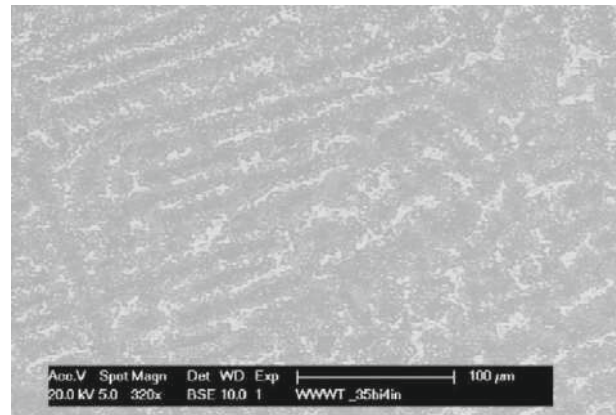


Figure 145: Picture of the microstructure of Sn35Bi4In with 320 times magnification

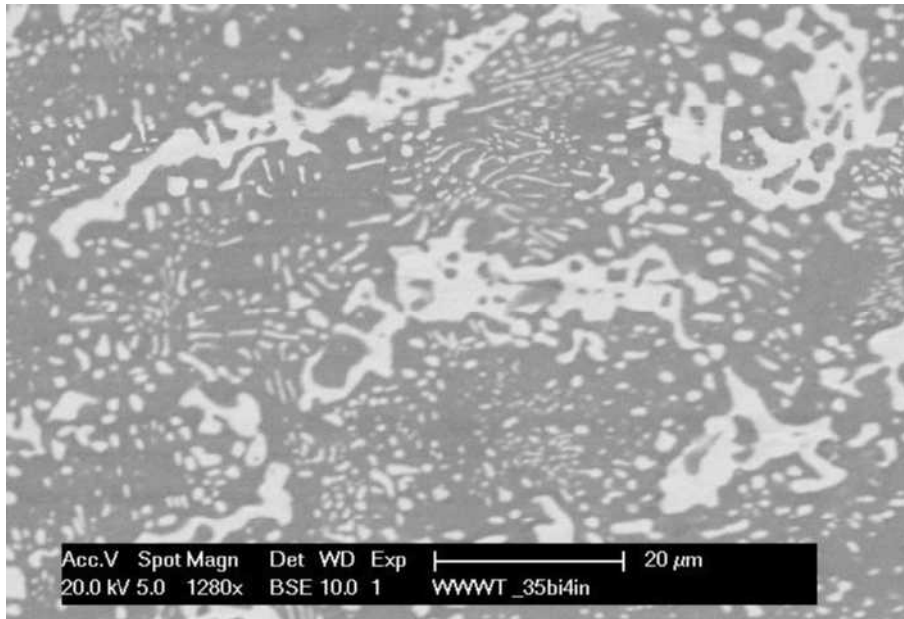


Figure 146: Picture of the microstructure of Sn35Bi4In with 1280 times magnification

### 5.3.2. Influence of In content on the microstructure

In contrast to the subtle differences in the Bi content variation, the In variation has a more pronounced impact on the present phases of the solder.

In the case of less In, the INSN\_GAMMA phase disappears completely while the BCT\_A5 phase fraction increases considerably to 76 % at room temperature. In is now solely found in the BCT\_A5 phase since RHOMBO\_A7 can only absorb minimum quantities of Sn or In along the contemplated temperature range (25 °C to 200 °C; see figure 72).

As expected, reducing the element with the lowest melting point lets the solidus temperature rise noticeably to 123 °C. From here on, the beginning of the liquid phase starts with a steep slope, accompanied by a fast decrease of the BCT\_A5 and RHOMBO\_A7 phases, slowing down at 132 °C when the RHOMBO\_A7 phase is fully gone. The BCT\_A5 phase lastly vanishes at 167 °C.

The increase of In leads to a significant change of the most prominent phase in the temperature range between 25 °C and 87 °C. In contrast to all other considered alloys in this work, the INSN\_GAMMA phase is here the primary phase in equilibrium at room temperature. At 87 °C, the INSN\_GAMMA dissolves in a solid/solid phase transition in the BCT\_A5 phase. Apart from a lower solidus (100 °C) and liquidus (158 °C) temperatures, the phase fraction diagram is from 87 °C on similar to the other alloys.



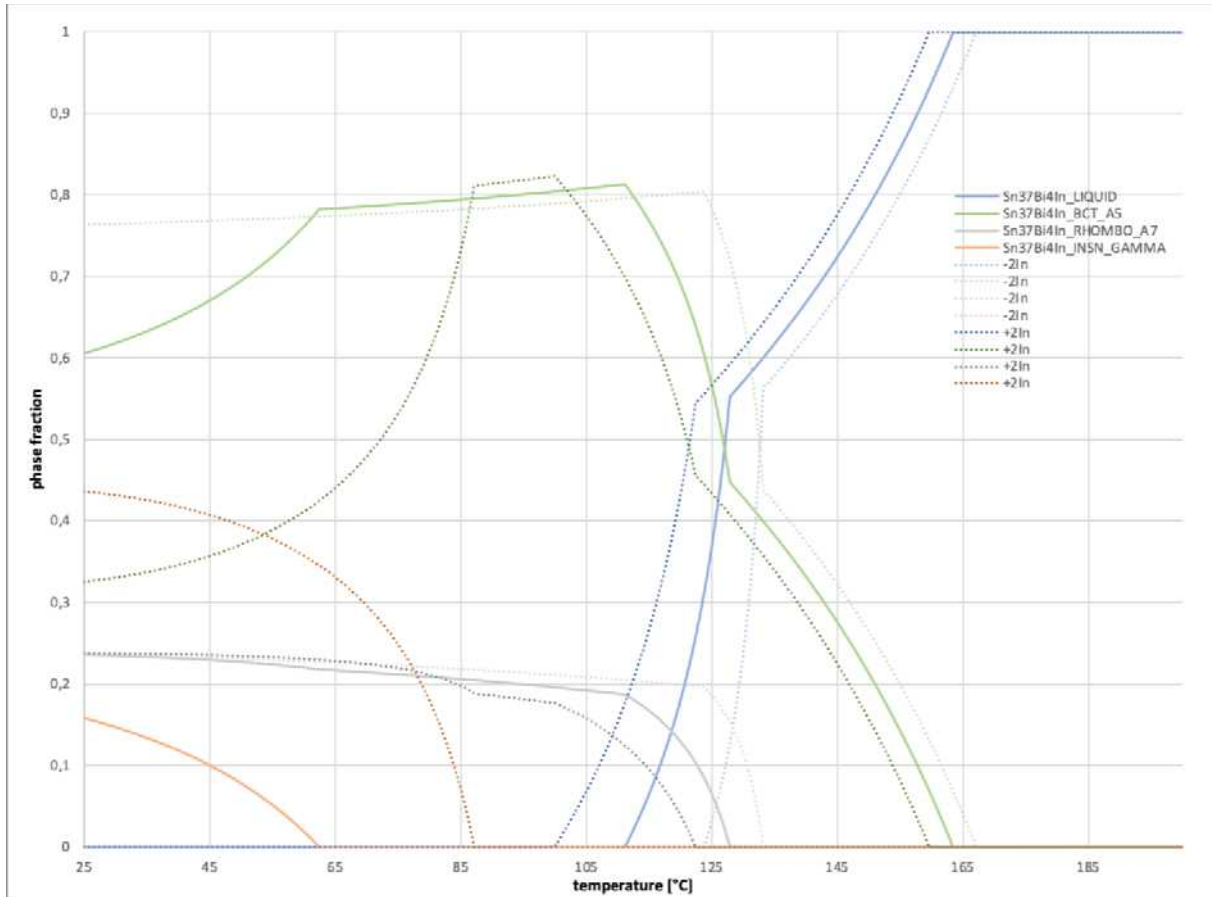


Figure 147: Phase fraction diagram of the Sn37Bi4In, Sn37Bi6In(+2In), and Sn37Bi2In(+2In) alloys between 25 °C and 200 °C; conducted with MatCalc 6.03 and MatCalc solder database.

### The microstructure of the +2 wt% In alloy (Sn37Bi6In)

The microstructure of Sn37Bi6In is very similar to the microstructure of Sn37Bi4In, with the difference that a notable amount of BiIn has formed. Although predicted by CALPHAD calculations (figure 147), the microstructure of the Sn37Bi6In alloy shows no INSN\_GAMMA phase, but unexpectedly BiIn (figures 148 and 149, 150). The absence of the INSN\_GAMMA phase may be explained by the “solid/solid transition”- nature of the INSN\_GAMMA development out of the BCT\_A5 phase. The fast cooling rate (see chapter 5.2.1. Microstructure of the reference samples (As cast)) of the sample in the silicon mold suppresses possible solid/solid transitions. The In surplus leads to the BiIn phase development, which forms on the edges of the Bi-rich RHOMBO\_A7 phase (see figure 150).

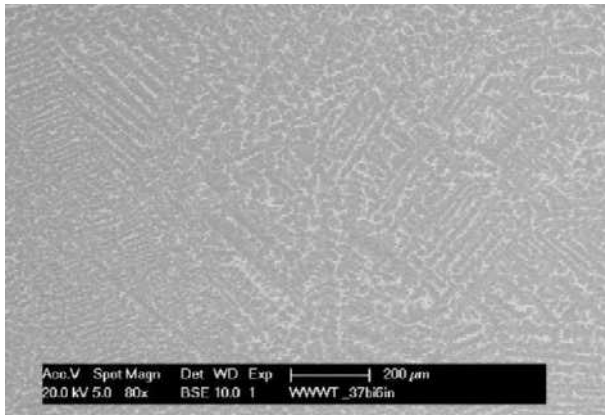


Figure 148: Picture of the microstructure of Sn37Bi6In with 80 times magnification

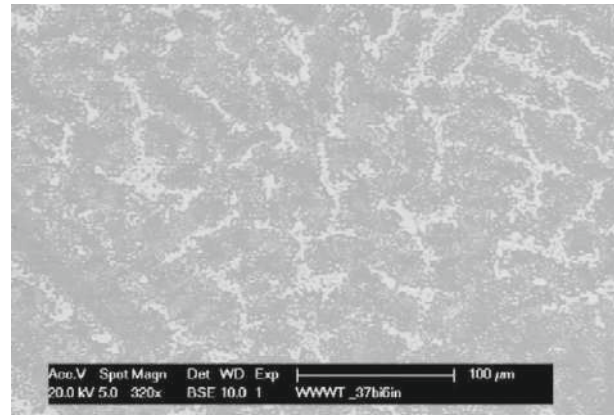


Figure 149: Picture of the microstructure of Sn37Bi6In with 320 times magnification

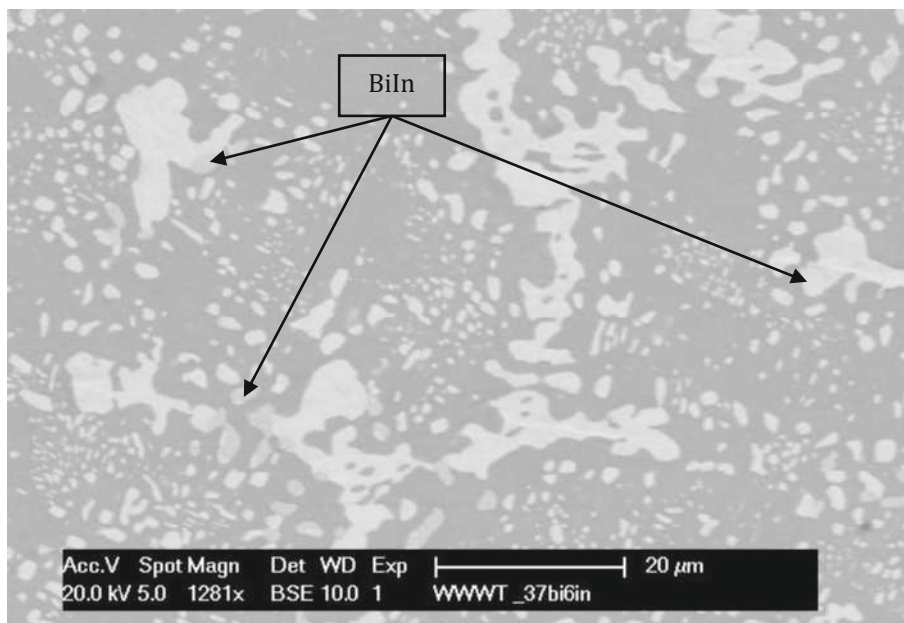


Figure 150: Picture of the microstructure of Sn37Bi6In with 1280 times magnification

### The microstructure of the -2 wt% In alloy (Sn37Bi2In)

Evenly distributed RHOMBO\_A7 particles characterize the Sn37Bi4In alloy microstructure (figures 151, 152, and 153) with sizes ranging up to 35  $\mu\text{m}$  as in the Sn37Bi4In alloy but with more small RHOMBO\_A7 particles like in the SN35Bi4In alloy (figure 146). Unlike in Sn35Bi4In, the main Bi branches are less linearly organized, and the Sn37Bi2In alloy tends to form more small particles ( $<10 \mu\text{m}$ ) than all the other alloys.

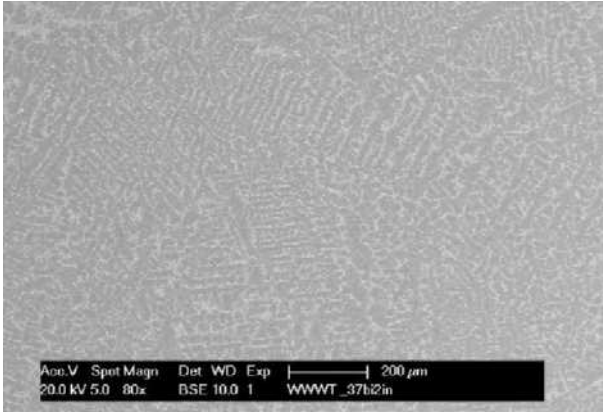


Figure 151: Picture of the microstructure of Sn37Bi2In with 80 times magnification

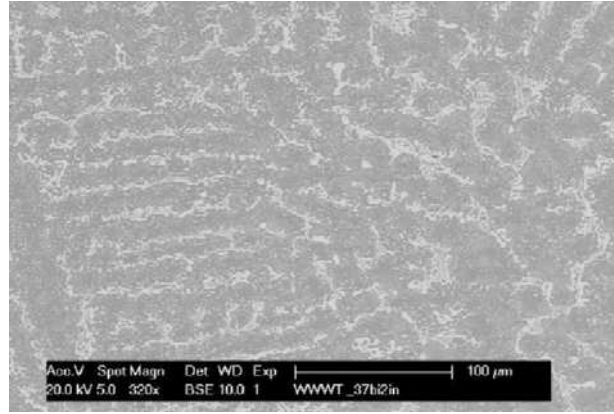


Figure 152: Picture of the microstructure of Sn37Bi2In with 320 times magnification

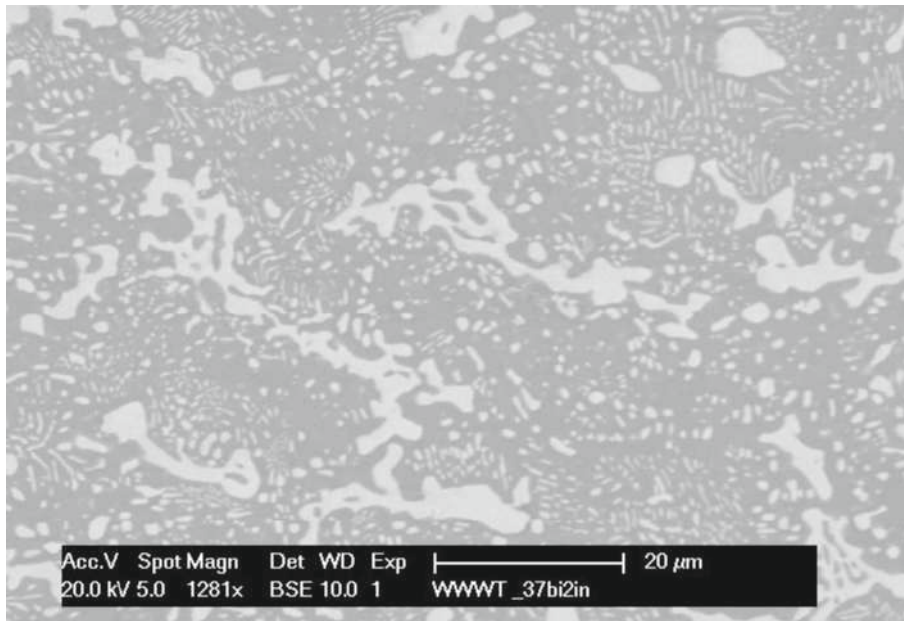


Figure 153: Picture of the microstructure of Sn37Bi2In with 1280 times magnification

### 5.3.3. Mechanical property changes induced by variation of composition

When the alloying elements are changed, the mechanical characteristics change, in some cases significantly. The results are summarized in table 11 and figures 154 to 157. Subsequently, the differences in Bi and In variation are addressed.

In the case of Bi variations (Sn39Bi4In, Sn35Bi4In), the pronounced tendency to necking in the tensile tests is no longer present. The specimens with lower Bi content showed tendencies to increase Young's modulus, while no changes in mechanical values from the Sn37Bi4In alloy can be detected in the Sn39Bi4In alloy. A different situation is seen with respect to the UTS. The Sn35Bi4In measurements show similar values to the Sn37Bi4In alloy, while the UTS of the Sn39Bi4In alloy drops slightly. The situation is similar for the uniform elongation. Increasing the Bi content tends to decrease the uniform elongation, and decreasing the Bi content tends to increase it, resulting in similar measurements to the Sn37Bi4In alloy.

Compared to the Bi variation, the In variation leads to substantial changes with respect to the Sn37Bi4In alloy. Again, the effect is seen most noticeably when considering toughness. While no necking starts in the Sn37Bi6In

alloy samples, the Sn37Bi2In samples behave similarly to the Sn37Bi4In reference alloy. Increasing the In content tends to decrease both the Young's modulus and the uniform elongation. Decreasing the In content, on the other hand, leads to an increase in both values. In terms of UTS, both alloys are similar to the Sn37Bi4In measurement.

Table 11: Important tensile test values of the Sn37Bi4In, Sn39Bi4In(+2Bi), Sn35Bi4In(-2Bi), Sn37Bi6In(+2In) and Sn37Bi2In(+2In) alloys. (only suitable for comparative purposes)

	Sn37Bi4In	Sn39Bi4In	Sn35Bi4In	Sn37Bi6In	Sn37Bi2In
Young's modulus [ $\frac{N}{mm^2}$ ]	31.6	31.5	34.0	29,7	35.0
UTS [ $\frac{N}{mm^2}$ ]	97.1	92.3	97.7	99.5	96.1
Uniform elongation [%]	9.4	7.3	8.9	8.2	11.2
Toughness [ $\frac{N}{mm^2}$ ]	4513	814	1630	648	4342

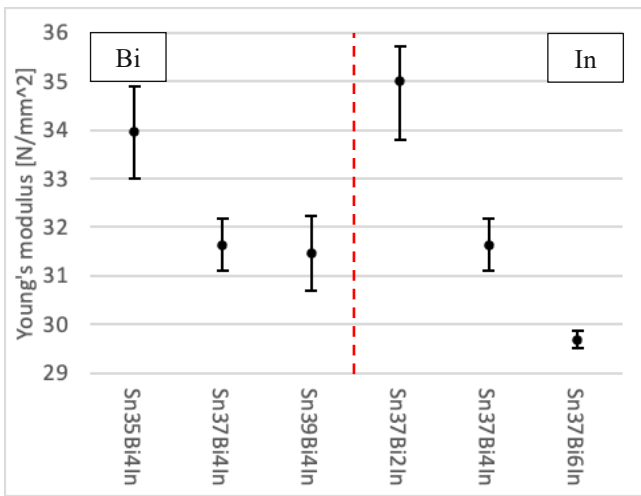


Figure 154: Comparison of the influence of alloying elements regarding Young's modulus

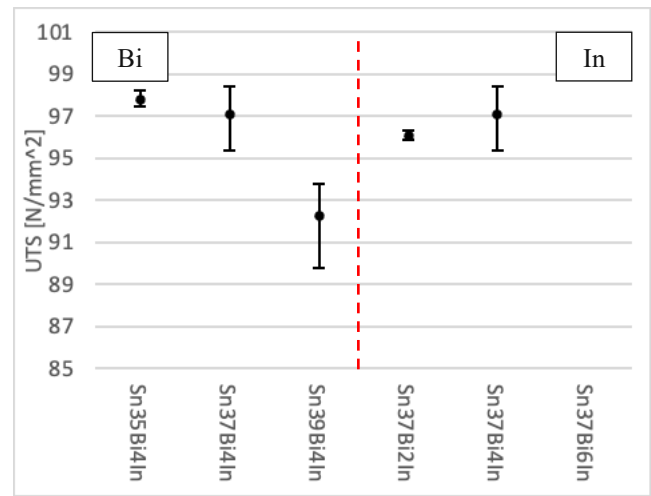


Figure 155: Comparison of the influence of alloying elements regarding UTS

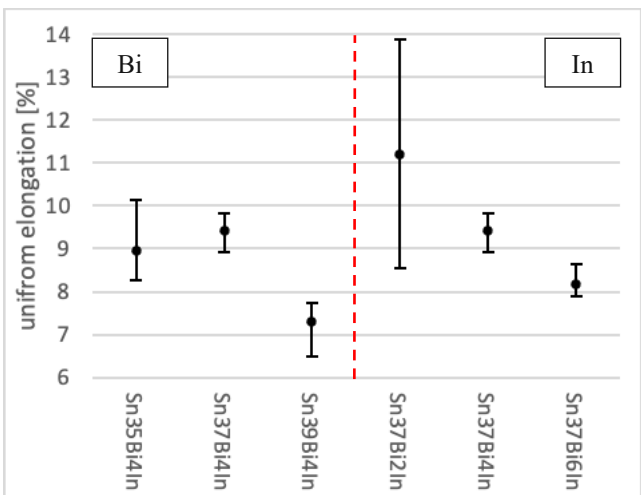


Figure 156: Comparison of the influence of alloying elements regarding uniform elongation

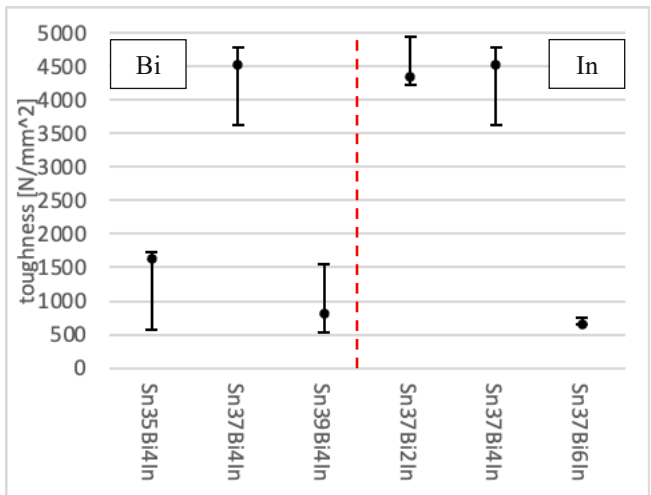


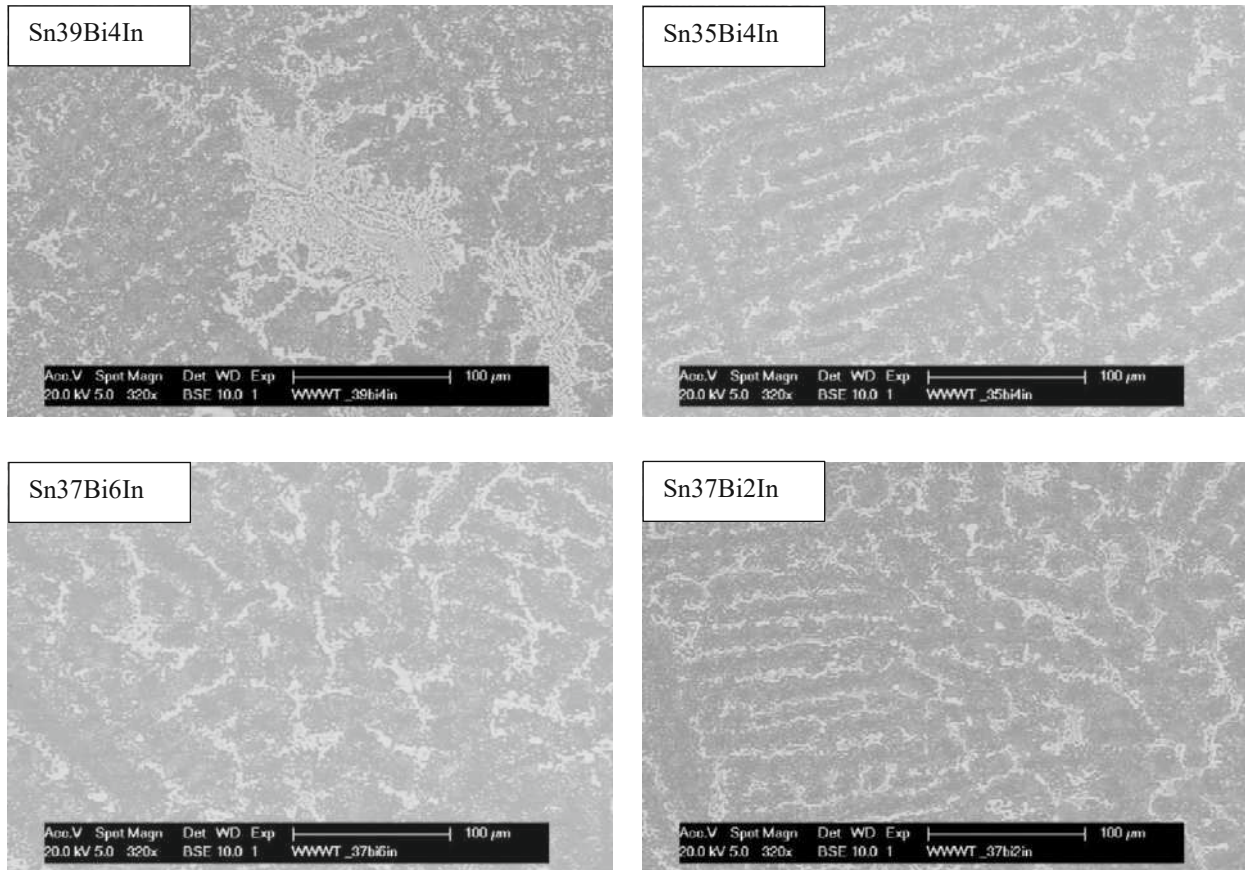
Figure 157: Comparison of the influence of alloying elements regarding toughness

### 5.3.4. Conclusions of the chapter

Local gradients regarding chemical concentration are hard to avoid. The exact composition can vary locally, which can change both mechanical and metallographic properties. To get an overview of potential local composition, the content of Bi and In has been varied by  $\pm 2$  wt% to get four related alloys to compare with the Sn37Bi4In solder (see BSE images in figures 158). Three samples of each group:

- Sn37Bi4In (as reference)
- Sn39Bi4In (+2 wt%-Bi)
- Sn35Bi4In (-2 wt%-Bi)
- Sn37Bi6In (+2 wt%-In)
- Sn37Bi2In (-2 wt%-In)

have been mold and tensile tested.



Figures 158: Comparison of the influence of the alloying elements on the microstructure with 1280 times magnification.

Minor alterations of the phase composition in the Sn39Bi4In alloy are predicted by CALPHAD calculations with a slightly enhanced RHOMBO\_A7 phase and reduced BCT\_A5 phase, leading to increased INSN\_GAMMA formation. The microstructure of the Sn39Bi4In alloy microstructure shows an enhanced tendency to form connected RHOMBO\_A7 networks with up to 100 µm in diameter and enclosed small BiIn particles. Nevertheless, unlike the surface in the heat-treated samples, the Sn-rich matrix still penetrates the Bi ramifications. The

Sn35Bi4In alloy calculations predict the reverse scenario to the previous group with a declining tendency to form RHOMBO\_A7 and INSN\_GAMMA while building more BCT\_A5 phase. The microstructure showed small Bi particles between the more extensive, familiar RHOMBO\_A7 structures in a linear, organized distribution.

With the addition of In, the microstructure should change from a BCT\_A5 matrix to an INSN\_GAMMA matrix, while the RHOMBO\_A7 content and the evolution of this phase are the same as in the Sn37Bi4In alloy. Due to the fast cooling rate during the casting process, the solid/solid transition from BCT\_A5 to INSN\_GAMMA at a lower temperature is suppressed entirely. The In concentrates in the form of BiIn particles on the edges of RHOMBO\_A7 regions. The liquid and solidus temperature of this alloy, on the other hand, drops by 10 °C and 8 °C, respectively. In the CALPHAD calculations, the BCT\_A5, RHOMBO\_A7, and liquid phase are the only appearing phases throughout the phase fraction diagram. The absence of In became obvious, contemplating the solidus and liquidus temperature, rising by 10 °C and 8 °C, respectively. The microstructure is similar in the - 2 wt%-Bi alloy with an even distribution of smallest particles between the linear, organized Bi structures of greater size.

Only Sn37Bi4In and Sn37Bi2In show a tendency to necking. The addition of Bi leads to a trend of decreasing UTS and uniform elongation. The Sn35Bi4In samples, on the other hand, show a tendency to increasing Young's modulus. Both addition and reduction lead to a significant reduction in toughness due to sudden breaking after reaching UTS. An In variation leads to substantial mechanical and metallographic property transformations. The addition of In leads to a decrease in Young's modulus, uniform elongation and toughness. UTS is not changing. Sn37Bi2In, on the contrary, increases Young's modulus and uniform elongation. A minimal decrease is noticeable for this alloy in toughness and UTS.



## 5.4. Long-term stability (non-eutectic system above $T_{sol}$ )

This chapter deals with the long-term stability of the Sn37Bi4In solder material in terms of microstructure and mechanical properties. Over time, in service or not, material properties can alter due to interactions and reactions with the environment. This can lead to sudden failure, making it necessary to assess the aging properties of the material. Since this process is enhanced at higher temperatures, an elevated temperature is selected. At 120 °C, the material is partially liquid, which further accelerates potential aging processes.

### 5.4.1. Influence of the aging duration on the microstructure

Since in chapter 5.2 Influence of the temperature on the microstructure of the Sn37Bi4In solder, apparent differences in the microstructure between the top and bottom side are evident, a distinction is also made here between the top and bottom side. However, the differences regarding chemical composition and microstructure development between the top and bottom surfaces are insignificant in the specimens considered in this chapter. Furthermore, no clear tendencies are noticeable between the aging stages 1 day and 40 days (see figures 159 to 169). Apart from the surface contamination with carbon, oxygen, and silicon, the composition of the surface is similar to the composition of the untreated reference sample. Tables 12 and 13 lists the composition and standard deviation  $\sigma$  of the top and bottom surface, respectively. Appendix B contains further images of the different ageing stages, which are not included in this chapter.

The Bi content varies, averaged over all aging stages, on the top side between 36 % and 48 % and on the bottom side between 43 % and 52 %. Thus, there is a slight tendency for more Bi on the bottom side. The other alloying elements Sn and In, show an inverse, top and bottom difference due to the lack of Bi on the top side.

Table 12: Composition and standard deviation of the top surfaces

	value [wt%]	$\sigma$
C K	6.4	2.6
O K	2.8	0.6
SiK	0.4	0.1
InL	4.9	0.5
SnL	43.5	5.8
BiL	42.0	6.1

Table 13: Composition and standard deviation of the bottom surfaces

	value [wt%]	$\sigma$
C K	6.6	1.4
O K	2.1	0.5
SiK	0.3	0.1
InL	4.5	0.3
SnL	40.3	5.6
BiL	47.0	4.5



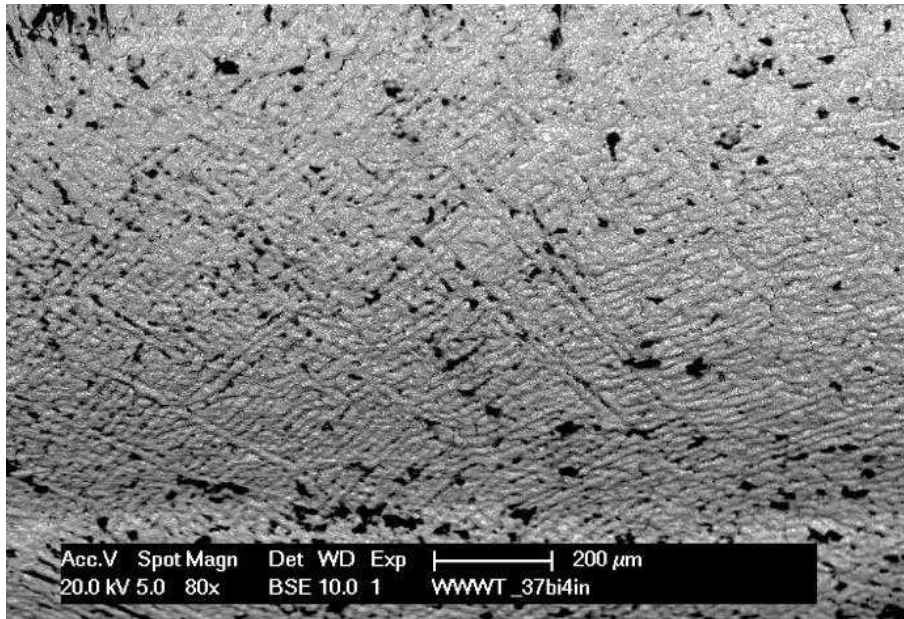


Figure 159: BSE image of the top surface after 10 minutes of aging at 120 °C

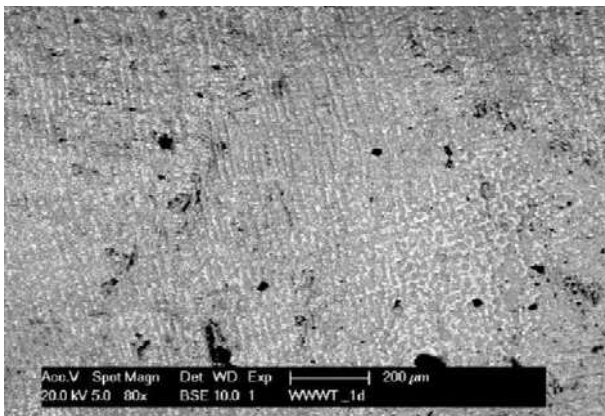


Figure 160: BSE image of the top surface after 1 day of aging at 120 °C

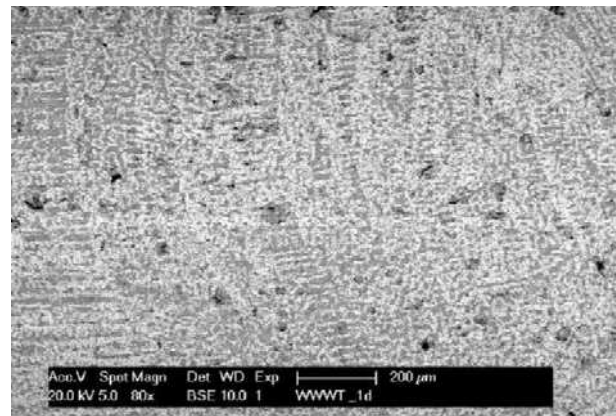


Figure 161: BSE image of the bottom surface after 1 day of aging at 120 °C

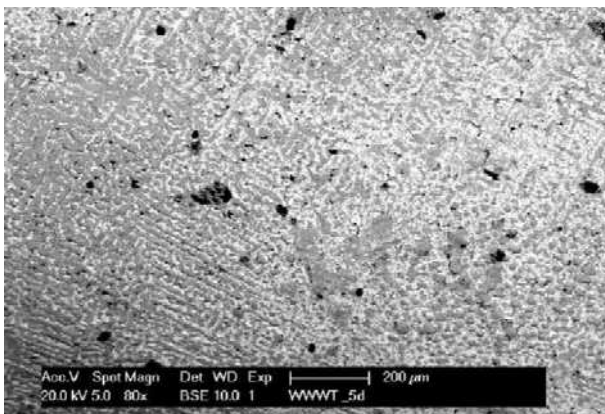


Figure 162: BSE image of the top surface after 5 days of aging at 120 °C

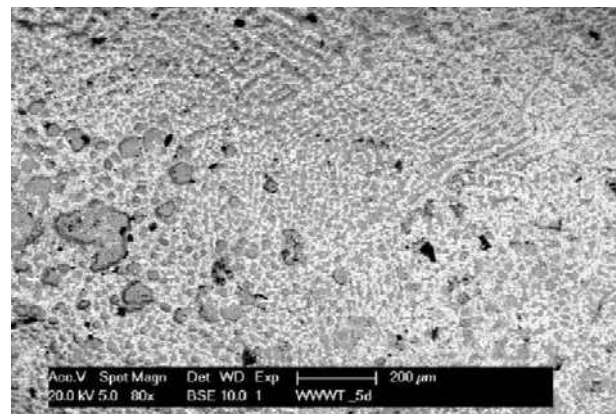


Figure 163: BSE image of the bottom surface after 5 days of aging at 120 °C

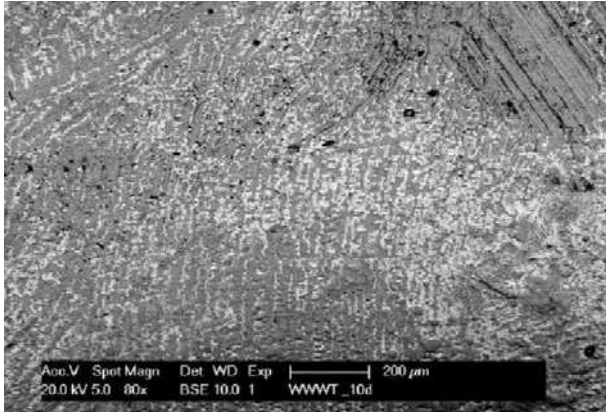


Figure 164: BSE image of the top surface after 10 days of aging at 120 °C

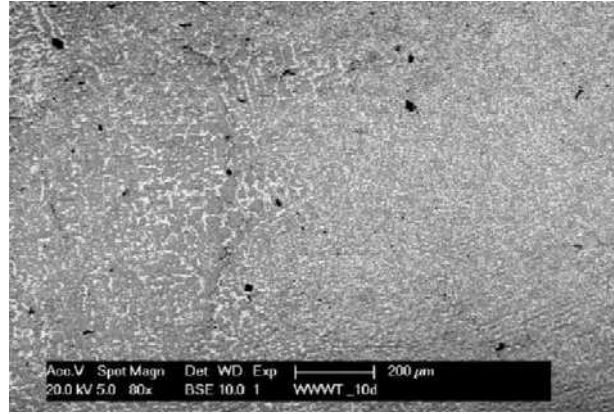


Figure 165: BSE image of the bottom surface after 10 days of aging at 120 °C

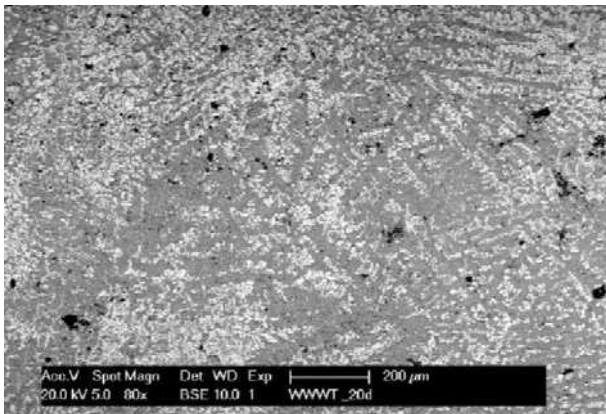


Figure 166: BSE image of the top surface after 20 days of aging at 120 °C

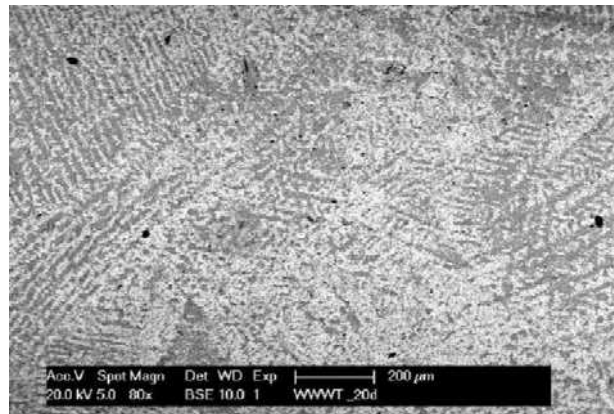


Figure 167: BSE image of the bottom surface after 20 days of aging at 120 °C

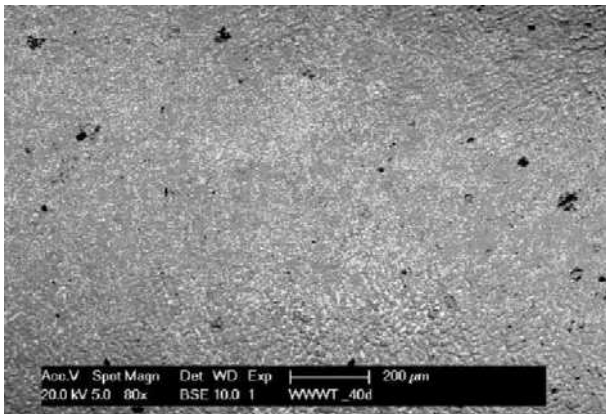


Figure 168: BSE image of the top surface after 40 days of aging at 120 °C

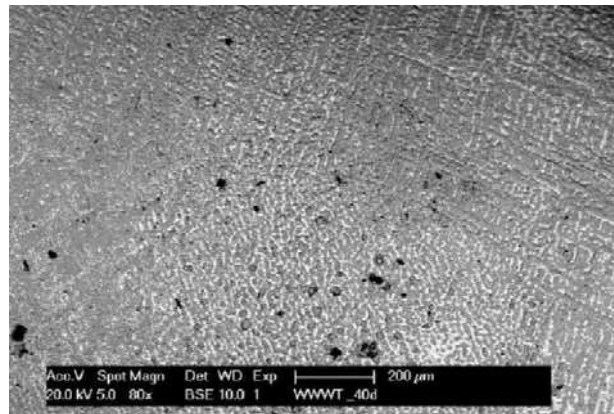


Figure 169: BSE image of the bottom surface after 40 days of aging at 120 °C

### 5.4.2. Mechanical properties induced by aging @120 °C

The mechanical characteristics of the Sn37Bi4In solder have overall a slight dependence on the duration of the aging process (see figures 170 to 174 and table 14). The longer the sample is in the furnace, the smaller the Young's modulus, UTS, and toughness tend to become. However, the reduction in Young's modulus and UTS is only measurable after 20 days. In the 10 minutes, 1 day, 5 days and 10 days groups, the aging effect is hardly measurable. The uniform elongation is approximately the same for all aging groups. Nevertheless, slight differences are recognizable here.

Table 14: Important tensile test values of the aged samples alloys (10min; 1day; 5days, 10days; 20 days; 40days) (only suitable for comparative purposes)

	1min	1d	5d	10d	20d	40d
Young's modulus [ $\frac{N}{mm^2}$ ]	35.4	34.9	34.6	35.0	33.0	32.3
UTS [ $\frac{N}{mm^2}$ ]	99.7	102.9	97.6	98.1	96.3	93.7
Uniform elongation [%]	9.8	12.0	10.7	11.3	12.6	10.0
Toughness [ $\frac{N}{mm^2}$ ]	1660	1497	752	1252	1009	1005

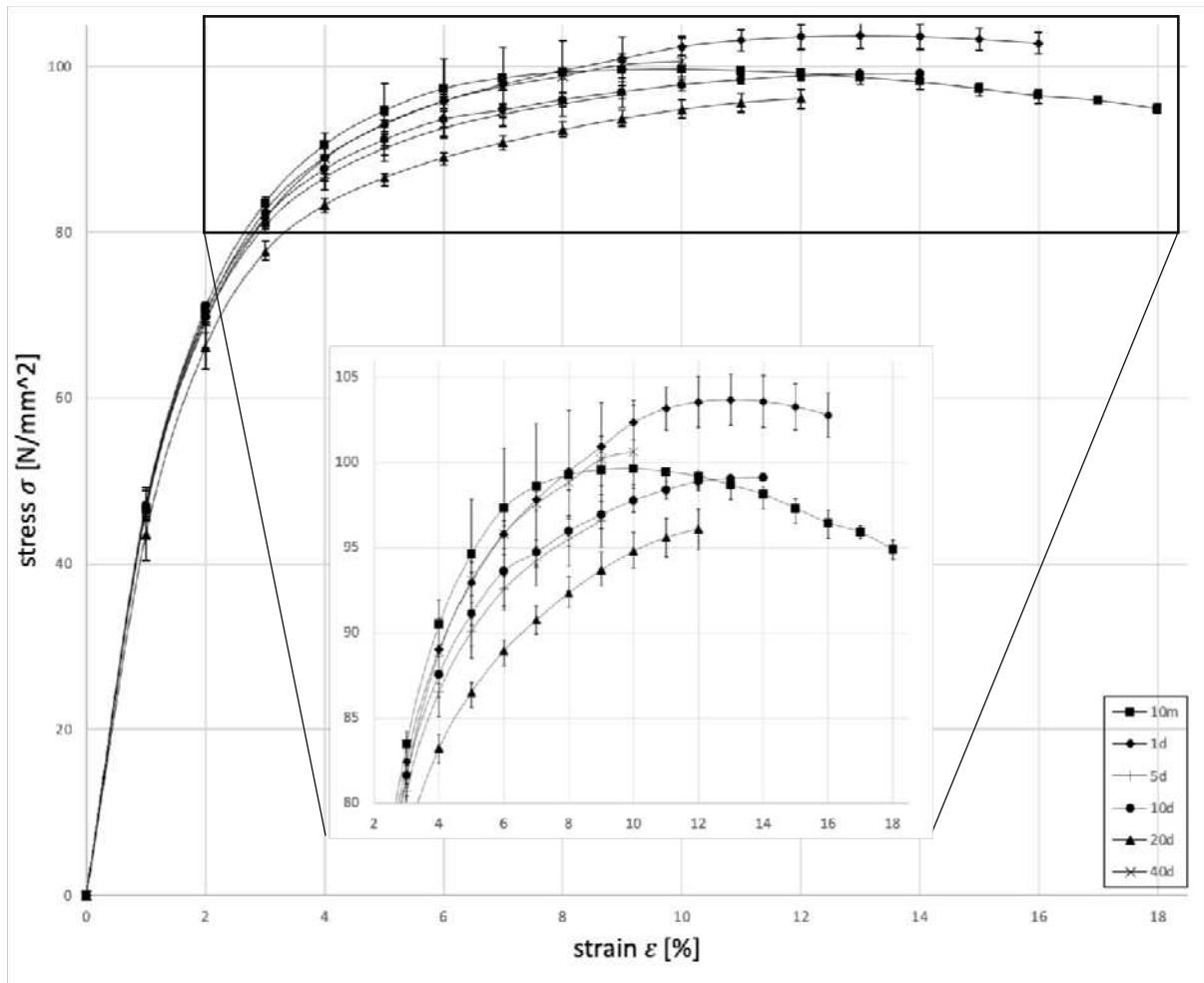


Figure 170: Tensile test of the aged samples alloys (10min; 1day; 5days, 10days; 20 days; 40days)

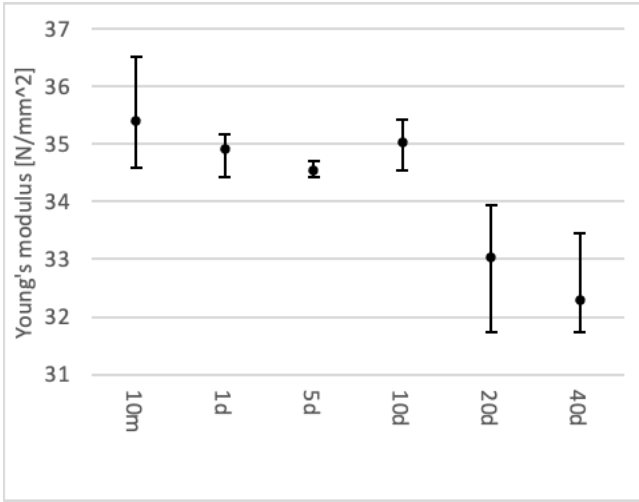


Figure 171: Influence of aging duration at 120 °C on Young's modulus

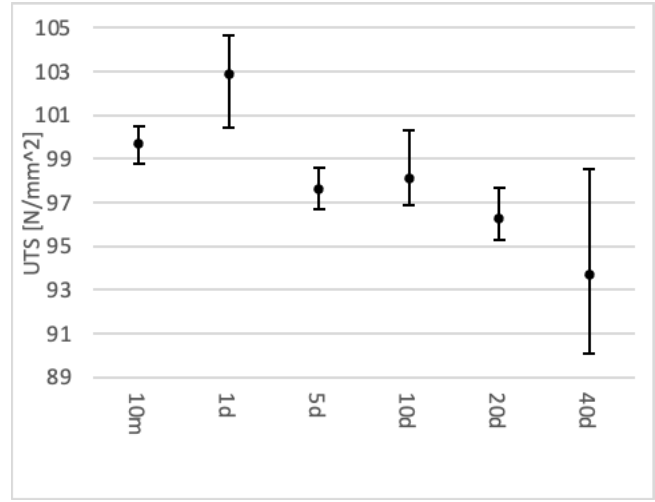


Figure 172: Influence of aging duration at 120 °C on UTS

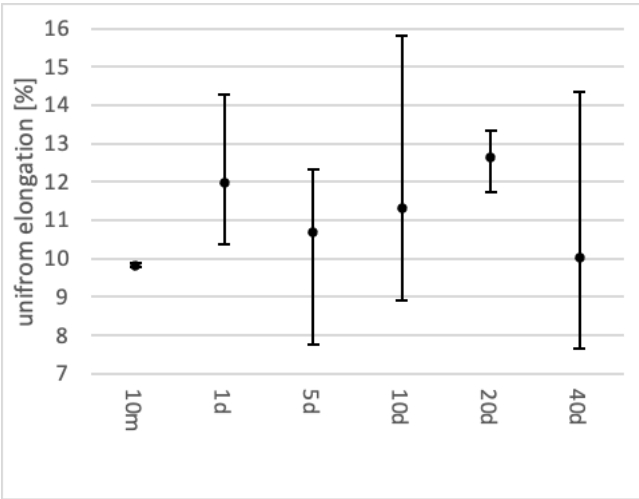


Figure 173: Influence of aging duration at 120 °C on uniform elongation

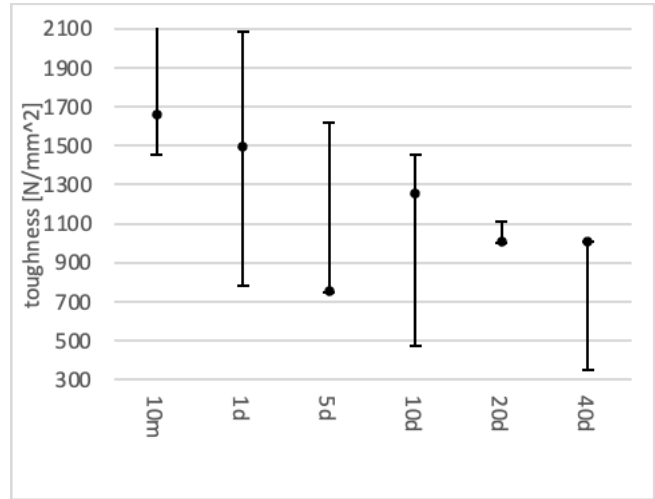


Figure 174: Influence of aging duration at 120 °C on toughness

### 5.4.3. Conclusions of the chapter

Materials (e.g., steel) are subject to a natural aging process, in which various properties (hardness and strength, uniform elongation, necking and notched impact strength) change throughout an extended period. This makes it necessary to analyze the aging effect of a product.

Concerning the microstructure, the aging duration at 120 °C shows very little influence in the case of the investigated solder. After a few hours, a slight distinction between the top and bottom sides develops. This effect is caused by the liquefaction of the Bi phase when the sample is heated over the solidus temperature, 110 °C. Over time, this phase sags slightly through the Sn matrix, resulting in a slight decrease of the Bi-rich phase on the upper side surface.

The changes in tensile test results due to aging are only minor. Subtle changes in the mechanical characteristics are measurable only after 20 days at 120 °C. In the 10 minutes, 1 day, 5 days, and 10 days groups, hardly any changes in the measured values are visible.

It can be concluded that the original properties are conserved after the casting process. As soon as the material is heated for the first time and cooled in air, an equilibrium is reached after a few minutes, hardly changing over time.

In general, the material shows only subtle changes in microstructure and mechanical characteristics due to aging.

## 5.5. Mechanical testing of Sn37Bi4In solder

The mechanical loading and testing are essential parts of this thesis. Solder samples are usually thermo-mechanically loaded due to a CTE mismatch between the attached components and the substrate. Yet, another loading approach is used since the temperature increase during a cyclic thermo-mechanical loading protocol would lead to a mixed state of loading and healing simultaneously.

The presented loading protocol fatigues the samples with cyclic mechanical applied stress in the LCF regime. This approach is used because of the possible adjustments regarding loading level, loading and unloading velocity, and durations in the different sections. According to tensile test results with the same loading velocities, the required loading level per cycle has been evaluated (see figure 175). Although a comparatively small strain amplitude of 250  $\mu\text{m}$  barely exceeds the yield strength of the solder material, the high velocity during testing leads to quick progressing fatigue damage of the sample (red line in figure 175 marks the strain amplitude during cyclic loading).

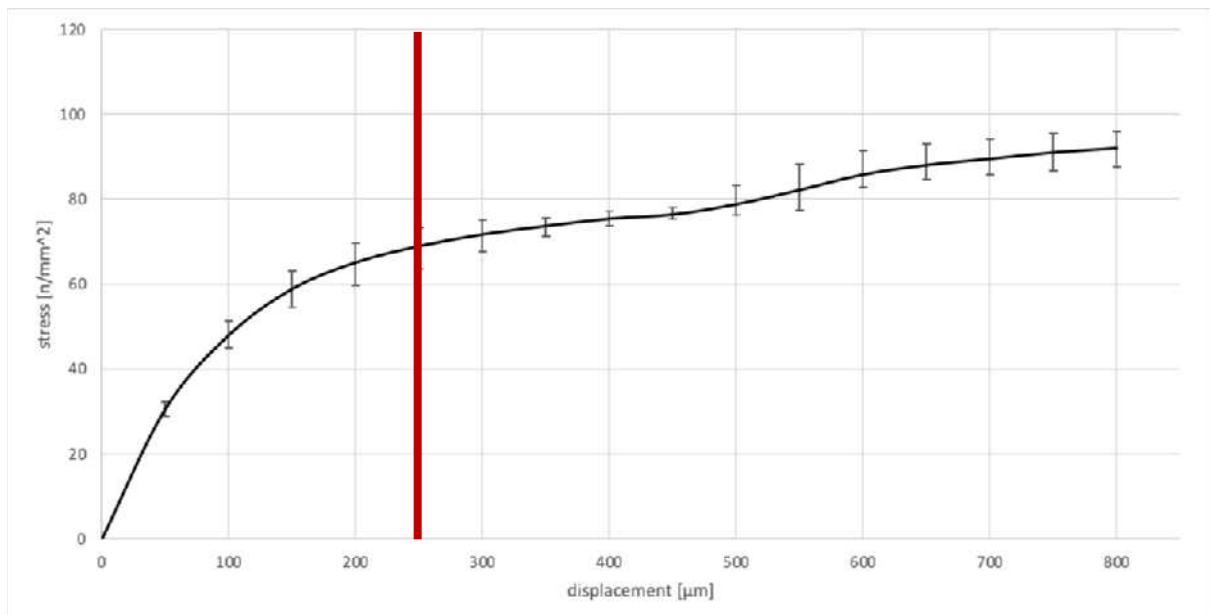


Figure 175: Tensile test conducted with 0.05 mm/s as guidance for determining loading parameters of the loading protocol with indicated strain level during cyclic loading (red line)

### 5.5.1. Cyclic loading protocol

Based on the damaging situation during application, a displacement-controlled protocol has been developed. The loading protocol is composed of three sections:

- Tensile regime
- Holding regime
- Compression regime

In the tensile section, the traverse moves from the point of origin to 250  $\mu\text{m}$  from the origin with a traverse velocity of 0.05 mm/s (blue line in Fig. 176). This section is primarily relevant for plastic deformation. The high velocity is chosen to amplify the plastic behavior of the ductile solder. Even highly ductile materials, such as Sn and In,

show a brittle behavior at higher velocity. Therefore, the samples can accumulate more fatigued damage per cycle if the velocity is increased. Based on the deformation, microvoids can develop as in a uniaxial tensile test (for more information, see chapter 3.9 Tensile test for mechanical validation).

A relaxation period of 10 s at 250  $\mu\text{m}$  is held (holding regime; orange line in 176). During the stress relaxation process, microvoids formed in the tensile section can develop further and coalesce to larger voids and form microscopic fatigue cracks in the sample.

The compression section starts directly where the holding regime ends at 250  $\mu\text{m}$  and ends at 0  $\mu\text{m}$  with a traverse velocity of -0.05 mm/s (grey line in Fig 176). It is necessary to return to the point of origin to produce enough damage while keeping the circumference of the sample unchanged.

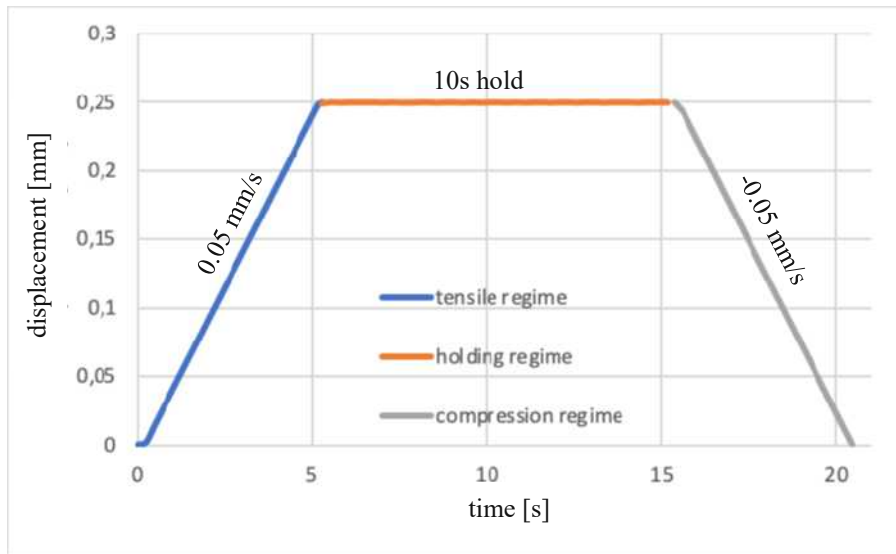


Figure 176: One cycle of the mechanical loading protocol conducted with the Zwick/Roell Z250 tensile test machine

### 5.5.2. The „Force over time“-diagram

The “force over time”-diagram is used to define the end of the loading protocol (figure 177). On average, in the case of Sn37Bi4In, three cycles are necessary to leave the cyclic softening stage (red section) and enter the stabilized section. From the third cycle, the maximum force is taken as the initial sample-specific value  $\kappa$ . A maximum-force reduction to 90 % of  $\kappa$  empirically proved for Sn37Bi4In samples to be a sufficient criterion to inflict enough damage to be verifiable via optical microscopy (see chapter 5.5.4 Assessment of fatigue damage production). When the maximum-force value of a cycle is below 90 % of  $\kappa$ , the loading protocol is stopped while the sample is still in the holding regime. Table 15 relates the occurring  $\kappa$  value and the corresponding end criterion for the example shown in figure 177.

Table 15: Example of a Sn37Bi4In sample mechanically cyclic loaded.

Parameter	Numerical value [N]
$\kappa$	614
0.93 $\kappa$	571
0.87 $\kappa$	534
0.9 $\kappa$	553

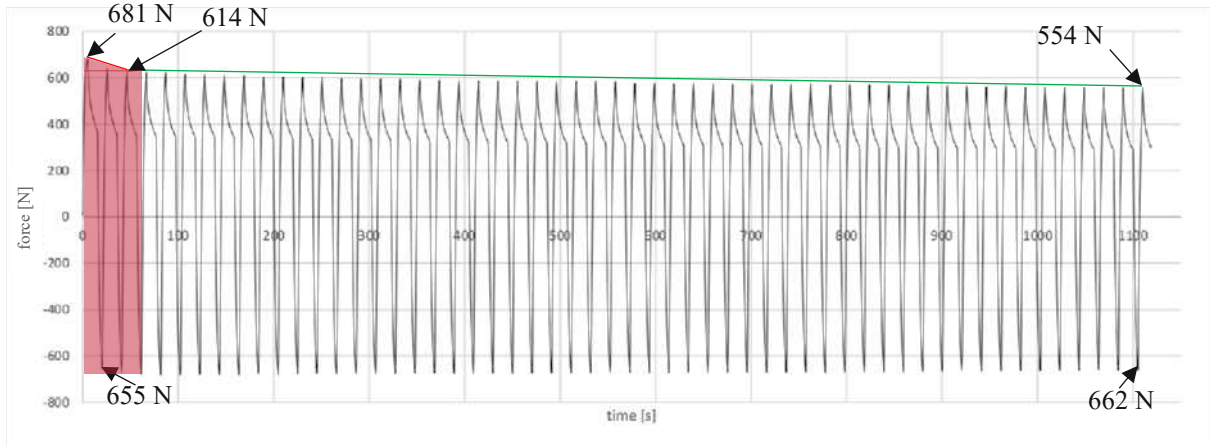


Figure 177: “Force over time”- diagram of a Sn37Bi4In sample

### 5.5.3. Hysteresis

Definite cycles presented in a “force over displacement”-hysteresis diagram (figure 178) ensure a more detailed view of the fatigue level during the loading protocol. Unfortunately, we cannot retrieve this information for single hysteresis loops during a running test. Nevertheless, the contained information in a hysteresis diagram of a failing sample can improve the insight into the fatiguing process after the test is stopped and helps to estimate the condition for subsequent samples.

The “force over displacement”-diagram can be used to illustrate a reduction of the load-bearing cross-section, due to the dependence of the Young’s modulus  $E$  on the cross-section  $A$ :

$$E = \frac{\sigma}{\epsilon} \quad \text{with } \sigma = \frac{F}{A} \xrightarrow{\text{yields to}} E = \frac{F}{A \cdot \epsilon}, \quad (15)$$

which appears in the linear section of the hysteresis (see figure 179). Whereby  $F$  is the force and  $\epsilon$  is the strain. A decrease of the Young’s modulus from cycle to cycle or an increase of the relation:

$$\frac{E_t}{E_c'} \quad (16)$$

signifies a reduction of the bearing cross-section (figure 179). Since the sample is not getting longer during cyclical loading and necking is not the case, reduction of the cross-section is consequently attributable to fatigue cracks caused by the formation and expansion of microvoids.

$E_c$  is determined at the beginning of the compression regime between 40 % and 80 % of the maximum force (see figure 179).  $E_t$  is the equivalent at the beginning of the tensile regime (see figure 179).  $E_c$  is yet the more important factor referring to fatigue damage analysis since in an elongated position, as after the holding regime, potential cracks are opened and these areas are not contributing to the supporting cross-section in contrast to the compressed situation. The evolution of  $E_c$  and the equation (16) are therefore indications of how much fatigue has been created at a given point of the loading protocol (see figure 180).



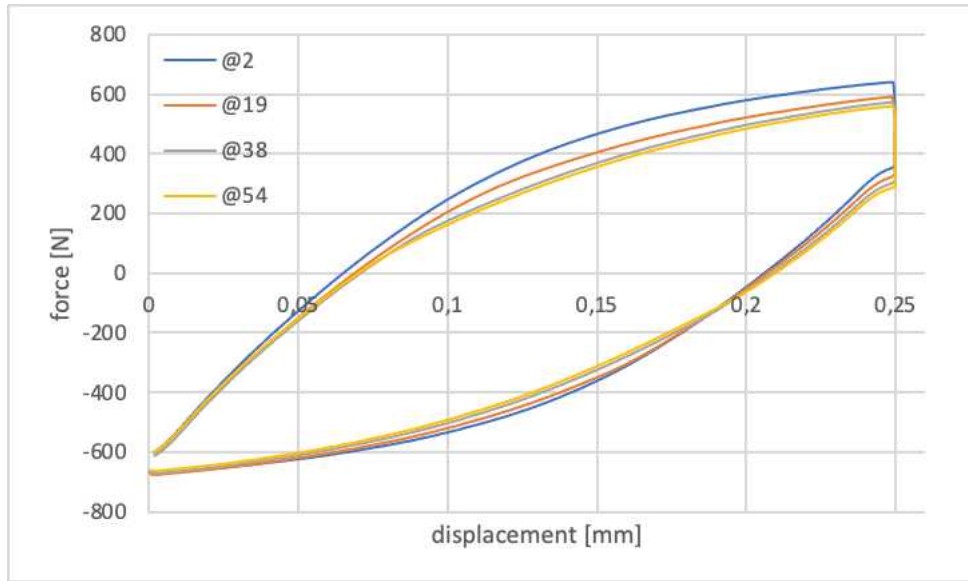


Figure 178: Definite cycles of a „force over displacement“-diagram (hysteresis)

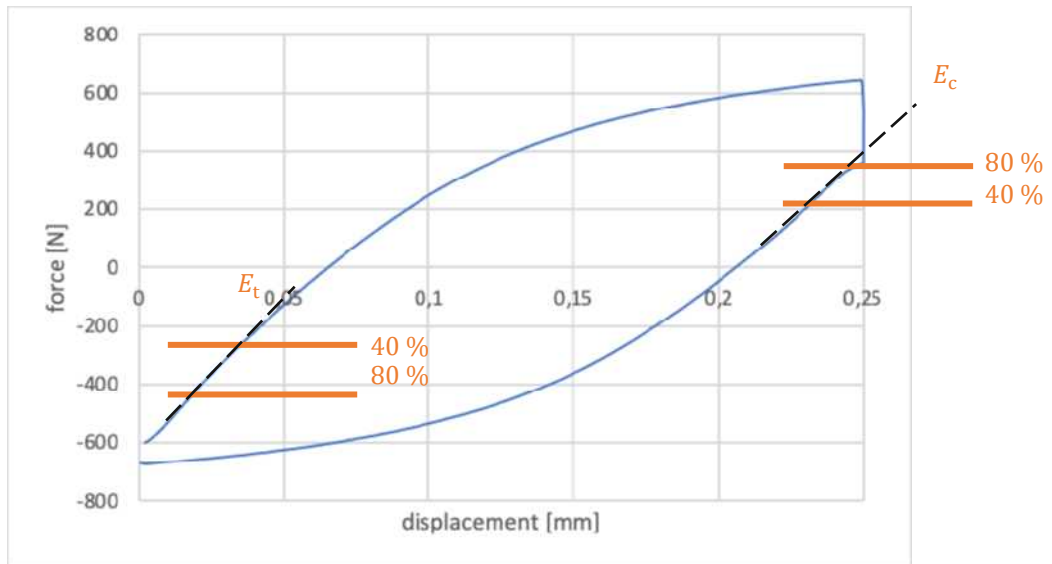


Figure 179: Determination of the stiffness in the tensile and compression regimes

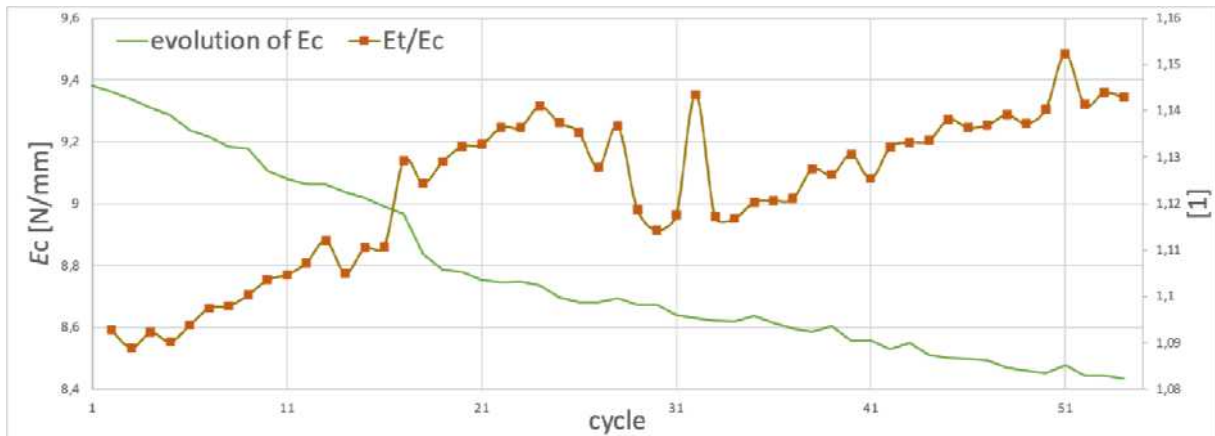


Figure 180: Evolution of  $E_c$  and the relation  $\frac{E_t}{E_c}$  for fatigue evaluation

## 5.5.4. Assessment of fatigue damage production

Since it is hardly possible to verify if a sample is damaged with in-situ non-destructive examination methods, ten samples of the Sn37Bi4In solder have been tested as a preliminary test to provide a basis for the damage evaluation. After the loading protocol, the fatigued samples have been embedded and analyzed to find fatigue cracks and therefore develop a sensitivity for the correlation of available information during testing and inflicted fatigue damage (see chapter 5.5.2. The „Force over time“-diagram). As shown in the specimen depicted in figure 181, fatigued samples typically develop several cracks on both edges of the sample with different lengths and at different positions. In the ten examined samples, no preferred orientation and position are apparent. The findings regarding crack length, the conducted number of cycles, and  $\kappa$  values are summarized in table 16. If more than one crack is found, only the most extended crack is considered.

Table 16: Summary of ten cyclic loaded samples regarding the inflicted crack length

sample #	crack length [ $\mu\text{m}$ ]	number of cycles [1]	$\kappa$ value in the last cycle [%]
1	900	110	85
2	600	100	86
3	150	100	90
4	300	100	90
5	50	51	92
6	180	60	90
7	180	60	87
8	600	57	85
9	100	47	90
10	200	64	92

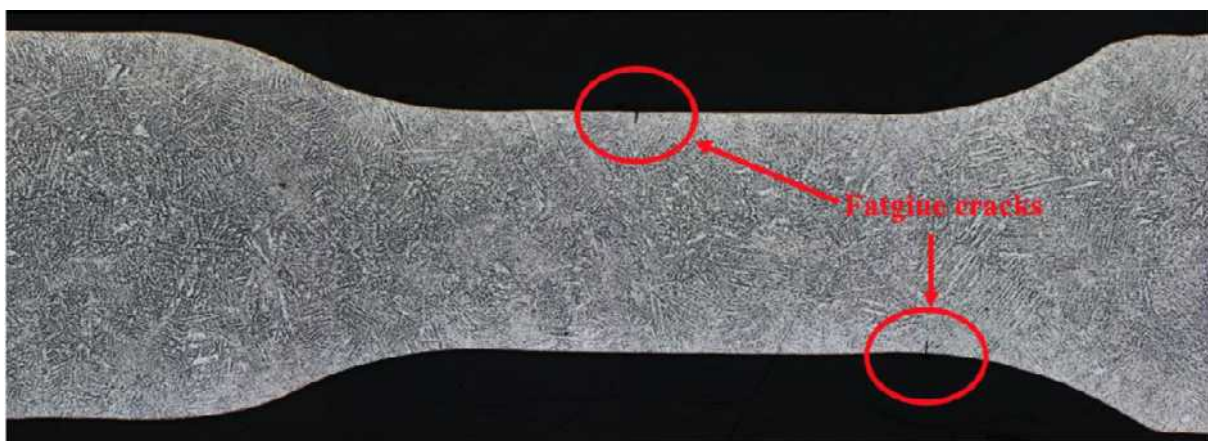


Figure 181: Sample 10 after 64 cycles

After determining the crack length with the optical microscope, the samples are investigated in the SEM and the brittle Bi-rich phase is identified as crucial for crack propagation. Figure 182 shows that, although the RHOMBO\_A7 phase formations (white) are not continuously connected, the crack grows primarily in this phase.

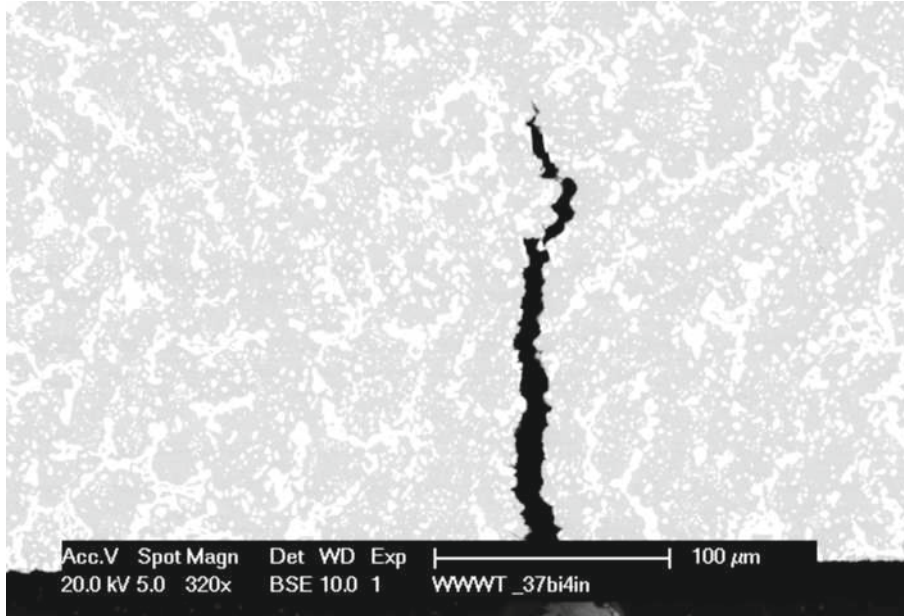


Figure 182: The crack in the sample propagates primarily in the Bi-rich RHOMBO\_A7 phase

### 5.5.5. Tensile tests of loaded and healed samples

The mechanical evaluation of the fatigued samples and the regain of mechanical integrity after undergoing a healing cycle have been analyzed in a stress/strain diagram. Three “as-cast” samples, “cyclically loaded” samples and samples healed for 10 minutes at different temperatures (120 °C, 130 °C, and 140 °C) have been tested in a tensile test (figure 183). The average values (Young’s modulus, UTS, uniform elongation, and toughness) of these test groups are summarized in table 17 and figures 184 to 187.

Table 17: Important tensile test values of “as-cast” and “cyclically loaded” samples compared to different healing states (120 °C, 130 °C, and 140 °C) (only suitable for comparative purposes)

	“as-cast”	“cyclically loaded”	120 °C	130 °C	140 °C
Young’s modulus [ $\frac{N}{mm^2}$ ]	14.9	10.9	7.6	12.2	13.8
UTS [ $\frac{N}{mm^2}$ ]	39.1	26.3	23.2	32.3	32.7
Uniform elongation [%]	5.7	5.5	9.4	6.2	5.4
Toughness [ $\frac{N}{mm^2}$ ]	697	482	419	563	571

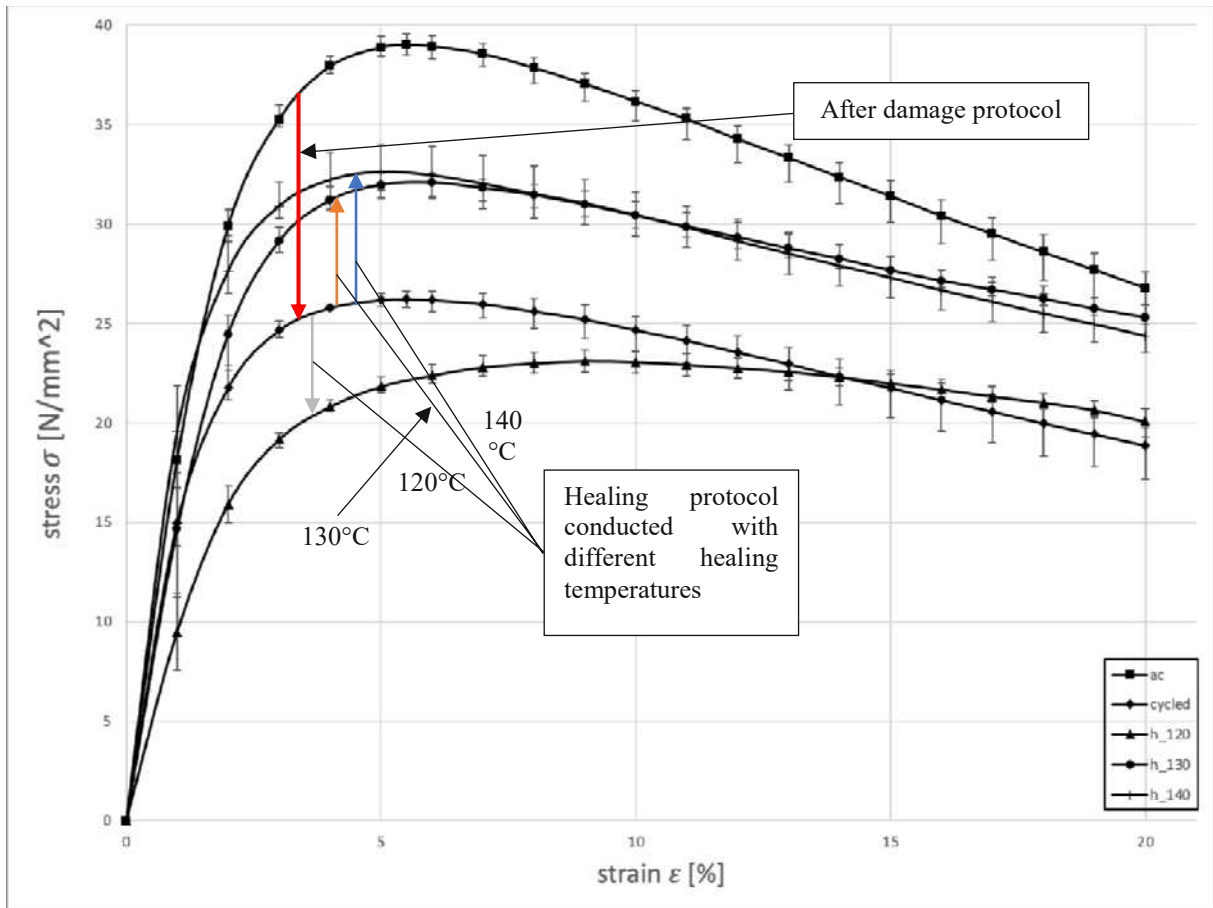


Figure 183: Tensile test of “as-cast” and “cyclic loaded” samples compared to different healing states (120 °C, 130 °C, and 140 °C)

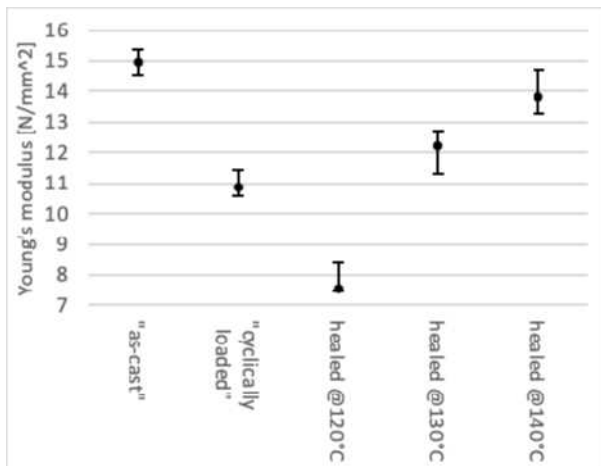


Figure 184: Comparison of heat-treated, damaged, and “as cast” samples regarding Young’s modulus

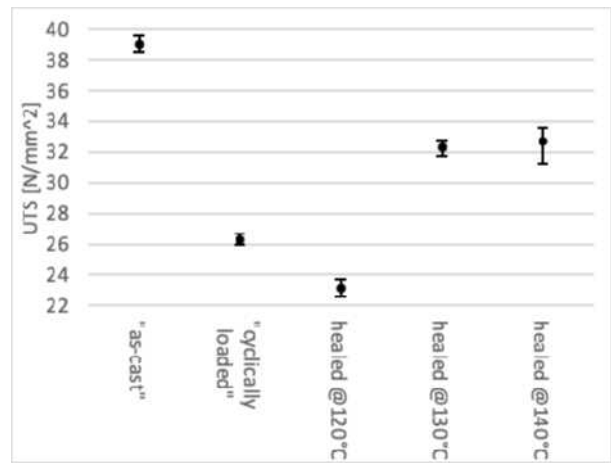


Figure 185: Comparison of heat-treated, damaged, and “as cast” samples regarding UTS

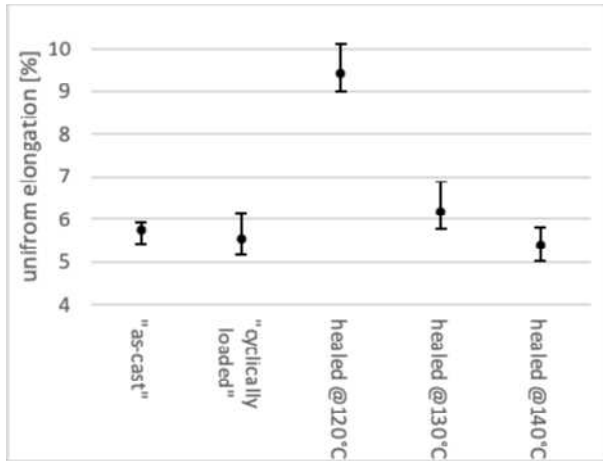


Figure 186: Comparison of heat-treated, damaged, and "as cast" samples regarding uniform elongation

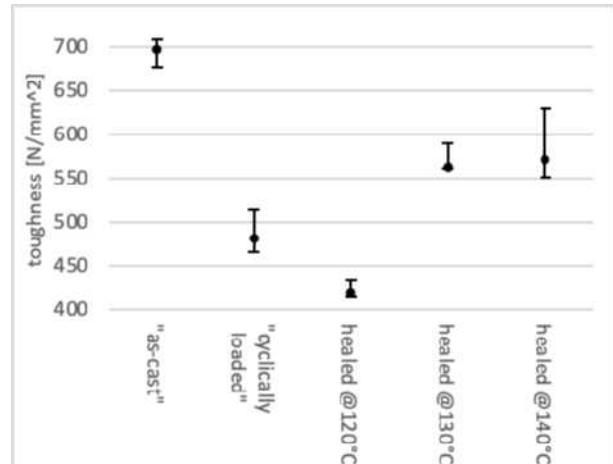


Figure 187: Comparison of heat-treated, damaged, and "as cast" samples regarding toughness

The "as-cast" samples (squared markers) act as a reference and are tested directly after the molding and grinding process.

The "cyclically loaded" samples have been mechanically fatigued with the presented loading protocol (see chapter 5.5.1 Cyclic loading protocol). Directly after loading, the mechanical characteristics of the samples are tested. The samples reveal a tendency to reduced Young's modulus, which can be attributed to a decrease of supporting cross-section of the samples due to the formation of fatigue cracks during loading. The UTS falls by 33 %. While the uniform elongation is slightly reduced, the toughness of the samples decreased by 31 %. This group forms another reference point for the samples undergoing a healing cycle.

The "healed at 120 °C"-samples show an additional decrease in Young's modulus, UTS, and toughness. This may be triggered by the heat treatment at 120 °C, which tends to decrease the Bi content on the surface and exposes cracks. In this group, an increase in uniform elongation is noticeable. Since the crack predominantly propagates in the RHOMBO\_A7 phase, uniform elongation may be increased over the "as-cast" and "cyclically loaded" samples. Owing to the higher availability of liquid phase, which permeates the sample, and can heal larger fatigue cracks, signs of healing are visible regarding Young's modulus and toughness. Therefore, the mechanical properties of the alloy improve significantly over the damaged sample values.

In the stress/strain curve of the "healed at 140 °C"-samples, the increased temperature and duration at elevated temperatures lead to further improvement of the Young's modulus. The toughness of the 140 °C-samples increases slightly compared to the "healed at 130 °C". UTS is equal to the "healed at 130 °C"-samples and the uniform elongation values return to the state of the "as-cast"-samples.

## 5.5.6. Conclusions of the chapter

Based on the tensile test results with a traverse velocity of 0.05 mm/s, the strain level during cyclic fatigue has been determined. A mechanical LCF approach is chosen for the cyclic loading protocol because it is better adjustable than a loading protocol based on thermo-mechanical damage. Furthermore, thermo-mechanical damage is, in particular, unsuitable for fatiguing a thermally-triggered, self-healing process in the solder since a hardly interpretable state of simultaneous damage and healing would have arisen. The cyclic loading process consists of three sections:

- Tensile regime: The traverse is displaced by 250  $\mu\text{m}$  from the origin with a traverse velocity of 0.05 mm/s (blue line in 176).
- Holding regime: A relaxation period of 10 s at 250  $\mu\text{m}$  off origin (orange line in 176).
- Compression regime: Return to 0  $\mu\text{m}$  (origin) with a traverse velocity of -0.05 mm/s (grey line in 176).

Due to the high loading and unloading velocity, the protocol effectively creates fast fatigue damage in sub-hundred cycles.

The crack development in a sample due to the loading protocol has been evaluated by examining ten samples. Therefore, each sample has been fatigued with different  $\kappa$  values and then metallographically investigated.

For the assessment of a healing effect, five groups have been evaluated with the tensile test and a low velocity of 0.00025 mm/s. The low velocity is chosen to prevent the samples from failing too early. The defined groups of three samples each are:

- “as cast”: samples tested directly after molding and grinding.
- “cyclically loaded”: samples that have been cyclically loaded and fatigued before tensile testing.
- “healed at 120 °C”: „cyclically loaded”-samples that have been exposed to 120 °C (17 % liquid phase).
- “healed at 130 °C”: „cyclically loaded”-samples that have been exposed to 130 °C (57 % liquid phase).
- “healed at 140 °C”: „cyclically loaded”-samples that have been exposed to 140 °C (67 % liquid phase).

All healed samples have been exposed to the heat source for ten minutes and then cooled on air (see figure 79).

The stress/strain-diagram depicted in figure 183 and summarized in table 17 shows that the mechanical properties (Young’s modulus, UTS, and toughness) of the unharmed “as-cast” samples can not be restored. The „cyclically loaded”-samples exhibit a significant drop in mechanical values caused by a reduction in bearing cross-section during cyclic loading. The fatigue damage is especially prominent compared to the “as-cast”-samples regarding Young’s modulus, UTS, and toughness, whereby the reduction of the cross-section is most evident in the Young’s modulus as it is directly proportional to the cross-section of a sample. In the case of the samples “healed at 120 °C”, the UTS, toughness, and Young’s modulus are reduced. An explanation can be that at 120 °C, the liquid phase primarily consists of Bi, which shrinks when melted, enhancing the fatigue cracks. The reduced Bi concentration on the surface leads to the increased Sn and In concentration, which might have influenced the later necking of the samples of this group. In the “healed at 130 °C”-samples, healing effects are apparent. Tendencies of increased Young’s modulus, UTS, uniform elongation, and toughness are noticeable. Although the involvement of the higher

liquid phase fraction, the “healed at 140 °C”-samples show marginally enhanced healing effects over the “healed at 130 °C” samples, regarding Young’s modulus, UTS and toughness.





## 6. Conclusions of the thesis

Through the specific analysis of the Sn/Bi/In system as a self-healing solder, the findings of this work are summarized below with reference to established knowledge.

- The wide variety of possible solidus and liquidus temperatures make the ternary Sn/Bi/In system an excellent candidate for different kinds of low-temperature solder applications. In the temperature region below 200 °C, various eutectic and non-eutectic alloys are available. Nevertheless, by changing the chemical composition, the mechanical and microstructural characteristics can vary enormously. In non-eutectic alloys, the section between the solidus and liquidus temperature (two-phase region) enables the utilization of the liquid phase for self-healing applications.
- The application temperature plays an essential role for the healing concept. Higher temperatures lead to a higher liquid phase content and a lower amount of mechanically stabilizing solid phase. Customization of the solder alloy composition regarding occurring application temperatures and joining materials is necessary to heal damage and not liquefy completely, which would lead to a complete loss of mechanical stability. In the Sn/Bi/In system, the Bi and In content are relevant for healing effects because they tend to form phases with low solidus and liquidus temperatures. The ductile mechanical characteristics of Sn, on the other hand, make it an excellent solid matrix that supports the solder even with high liquid phase fractions.
- The composition of the alloying elements can immensely influence the microstructure and, therefore, the mechanical characteristics and melting behavior. In the case of the investigated Sn<sub>37</sub>Bi<sub>4</sub>In solder alloy, the Bi content variation did not influence the melting characteristics a lot but changed the microstructure when reduced to a fine-grained or if increased to a net-like Bi-phase formation. In accordance with the development of appearing damage formations, both microstructure formations can be beneficial. Smaller Bi particles may hinder the progress of the crack development but supply less healing material in the case of a large-sized crack. On the other hand, the variation of In content significantly impacts the microstructure, mechanical, and melting properties. A reduction of the In content forms a fine-grained microstructure with a tendency to higher Young's modulus and uniform elongation. The increase of the In content leads to a decrease in the melting temperature and a tendency to reduce Young's modulus, uniform elongation and toughness.
- Due to the finite cooling rates during sample production, the microstructure of a non-eutectic alloy can show deviations from the expected phases. Aging processes can further lead to alterations of microstructure, which can cause sudden failure. This effect is enhanced at higher temperatures due to the temperature dependence of diffusion processes. The Sn<sub>37</sub>Bi<sub>4</sub>In solder showed no definite signs of microstructure alteration after aging for 40 days above solidus temperature. The mechanical characteristics of the aged samples tend to change marginally after 20 days in regard to the Young's modulus and toughness.
- Dependent on the position of a defect, the mechanical resistance of a damaged product against external forces can vary massively. Cracks on the surface are in most materials more influential to failure than internal damage and can progress fast through the remaining cross-section. In microelectronic applications, cyclic thermo-mechanical loads are typical and lead to fatigue cracks from the surface to the

inner, whereby the solder joint can fail rapidly. Irregularities on the surface can act as crack initiation sites. The “cyclically loaded” Sn37Bi4In solder samples showed significant signs of fatigue when tested in a tensile test and compared to the “as-cast” samples. A tendency to reduced Young’s modulus, UTS, and toughness certify the proceeding fatigue damage. When heat-treating at application-typical temperatures, the stress/strain curves imply a regain of load-bearing cross-section, UTS, and toughness improvement. This is a direct consequence of the formation of the liquid phase, which potentially closes cracks on the surface. When the Bi is liquid, the Bi particles can coalesce and help to reduce roughness and cracks on the surface.

## 7. Summary

This work deals with investigating the self-healing properties of the ternary Sn/Bi/In system. In the course of this work, the binary and ternary phase diagrams of the alloying elements have been examined, and the Sn37Bi4In solder is chosen as a potential candidate to represent the ternary system regarding examining the idea of heat-triggered healing-effects in solders. The performed study of the mechanical and metallographic characteristics of the solder includes the influence of temperature, long-term stability above solidus temperature, and the impact of alloying elements. The analyses reveal that a definite change of microstructure and mechanical properties can be achieved by adjusting heat treatment and composition. Dog bone-shaped specimens of the Sn37Bi4In alloy have been damaged by a fatigue damage protocol in the low cycle fatigue regime and healed by partial liquefaction of the material with different liquid contents. Although the Sn37Bi4In alloy has a solidus temperature at 110 °C and a liquidus temperature at 165 °C, at 130 °C, a significant amount of liquid phase is already present, and healing effects are measurable. While the mechanical examination confirms a significant improvement of the “healed at 130 °C” and “healed at 140 °C” groups, regarding Young’s modulus, UTS and toughness over the “cyclically loaded”-reference group, the 120 °C heat treatment for 10 minutes has not been sufficient to noticeable heal any damage.

## References

- [1] M. Ciappa, „Selected failure mechanisms of modern power modules,“ *Microelectronics reliability*, Bd. 42, Nr. 4-5, pp. 653-667, 2002.
- [2] S. Cheng, C. Huang und M. M. Pecht, „A review of lead-free solders for electronics applications,“ *Microelectronics Reliability*, Bd. 75, p. 77-95, 2017.
- [3] O. Mokhtari und H. Nishikawa, „Correlation between microstructure and mechanical properties of Sn-Bi-X solders,“ *Materials Science & Engineering*, Nr. 651, p. 831-839, 2016.
- [4] X. Chen, F. Xue, J. Zhou und Y. Yao, „Effect of In on microstructure, thermodynamic characteristic and mechanical properties of Sn-Bi based lead-free solder,“ *Journal of Alloys and Compounds*, Nr. 633, p. 377-383, 2015.
- [5] Y. Kima, K. Kima, C. Hwanga und K. Suganumab, „Effect of composition and cooling rate on microstructure and tensile properties of Sn-Zn-Bi alloys,“ *Journal of Alloys and Compounds*, Bd. 352, p. 237-245, 2003.
- [6] H. Fang, C. Versteyleen, S. Zhanga und Y. Yang, „Autonomous filling of creep cavities in Fe-Au alloys studied by synchrotron X-ray nano-tomography,“ *Acta Materialia*, Bd. 121, p. 352-364, 2016.
- [7] R. Lumley, *Self-Healing Materials: An Alternative Approach to 20 Centuries of Materials Science*, Dordrecht, The Netherlands: Springer Series in Materials Science, pages 219-254, 2007.
- [8] J. Buha, R. Lumley und A. Crosky, „Microstructural development and mechanical properties of interrupted aged Al-Mg-Si-Cu alloy,“ *Metallurgical and Materials Transactions A*, Bd. 37, p. 3119-3130, 2006.
- [9] R. Lumley, R. O'Donnell, I. Polmear und J. Griffiths, „Enhanced fatigue resistance by underageing an Al-Cu-Mg-Ag alloy,“ *Materials Forum*, Bd. 29, pp. 256-261, 2005.
- [10] T. Baxevanis, A. Parrinello und D. Lagoudas, „On the fracture toughness enhancement due to stress-induced phase transformation in shape memory alloys,“ *International Journal of Plasticity*, Bd. 50, pp. 158-169, 2013.
- [11] B. Grabowski und C. Tasan, *Towards self-healing metals by employing optimally-dispersed Ti-Ni shape-memory nano-particles*, Project within DFG SPP 1568: Design and generic principles of self-healing materials: DFG, Bonn, 2014.
- [12] S. Danzi, V. Schnabel, J. Gabl, A. Sologubenko, H. Galinski und R. Spolena, „Rapid On-Chip Healing of Metal Thin Films,“ *Advanced Materials Technology*, Bd. 4, pp. 1-6, 2019.
- [13] M. Wright, M. Manuel und T. Wallace, *Fatigue resistance of liquid-assisted self-repairing aluminum alloys reinforced with shape memory alloys*, National Aeronautics and Space Administration, Hampton: NASA/TM-2013-216629, 2013.
- [14] P. Leser, J. Newman und S. Smith, *Mitigation of crack damage in metallic materials*, National Aeronautics and Space Administration, Hampton: NASA/TM-2014-218272, 2014.
- [15] M. Manuel und G. Olson, „Biomimetic Self-Healing Metals,“ in *Proceedings 1st Intl. Conference on Self-Healing Materials*, Noordwijk aan Zee, 2017.
- [16] C. Fisher, H. Henderson, M. Kesler, P. Zhu, G. Bean und M. Wright, „Repairing large cracks and reversing fatigue damage in structural metals,“ *Applied Materials Today*, Bd. 13, pp. 64-68, 2018.
- [17] G. Siroky, E. Kraker, J. Magnien, D. Melinc, D. Kieslinger, E. Kozeschnik und W. Ecker, „Effect of solder joint size and composition on liquid-assisted healing,“ *Microelectronics Reliability*, Bd. 119, 2021.
- [18] K. Lee, „Low-Cycle Fatigue Characteristics of Sn-Based Solder Joints,“ *Journal of ELECTRONIC MATERIALS*, Bd. 33, Nr. 4, p. 249-257, 2004.
- [19] X. Chen, J. Zhou, F. Xue und Y. Yao, „Mechanical deformation behavior and mechanism of Sn-58Bi solder alloys under different temperatures and strain rates,“ *Materials Science and Engineering: A*, Bd. 662, pp. 251-257, 2016.
- [20] F. Wang, Y. Huang, Z. Zhang und C. Yan, „Interfacial reaction and mechanical properties of Sn-Bi solder joints,“ *Materials (Basel)*, Bd. 10, 2017.
- [21] Y. Y. Liu und K. Tub, „Low melting point solders based on Sn, Bi, and In elements,“ *Materialstoday ADVANCES*, Bd. 8, 2020.
- [22] Q. Li, N. Ma und Y. Lei, „Characterization of Low-Melting-Point Sn-Bi-In Lead-Free Solders,“ *Journal of Electronic Materials*, Bd. 45, Nr. 11, 2016.
- [23] R. Shalaby, „Effect of silver and indium addition on mechanical properties and indentation creep behavior of rapidly solidified Bi-Sn based lead-free solder alloys,“ *Materials Science and Engineering: A*, Bd. 560, pp. 86-95, 2013.

- [24] V. Schuler und J. Twrdek, *Praxiswissen Schweißtechnik*, Wiesbaden: Springer, 2019.
- [25] M. Judd und K. Brindley, *Soldering in electronics assembly*, Oxford: Newnes, 1999.
- [26] J. Lau und L. N., *Assembly and Reliability of Lead-Free Solder Joints*, Singapore: Springer, 2020.
- [27] R. Wild, „Fatigue Properties of Solder Joints,“ *Welding Journal*, Bd. 11, p. 521–526, 1972.
- [28] S. Yang, I. Kim und S. Lee, „A Study on the Thermal Fatigue Behavior of Solder Joints Under Power Cycling Conditions,“ *IEEE Transactions on Components and Packaging Technologies*, Bd. 31, Nr. 1, pp. 3-12, 2008.
- [29] E. Macherauch und H. Zoch, „Ausbreitung von Ermüdungsrissen,“ in *Praktikum in Werkstoffkunde*, Wiesbaden, Vieweg+Teubner, 2011, pp. 396-402.
- [30] A. Lövberg und P. Tegehall, „The Stress State of BGA Solder Joints Influenced by the Grain Orientations of Neighboring Joints,“ in *2018 IEEE 68th Electronic Components and Technology Conference (ECTC)*, 2018.
- [31] Y. Shen, N. Chawla, E. Ege und D. X., „Deformation analysis of lap-shear testing of solder joints,“ *Acta Materialia*, Bd. 53, Nr. 9, p. 2633–2642, 2005.
- [32] K. Aluru, F. Wen und S. Y., „Direct simulation of fatigue failure in solder joints during cyclic shear,“ *Materials & Design*, Bd. 32, Nr. 4, p. 1940–1947, 2011.
- [33] G. Siroky, J. Magnien, D. Melinc, E. Kozeschnik, D. Kieslinger, E. Kraker und W. Ecker, „Lap shear test for solder materials: Local stress states and their effect on deformation and damage,“ *Microelectronics Reliability*, Bd. 109, 2020.
- [34] J. Schijve, *Fatigue of Structures and Materials*, Delft: Springer, 2003.
- [35] J. Moverare, M. Segersäll, A. Sato, S. Johansson und R. Reed, „Thermomechanical Fatigue of Single-Crystal Superalloys : Influence of Composition and Microstructure,“ *Superalloys*, pp. 369-377, 2012.
- [36] A. Bhaduri, *Mechanical Properties and Working of Metals and Alloys*, Singapore: Springer, 2018.
- [37] W. Leea, L. Nguyena und G. Selvaduray, „Solder joint fatigue models: review and applicability to chip scale packages,“ *Microelectronics Reliability*, Bd. 40, pp. 231-244, 2000.
- [38] S. van der Zwaag, „Self Healing Materials: An Alternative Approach to 20 Centuries of Materials Science,“ Dordrecht, Netherland, Springer, 2007, pp. 1-18.
- [39] S. van der Zwaag, N. van Dijk, H. Jonkers, S. Mookhoek und W. Sloof, „Selfhealing behaviour in man-made engineering materials: bioinspired but taking into account their intrinsic character,“ *Philosophical Transactions of The Royal Society A Mathematical Physical and Engineering Sciences*, Bd. 367, p. 1689–1704, 2009.
- [40] M. Hager, P. Greil, C. Leyens, S. van der Zwaag und U. Schubert, „Self-Healing Materials,“ *Advanced Materialis*, Bd. 22, pp. 5424-5430, 2010.
- [41] S. van der Zwaag, „Routes and mechanisms towards self healing behaviour in engineering materials,“ *Bulletin of the Polish Academy of Sciences: Technical Sciences*, Bd. 58, Nr. 227, 2010.
- [42] J. Kötteritzsch, U. Schubert und M. Hager, „Triggered and self-healing systems using nanostructured materials,“ *Nanotechnology Reviews*, Bd. 2, Nr. 6, p. 699–723, 2013.
- [43] J. Sobczak und L. Drenchev, *Self-healing materials as biomimetic smart structures*, Poland: Foundry Research Institute, 2014.
- [44] J. Ferguson, B. Schultz und P. Rohatgi, „Self-Healing Metals and Metal Matrix Composites,“ *JOM*, Bd. 66, p. 866–871, 2014.
- [45] M. Hager, S. van der Zwaag und U. Schubert, *Self Healing Materials, Advances in Polymer Science*, Basel, Schweiz: Springer, 2016.
- [46] J. Dahlke, S. Zechel und M. Hager, „How to Design a Self-Healing Polymer: General Concepts of Dynamic Covalent Bonds and Their Application for Intrinsic Healable Materials,“ WILEY, Weinheim, 2008.
- [47] Y. Yang und M. Urban, „Self-Healing of Polymers via Supramolecular Chemistry,“ Wiley, Weinheim, 2018.
- [48] N. Zhong und W. Post, „Self-repair of structural and functional composites with intrinsically self-healing polymer matrices: A review,“ *Composites Part A: Applied Science and Manufacturing*, Bd. 69, pp. 226-239, 2015.
- [49] B. Grabowski und C. Tasan, „Self-Healing Metals,“ in *Self-healing Materials*, Delft, Netherland, Springer, 2016, pp. 387-408.

- [50] S. He, S. van Dijk, N. He, H. van Dijk, E. Schut, S. H. Peekstok, E. Peekstok und S. van der Zwaag, „Thermally activated precipitation at deformation-induced defects in Fe-Cu and Fe-Cu-B-N alloys studied by positron annihilation spectroscopy,“ *PHYSICAL REVIEW B*, Bd. 81, Nr. 9, 2010.
- [51] K. Laha, J. Kyono und N. Shinya, „An advanced creep cavitation resistance Cu-containing 18Cr–12Ni–Nb austenitic stainless steel,“ *Scripta Materialia*, Bd. 56, Nr. 10, pp. 915-918, 2007.
- [52] R. Lumley, A. Morton und I. Polmear, „Enhanced creep performance in an Al–Cu–Mg–Ag alloy through underageing,“ *Acta Materialia*, Bd. 50, Nr. 14, pp. 3597-3608, 2002.
- [53] M. Mahdavi Shahri, R. Alderliesten, S. van der Zwaag und H. Schut, „Postponing crack nucleation in 2024 aluminium alloy by dynamic precipitation from the supersaturated state,“ *Advanced Materials Research*, Bd. 891–892, pp. 1577-1584, 2014.
- [54] P. Rohatgi, „Al-shape memory alloy self-healing metal matrix composite,“ *Materials Science and Engineering: A*, Bd. 619, pp. 73-76, 2014.
- [55] S. White, R. Sottos, P. Geubelle, J. Moore und M. Kessler, „Autonomic healing of polymer composites,“ *Nature*, Bd. 409, p. 794–797, 2001.
- [56] J. Lucci, R. Amano, P. Rohatgi und B. Schultz, „Experiment and Computational Analysis of Self-Healing in an Aluminum Alloy,“ *Conference: ASME 2008 International Mechanical Engineering Congress and Exposition*, pp. pp. 1759-1768, 2009.
- [57] M. Abdollah Zadeh, S. van der Zwaag und S. Garcia, „Self-Healing Corrosion-Protective Sol–Gel Coatings Based on Extrinsic and Intrinsic Healing Approaches,“ in *Self-healing Materials*, Delft, Netherlands, Springer, 2015, pp. 185-218.
- [58] X. Zheng, Y. Shi und K. Lu, „Electro-healing cracks in nickel,“ *Materials Science and Engineering: A*, Bd. 561, pp. 52-59, 2013.
- [59] T. Crompton, Battery Reference Book, Newnes, 2000.
- [60] R. Dougal, L. Gao und Z. Jiang, „Effectiveness analysis of energy reclamation from partially depleted batteries,“ *Journal of Power Sources*, Bd. 140, Nr. 2, pp. 409-415, 2005.
- [61] E. Kozeschnik, „MatCalc,“ [Online]. Available: <https://www.matcalc-engineering.com>. [Zugriff am 22.02.2021].
- [62] N. Saunders und A. Miodownik, CALPHAD (Calculation of Phase Diagrams): A Comprehensive Guide, Pergamon, 1998.
- [63] H. Ipser und A. WATSON, „Cost531,“ [Online]. Available: <https://www.cost.eu/actions/531/#tabs|Name:overview>. [Zugriff am 25.01.2021].
- [64] V. Witusiewicz, U. Hecht, S. Rex und M. Apel, „In situ observation of microstructure evolution in low-melting Bi-In-Sn alloys by light microscopy,“ *Acta Materialia*, Bd. 53, Nr. 13, pp. 3663-3669, 2005.
- [65] D. Zivkovic, I. Katayama, L. Gomidzelovic, D. Manasijevic und R. Novakovic, „Comparative Thermodynamic Study and Phase Equilibria of the Bi-Ga-Sn Ternary System,“ *International Journal of Materials Research*, Bd. 98, Nr. 10, pp. 1025-1030, 2007.
- [66] S. Yoon, J. Soh, H. Lee und B. Lee, „Thermodynamics-aided alloy design and evaluation of Pb-free solder, Sn-Bi-In-Zn system,“ *Acta Materialia*, Bd. 45, Nr. 3, pp. 951-960, 1997.
- [67] Q. Wang, X. Cheng und Y. Li, „Microstructures and Thermal Properties of Sn–Bi–Zn–Ga Alloys as Heat Transfer and Heat Storage Materials,“ *Wuhan University of Technology and Springer-Verlag*, Bd. 34, p. 676–683, 2019.
- [68] C. Yang, S. Zhou, S. Lin und H. Nishikawa, „A Computational Thermodynamics-Assisted Development of Sn-Bi-In-Ga Quaternary Alloys as Low-Temperature Pb-Free Solders,“ *Materials*, Bd. 12, Nr. 4, p. 631, 2019.
- [69] L. Wang und A. Xian, „Density Measurement of Sn-40Pb, Sn-57Bi, and Sn-9Zn by Indirect Archimedean Method,“ *Journal of Electronic Materials*, Bd. 34, p. 1414–1419, 2005.
- [70] G. Siroky, E. Kraker, D. Kieslinger, E. Kozeschnik und W. Ecker, „A micromechanics-based model for liquid-assisted healing,“ *International Journal of Damage Mechanics*, Bd. 30, Nr. 1, pp. 123-144, 20.
- [71] P. Gill, T. Moghadam und B. Ranjbar, „Differential Scanning Calorimetry Techniques: Applications in Biology and Nanoscience,“ *Association of Biomolecular Resource Facilities*, Bd. 21, Nr. 4, p. 167–193, 2010.
- [72] S. Tanaka, „Theory of power-compensated DSC,“ *Thermochimica Acta*, Bd. 210, pp. 67-76, 1992.
- [73] W. Boettinger und J. Perepezko, „DTA and heat-flux DSC measurements of alloy melting and freezing,“ *Methods for Phase Diagram Determination*, pp. 151-221, 2007.

- [74] G. Höhne, W. Hemminger und H. Flammersheim, *Differential Scanning Calorimetry*, Berlin: Springer, 2003.
- [75] „Plastics- Differential scanning calorimetry“. Patent EN ISO 11357-1:2016, 2016.
- [76] R. Bürgel, „Zugbelastung und Druckbelastung,“ in *Festigkeitslehre und Werkstoffmechanik Band 1*, Wiesbaden, Vieweg, 2005, pp. 13-43.
- [77] J. Davis, *Tensile Testing*, ASM International, 2004.
- [78] P. G. Kossakowski, „Influence of Initial Porosity on Strength Properties of S235JR Steel at Low Stress Triaxiality,“ *Archives of Civil Engineering*, Bd. 58, Nr. 3, pp. 293-308, 2012.
- [79] D. Yalcin, „How do different specimen geometries affect tensile test results?,“ *Project: ADMET Materials Testing*, 2017.
- [80] „www.nuclear-power.net,“ [Online]. Available: <https://www.nuclear-power.net/nuclear-engineering/materials-science/material-properties/toughness/>. [Zugriff am 22 01 2021].
- [81] C. Yang, S. Zhou, S. Lin und N. H., „A Computational Thermodynamics-Assisted Development of Sn-Bi-In-Ga Quaternary Alloys as Low-Temperature Pb-Free Solders,“ *Materials*, Bd. 12, Nr. 631, 2019.
- [82] C. Handwerker, U. Kattner und K. Moon, „Fundamental Properties of Pb-Free,“ in *Lead-Free Soldering*, Boston, Springer, 2006, pp. 21-69.
- [83] Y. Shu, W. Hu, Z. Zhao und L. Wang, „Anomalous melting behavior of polycrystalline bismuth quenched at high temperature and high pressure,“ *Materials Letters*, Bd. 168, pp. 36-39, 2016.
- [84] R. Ritchie, „Mechanisms of fatigue-crack propagation in ductile and brittle solids,“ *Fatigue & Fracture of Engineering Materials & Structures*, Bd. 100, Nr. 55, pp. 1-16, 1999.
- [85] P. Paris und F. Erdogan, „A Critical Analysis of Crack Propagation Laws,“ *Journal of Basic Engineering*, Bd. 85, p. 528–534, 1963.
- [86] Q. Li, N. Ma und Y. Lei, „Characterization of Low-Melting-Point Sn-Bi-In Lead-Free Solders,“ *Journal of ELECTRONIC MATERIALS*, Bd. 45, Nr. 11, pp. 5800-5810, 2006.
- [87] N. van Dijk und S. van der Zwaag, „Self-Healing Phenomena in Metals,“ *Advanced Material Interfaces*, Bd. 5, Nr. 11, 2018.
- [88] J. Kim und H. Kim, „Thermally-triggered Dual In-situ Self-healing Metallic Materials,“ *Scientific Reports (nature research)*, Bd. 8, Nr. 1, pp. 2-11, 2018.
- [89] V. Kilicli, X. Yan, N. Salowitz und P. Rohatgi, „Recent Advancements in Self-Healing Metallic Materials and Self-Healing Metal Matrix Composites,“ *The Journal of The Minerals*, Bd. 70, p. 846–854, 2018.
- [90] G. Siroky, E. Kraker, J. Rosc, D. Kieslinger, R. Brunner, S. van der Zwaag, E. Kozeschnik und W. Ecker, „Analysis of Sn-Bi Solders: X-ray Micro Computed Tomography Imaging and Microstructure Characterization in Relation to Properties and Liquid Phase Healing Potential,“ *Materials (MDPI)*, Bd. 14, Nr. 1, 2021.
- [91] D. Ye, C. Du, M. Wu und Z. Lai, „Microstructure and mechanical properties of Sn-xBi solder alloy,“ *Journal of Materials Science: Materials in Electronics*, Bd. 26, p. 3629–3637, 2015.
- [92] G. Siroky, „Modelling and experiments of liquid phase healing in solder alloys,“ TU Wien, 2021.

## List of figures

Figure 1: Typical SMD component mounted on a PCB with a rigid lap joint .....	1
Figure 2: Graphical classification of soldering processes [DIN ISO 857-2:2005-A.1].....	4
Figure 3: Graphical classification of brazing (and high temperature soldering) processes [DIN ISO 857-2:2005-A.1].....	5
Figure 4: Plated through-hole, clinched lead; Taken from [25], page 29 .....	6
Figure 5: Compliant surface mount butt joint; Taken from [25], page 39.....	7
Figure 6: Illustration of CTE mismatch during application .....	8
Figure 7: Permanent damage, due to CTE fatigue; Taken from [28], page 6.....	9
Figure 8: Illustration of fatigue damage due to clamped expanding PCB board .....	9
Figure 9: Different lap shear geometries; Taken from [33].....	10
Figure 10: Temperature-strain cycles for different TMF tests; Taken from [35] .....	11
Figure 11: S-N diagram with marked LCF/HCF; reproduced from [34].....	12
Figure 12: Completely reversed stress cycle; Inspired by [36], page 320 .....	13
Figure 13: Stress alternating between tension and compression; Inspired by [36], page 320.....	13
Figure 14: Stress alternating between tension and no stress; Inspired by [36], page 320.....	13
Figure 15: Stress alternating between higher and lower tension; Inspired by [36], page 320.....	13
Figure 16: Influencing factors of cyclic fatigue.....	14
Figure 17: Schematic stress-strain loop of a high-stress amplitude cycle after the first application of $\sigma_{max}$ ; Reproduced from [34], page 146 .....	15
Figure 18: Evolution of the crack growth, due to mechanical fatigue; Taken from [34], page 218.....	15
Figure 19: Total strain vs. number of cycle equation is a combination of the Coffin Manson and Basquin equation; Inspired by [37], page 235 .....	17
Figure 20: Cyclic hardening; Taken from [34], page 163.....	20
Figure 21: Cyclic softening; Taken from [34], page 163 .....	20
Figure 22: Plastic shake-down, or stress relaxation; Taken from [34], page 166.....	21
Figure 23: Cyclic creep; Taken from [34], page 166 .....	21
Figure 24: Self-healing mechanisms ordered by length scale; Taken from [49], page 390.....	23
Figure 25: Different acuity levels of test temperatures defined by automotive producers.....	27
Figure 26: Periodic table of elements with highlighted potential alloying elements .....	29
Figure 27: Potential alloying elements for lead-free solder and their melting temperature with indicated maximal temperature area for low-temperature applications; The black line marks the maximum temperature for major constituents.....	29
Figure 28: In-situ heating experiment of Sn-30 wt%-Bi. a) Initial microstructure, indicating a 10 $\mu\text{m}$ void (dashed .....	30
Figure 29: Heat-flux-DSC furnace with reference on the left and sample on the right .....	31
Figure 30: Power-compensated DSC; Taken from [75], page 15.....	32
Figure 31: Heat-flux DSC; Taken from [75], page 14.....	32
Figure 32: Determination of the starting temperature of an event when smearing occurs, with $\phi_r$ being the true heat flow into the sample, the measured temperature $T_m$ , the thermal conductivity between the crucible and the sample $L$ , the extrapolated peak onset temperature $T_e$ and the temperature, at the sample temperature and the measured temperature coincide, $T_{limit}$ ; Taken from [74], page 136 .....	32
Figure 33: - - - -: Hypothetic (measured) curves of the individual events at $T_1$ , $T_2$ ; -: Recorded (superposed) curve measured for two successive events; Taken from [74], page 131.....	32
Figure 34: Evolution of a failing ductile sample under uniaxial tensile stress. Taken from [78], page 294.....	34
Figure 35: Stress/strain diagram of a ductile material; Taken from [79], page 3 .....	35
Figure 36: Stress/strain curve of different materials; Taken from [76], page 18.....	35
Figure 37: Stress/strain curve of a brittle and ductile material, respectively; Taken from [80].....	35
Figure 38: Enamel crucible on the inductive heating plate with high-temperature Perspex lid on, gas inlet and thermo-gauge in Copper block to solidify remaining solder material. ....	36
Figure 39: 6 solid solder samples after molding process in a high-temperature silicone mold.....	37
Figure 40: Dimensions of a solder sample; Measurements in mm.....	37
Figure 41: A solder sample before (upper) and after (lower) machining in its final form. ....	38
Figure 42: Milled block for grinding the samples in dog bone shape; Measurements in mm.....	38
Figure 43: a) Complete DSC sample; b) simplified structure of a DSC sample.....	39
Figure 44: Heating, cooling rates, and isothermal steps in a DSC run .....	39



Figure 45: Typical DSC measurements, including the settling cycle (cycle_1) and the two measurement cycles (cycle_2 and cycl_3).	39
Figure 46: Damaged solder sample embedded in slow curing resin after grinding and polishing.	40
Figure 47: sample holder with three chucked samples	41
Figure 48: optical microscopy sample on modeling clay in alignment press.	41
Figure 49: Dog bone shaped solder sample	41
Figure 50: Keyence VHX 6000 digital microscope	42
Figure 51: Attachment of 6 samples on a conductive plate in the SEM microscope	43
Figure 52: Typical S.E. image of a Sn37Bi4In-sample after heat treatment	43
Figure 53: Typical BSE image of a Sn37Bi4In-sample after heat treatment with 320 times magnification	43
Figure 54: Representative EDX analysis of a Sn37Bi4In-sample after heat treatment with analysis table	43
Figure 55: Components for the healing protocol	45
Figure 56: Oven used for long-term stability test on air; Insert shows tile with samples.	46
Figure 57: Clamped sample in Zwick/Roeller Z250 tensile/compression machine	46
Figure 58: Phase fraction diagram of the Bi24In alloy calculated with MatCalc v6.03 using the Cost 531 database	48
Figure 59: Bi/In binary phase diagram calculated with ThermoCalc ( <a href="https://thermocalc.com">https://thermocalc.com</a> ) using the Cost 531 database	49
Figure 60: In-Sn binary phase diagram calculated with ThermoCalc ( <a href="https://thermocalc.com">https://thermocalc.com</a> ) using the Cost 531 database	49
Figure 61: Bi-Sn binary phase diagram calculated with ThermoCalc ( <a href="https://thermocalc.com">https://thermocalc.com</a> ) using the Cost 531 database	50
Figure 62: Liquid surface projection of the Sn/Bi/In ternary, calculated with MatCalc v6.03 using the MatCalc solder database	51
Figure 63: The ternary system Sn/Bi/In calculated with MatCalc v6.03 using the MatCalc solder database; View on the In = 0 plane.	52
Figure 64: The ternary system Sn/Bi/In calculated with MatCalc v6.03 using the MatCalc solder database; View on the Sn = 0 plane.	52
Figure 65: The ternary system Sn/Bi/In calculated with MatCalc v6.03 using the MatCalc solder database; View on the Bi = 0 plane.	52
Figure 66: The ternary system Sn/Bi/In calculated with MatCalc v6.03 using the MatCalc solder database. View on the $T_{liq}$ plane	53
Figure 67: The ternary system Sn/Bi/In calculated with MatCalc v6.03 using the MatCalc solder database. View on the $T_{sol}$ plane.	53
Figure 68: Picture of the microstructure of Sn37Bi4In taken with SEM Philips XL30	54
Figure 69: Phase fraction diagram of the SN37Bi4In alloy between 25 °C and 170 °C.	54
Figure 70: Chemical composition of the liquid phase of the SN37Bi4In alloy between 25 °C and 170 °C	54
Figure 71: Chemical composition of the BCT_A5 phase of the SN37Bi4In alloy between 25 °C and 170 °C.	55
Figure 72: Chemical composition of the RHOMBO_A7 phase of the SN37Bi4In alloy between 25 °C and 170 °C	55
Figure 73: Chemical composition of the INSN_GAMMA phase of the SN37Bi4In alloy between 25 °C and 170 °C	55
Figure 74: Picture of the microstructure of Sn37Bi4In with 80 times microscope magnification	56
Figure 75: Picture of the microstructure of Sn37Bi4In with 320 times microscope magnification	56
Figure 76: Picture of the microstructure of Sn37Bi4In with 1280 times microscope magnification	57
Figure 77: DSC test of the Sn37Bi4In solder alloy with a heating rate of 10K/min; The heat flow (hf) (grey curve) is superimposed with the slope of the hf measurement (green curve) and the comparison of the calculated (dashed black curve) and estimated liquid phase evolution (blue curve).	58
Figure 78: Liquid phase fraction at 120 °C, 130 °C, and 140 °C.	60
Figure 79: Cooling curve of the different temperatures 120 °C, 130 °C, and 140 °C	61
Figure 80: Cooling curve in the silicon mold during casting process with zoomed-in inlay of the point of stagnation	62
Figure 81: SE image of an "as cast"-sample with 80 times magnification	62
Figure 82: BSE image of an "as cast"-sample with 80 times magnification	62
Figure 83: SE image of an "as cast"-sample with 320 times magnification	62
Figure 84: BSE image of an "as cast"-sample with 320 times magnification	62
Figure 85: SE image of an "as cast"-sample with 1280 times magnification	63
Figure 86: BSE image of an "as cast"-sample with 1280 times magnification	63
Figure 87: EDX analysis of an "as-cast" sample	63

Figure 88: SE image of a „120 °C“-sample with 80 times magnification.....	64
Figure 89: BSE image of a „120 °C“-sample with 80 times magnification .....	64
Figure 90: SE image of a „120 °C“-sample with 320 times magnification .....	64
Figure 91: BSE image of a „120 °C“-sample with 320 times magnification .....	64
Figure 92: SE image of a „120 °C“-sample with 1280 times magnification.....	64
Figure 93: BSE image of a „120 °C“-sample with 1280 times magnification .....	64
Figure 94: EDX analysis of a "120 °C"-sample .....	65
Figure 95: BSE image of the cross-section of a „120 °C“-sample with 320 times magnification .....	65
Figure 96: BSE image of the top side cross-section of a „130 °C“-sample with 80 times magnification.....	66
Figure 97: BSE image of the top side cross-section of a „130 °C“-sample with 320 times magnification.....	66
Figure 98: BSE image of the bottom side cross-section of a „130 °C“-sample with 80 times magnification .....	66
Figure 99: BSE image of the bottom side cross-section of a „130 °C“-sample with 320 times magnification .....	66
Figure 100: SE image of the top side of a „130 °C“-sample with 80 times magnification.....	67
Figure 101: BSE image of the top side of a „130 °C“-sample with 80 times magnification .....	67
Figure 102: SE image of the top side of a „130 °C“-sample with 320 times magnification.....	67
Figure 103: BSE image of the top side of a „130 °C“-sample with 320 times magnification showing bulking Bi areas.....	67
Figure 104: SE image of the top side of a „130 °C“-sample with 1280 times magnification with typical rectangular Bi crystals in between the homogenous matrix.....	67
Figure 105: BSE image of the top side of a „130 °C“-sample with 1280 times magnification with typical rectangular Bi crystals in between the homogenous matrix.....	67
Figure 106: EDX analysis of the top side of a "130 °C"-sample .....	68
Figure 107: SE image of the bottom side of a "130 °C"-sample with 80 times magnification .....	69
Figure 108: BSE image of the bottom side of a "130 °C"-sample with 80 times magnification .....	69
Figure 109: SE image of the bottom side of a "130 °C"-sample with 320 times magnification .....	69
Figure 110: BSE image of the bottom side of a "130 °C"-sample with 320 times magnification .....	69
Figure 111: SE image of the bottom side of a "130 °C"-sample with 1280 times magnification .....	69
Figure 112: BSE image of the bottom side of a "130 °C"-sample with 1280 times magnification .....	69
Figure 113: EDX analysis of the bottom side of a "130 °C"-sample.....	70
Figure 114: BSE image of the top side cross-section of a "140 °C"-sample with 80 times magnification.....	70
Figure 115: BSE image of the top side cross-section of a "140 °C"-sample with 320 times magnification.....	70
Figure 116: BSE image of the bottom side cross-section of a "140 °C"-sample with 80 times magnification .....	71
Figure 117: BSE image of the bottom side cross-section of a "140 °C"-sample with 320 times magnification ....	71
Figure 118: SE image of the top side of a „140 °C“-sample with 80 times magnification.....	71
Figure 119: BSE image of the top side of a „140 °C“-sample with 80 times magnification .....	71
Figure 120: SE image of the top side of a „140 °C“-sample with 320 times magnification.....	72
Figure 121: BSE image of the top side of a „140 °C“-sample with 320 times magnification .....	72
Figure 122: SE image of the top side of a „140 °C“-sample with 1280 times magnification.....	72
Figure 123: BSE image of the top side of a „140 °C“-sample with 1280 times magnification .....	72
Figure 124: EDX analysis of the top side of a "140 °C"-sample .....	72
Figure 125: SE image of the bottom side of a „140 °C“-sample with 80 times magnification .....	73
Figure 126: BSE image of the bottom side of a „140 °C“-sample with 80 times magnification .....	73
Figure 127: SE image of the bottom side of a „140 °C“-sample with 320 times magnification .....	73
Figure 128: BSE image of the bottom side of a „140 °C“-sample with 320 times magnification .....	73
Figure 129: SE image of the bottom side of a „140 °C“-sample with 1280 times magnification .....	74
Figure 130: BSE image of the bottom side of a „140 °C“-sample with 1280 times magnification.....	74
Figure 131: EDX analysis of the bottom side of a "140 °C"-sample.....	74
Figure 132: Comparison of heat-treated and untreated reference samples (Sn37Bi4In) regarding Young's modulus.....	75
Figure 133: Comparison of heat-treated and untreated reference samples (Sn37Bi4In) regarding UTS.....	75
Figure 134: Comparison of heat-treated and untreated reference samples (Sn37Bi4In) regarding uniform elongation .....	75
Figure 135: Comparison of heat-treated and untreated reference samples (Sn37Bi4In) regarding toughness ...	75
Figure 136: Tensile test of the Sn37Bi4In and heat-treated samples ( @120 °C, @130 °C, @140 °C) .....	76
Figures 137: Comparison of the surfaces after heat treating at different temperatures with 1280 times magnification .....	77
Figure 138: Phase fraction diagram of the Sn37Bi4In, Sn39Bi4In(+2Bi), Sn35Bi4In(-2Bi), Sn37Bi6In(+2In) and (+2In) alloys between 25 °C and 200 °C; conducted with MatCalc 6.03 and the MatCalc solder database.....	80

Figure 139: Tensile test of the Sn37Bi4In, Sn39Bi4In, Sn35Bi4In, Sn37Bi6In, and Sn37Bi2In alloys.....	81
Figure 140: Phase fraction diagram of the Sn37Bi4In, Sn39Bi4In(+2Bi), and Sn35Bi4In(-2Bi) alloys between 25 °C and 200 °C; conducted with MatCalc 6.03 and MatCalc solder database. ....	82
Figure 141: Picture of the microstructure of Sn39Bi4In with 80 times magnification.....	82
Figure 142: Picture of the microstructure of Sn39Bi4In with 320 times magnification .....	82
Figure 143: Picture of the microstructure of Sn39Bi4In with 1280 times magnification .....	83
Figure 144: Picture of the microstructure of Sn35Bi4In with 80 times magnification.....	83
Figure 145: Picture of the microstructure of Sn35Bi4In with 320 times magnification .....	83
Figure 146: Picture of the microstructure of Sn35Bi4In with 1280 times magnification .....	84
Figure 147: Phase fraction diagram of the Sn37Bi4In, Sn37Bi6In(+2In), and Sn37Bi2In(+2In) alloys between 25 °C and 200 °C; conducted with MatCalc 6.03 and MatCalc solder database. ....	85
Figure 148: Picture of the microstructure of Sn37Bi6In with 80 times magnification.....	86
Figure 149: Picture of the microstructure of Sn37Bi6In with 320 times magnification .....	86
Figure 150: Picture of the microstructure of Sn37Bi6In with 1280 times magnification .....	86
Figure 151: Picture of the microstructure of Sn37Bi2In with 80 times magnification.....	87
Figure 152: Picture of the microstructure of Sn37Bi2In with 320 times magnification .....	87
Figure 153: Picture of the microstructure of Sn37Bi2In with 1280 times magnification .....	87
Figure 154: Comparison of the influence of alloying elements regarding Young's modulus .....	88
Figure 155: Comparison of the influence of alloying elements regarding UTS .....	88
Figure 156: Comparison of the influence of alloying elements regarding uniform elongation .....	88
Figure 157: Comparison of the influence of alloying elements regarding toughness .....	88
Figures 158: Comparison of the influence of the alloying elements on the microstructure with 1280 times magnification. ....	89
Figure 159: BSE image of the top surface after 10 minutes of aging at 120 °C .....	93
Figure 160: BSE image of the top surface after 1 day of aging at 120 °C .....	93
Figure 161: BSE image of the bottom surface after 1 day of aging at 120 °C.....	93
Figure 162: BSE image of the top surface after 5 days of aging at 120 °C.....	93
Figure 163: BSE image of the bottom surface after 5 days of aging at 120 °C .....	93
Figure 164: BSE image of the top surface after 10 days of aging at 120 °C.....	94
Figure 165: BSE image of the bottom surface after 10 days of aging at 120 °C .....	94
Figure 166: BSE image of the top surface after 20 days of aging at 120 °C.....	94
Figure 167: BSE image of the bottom surface after 20 days of aging at 120 °C .....	94
Figure 168: BSE image of the top surface after 40 days of aging at 120 °C.....	94
Figure 169: BSE image of the bottom surface after 40 days of aging at 120 °C .....	94
Figure 170: Tensile test of the aged samples alloys (10min; 1day; 5days, 10days; 20 days; 40days) .....	95
Figure 171: Influence of aging duration at 120 °C on Young's modulus .....	96
Figure 172: Influence of aging duration at 120 °C on UTS .....	96
Figure 173: Influence of aging duration at 120 °C on uniform elongation.....	96
Figure 174: Influence of aging duration at 120 °C on toughness .....	96
Figure 175: Tensile test conducted with 0.05 mm/s as guidance for determining loading parameters of the loading protocol with indicated strain level during cyclic loading (red line).....	98
Figure 176: One cycle of the mechanical loading protocol conducted with the Zwick/Roell Z250 tensile test machine.....	99
Figure 177: "Force over time"- diagram of a Sn37Bi4In sample .....	100
Figure 178: Definite cycles of a „force over displacement"-diagram (hysteresis).....	101
Figure 179: Determination of the stiffness in the tensile and compression regimes .....	101
Figure 180: Evolution of $E_c$ and the relation $E_t E_c$ for fatigue evaluation .....	101
Figure 181: Sample 10 after 64 cycles.....	102
Figure 182: The crack in the sample propagates primarily in the Bi-rich RHOMBO_A7 phase .....	103
Figure 183: Tensile test of "as-cast" and "cyclic loaded" samples compared to different healing states (120 °C, 130 °C, and 140 °C).....	104
Figure 184: Comparison of heat-treated, damaged, and "as cast" samples regarding Young's modulus.....	104
Figure 185: Comparison of heat-treated, damaged, and "as cast" samples regarding UTS.....	104
Figure 186: Comparison of heat-treated, damaged, and "as cast" samples regarding uniform elongation .....	105
Figure 187: Comparison of heat-treated, damaged, and "as cast" samples regarding toughness .....	105
Figure 188: Surface of the top surface after one day of aging at 120 °C .....	125
Figure 189: Surface of the bottom surface after one day of aging at 120 °C.....	125
Figure 190: Surface of the top surface after 5 days of aging at 120 °C.....	125

Figure 191: Surface of the bottom surface after 5 days of aging at 120 °C .....	125
Figure 192: Surface of the top surface after 10 days of aging at 120 °C.....	125
Figure 193: Surface of the bottom surface after 10 days of aging at 120 °C .....	125
Figure 194: Surface of the top surface after 20 days of aging at 120 °C.....	126
Figure 195: Surface of the bottom surface after 20 days of aging at 120 °C .....	126
Figure 196: Surface of the top surface after 40 days of aging at 120 °C.....	126
Figure 197: Surface of the bottom surface after 40 days of aging at 120 °C .....	126

## List of tables

Table 1: Influencing factors of cyclic fatigue	12
Table 2: Overview of solder joint fatigue models; Reproduced from Lee et al. [37]	18
Table 3: Typical temperature ranges, corresponding designations and applications	26
Table 4: Elements included in the COST 531 database	28
Table 5: Grinding Process of embedded samples for optical and SEM microscopy	40
Table 6: Parameters for the loading protocol conducted with the Zwick/Roell Z250 tensile test machine	44
Table 7: Three different healing protocols, including temperatures of the set heating temperature, the logged temperature near the sample, and healing duration	45
Table 8: Relevant properties for solder applications	50
Table 9: Significant values during the cooling process	61
Table 10: Important tensile test values of the Sn37Bi4In compared to samples heat-treated at different temperatures. (only suitable for comparative purposes)	75
Table 11: Important tensile test values of the Sn37Bi4In, Sn39Bi4In(+2Bi), Sn35Bi4In(-2Bi), Sn37Bi6In(+2In) and Sn37Bi2In(+2In) alloys. (only suitable for comparative purposes)	88
Table 12: Composition and standard deviation of the top surfaces	92
Table 13: Composition and standard deviation of the bottom surfaces	92
Table 14: Important tensile test values of the aged samples alloys (10min; 1day; 5days, 10days; 20 days; 40days) (only suitable for comparative purposes)	95
Table 15: Example of a Sn37Bi4In sample mechanically cyclic loaded.	99
Table 16: Summary of ten cyclic loaded samples regarding the inflicted crack length	102
Table 17: Important tensile test values of "as-cast" and "cyclically loaded" samples compared to different healing states (120 °C, 130 °C, and 140 °C) (only suitable for comparative purposes)	103

# Appendix

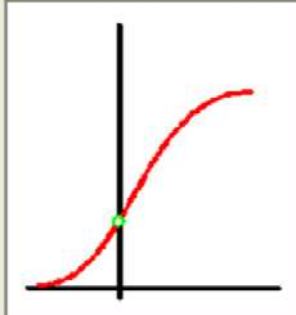
## A. Settings for the tensile test

**Assistent - Vorkraft**

Übersicht:

- Einrichten ✓
- Ergebniswahl ✓
- Toleranzen ✓
- Probendaten ✓
- Vorkraft ✓**
- E-Modul Vorgaben
- Streck- und Dehngrenzen
- Prüfung / Prüfungsende
- LE-Positionen
- Aktionen nach Prüfung
- Dehnungsaufnehmer
- Messwertspeicher
- Parameter fürs Protokoll

Hier parametrisieren Sie die Prüfungsphase bis zur Vorkraft.



Vorkraft 5 N

Vorkraft-Geschwindigkeit 10 mm/min

Vorkraft Haltezeitmodus keine Haltezeit

Zeit bis Vorkraft 60 s

Kraft nullen nach Vorkraft

Nach Erreichen der Vorkraft wird die eigentliche Prüfung begonnen.

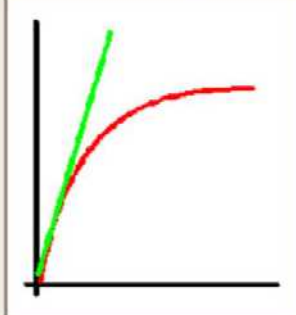
< Zurück Weiter > Beenden Hilfe

**Assistent - E-Modul Vorgaben**

Übersicht:

- Einrichten ✓
- Ergebniswahl ✓
- Toleranzen ✓
- Probendaten ✓
- Vorkraft ✓
- E-Modul Vorgaben ✓**
- Streck- und Dehngrenzen
- Prüfung / Prüfungsende
- LE-Positionen
- Aktionen nach Prüfung
- Dehnungsaufnehmer
- Messwertspeicher
- Parameter fürs Protokoll

Hier parametrisieren Sie die Bestimmung des E-Moduls



Art der E-Modulermittlung Regression

Beginn E-Modulermittlung Dehnung 0,05 %

Ende E-Modulermittlung Dehnung 200 %

E-Modul bei 95% abbrechen ?

Geschwindigkeit E-Modul lagegerecht 0,00025 mm/s

E-Modul per Hystereseschleife

Verschiedene Arten der E-Modulermittlung.

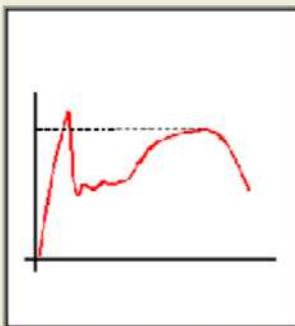
< Zurück Weiter > Beenden Hilfe

### Assistent - Streck- und Dehngrenzen

**Übersicht:**

- Einrichten ✓
- Ergebnisauswahl ✓
- Toleranzen ✓
- Probendaten ✓
- Vorkraft ✓
- E-Modul Vorgaben ✓
- Streck- und Dehngrenze ✓**
- Prüfung / Prüfungsende ✓
- LE-Positionen ✓
- Aktionen nach Prüfung ✓
- Dehnungsaufnehmer ✓
- Messwertspeicher ✓
- Parameter fürs Protokoll ✓

**Eingaben zur der Erfassung von Streck- und Dehngrenzen**



- F max kleiner Fs
- Ende Rp, ReH-Ermittlung  
Dehnung (pla)  %
- Empfindlichkeit Ermittlung Obere Streckgrenze  
Dehnung  %
- Empfindlichkeit Reh in % Kraftabfall  %Fmax
- Geschwindigkeit Rp, ReH  
lagegeregelt  mm/s
- Maximale Fließdehnung  
Dehnung  %
- Ende Fließdehnung Ae (Reh)  %
- Geschwindigkeit im Fließbereich  
lagegeregelt  mm/s

Soll nach einer oberen Streckgrenze nach einem neuen Fmax gesucht werden.

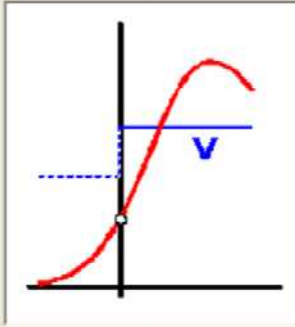
< Zurück
Weiter >
Beenden
Hilfe

### Assistent - Prüfung / Prüfungsende

**Übersicht:**

- Einrichten ✓
- Ergebnisauswahl ✓
- Toleranzen ✓
- Probendaten ✓
- Vorkraft ✓
- E-Modul Vorgaben ✓
- Streck- und Dehngrenze ✓
- Prüfung / Prüfungsende ✓**
- LE-Positionen ✓
- Aktionen nach Prüfung ✓
- Dehnungsaufnehmer ✓
- Messwertspeicher ✓
- Parameter fürs Protokoll ✓

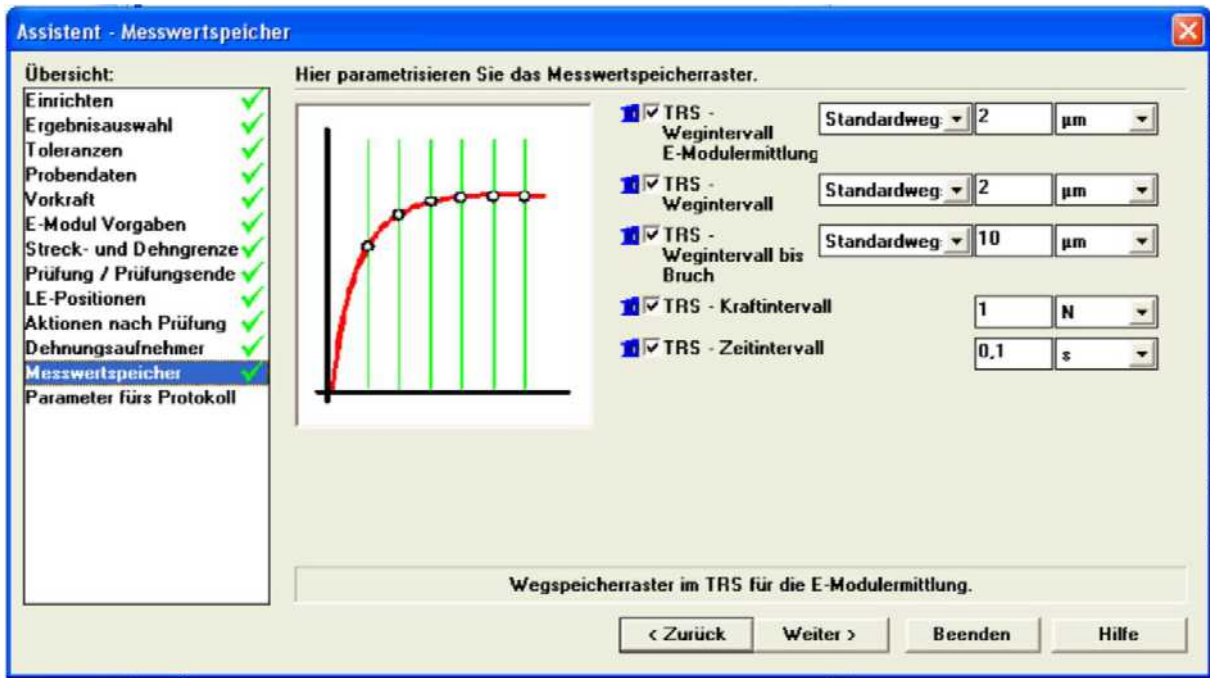
**Eingaben für die Prüfung und die Brucherkennung**



- Prüfgeschwindigkeit  
lagegeregelt  1/min
- Prozent Kraftabfall für Geschwindigkeitsumschaltung  
 %Fmax
- Verzögerung bei Geschwindigkeitsumschaltung
- Kraftabschaltsschwelle  
 %Fmax
- max. zeitlicher Kraftabfall  
 N
- Kraftschwelle für Bruchuntersuchung  
 %Fnom
- Weg nach Bruch  
 mm
- obere Kraftgrenze  
 N

Geschwindigkeit der Fahrtverse bis zum Ende der Prüfung.

< Zurück
Weiter >
Beenden
Hilfe







## B. Ageing effect on the surface microstructure at 120 °C

### Overview of all ageing durations

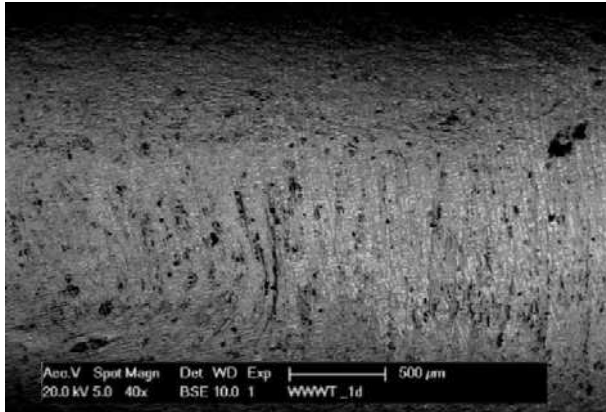


Figure 188: Surface of the top surface after one day of aging at 120 °C

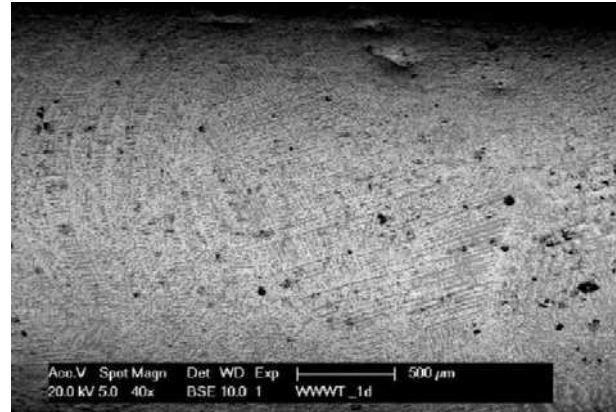


Figure 189: Surface of the bottom surface after one day of aging at 120 °C

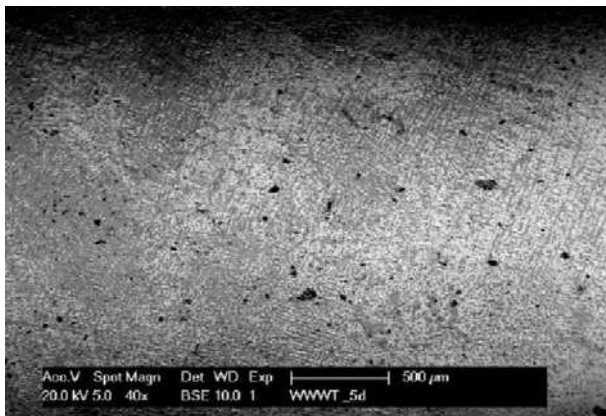


Figure 190: Surface of the top surface after 5 days of aging at 120 °C

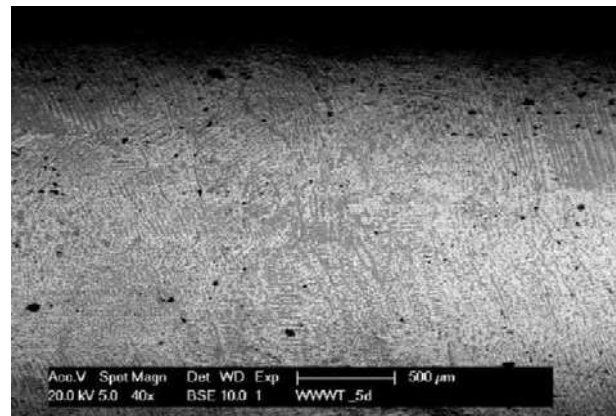


Figure 191: Surface of the bottom surface after 5 days of aging at 120 °C

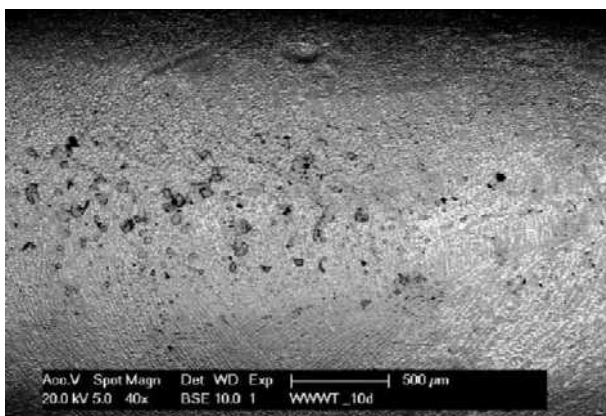


Figure 192: Surface of the top surface after 10 days of aging at 120 °C

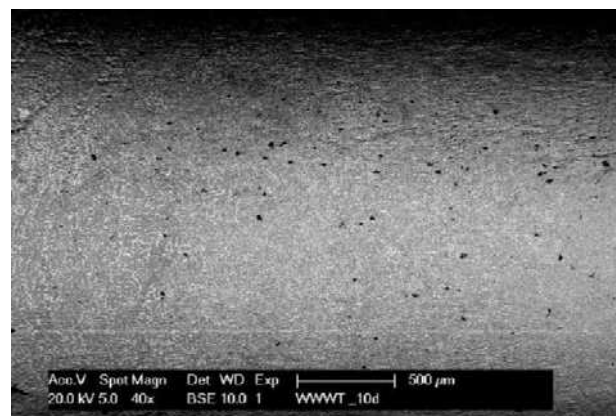


Figure 193: Surface of the bottom surface after 10 days of aging at 120 °C

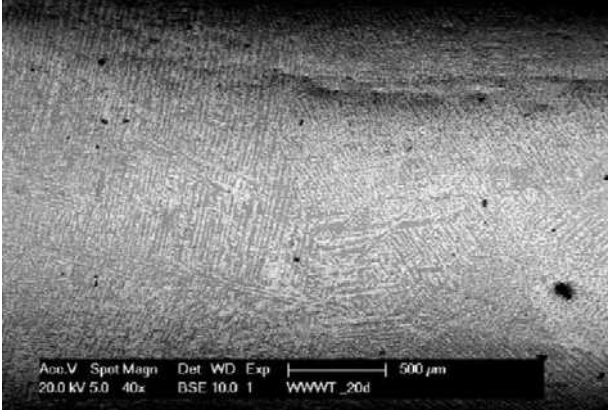


Figure 194: Surface of the top surface after 20 days of aging at 120 °C

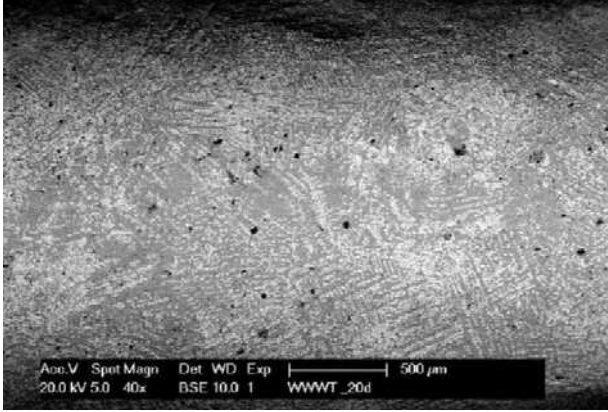


Figure 195: Surface of the bottom surface after 20 days of aging at 120 °C

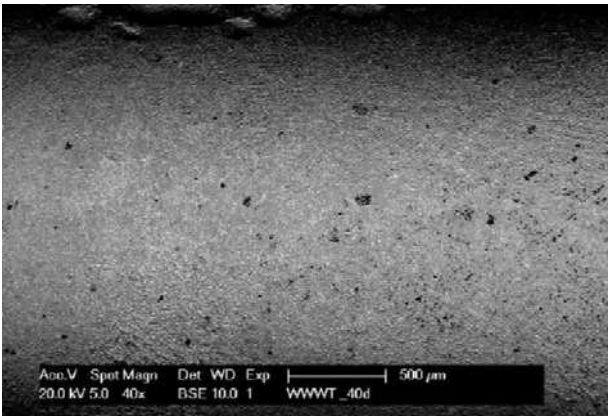


Figure 196: Surface of the top surface after 40 days of aging at 120 °C

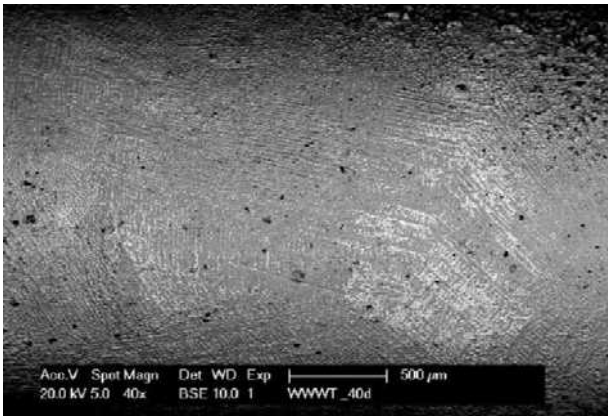
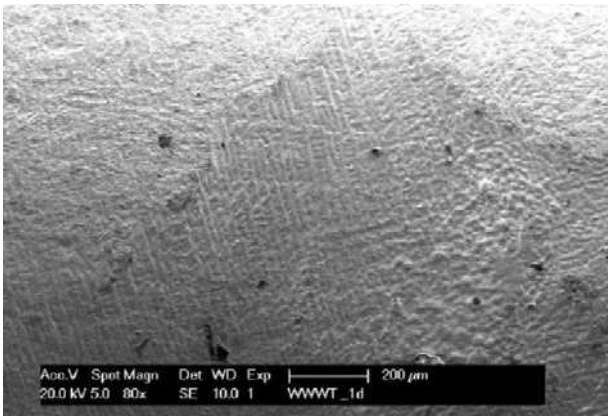
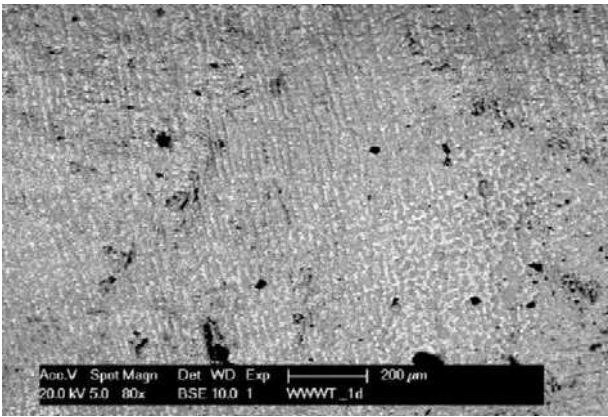
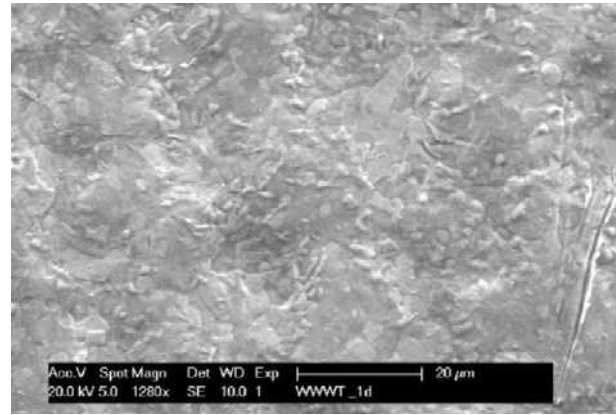
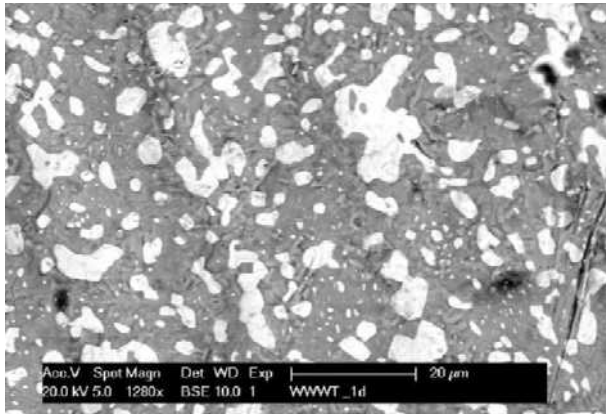
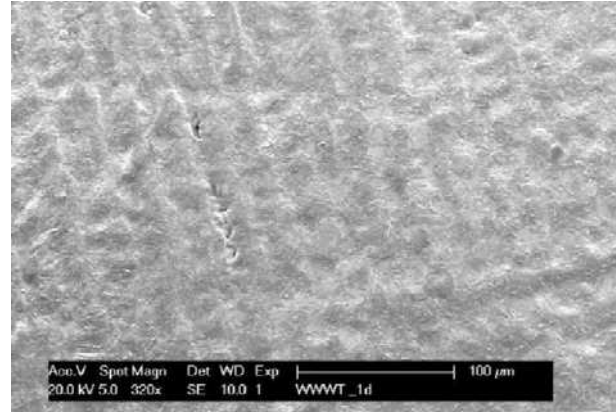
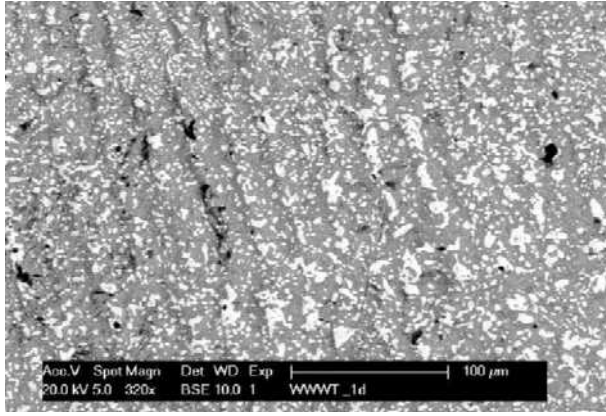


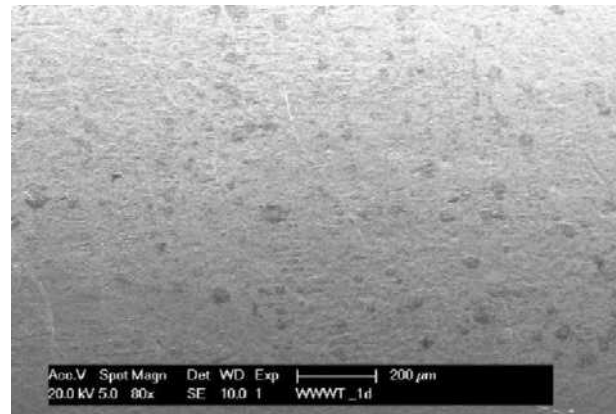
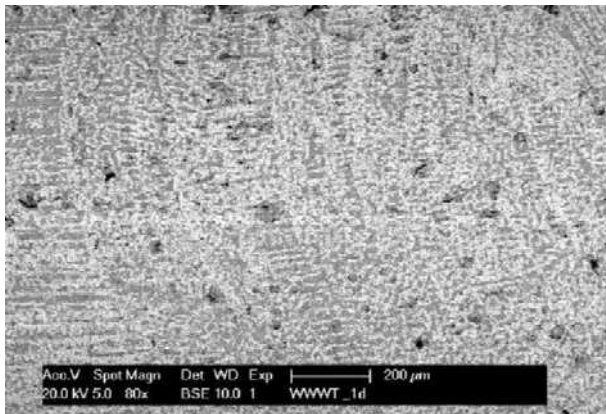
Figure 197: Surface of the bottom surface after 40 days of aging at 120 °C

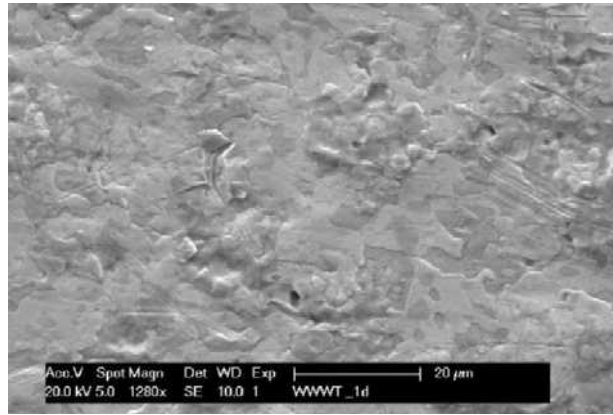
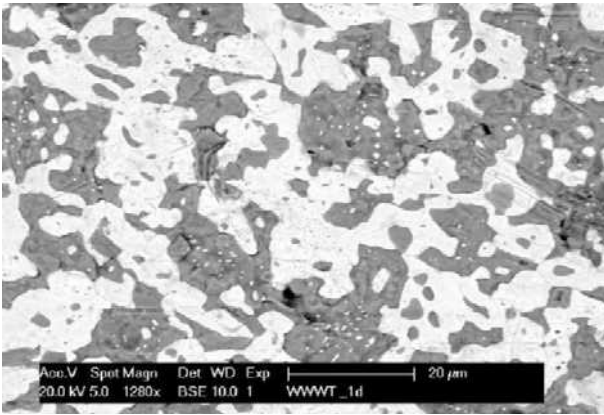
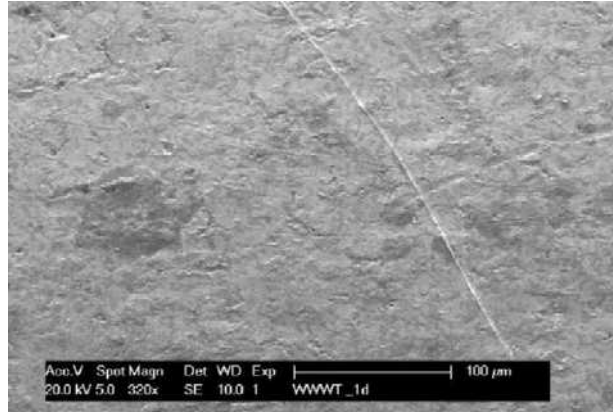
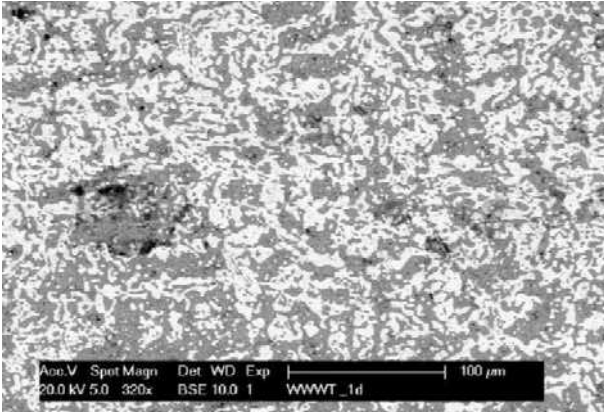
Different magnifications of the top side after 1 day of ageing at 120 °C (BSE images on the left and SE images on the right):



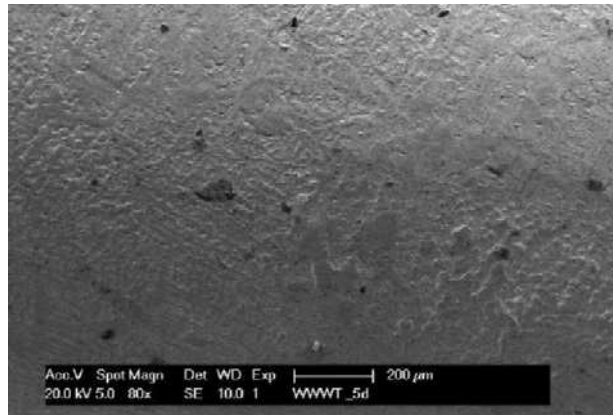
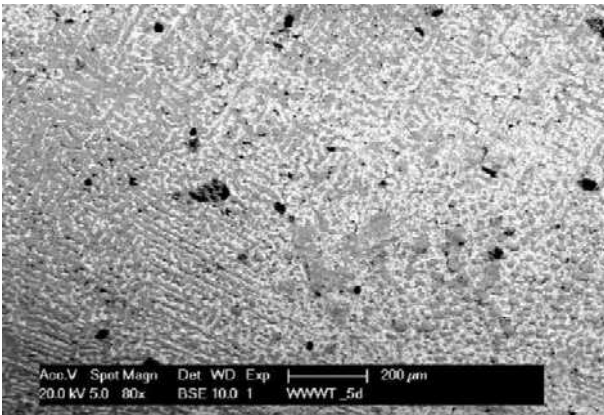


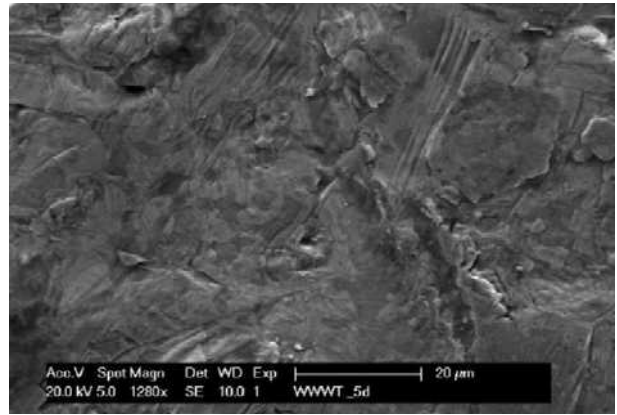
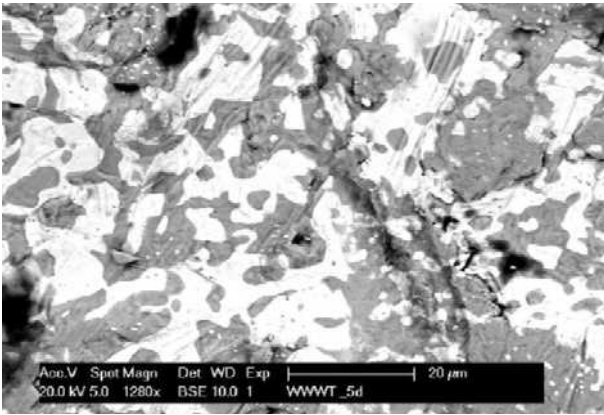
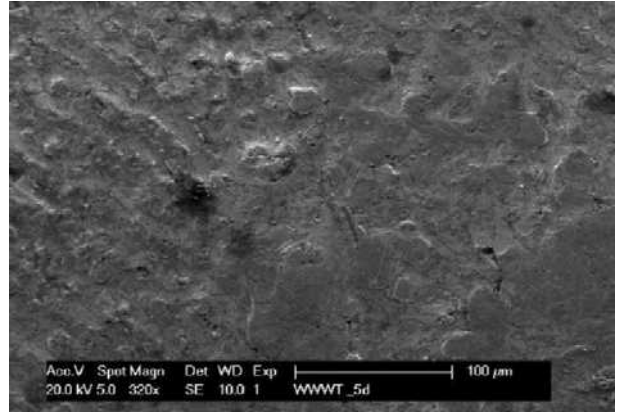
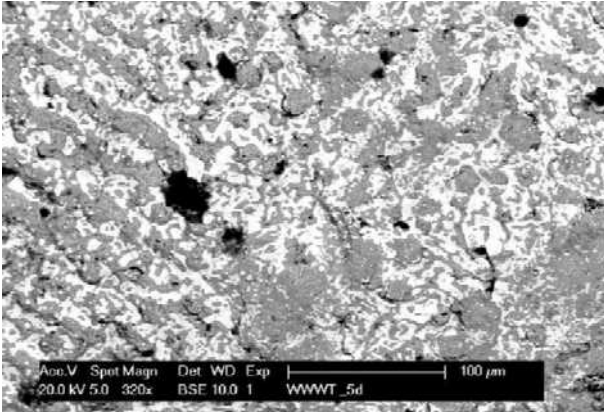
Different magnifications of the bottom side after 1 day of ageing at 120 °C (BSE images on the left and SE images on the right):



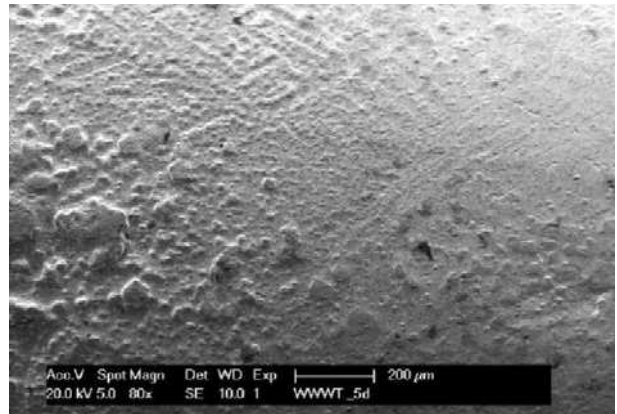
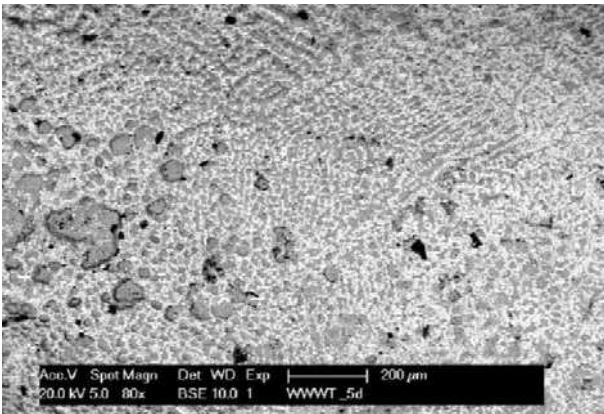


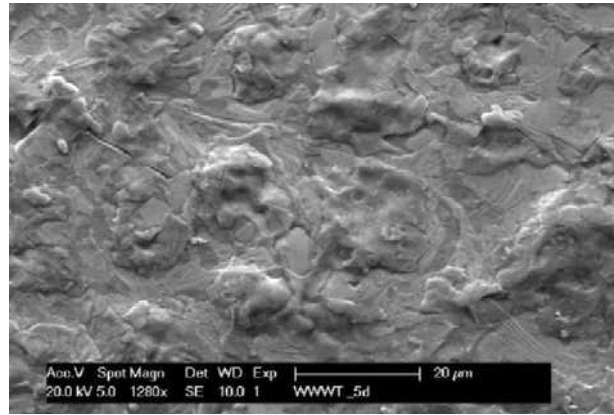
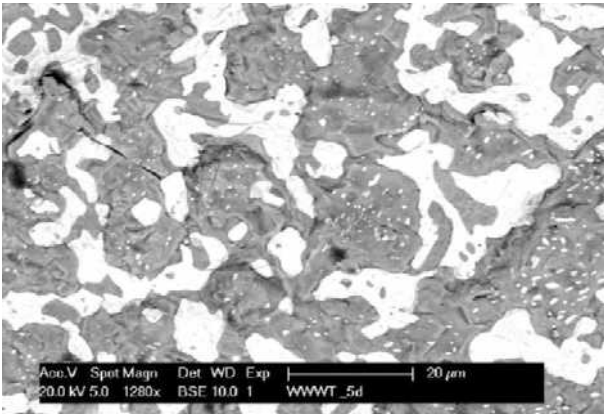
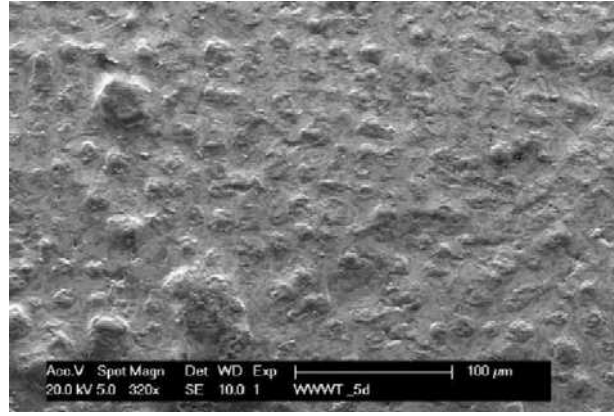
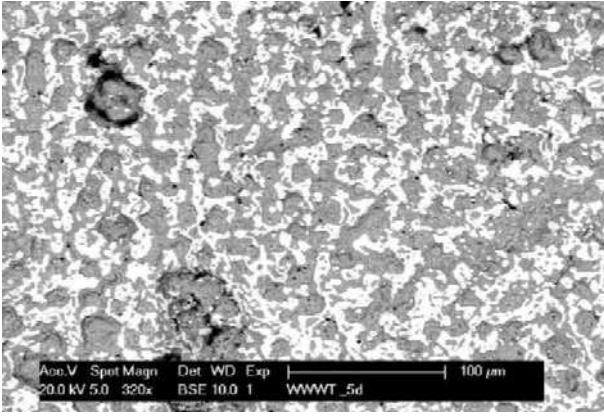
Different magnifications of the top side after 5 days of ageing at 120 °C (BSE images on the left and SE images on the right):



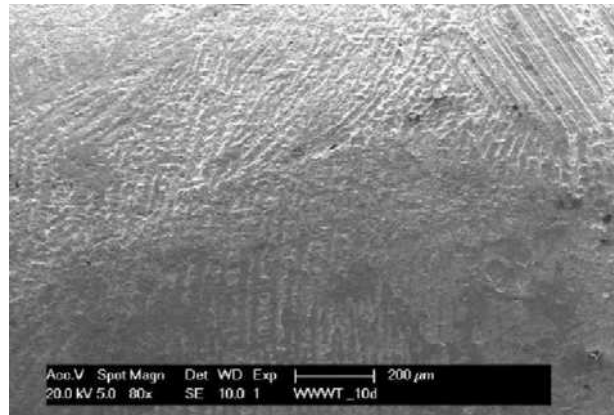
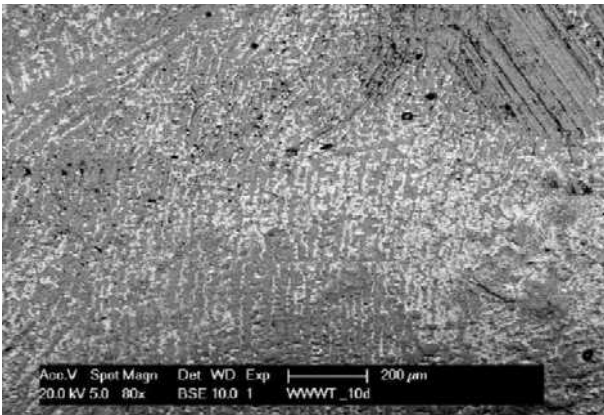


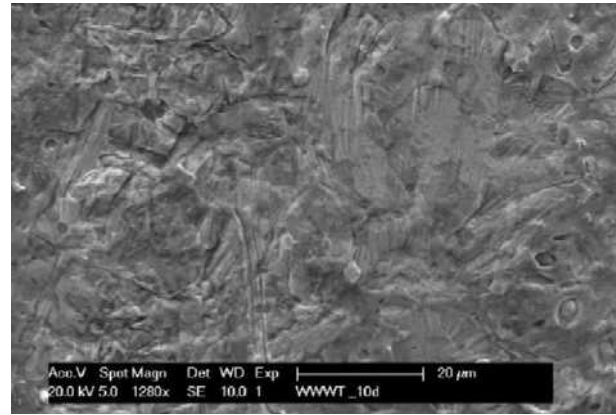
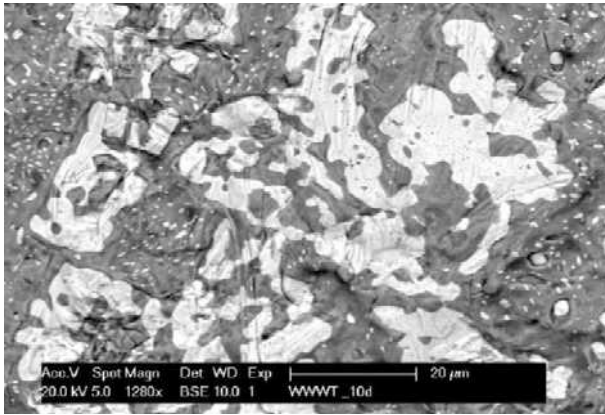
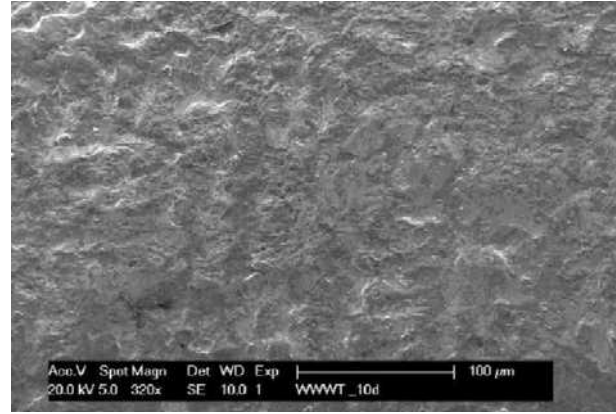
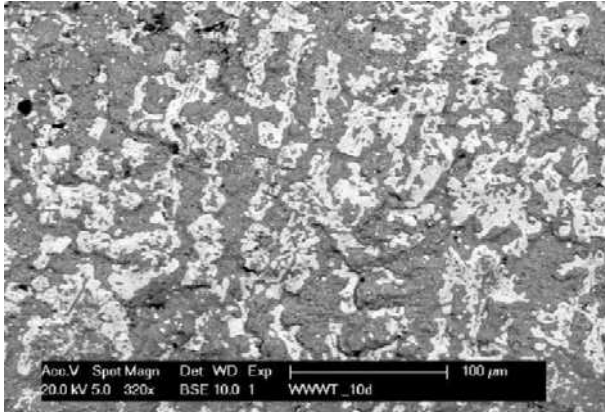
Different magnifications of the bottom side after 5 days of ageing at 120 °C (BSE images on the left and SE images on the right):



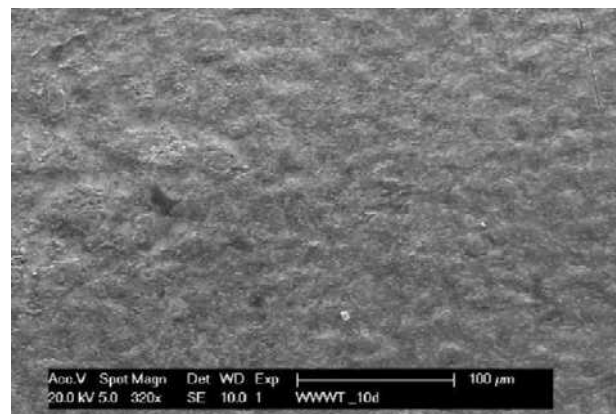
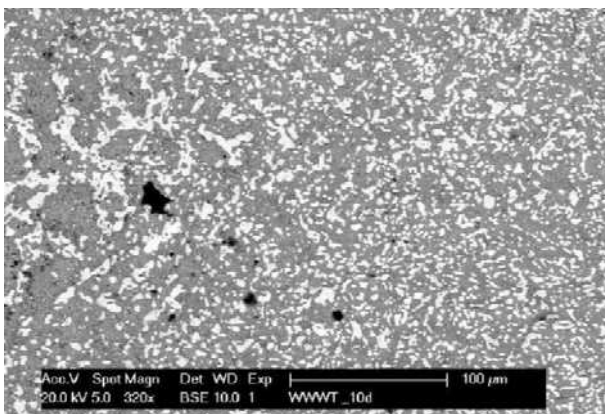
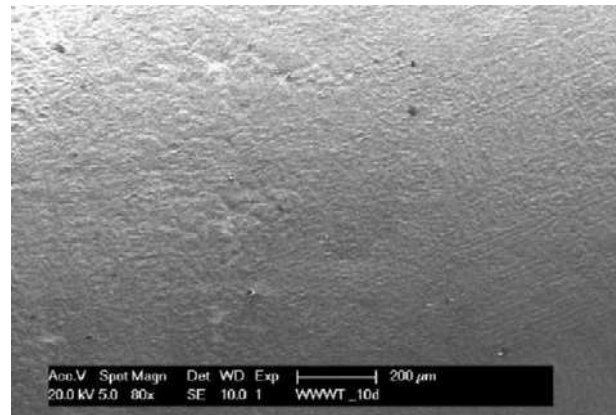
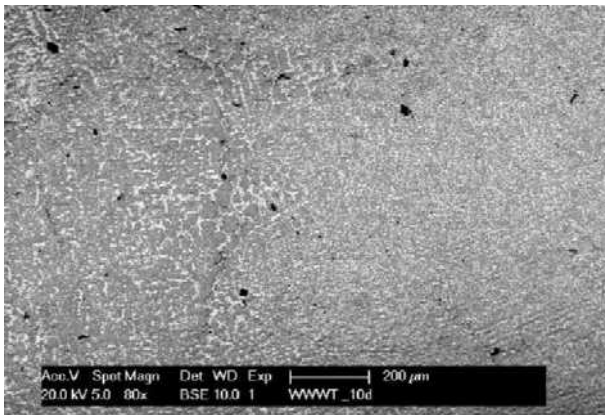


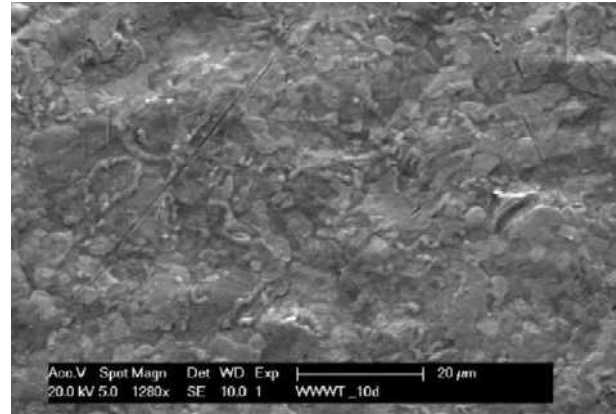
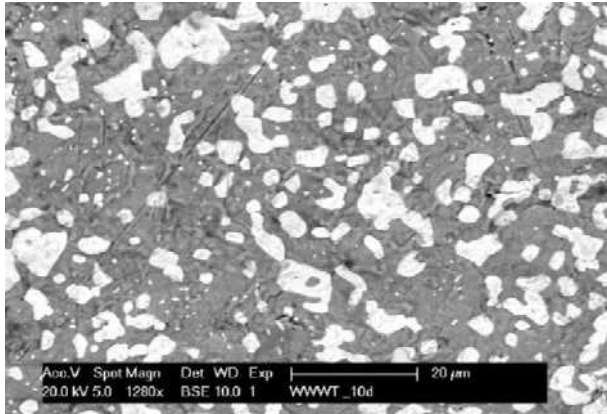
Different magnifications of the top side after 10 days of ageing at 120 °C (BSE images on the left and SE images on the right):



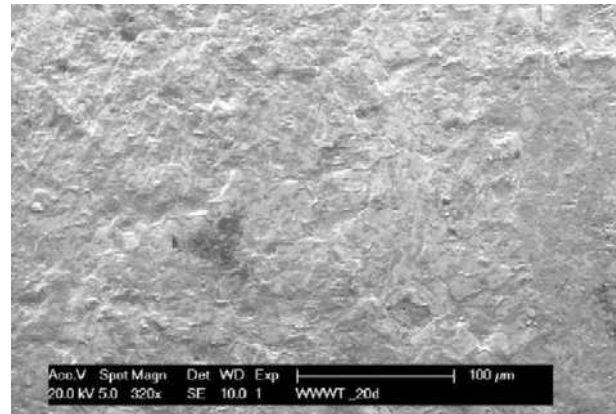
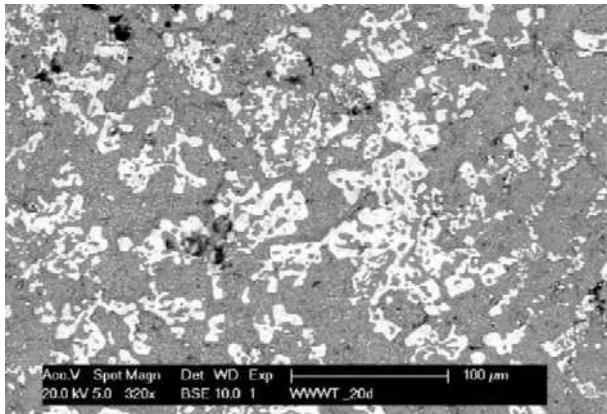
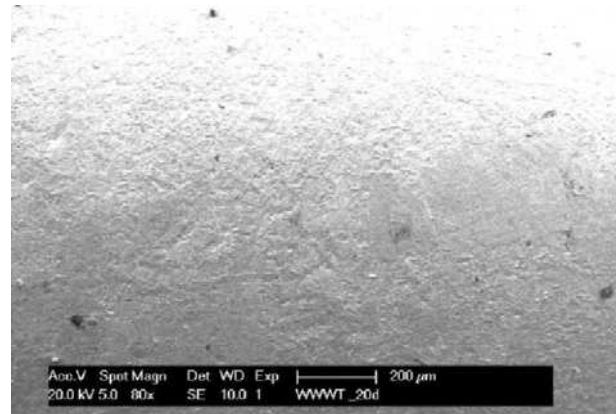
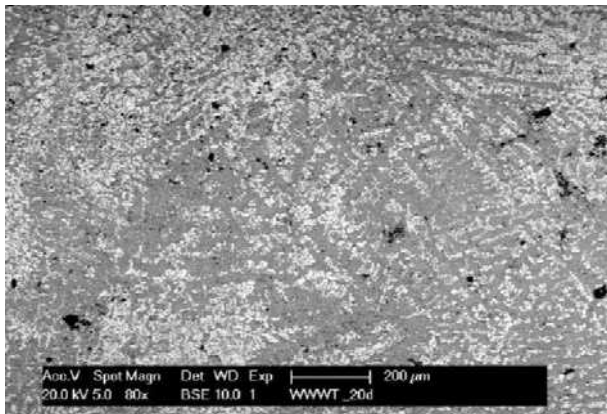


Different magnifications of the bottom side after 10 days of ageing at 120 °C (BSE images on the left and SE images on the right):

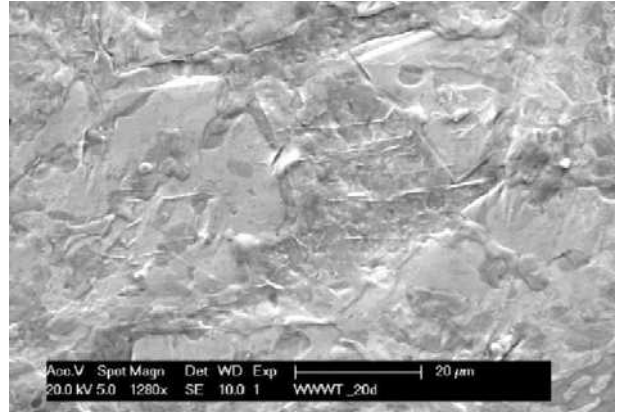
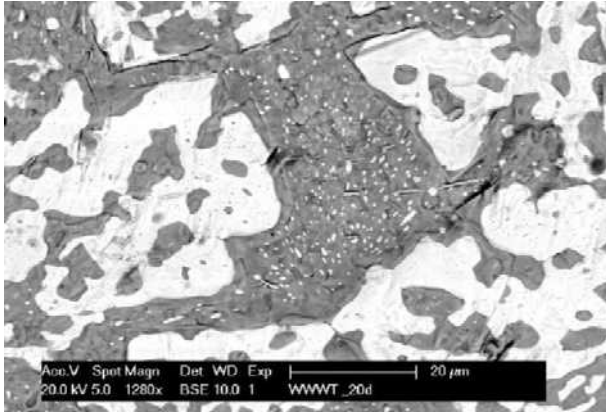




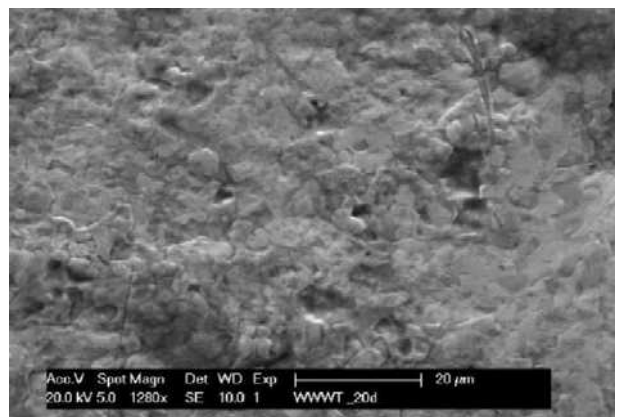
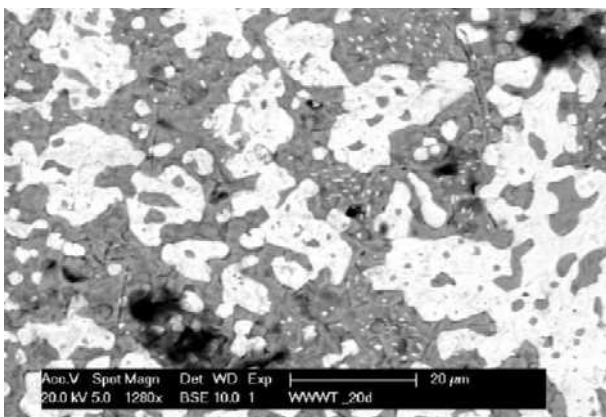
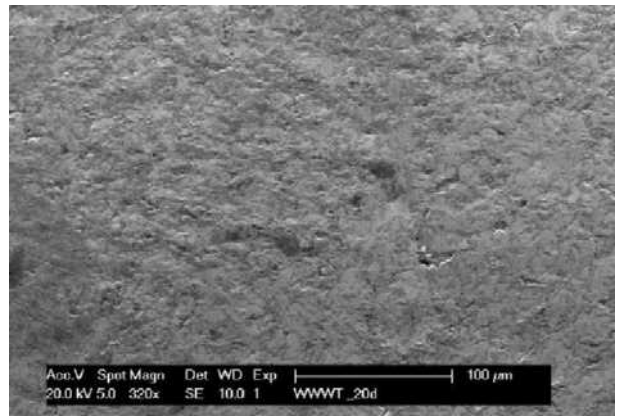
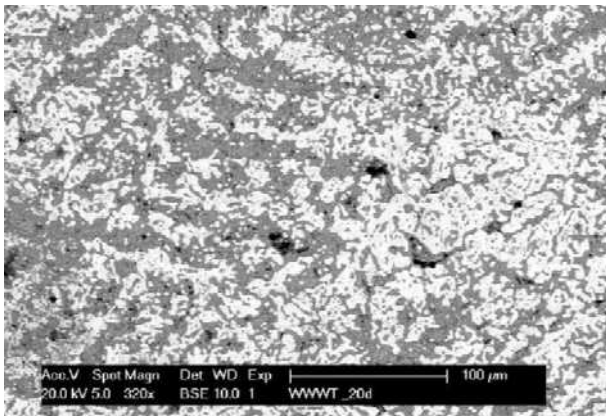
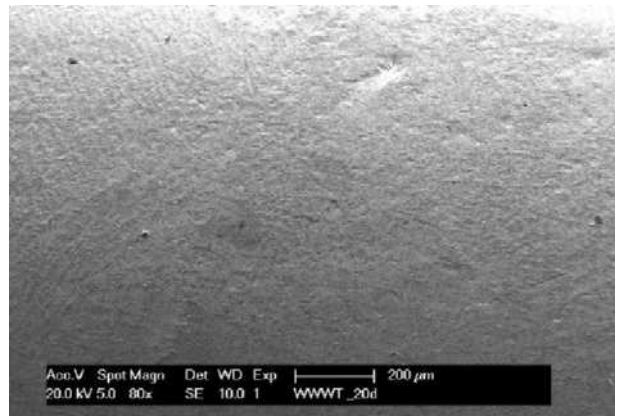
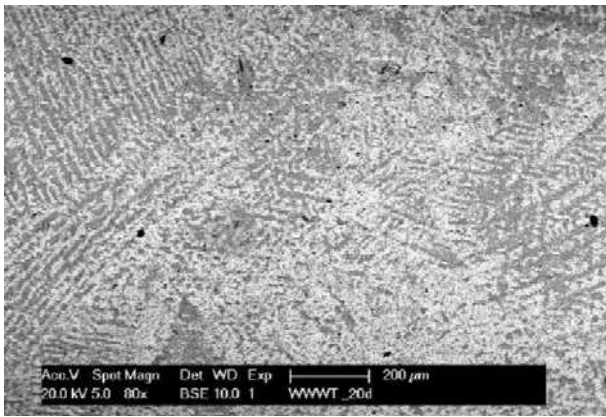
Different magnifications of the top side after 20 days of ageing at 120 °C (BSE images on the left and SE images on the right):



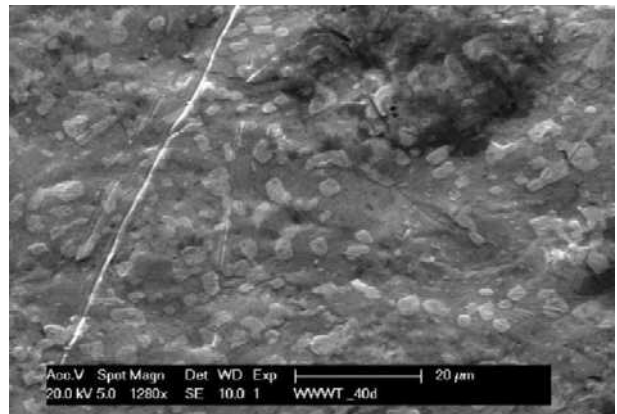
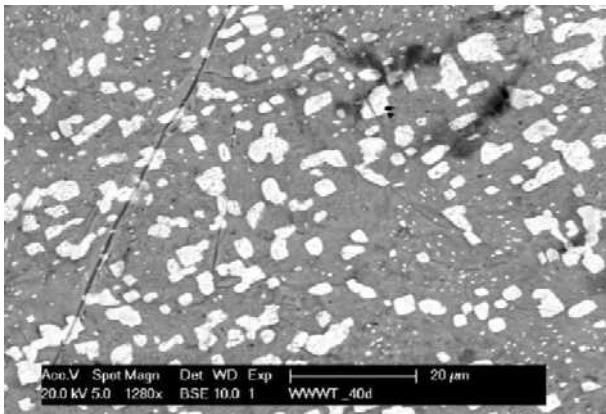
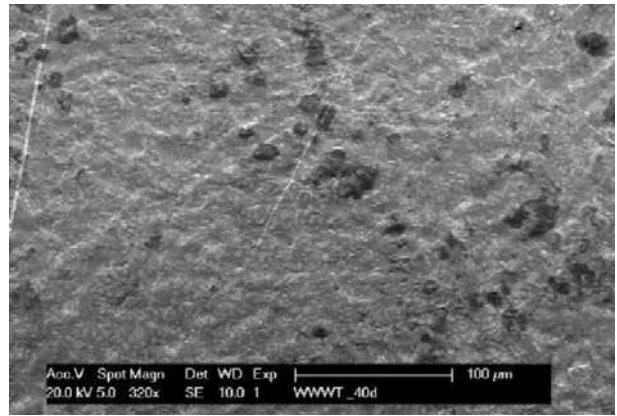
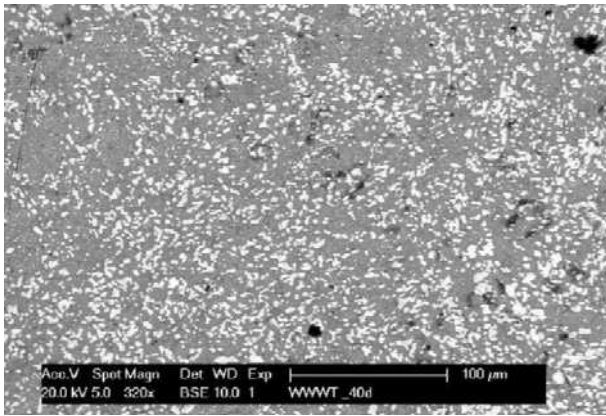
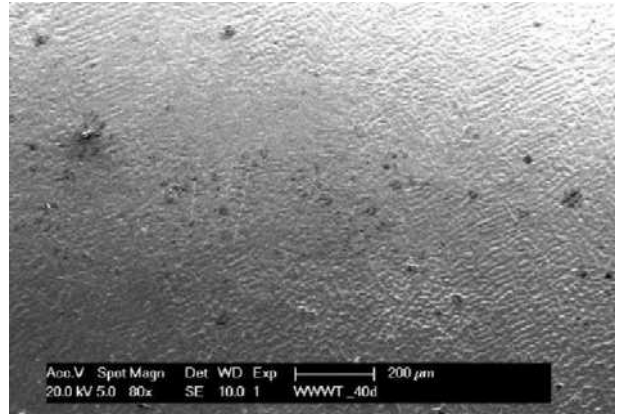
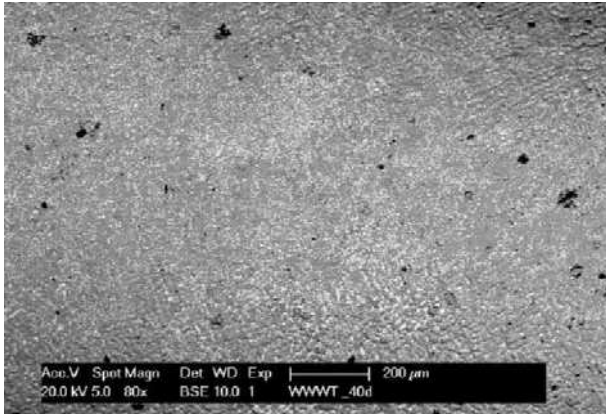




Different magnifications of the bottom side after 20 days of ageing at 120 °C (BSE images on the left and SE images on the right):



Different magnifications of the top side after 40 days of ageing at 120 °C (BSE images on the left and SE images on the right):



Different magnifications of the bottom side after 40 days of ageing at 120 °C (BSE images on the left and SE images on the right):

